Investigations of Thermally Induced Morphology in P3HT/PCBM Thin Films: Influence of Composition and Thermal Annealing on Photovoltaic Properties

Ochai Oklobia

A thesis submitted in partial fulfilment of the requirement of Staffordshire University for the degree of Doctor of Philosophy

February 2016

ABSTRACT

Organic solar cells based on P3HT: PCBM bulk heterojunctions show promise for high power conversion efficiencies. The properties of composite donor polymers and acceptor materials play a significant role; hence the need for optimised bulk heterojunctions active layer morphologies is critical for efficient devices.

To achieve optimised bulk heterojunctions, compositional factors and processing conditions are two primary aspects to focus on. Thermal annealing has been demonstrated to be one of the most successful processing techniques for morphology optimisation in P3HT – based organic solar cells. However the crucial correlation between composite composition and thermal annealing in P3HT – based devices is not fully understood yet.

Combining optical absorption spectroscopy, structural and electrical methods; the properties of P3HT: PCBM blend thin films, with different PCBM percentage weight ratios were studied in this work. Optical absorption spectra results for all three blend ratios, i.e., 1:1, 1:0.8, and 1:0.6, showed that the peak absorption intensity associated with PCBM reduced the most for the 1:1 ratio, after thermal annealing at 175°C. The impact of the correlation between PCBM composition and thermal annealing on photovoltaic performance parameters was demonstrated. For the three different PCBM compositions, the optimum power conversion efficiencies were determined at different optimum thermal annealing conditions. Optimum power conversion efficiency of 3.38% (1:1) was obtained at 175°C, whilst 2.27% (1:0.8) and 1.44% (1:0.6) were demonstrated at 125°C respectively.

To further probe the influence of thermally induced PCBM molecular segregation and aggregations, three different thermal annealing strategies were employed; namely, annealing (i) gradually from 50°C – 175°C, in steps of 25°C, 10 minutes each (ii) at high temperature 175°C, for 10 minutes once, and (iii) at 175°C for a longer time, i.e., 60 minutes . Optical absorption spectroscopy results reveal the dependence of PCBM aggregation on different thermal annealing strategies. Employing Raman spectroscopy mapping methods, the surface of thin films were mapped revealing and confirming PCBM rich regions upon thermal annealing. Furthermore exciton generation rate studies proved useful in establishing a good correlation between the estimated excitons generated, with short circuit current densities. The observed increase in excitons generated was also consistent with the photoluminescence spectra results which showed an enhancement in intensities upon thermal annealing.

Importantly, this work has shown the significance of employing different thermal annealing strategies in nanomorphology control of the bulk of active layers of organic photovoltaic devices. Importantly, it has also been demonstrated in the work of this thesis that gradual thermal annealing, in a controlled manner revealed a more stable and efficient control in tuning the nanomorphologies of P3HT – based solar cells.

In addition, impedance spectroscopy and capacitance – voltage measurement techniques have been shown to be very useful tools for characterising organic photovoltaic devices. Herein, it was shown that after thermal annealing at the optimum temperature of 150°C, impedance spectroscopy characterisation revealed extended charge carrier lifetimes in devices. This highlights the significance of having an optimised interpenetrating network within active layers of organic solar cells, as this have a critical impact on charge carrier lifetimes. Capacitance – voltage measurements was used to demonstrate the thermally induced vertical segregation of PCBM molecular aggregates also. The decrease in measured built – on potential from 0.68V (at film/cathode interface) from as cast device to about 0.35V after thermal annealing at 150°C, was shown to be indicative of vertical segregation.

ACKNOWLEDGEMENTS

Firstly, I would like to thank God for everything; by whose grace, He has helped, and sustained me through from the beginning to the end of this program.

I am so indebted to my supervisor Professor T. S. Shafai, who first and foremost offered me the chance at this program via a partial scholarship at Staffordshire University. I am deeply grateful for all his invaluable support, training, guidance and encouragement, and motivating enthusiasm. For his patience with me and also believing in me, it is much appreciated. I could not have asked for a better supervisor and a mentor, I am really appreciative, and I am proud to say that I have learnt from the best. For the partial scholarship awarded me by Staffordshire University, together with the working environment and laboratory facilities provided, I am thankful.

I want to acknowledge all the technical staff in the school of engineering and sciences for all the support and assistance they have kindly provided in various capacities.

I acknowledge also my family, for all their support and encouragement, I am very grateful for the blessing they have been in my life.

And for my friends, I am also thankful for all their prayerful support and encouragement that they have given me throughout the time of doing a PhD.

God bless everyone that has been involved in one way or the other in making this work a success.

LIST OF PUBLICATIONS

O. **Oklobia,** and T. Sadat-Shafai, (2014). Correlation between charge carriers mobility and PCBM cluster formation and its impact on recombination process in a blend of PCBM/P3HT bulk Heterojunction solar cell. *Solar Energy Materials and Solar Cells*. 122, 158-163

T. Sadat-Shafai, and **O**. **Oklobia,** (2014). Effects of PCBM loading and Thermal annealing on the nanomorphology of blend of polymer/fullerene thin films solar cells: Impact on charge carrier mobility and efficiency. *Applied Mechanics and Materials*, 467, 160-165.

O. **Oklobia,** and T. Sadat-Shafai, (2013). A quantitative study of the formation of PCBM clusters upon thermal annealing of P3HT/PCBM bulk Heterojunction Solar Cell. *Solar Energy Materials and Solar Cells*. 117, 1-8

O. **Oklobia,** and T. Sadat-Shafai, (2013). A study of donor/acceptor interfaces in a blend of P3HT/PCBM solar cells: Effects of annealing and PCBM loading on optical and electrical properties. *Solid-State Electronics*. 87, 64 – 68

TABLE OF CONTENTS

Chapter 3

Chapter 4

LIST OF TABLES

Chapter 4

Chapter 5

Chapter 6

LIST OF FIGURES

Chapter 1

Chapter 2

Chapter 4

NOMENCLATURE

The following is a list of the main abbreviations used throughout the text. Any abbreviation not included here is properly defined in the text.

PV	Photovoltaic
OSC	Organic solar cell
CO_2	Carbon dioxide
Si-based	Silicon based
D/A	Donor/Acceptor
BHJ	Bulk heterojunction
PCE	Power conversion efficiency
C_{60}	Fullerene
HOMO	Highest occupied molecular orbital
LUMO	Lowest unoccupied molecular orbital
UV	Ultra-violet
P3HT	Poly (3-hexylthiophene)
PCBM	[6, 6] phenyl-C_{61}-butyric acid methyl ester
OFET	Organic field effect transistor
OTFT	Organic thin film transistors
OLEDs	Organic light emitting diodes
E_g	Energy band gap
ϕ	Work function
V_{bi}	Built - in potential
MEH-PPV	Poly[2-methoxy-5-(2-ethylhexyloxy)-1,4-phenylenevinylene]
MDMO-PPV	Poly[2-methoxy-5-(3′,7′-dimethyloctyloxy)-1,4-phenylenevinylene]
FWHM	Full width at half maximum
AFM	Atomic force microscopy
GIXRD	Grazing Incidence X-ray Diffraction
LCDs	Liquid crystal displays
ITO	Indium tin oxide
PL spectra	Photoluminescence spectra
TOF	Time of Flight
SCLC	Space charge limited current
GPIB	General purpose interface bus
LCR	Inductor, capacitor, resistance
Al	Aluminium

Chapter 1

Introduction

"I'd put my money on the sun and solar energy. What a source of power! I hope we don't have to wait until oil and coal run out before we tackle that."

– ***Thomas Edison, 1931***

1.1 Overview

Energy from fossil fuels mostly includes coal, crude oil or natural gas. These are natural resources that the earth is endowed with. Fossil fuels supply nearly 90 percent of the energy consumed globally, according to the U.S. Department of Energy. Of this amount, oil accounts for about 41%, coal 24% and natural gas provides about 22%. It is also expected that global energy consumption will increase by 50% over the current rate by the year 2020. One of the problems with fossil fuels is that they are limited. According to international organisations, the estimated length of time left for fossil fuels are: oil (50 years), natural gas (70 years), and coal (250 years). The probable consequence of this fact could be a sudden rise in energy prices in the long run. Another identified problem however is concerned with the environment; release of greenhouse emissions, resulting in global warming, which is hazardous for the planet. On an average, it is estimated that the quantity of carbon dioxide (CO_2) emitted per mega joule of energy produced from burning fossil fuels are as follows (Metz et al. 2007): 92.0g (coal), 76.3g (conventional oil), and 52.4g (conventional gas).

On the other hand however, there are the energy income sources (Neville, 1978, Lynn, 2010), or renewable energy sources. These unlike fossil fuels are considered to be in limitless supply, as they quickly replenish themselves and can be used again and again. Examples of renewable energy sources include hydropower, wind and solar energy. These renewable

forms of energy in contrast to fossil fuels do not pose any threat to the environment, thus making them suitable alternatives. Available technologies for harnessing such renewable energy sources include dams for hydropower, wind turbines for wind energy, and photovoltaic (PV) technologies for solar energy.

It is interesting to note that solar energy offers a wide range of benefits; such as its regular availability, and it can be harnessed without sacrificing valuable land space. In addition, unlike other renewable energy technologies, PVs employing photovoltaic devices not possess moving parts. Hence they do not require regular maintenance. This makes the PV technology an attractive renewable energy technology.

In less than an hour, the surface of the earth receives on average, about 1.2×10^{17} W of solar power (Chen, 2011). This is more than enough to meet the global demand for an entire year. Assuming 30% of the Sun's energy is lost in the atmosphere, and that there is appreciable sunshine for an average of 6 hours a day, it is estimated that 2.88 kWh/day per unit area of power is delivered to the earth from the Sun. If for one hour, this energy arriving at just a single square meter area can be captured and reused, it is enough to run a number of household electrical appliances for a day.

As a renewable distributed resource, PVs could in the long run make a major contribution to national energy security and carbon dioxide reduction. In the UK, for example, each kWp (kilo peak watts) of PV installed avoids the emission of about 1 tonne CO_2 per year (Nelson et al. 2014).

Today, for a growing number of power needs, solar cell electricity stands out as the cheapest, cleanest and best way to generate electricity. As the saying goes, not all that glitters is gold. So in the same vein, PVs particularly Silicon-based PV cells are not without disadvantages. Among some of the major disadvantages, cost ranks high in the list; for the cost associated with their processing and manufacturing technologies (high-temperature requirement for processing the semiconductor in a high vacuum environment) are still very high (Perlin, 2004; Wenham et al. 2007). An alternative approach is needed, one that will address the issues of cost associated with Si-based PVs. Such an alternative will involve the use of organic semiconducting materials, which can be processed at relatively low temperatures, such as by vacuum deposition, or, preferably from solution. Ease of processing, together with facile material synthesis, flexibility, and low cost fabrication, are the various attributes that make the organic solar cells attractive and a potentially suitable alternative to the Si-based

PVs. In the next section, a brief history and description of organic solar cells will be presented.

1.2 Organic Solar Cells (OSCs)

Although inorganic based PVs as earlier mentioned have demonstrated relatively high power conversion efficiencies (Green et al. 2011), organic based solar cells have in recent years attracted great attention. In the last few years, organic solar cell technologies have received a growing interest amongst university research groups, and industries alike. This is owing to their potential for low-cost production, flexible device applications, and facile fabrication from materials that are easily synthesized (Brabec, 2004; Shaheen et al. 2005). The characteristic low cost production technology of OSCs allows for high throughput of devices on flexible substrates for example. It has been shown that this can be achieved by implementing processes like reel-to-reel, ink-jet printing or spray deposition techniques (Nelson 2002; Günes et al. 2007). All of these attributes are at the heart of the organic solar cell technology advantage.

The study of organic solar cells dates back to the late 1950s albeit at a low level until recently. Interestingly in the years leading up to the 1970s, the field received a boost as a result of realizing conductivity in the polymer polyacetylene (Chiang et al.1977). Following this breakthrough, Chiang and co - workers were awarded a Nobel Prize in Chemistry, in 2000. On the basis of their work at the time, the so – called homojunction devices were successfully fabricated (Nelson, 2002). These devices were fabricated using a single organic material sandwiched between two electrodes, with an efficiency yield of less than 0.1%. The asymmetry in the metal electrode work functions provided an electric field which drives separated charges towards the respective electrodes. The challenge with this device structure however, was that the electric field was insufficient to dissociate photo generated excitons (Nelson, 2002). Due to the very nature of their low power conversion efficiencies, they are considered unsuitable for application.

A major advancement was introduced by Tang (1986), which utilized an electron donating material in conjunction with an electron accepting material, sandwiched between electrodes. The electron donating material has a high tendency to lose electrons (i.e., high ionization potential), whilst the electron accepting material on the other hand has a characteristic high electron affinity. The interface between these two materials is referred to as a donor – acceptor (D/A) heterojunction (bilayer junction). At this junction a chemical potential offset

is created. This chemical potential, due to the differences in electron affinity and ionisation potentials of the two materials, facilitates the dissociation of excitons generated near them (Tang, 1986). This photovoltaic device at the time showed limited power conversion efficiency (PCE) of only ~1%, under simulated AM2 illumination. The bottleneck with the device structure however, is with the exciton diffusion lengths. This is the distance an exciton can travel before it decays radiatively and/or non-radiatively (Bradley, 1993; Pacios & Bradley, 2002; Günes et al. 2007), thus failing to yield free charges. Unlike Silicon, excitons in organic semiconductors are tightly bound by Columbic forces (Bradley, 1991). In order to generate photocurrent in these devices, excitons must be created within a few nanometers of a D/A interface. At the interface, charge transfer occurs, with electrons to the material of higher electron affinity, and holes retained in that with higher ionisation potential. The typical exciton diffusion lengths in organic semiconductor materials are generally small, in the range of 5-10 nm (Hoppe & Sariciftci, 2004). Therefore it is expected that they should be formed within their exciton diffusion length of the interface, in order to generate photocurrent efficiently (Blom et al. 2007; Nicholson & Castro, 2010). Unfortunately this was the case observed in the bilayer device structure. Since it consisted a single interface (at the planar junction), only the excitons created very close to the interface are dissociated. Additionally, it was also noted that the diffusion lengths of organic materials are much shorter than the absorption depth of the film, which is roughly about two orders of magnitude smaller (Pacios & Bradley, 2002). This was found to place a limitation on the thickness of the light absorbing layer, and hence optical absorption of the device.

Following the development of bulk heterojunction (BHJ) structure (Yu et al. 1995), a much more significant advancement came about in the mid 1990s. As a result of this, a dramatic improvement in the efficiency of organic solar cells was demonstrated. In contrast to bilayer heterojunction device architecture, the BHJ consists of dispersed D/A interfaces on a nanostructured scale throughout the bulk of the active layer. This structure was achieved by blending the electron donating and accepting materials in suitable organic solvents. Therefore in such structures, excitons are more likely to be created within a few nanometers of D/A interfaces, and then dissociated before decaying (Pacios & Bradley, 2002; Nicholson & Castro, 2010). This significantly increases the chance of dissociating a majority of created excitons efficiently. The BHJ architecture happens to be one of the most important advances in the field of OSCs.

In their work, Heeger and co-workers (1995) reported a monochromatic PCE of 2.9%, based on the BHJ device structure, by blending a polymer with buckminsterfullerene. The class of materials employed as the photoactive layer in their work are semiconducting conjugated polymers and small molecules (Yu et al. 1995; Blom et al. 2007). These classes of materials have received widespread attention over the recent years. The polythiophenes are amongst the most popular electron donating semiconducting materials investigated in BHJ OSCs (McCullough, 1998). Their applications have been demonstrated to extend even beyond OSCs. Such applications include light emitting diodes (Bradley, 1991; Bradley et al. 1998), and organic thin film transistors (Kim & Bradley, 2005). On the other hand, fullerenes are by far the most successfully implemented acceptor materials in BHJ OSCs (Shaheen et al. 2001; Hoppe & Sariciftci, 2004). In particular, due to their limited solubility, other derivatives of the fullerene, C_{60} have been synthesised (eds. Rand & Richter, 2014), and as a result the ease of processing BHJ OSCs from solution is improved. Figure 1.1 shows a 3D schematic illustration of a bilayer and BHJ device structure.

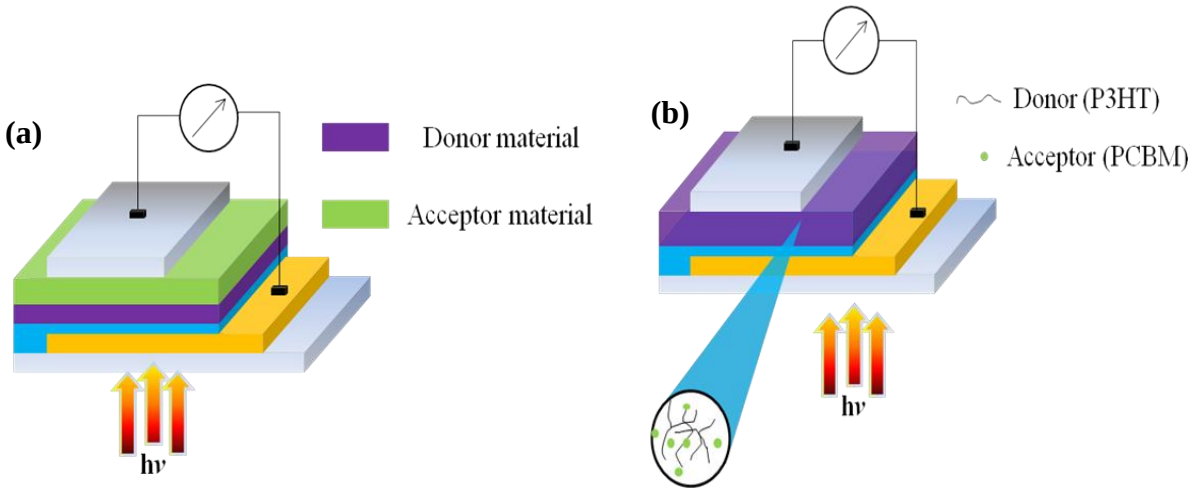

Figure 1.1: 3D schematic design of (a) Bilayer heterojunction OSC, and (b) BHJ OSC. The photoactive layer is sandwiched between a cathode and hole extracting anode.

1.3 Working Principles of Organic Solar Cells

The basic principles of operation of the organic solar cell are as follows:

i. ***Photon absorption***, which leads to the formation of coulombically bound electron-hole pairs (excitons),

ii. ***Exciton generation and diffusion*** to a D/A interface, followed by

iii. ***Charge separation*** (preceded by an initial charge transfer) and

iv. ***Charge transport to and collection*** *at* the electrode contacts (anode-holes and cathode-electrons), yielding direct current to an external circuit.

The fundamental mechanisms of operation of the BHJ organic solar cell, from photon absorption to the generation of photocurrent in devices are illustrated in Figure 1.2. Each process outlined above leading up to charge generation, contributes to the external quantum efficiency (Forrest, 2005). The efficiency of each of these processes together contributes towards the useful electric current that the organic solar cell can yield. In other words, the photoelectric current delivered by the device depends on efficiency of (Hoppe & Sariciftci, 2004): photon absorption (η_A), electron – hole pair dissociated (η_{ED}), charge transport (η_{CT}), and charges that are collected at the electrodes (η_{CC}). The product of these efficiencies together defines the external quantum efficiency, i.e. $\eta_{EQE} = \eta_A \times \eta_{ED} \times \eta_{CT} \times \eta_{CC}$.

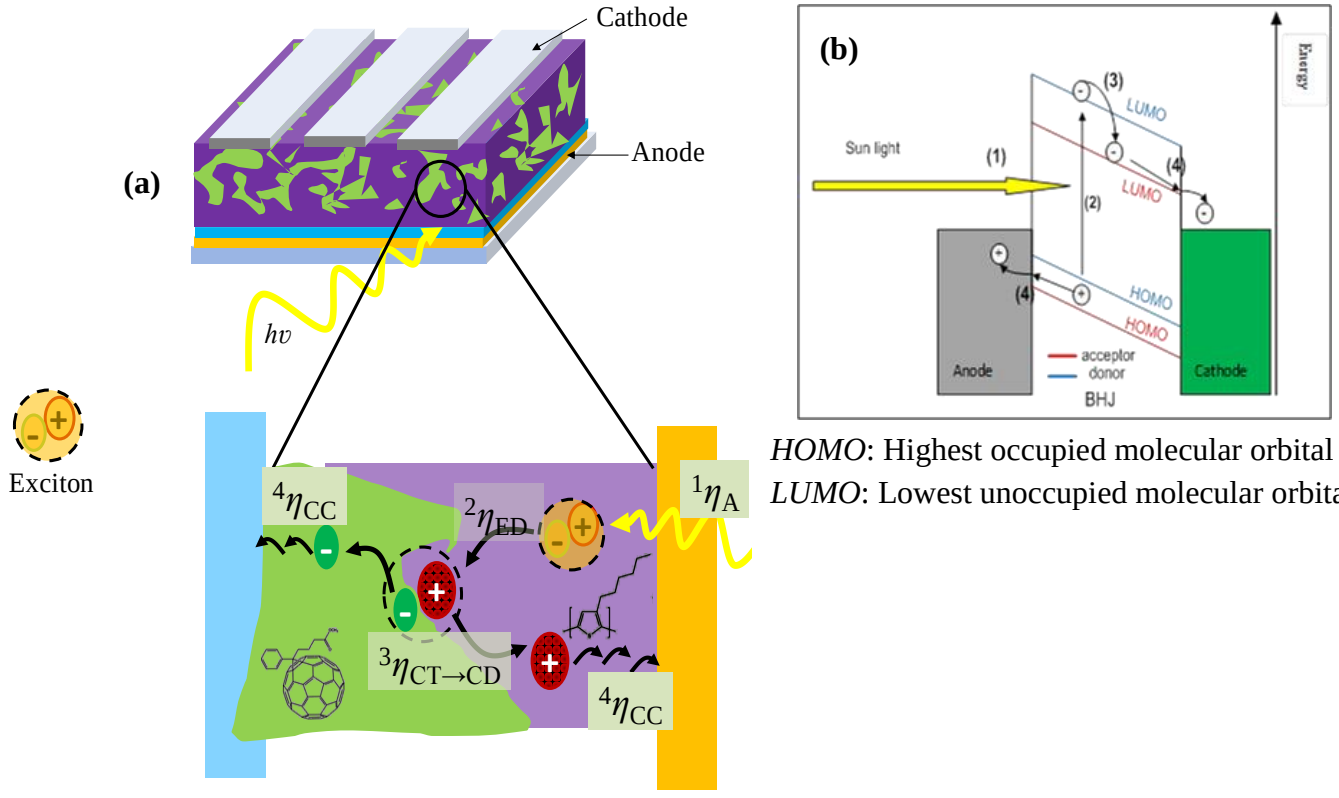

HOMO: Highest occupied molecular orbital
LUMO: Lowest unoccupied molecular orbital

Figure 1.2: (a) A schematic of the BHJ OSC, illustrating the significant processes within the photoactive layer of the device, following photo excitation. (b) Energy band diagram representation of the process of operation in an OSC.

As indicated in Figure 1.2, the efficiencies of photon absorption, exciton diffusion to the nearest D/A interface, charge separation (following initial charge transfer), and charge transport to and collection at respective electrodes are represented as ${}^{1}\eta_{A}$, ${}^{2}\eta_{ED}$, ${}^{3}\eta_{CT\rightarrow CD}$, and ${}^{4}\eta_{CC}$. The efficiencies of these processes are crucial to device parameters such as current densities, open circuit voltage, and the fill factor (which shall be discussed in the next chapter). These in turn directly influence the power conversion efficiencies (PCEs) of the OSC devices.

1.4 Challenges

From reports, OSC devices have achieved at best PCEs in the range of 3.5 – 9.5% with the single junction BHJ device architectures (Liang & Yu, 2010; Green et al. 2011; Liao et al. 2013). Despite the progress made so far in improving PCEs, OSCs are generally still not as widely commercially viable as their Si-based PV counterparts. To achieve commercial viability however, it is generally accepted that OSCs exhibit a PCE yield of more than 10%, in addition to demonstrating long – term stability as well (Brabec et al. 2010). The PCE of OSCs is mainly a function of the devices' photogenerated current density, open circuit voltage and fill factor (Nelson, 2002). These together are regarded as the PV performance parameters. Improvement of these parameters is necessary for maximizing PCEs. To do so however, there are a number of significant challenges OSCs are faced with, that needs to be addressed. Addressing these has been the major driving force behind current research in this field. Some of these challenges are briefly discussed further in the following sections.

1.4.1 Increasing the Absorption range of the photoactive layer

By increasing the absorption spectrum of the device's photoactive layer materials, the potential for harvesting useful incident solar radiation increases (Nelson, 2002). Consequently this contributes to improvement in photogenerated charges. Unlike their inorganic counterparts, most organic semiconductors are known to have wide band gaps, (*1.9-2.2*eV) (Liang et al 2009). Such wide band gaps translate to absorbing small fractions of the solar spectrum. Therefore resulting in limited absorption efficiencies (η_A), and ultimately limiting the device's photocurrents. Having band gaps which corresponds to an extended absorption spectrum, preferably towards the infra-red region is desirable. It has been suggested that utilizing low band-gap organic semiconductors (*band gaps preferably <1.8*eV) is beneficial, as the absorption spectra of photoactive layers will increases respectively.

Consequently, the spectral photon harvesting efficiencies of devices is enhanced (Brabec et al. 2001; Wen et al. 2008). The development of new classes of semiconductors with low band gaps is therefore essential. Recently, OSCs based on newly developed low band polymers have demonstrated efficiencies of well over 4-5% (Peet et al. 2007). This was not however without extensive device engineering efforts. It is also important to note that the structure and synthesis of these materials does require judicious design, and the cost of doing so should be taken into consideration.

1.4.2 Enhancing the Efficiency of Exciton Dissociation

In addition to wide band gaps, which are material dependent, the other issue is system dependent. The system here refers to the nanoscale configuration formed by the donor and acceptor materials within the bulk of the photoactive layer following fabrication. To ensure that majority of (if not all) generated excitons in the absorbing material are dissociated effectively (see steps 2 and 3 in Figure 1.2), there must exists D/A interfaces in the region within the exciton diffusion lengths. For the OSCs, this is not entirely the case, as reports have suggested that not all generated excitons are successfully dissociated (Li et al. 2005; Mihailetchi et al. 2006). Having well defined nanostructured D/A interfaces uniformly distributed throughout the bulk of the photoactive layer is desirable and crucial for efficient exciton dissociation. The well defined nanostructure will not only ensure efficient exciton dissociation, but will also have an impact on the transport and collection of charges (Moule & Meerholz, 2009; Chen et al. 2009). Figure 1.3 illustrates an ideal nanostructured photoactive layer (morphology) for an OSC. This structure is characterised by a bi-continuous networks of D/A phases spanning between the two electrodes. This should almost guarantee 100% efficient exciton dissociation and subsequent transport and collection of separated charges.

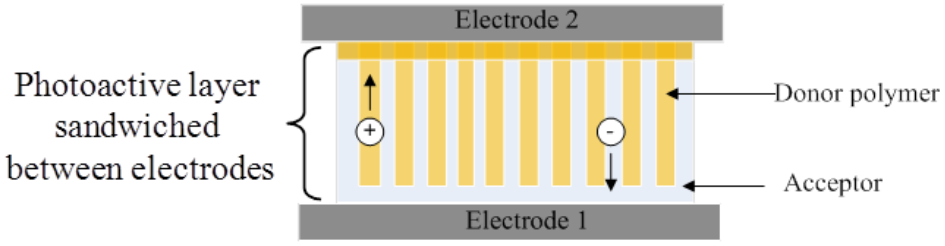

Figure 1.3: Schematic illustration of an ideal structure of a bulk heterojunction organic solar cell (Adapted from: Hoppe & Sariciftci, 2004).

Additionally, the photoactive layer thickness must be optimised for maximum absorption of useful photons. The bi-continuous pore radius is within exciton diffusion lengths, ensuring

maximum exciton harvesting. The same pores which are straight, also provides uninterrupted pathways for charge transport to the respective electrodes (Mayer et al. 2007). Although the current state of OSCs is far from this ideal, a number of methods have been developed for nanostructuring photoactive layers. One of these includes thermal annealing, which involves subjecting OSC devices to heat treatment, at a particular temperature and duration (Padinger et al. 2003; Kim et al. 2004). Others include exposing thin films to solvent vapour annealing (Li et al. 2007), exploiting the differential solubilities of donor and acceptor materials in various organic solvents for fabricating photoactive layers (Park et al. 2009; Dang et al. 2011). These methods have been shown to induce morphology variations to various extents.

Most morphology studies have shown that nanostructuring remains a challenge because a fine balance between exciton dissociation and charge transport properties is needed within the photoactive layers, for efficient devices. This is crucial as the balance, however largely depends on how precise and effective these methods are in tuning nanoscale morphologies to achieve an optimum phase separation, with respect to the processing conditions. Such conditions include donor – acceptor compositions, type of solvents and/or fabrication procedures, etc. Besides having optimum D/A phase separations, there also remains the question on how stable they are against aging effects (Hermans et al. 2009; Mayer et al. 2007). This is an important issue that requires addressing as OSCs operate under conditions where elevated temperatures must be expected (Hoppe & Sariciftci, 2004). Figure 1.4 summarizes the relationship between molecular structures (as it pertains to band gap), morphology (nanoscale structuring of D/A domains) and device properties. This suggests that the concurrent optimisation of these closely interconnected parameters is necessary for the design of highly efficient OSCs.

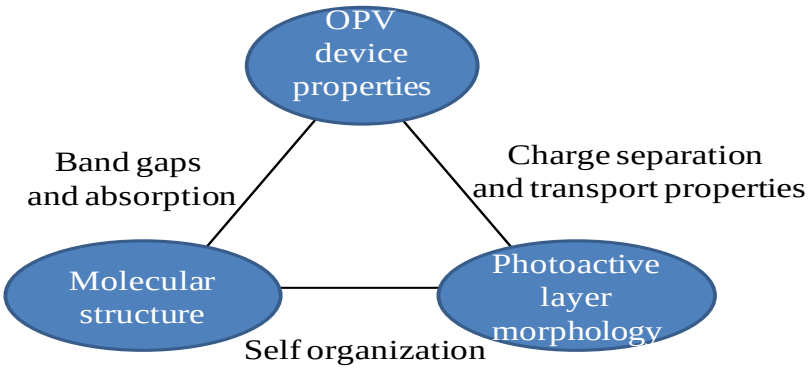

Figure 1.4: An illustration of the interrelationship between the molecular structure, nanoscale morphology and the device properties.

1.4.3 Charge Transport

Charge transport properties can also be indirectly influenced by the nanostructuring of photoactive layers as highlighted in the previous section. However, for most organic semiconductors, their charge - carrier mobilities are inherently low, with typical values < 10^{-2} cm^2/Vs, in contrast to their inorganic counterparts (e.g., 0.1 – 1 cm^2/V.s, for amorphous silicon) (Coropceanu et al. 2007). For the majority of donor – acceptor combinations in the BHJ OSCs, carrier mobilities are not similar, since hole mobilities in the donor phase are often lower than that of electrons in the acceptor phase (Milhailetchi et al 2005). This leads to unbalanced carrier mobilities in the systems, consequently creating the problem of charge build – up (mostly holes). This is a phenomenon known as space charge limited conductivity which shall be further discussed in chapter 2. Studies have indicated that one of the ways of addressing this problem is to have a preferred interpenetrating network of crystalline domains, with increased connections between them. Therefore the active layer will comprise a network of uninterrupted percolating pathways for efficient charge transport (Moulé & Meerholz, 2008). This will not only benefit efficient charge transport, but will also contribute to reducing series resistance, hence improving charge collection (Li et al. 2005). This approach is particularly associated with the nanostructuring of most existing donor – acceptor combinations in the bulk photoactive layer of the device. The development of newer materials can provide an alternate route for also addressing the problems of low charge – carrier mobilities. However, in developing new classes of polymers as suggested in section 1.4.1, it is imperative not only to develop new materials with optimum band gaps, but also with improved charge – carrier transport properties concurrently. This is a task that is in itself rigorous and challenging.

1.5 Research Motivation and Objectives

The need for optimised BHJ active layers, characterised by a preferred nanoscale interpenetrating and percolating system for efficient exciton dissociation, charge transport and collection, is critical for efficient devices. P3HT: PCBM BHJ OSCs have been reported to demonstrate efficiencies in the region of 3 – 6% (Reyes-Reyes et al. 2005, Kim et al. 2005; Li et al. 2005). A number of investigations utilizing a range of morphology tuning methods to achieve this have been reported (Li et al 2005; Shrotriya et al. 2006; Li et al. 2007; Huang et al. 2009; Pivrikas et al. 2011). Among these methods, thermal annealing is one of the most successful processing techniques for optimizing morphologies of P3HT – based solar cells.

The effectiveness of the induced morphology is primarily a function of the method and processing conditions employed (Roman, 2005). Other than the processing methods, PCBM composition also plays a significant role in influencing PV performance properties. The interplay of composition and thermal annealing in optimising active layer morphologies in P3HT: PCBM solar cell is an area that has not been fully understood yet. Understanding the impact of the correlation between PCBM composition and thermal annealing on PV performance parameters is crucial for optimising the OSC. To achieve this, it is necessary to provide a qualitative and quantitative evaluation of thermally induced PCBM aggregation within P3HT: PCBM blend thin films (for varying PCBM compositions).

Optical absorption spectroscopic characterisation of P3HT: PCBM thin films have mostly been reported only in the visible range and near infra-red (i.e., 400 – 700 nm), neglecting in most part the significant ultra-violet (UV) range where PCBM absorption is prominent (Jeong et al. 2011; Jamieson et al. 2012). By observing the UV region of the spectra of P3HT: PCBM thin films; it is possible to evaluate donor/acceptor phase separations as a function of thermal annealing.

Since donor/acceptor phase separation has a significant impact on how efficient excitons are dissociated, engineering the formation of PCBM molecular aggregates within the active layer in a controlled and systematic manner is a necessary prerequisite for maximising PCEs. Most studies have reported the variation of PV properties with temperature (Ma et al. 2005; Li et al. 2005) or with differing thermal annealing times (Huang et al. 2009; Jo et al. 2009). These conditions, (either optimum annealing temperature or time), all constitute different strategies which is expected to induce different morphologies of the active layer. By employing three different thermal annealing strategies, this work will seek to provide a comprehensive set of morphology engineering protocols significant for the optimisation of PV performance properties. Other factors such as charge transport pathways, and loss mechanisms via recombination, which have a significant impact on device PCEs (Koster et al. 2006; Kim et al. 2007; Pivrikas et al. 2011), will also be probed.

Reports have suggested that a relationship may exist between charge carrier mobilities with exciton dissociation and recombination processes (Clarke & Durrant, 2010). The latter process is believed to be a function of trap centres within the active layer, which may be created during thermal induced nanostructuring (Milhailetchi et al. 2006). In the P3HT: PCBM systems, most discussions on thermal annealing have been centred on the significance

of the glass transition temperature of P3HT. The induced donor/acceptor phase separations around the polymer glass transition temperature is considered to be at a critical point, beyond which deterioration possibly occurs. Of particular interest however in this work, is to probe and address the impact of created trap centres on charge carrier mobility over a range of thermal annealing temperatures above the polymer glass transition temperature. Since at elevated temperatures, phase separations will be expected to be much pronounced.

Furthermore, by employing impedance spectroscopy measurements complimented with capacitance – voltage measurements, thermally induced vertical segregation mechanisms in P3HT: PCBM OSCs will be probed. The use of these techniques is not common, but has the potential for providing useful insight into the mechanism of vertical segregation. This is significant, as compositional gradient is expected to enhance contact selectivity towards one type of charge, thus reducing leakage currents (Campoy-Quiles et al. 2008).

It is expected that this work will provide a comprehensive understanding of key factors related to improving the efficiencies of P3HT: PCBM – based OSCs. The thesis will also be providing a framework relevant for designing high performance OSCs.

1.6 Thesis Organization

A brief review of organic semiconductors and concepts related to organic solar cells in particular are presented in Chapter 2. It includes discussions on the energy band model, and the physics contacts in semiconductor devices. Charge transport in organic semiconductors, in view of understanding current limiting characteristics is briefly described. In addition, the working principles of organic solar cells are further discussed in detail.

In Chapter 3, a brief outline of conjugated polymers employed in OSC devices is given. The conjugated polymer, P3HT and its properties will be described. Additionally, the properties of the fullerene acceptor material, used in conjunction with P3HT and other key OSC materials in this thesis are briefly discussed.

The list of materials used in the work of this thesis is presented in Chapter 4. Also in this chapter, details of characterisation methods and respective instrumentations are presented. This included discussions on the background approach of the experimental techniques employed in the work of thesis. The results obtained following the various measurements described in chapter 4, are presented in Chapter 5 and 6.

Chapter 5 is detailed discussion on optical and structural characteristics of thin films of P3HT, PCBM and P3HT: PCBM blend, whilst in chapter 6, the corresponding electrical and PV properties of thin films for an OSC application are presented.

Chapter 7 summarises the thesis, and provides an outlook on future works.

Chapter 2

Theory of Organic Semiconductors

"Even if there is only one possible unified theory, it is just a set of rules and equations..."

— Stephen Hawking, Astrophysicist.

2.1 Introduction

Solid materials are generally classified into three main categories, namely; conductors, insulators and, semiconductors. Conductors are commonly described as materials that permit current conduction, while an insulator does not. The semiconductor on the other hand is often defined rather loosely as a material, whose electrical resistivity lies in the range between typical conductors and insulators, i.e., $10^{-2} – 10^{9}$ Ωcm^{-1} (Bar-Lev, 1993; Yacobi, 2002). Due to this range of resistivity exhibited by semiconductors, they have been known to typically demonstrate a negative temperature coefficient of resistance and variable electrical conductivity. These unique properties of semiconductors make them suitable for a wide range of applications in electronic devices. Additionally, another class of materials referred to as organic semiconductors have now been recognized as the bedrock of organic electronics. These are organic materials in contrast to inorganic materials, such as silicon, which exhibit semiconducting properties. Following the works of Shirakawa and co-workers (Nunzi, 2003), where they reported electrical conduction in polyacetylene, extensive researches have been motivated in the area of organic semiconductors. Today organic semiconductors are increasingly employed as active materials in electronic devices such as organic light emitting diodes (OLEDs), organic field effect transistor or thin film transistors (OFET, or OTFT), and organic solar cells (OSCs) (eds. Brütting & Adachi, 2012). In this chapter, the physical

principles underlying the electrical conductivity processes in organic semiconductors are reviewed. In addition, the review encompasses a number of properties of organic semiconductors for photovoltaic applications.

2.2 Organic Semiconductors

Organic semiconductors in contrast to inorganic semiconductors (for example Si) are generally considered as semiconductors with 'intrinsic wide band gaps' in the order of 2 – 3 eV, exceeding typical semiconductor band gaps (e.g., 1.12 eV for Si) (Peter, 2009). The extent to which organic semiconductors have been applied in electronic devices is limited in comparison to its inorganic counterpart. The reason for this limited application of the organic semiconductor has been pinned down to their characteristic carrier trapping and relative low charge – carrier mobility (Yacobi, 2002). However, organic semiconductors posses relatively high absorption coefficients (typically $\geq 10^5$ cm^{-1}), meaning even thin films (< 100 nm) of such material can give rise to relatively high absorption of photons, this in a way partly compensates for its low mobilities (Hoppe & Sariciftci, 2004). An interesting property of the organic semiconductor is its unique advantage of diversity (i.e., flexible chemical structure) and relative simplicity with which their properties can be tuned to specific applications (Yacobi, 2002; Hoppe & Sariciftci, 2004). Another important difference between the organic and inorganic semiconductor is that the former has a relatively small exciton diffusion length (in the range of ~ 10 nm) (Halls et al, 1996; Haugeneder et al, 1999; Stübinger et al, 2001).

An example of an organic semiconductor material is the conjugated polymer which has over the years also received widespread attention, particularly following the award of the Nobel Prize in Chemistry in the year 2000, for the discovery and development of electrically conductive polymers (Peter, 2009). The basic feature of conjugated polymers is that they are made of alternating single and double bonds between carbon atoms, i.e., – C = C – C = C –. This is referred to as conjugation, hence conjugated polymer semiconductors. In the next section, the theory explaining the resulting formation of a band gap and energy levels due to the conjugation process in polymeric semiconductors is discussed.

2.2.1 Energy Band Theory

Originally developed on the basis of inorganic semiconductors, the energy band theory can be extended to encompass organic semiconductors, which are generally less ordered compared to their inorganic counterparts (Petty, 2007). The theory will help to provide an understanding of the underlying electronic structure of organic semiconductors. This is

achieved, in light of the unique bonding and molecular structures present in organic molecules. As previously mentioned, the essential ingredient of organic semiconductors is conjugation, i.e., a chain of alternating single and double bonds between carbon atoms. Conjugation produces two important changes in the organic molecule, namely; the splitting of discrete energy levels into nearly continuous bands of energy, and the characteristic delocalisation of charges in these levels (Peter, 2009). Figure 2.1 shows an illustration of the principle of conjugation and chemical structure of the simplest organic polymeric semiconductor, polyacetylene.

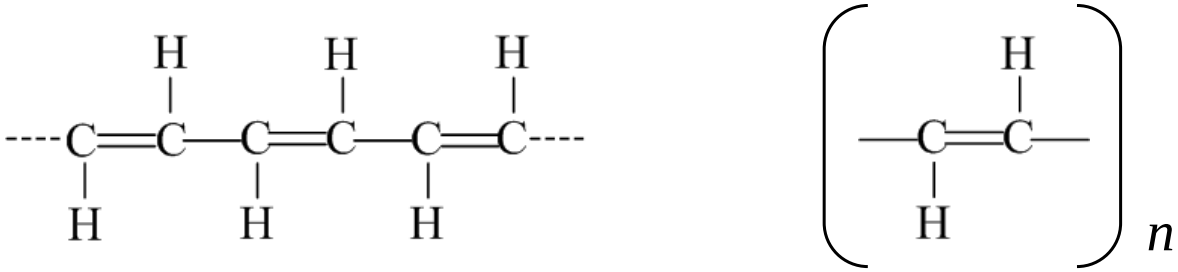

Figure 2.1: (a) Principle of conjugation in organic electronic materials (alternating single and double bonds), (b) Polyacetylene, the simplest organic polymeric semiconductor (Peter, 2009).

The construction of energy bands in organic semiconductors is interpreted in terms of molecular orbital interaction. Four electrons are available in carbon for forming bonds; three are considered to occupy the sp^2 hybridized orbitals and the fourth p_z orbital. During the process of bonding in organic materials, such as ethylene (C_2H_4), the three sp^2 electrons form covalent bonds via σ molecular orbitals to the next carbon atom and to the hydrogen atom. The remaining p_z electron is available to form covalent bond via a π molecular orbital. This is illustrated in Figure 2.2. Therefore in organic polymeric materials made of long chains of carbon atoms, the result of conjugation is a chain of alternating single (σ only) and double (σ and π) bonds. The interaction between neighbouring orbitals (p_z atomic orbitals) results in the splitting between π and π^* molecular orbitals. In additional chains of carbon atoms, this is seen as smaller splitting of the levels of discrete bonding π and antibonding π^* states. π electrons are considered to reside in the π band, whilst the π^* is empty at lower energy states (Jaiswal & Menon, 2006). These are recognized as the highest occupied molecular orbital (HOMO) and lowest unoccupied molecular orbital (LUMO). Figure 2.3 shows the process of the formation of HOMO and LUMO levels in a typical organic polymeric semiconductor. The energy levels HOMO and LUMO are synonymous to the valence and conduction band of

semiconductor physics respectively. The energy difference between HOMO and LUMO level represents the energy band gap (E_g).

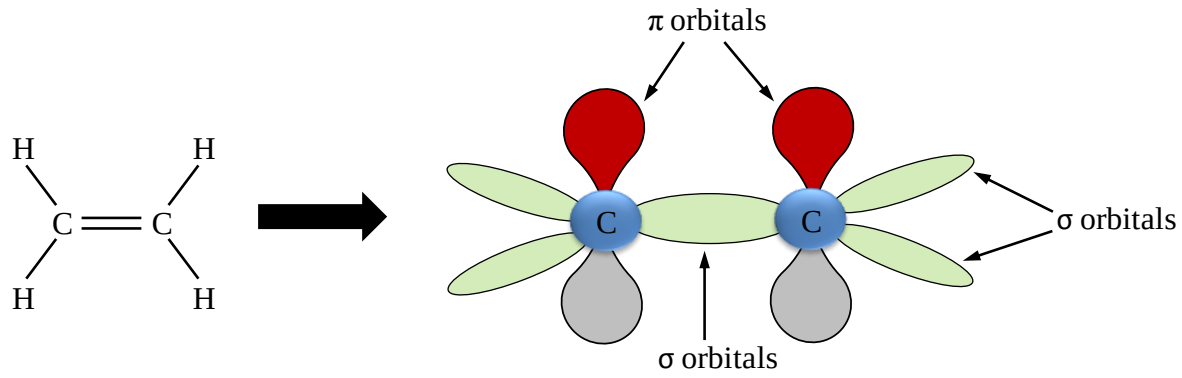

Figure 2.2: Model conjugated organic molecule, showing σ and π orbitals.

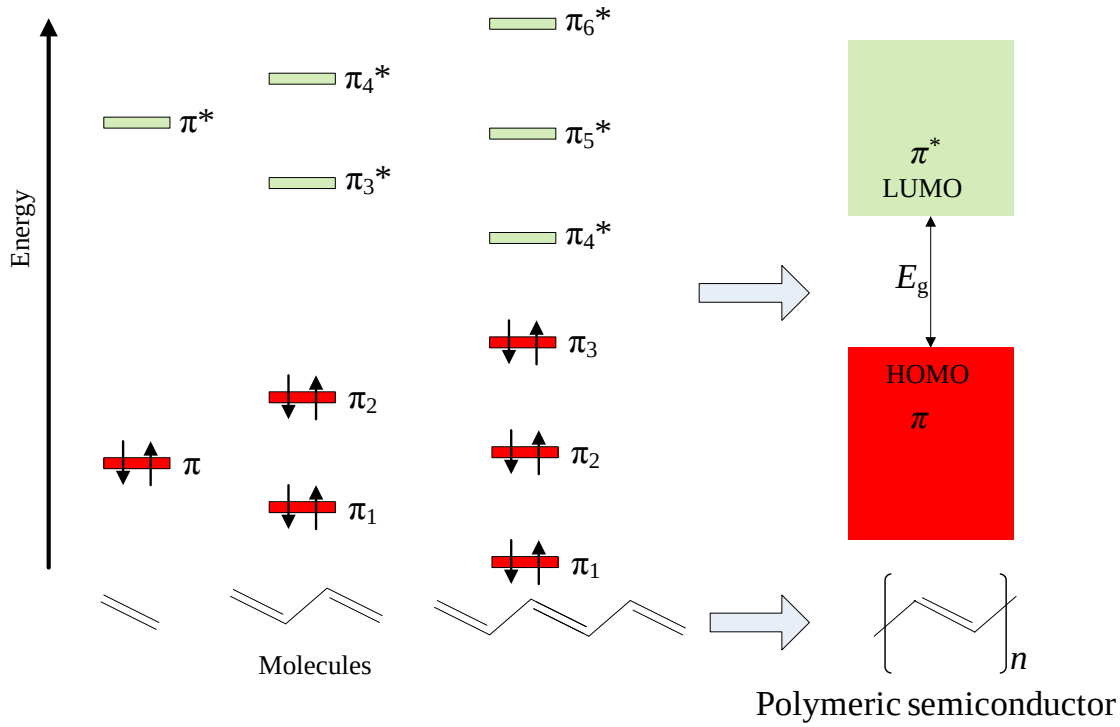

Figure 2.3: Molecular orbital interaction in the construction of energy bands in polyacetylene.

2.3 Charge Transport in Organic Semiconductors

In the ground state, the HOMO of the organic molecule is considered to be filled, similar to the valence band in inorganic semiconductors, and the LUMO remains empty. For charge transport to occur in such organic solids there must be a charge in the LUMO level. This can

be achieved by the injection or extraction of an electron at the interface of a metal electrode and the molecule (Peter, 2009), or through the dissociation of a neutral excited state in a molecule and subsequent charge transfer (Clarke & Durrant, 2010). The latter resulting in the generation of bound electron – hole pairs, which is a precursor of free charges in OSCs. The electron taken from or added to the π or π^* orbitals, result in the excited state of the organic molecule.

Due to weak intermolecular bonds in organic molecules, the delocalization of charges is not strong, in contrast to inorganic semiconductors, which possess rigid molecular structures with long – range order and periodicity. Furthermore, as a result of excitation or electron injection, there is a spatial distribution of electrons in the σ orbital, resulting in changes to the molecular geometry. For these reasons, organic semiconductors possess more localised charges and their characteristic transport is regarded as hopping from molecule to molecule (Lampert & Mark, 1970).

In the following sections, a review of important physical principles underlying the electrical processes in organic semiconductors for electronic devices, are presented. These are outlined referencing mainly OSCs.

2.4 Metal – semiconductor interface

Understanding the properties of metal – semiconductor interface is significant to the working processes in most organic electronic devices, such as an OSC. The organic semiconductor/metal electrode contact in organic solar cells is an example of a typical metal – semiconductor interface (junction). Such an interface is usually formed by the deposition of a metal on to a semiconductor material. Depending on the metal's work function relative to the semiconductor and the semiconductor type (*n* – or *p* – type), a rectifying junction or an Ohmic contact can be obtained. Figure 2.4 is a schematic representation of a metal – semiconductor interface, showing the energy band profiles before and after making contact. $e\phi_m$ and $e\phi_s$ are the work functions of the metal and the semiconductor respectively.

The built-in potential, V_{bi} is the difference between the work functions of metal and semiconductor ($\phi_m - \phi_s$), whereas the barrier height is expressed as

$$e\phi_B = e\phi_m - e\chi_s \tag{2.1}$$

where χ_s is the electron affinity of the semiconductor. The *depletion width*, *W* as a function of applied voltage, is given as

$$W = \left(\frac{2\varepsilon(V_{bi} \pm V)}{eN_d}\right)^{1/2} \tag{2.2}$$

The (±) in equation 2.2 indicates the forward and reverse bias conditions. Under thermal equilibrium, $V = 0$.

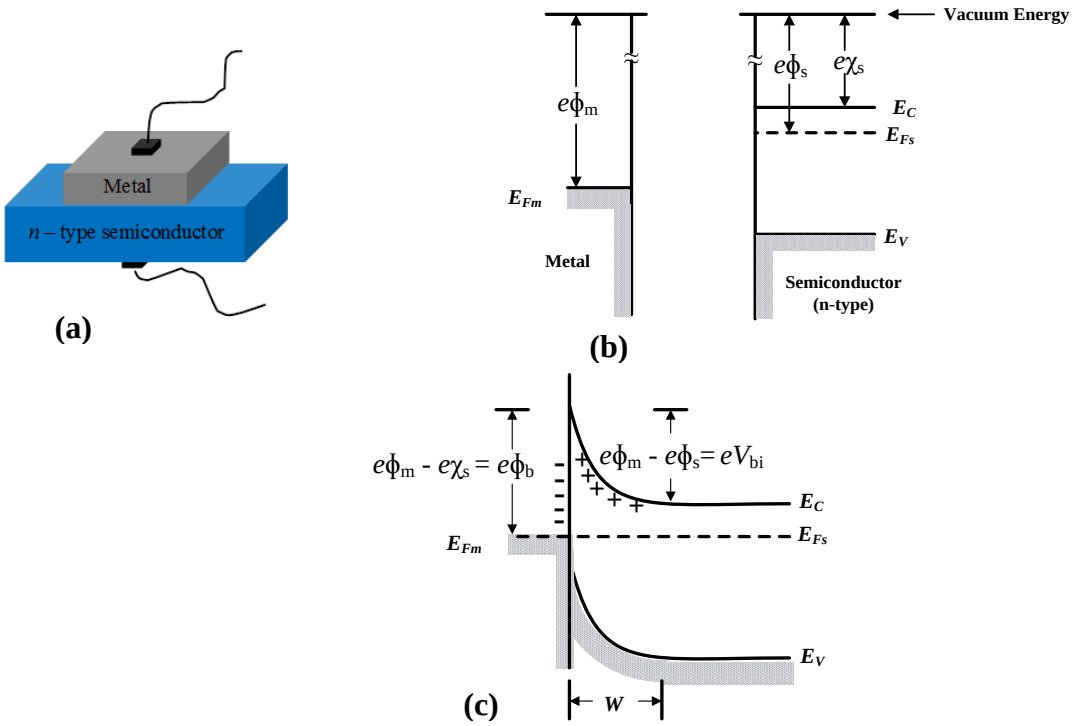

Figure 2.4: Schematic illustration of (a) a Schottky barrier junction, and energy band profile of a Schottky barrier junction (metal – *n* – type semiconductor) formation (for $\phi_m > \phi_s$) (b) before and (c) after contact (Adapted from Singh, 1994).

From the alignment criterion of Fermi level across a junction, it follows (for an *n* – type semiconductor) that if $e\phi_m > e\phi_s$, electrons flow is from semiconductor to metal. This result in the formation of a depletion layer, with a positive space charge on the semiconductor and negative on the metal side of the junction, see Figure 2.4(c).

When a positive voltage is applied to the semiconductor (for an *n* – type), as in Figure 2.4(c), $e\phi_B$ is increased. This corresponds to a reverse – bias condition, in which electron flow from semiconductor to metal is impeded. On the other hand $e\phi_B$ decreases for a negatively biased

semiconductor, electron flows from semiconductor to metal, thus a forward – bias condition. In the case of $e\phi_m < e\phi_s$, for the same *n* – type semiconductor in contact with a metal, an Ohmic junction is formed. As is evident in Figure 2.5(b), there is a downward bending (in the semiconductor) of the energy band edge upon the junction formation. The absence of a potential barrier at the junction means electrons can flow for either applied voltage – bias conditions.

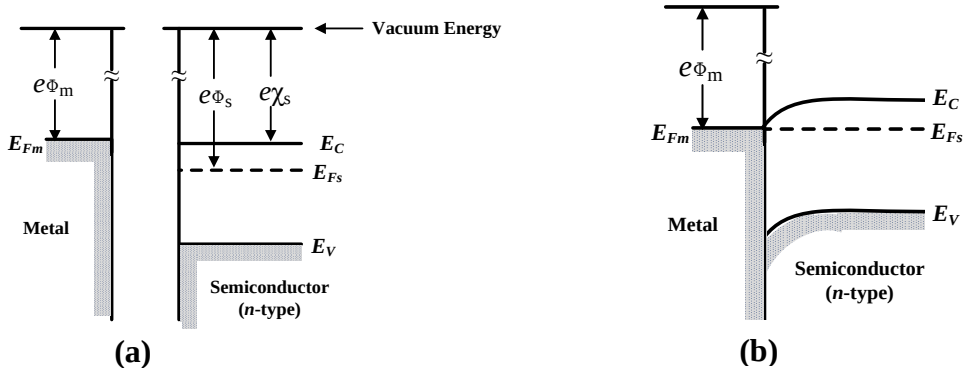

Figure 2.5: Schematic representation of the energy band structure of a metal – semiconductor junction for the formation of an Ohmic junction; (a) before and (b) after contact (Adapted from Bar-Lev, 1993).

If the semiconductor is a *p* – type, the considerations outlined previously applies; such that the junction is rectifying if $e\phi_m < e\phi_s$, whereas it is Ohmic if $e\phi_m > e\phi_s$.

2.5 Bulk Heterojunctions (BHJ)

When two semiconductor materials with different energy gaps are brought in contact, the resulting junction formed is referred as a heterojunction (Yacobi, 2002). Organic semiconductor applications in electronic devices such as OSCs, fundamentally incorporates heterojunctions. The semiconductor materials are usually termed as donor (electron donating) and acceptor (electron accepting) materials. Generally bulk heterojunctions can be achieved by co – deposition of the donor and acceptor inks (Geens et al, 2002; Peumans et al, 2003), or solution casting of donor – acceptor blend solutions (eds. Krebs, 2008). Donor materials are considered as *p* – type semiconductor (e.g., a conjugated polymer, as the electron donor), whereas acceptor materials are *n* – type semiconductor (e.g., a fullerene, as an acceptor) (Ma et al, 2005). Of the three types of OSC architectures discussed in section 1.2, both the bilayer and bulk are based on heterojunctions. The significance of the BHJ is have an intimately mixed donor and acceptor composition distributed throughout a bulk volume, such that donor/acceptor (D/A) interfaces are within the exciton diffusion length at each absorbing site

(Hoppe & Sariciftci, 2004). Figure 2.6 shows a schematic illustration of a heterojunction (between a *p* – type semiconductor, poly (3-hexylthiophene) (P3HT), and an *n* – type semiconductor, C_{60} (Jiang, 2007).

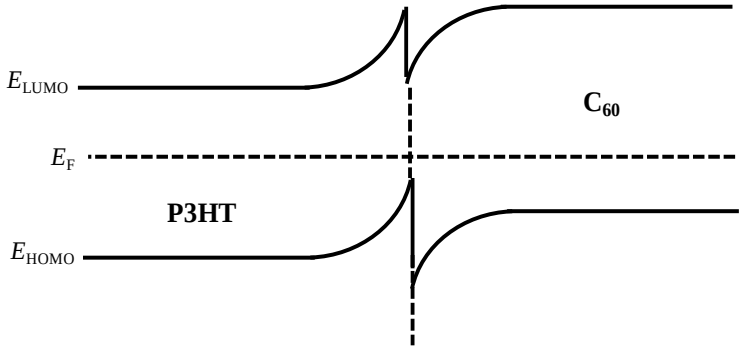

Figure 2.6: Schematic illustration of the energy band structure of P3HT/C_{60} heterojunction.

The schematic energy band diagram of the heterojunction (bilayer and bulk) in a typical OSC application is shown in Figure 2.7.

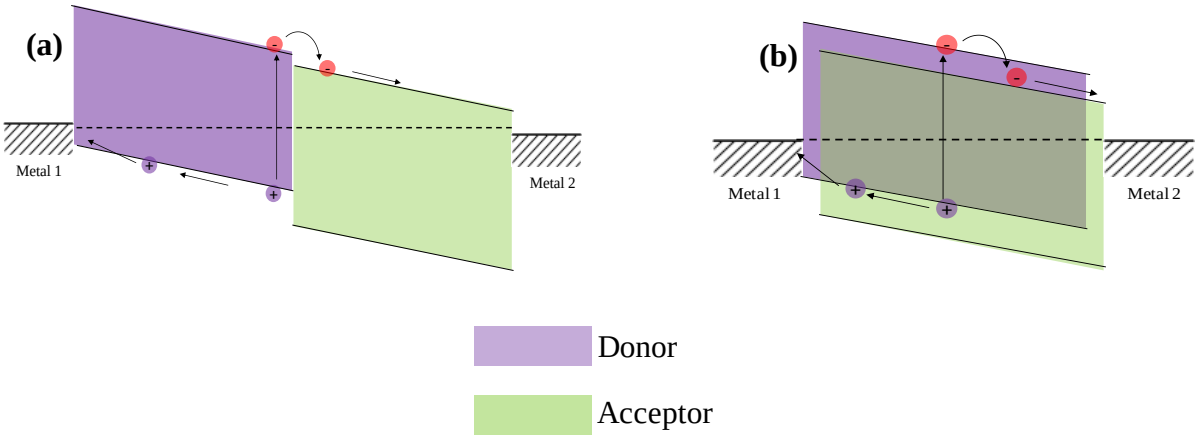

Figure 2.7: Energy band diagram of (a) bilayer and (b) bulk heterojunction device structures. (Adapted from Yacobi, 2002; Hoppe & Sariciftci, 2004).

Figure 2.7 represents schematics of the bilayer and bulk heterojunction device structures under illumination conditions (applied voltage, $V = 0$) respectively. It is also important to note that the work functions of metal contacts 1 and 2 are asymmetrical (i.e., $\phi_1 > \phi_2$); as this is necessary, to ensure selective collection of holes and electrons respectively. This is achieved when there is an electrically stable contact between hole – collecting electrode and the donor material, and also between electron – collecting electrode and the acceptor (see Figure 2.7).

2.6 Capacitance Voltage characteristics

The charge within the depletion region of the metal – semiconductor junction (see Figure 2.8) is proportional to the concentration of ionised donors (N_d) and the depletion width, expressed as

$$Q_d = eN_dW \tag{2.3}$$

Substituting for W from equation 2.9, therefore

$$Q_d = \left(2e\varepsilon N_d(V_{bi} \pm V)\right)^{1/2} \tag{2.4}$$

Since $C = A\,(\partial Q/\partial V)$, therefore the depletion region capacitance can be expressed as

$$C = A\left(\frac{e\varepsilon N_d}{2(V_{bi}\pm V)}\right)^{1/2} \tag{2.5}$$

, where A is the device's cross – section area. Equation 2.14 can also be expressed in the form

$$C^{-2} = \frac{2(V_{bi}\pm V)}{A^2 e\varepsilon N_d} \tag{2.6}$$

The plot of C^{-2} versus V gives a straight line from which the values of both V_{bi} and N_d can be extracted. The intercept on V axis at $C^{-2} = 0$, gives the value of V_{bi}.

2.7 Ohmic and Space charge limited conductivity in semiconductor thin films

An Ohmic contact between a metal and semiconductor has a negligible contact resistance relative to that of the bulk of the semiconductor (Sze, 1985). Ohmic conduction particularly in wide band semiconductors is known to be due to thermally generated carriers. For this reason, conduction occurs even at low applied voltages, due to the excess thermally generated carriers relative to injected ones. The current density at low voltages obeys ohm's law

$$J = p_0\mu_{p(n)}e\frac{V}{d} \tag{2.7}$$

, where p_0 is the electron or hole concentration (in either an n – or p – type semiconductor), $\mu_{n(p)}$ is the electron (hole) mobility, e is the electronic charge, V is the DC applied voltage, and d is the semiconductor layer thickness. However this condition breaks down in the space charge limit, when at high electric fields, the density of injected carriers becomes so high. The field due to carriers themselves become dominant over that of applied bias, and the

condition becomes space charge limited. This behaviour is characterised by a quadratic dependence of current density on applied voltage, also referred to as the Mott and Gurney relationship (Mott & Gurney, 1940).

$$J = \frac{9}{8}\varepsilon\mu_{\mathrm{p(n)}}\frac{V^2}{d^3} \tag{2.8}$$

It is important to note that the above relation does not necessarily imply the absence of traps, as in reality semiconductors are imperfect and contain traps, but rather that they are all filled.

2.8 Characteristics of Photovoltaic cells

Photovoltaic (PV) cell is a prominent electronic device with increasing application of organic semiconductor materials. In terms of semiconductor physics the PV cell is essentially based on the $p - n$ junction diode. In principle, the junction formed between two semiconductor materials of the same type but of opposite doping type is considered a $p - n$ junction. p – type being characteristic of majority of holes, and n – type, rich in negative charge carriers, as a result of doping with *donor* impurities (Sze, 1985; Tyagi, 1988; Singh, 1994). Using the $p - n$ junction diode as a reference device, and with equivalent circuits' theory, the underlying working principle of a typical PV cell will be outlined.

2.8.1 Equivalent circuit model

In the dark, the current density – voltage characteristics of a solar cell can be described in terms of a typical ideal diode ($p - n$ junction), with current density given by the following equation (Sze, 1985).

$$J = J_{\mathrm{S}}\left[\exp\left(\frac{qV}{k_{\mathrm{B}}T}\right) - 1\right] \tag{2.9}$$

, where J_{S} is the saturation current under reverse bias, V is the applied bias, q the electronic charge, k_{B} the Boltzmann constant, and T the temperature. From equation 2.9, it follows that larger currents pass through the device under forward bias ($V > 0$) compared to reverse bias ($V < 0$). This rectifying behaviour is a typical characteristic of PV cells. On the other hand, if the cell is exposed to sunlight, the ideal $J - V$ characteristics is given by

$$J = J_{\mathrm{S}}\left[\exp\left(\frac{qV}{k_{\mathrm{B}}T}\right) - 1\right] - J_{\mathrm{SC}} \tag{2.10}$$

, where J_{SC} is the short circuit current density, at $V = 0$, and is a function of the illumination intensity. When the contacts of the device are isolated (open circuit condition), it yields its

maximum voltage (open circuit voltage). At this condition, $J = 0$, and from equation 2.10, it follows that the open circuit voltage, V_{OC} (measured in volts) can be expressed as

$$V_{OC} = \frac{k_B T}{q} \ln\left(\frac{J_{SC}}{J_S} + 1\right) \tag{2.11}$$

It is obvious from equation 2.11 that V_{OC} increases logarithmically with the short circuit current density (which is directly proportional to the illumination intensity). Figure 2.8 shows the equivalent circuit model of an ideal diode; $J - V$ curves in the dark and under illumination.

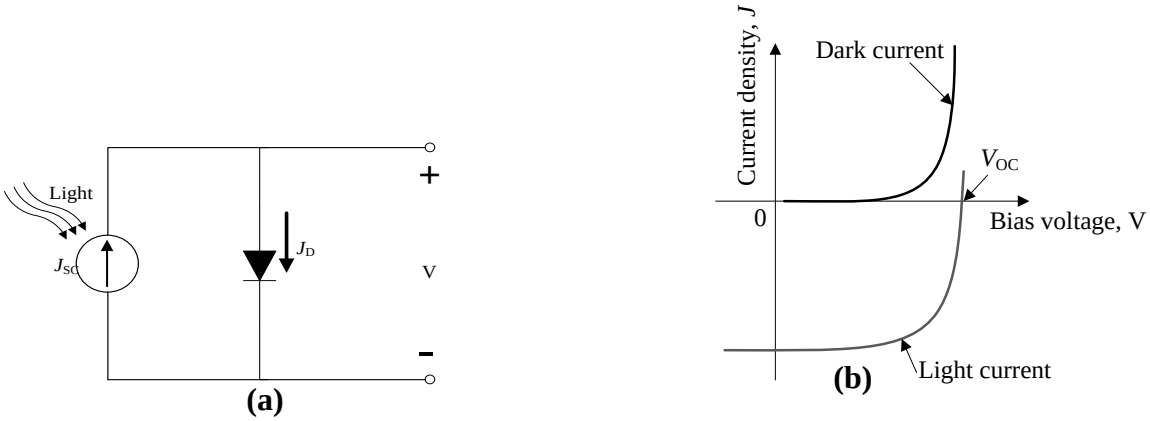

Figure 2.8: (a) Equivalent circuit model of an ideal solar cell (b) $J - V$ characteristics of an ideal solar cell in the dark and under illumination.

2.8.2 Efficiency

The characteristic $J - V$ curve of a PV cell under illumination is shown in Figure 2.9, depicting the major PV parameters.

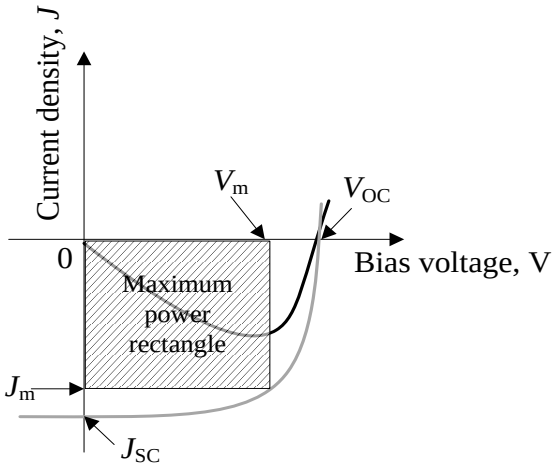

Figure 2.9: $J - V$ (grey) and power – voltage (black) characteristics of a typical solar cell under illumination.

In Figure 2.9, J_m and V_m represent the maximum point current density and voltage, for maximum power output ($P_{MAX} = J_m \times V_m$). This also corresponds to the shaded area, the largest rectangle that can fit under the $J - V$ curve. The power conversion efficiency of the cell can be determined from the relationship

$$\text{PCE}(\%) = \frac{P_{out}}{P_{in}} \times 100 = FF \times \frac{J_{SC} \times V_{OC}}{P_{in}} \times 100 \tag{2.12}$$

From equation 2.12;

$$FF = \frac{J_m \times V_m}{J_{SC} \times V_{OC}} \tag{2.13}$$

FF in equation 2.13 is referred to as the fill factor of the device, which essentially defines its quality (Mayer et al, 2007). An ideal solar cell will have a *FF* value of unity.

The discussion so far is in terms of an ideal solar cell. However, in a non – ideal case, it is known that there are power losses present via contact resistances and leakage currents around the sides of the device (Nelson, 2003). These effects are equivalent to parasitic resistances namely series and shunt resistances (R_S and R_{SH}). These are illustrated in Figure 2.10. R_S originates from the cell's material resistance to current flow, mostly through the front surface to the semiconductor/metal interface, and metallic contacts. In the case of OSCs, the series resistance will therefore be a combination of both the bulk of active layer and contact resistances. Shunt resistances on the other hand arises from the leakage currents through the cell, around the device edges, and between contacts of different polarity.

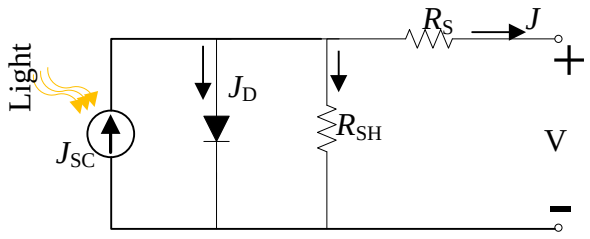

Figure 2.10: Equivalent circuit of a non – ideal solar cell including parasitic resistances (R_S and R_{SH}).

The effect of increasing R_S and decreasing R_{SH} on the PV cell's $J - V$ characteristics is further illustrated in Figure 2.11. From equation 2.13 (and with reference to Figure 2.9), it is obvious that increasing R_S and decreasing R_{SH} will result in a low fill factor.

Figure 2.11: Effect of (a) increasing R_S and (b) decreasing R_{SH}, on $J - V$ characteristics of the solar cell (Adapted from Nelson, 2003).

To achieve a highly efficient cell (one with reasonably high *FF*), it is desirable to have a very small R_S and a large R_{SH}. Taking into account the effects of parasitic resistances in a non – ideal cell, equation 2.10 and 2.11 can be rewritten as

$$J = J_{SC} - J_S\left[\exp\left(\frac{q\left(V - JR_S\right)}{nk_BT}\right) - 1\right] - \frac{V - JR_S}{R_{SH}} \tag{2.14}$$

$$V_{OC} = \frac{nk_BT}{q}\ln\left(\frac{J_{SC}}{J_S} + 1\right) \tag{2.15}$$

, where *n* is the ideality factor.

2.9 Charge Photogeneration in Donor/Acceptor Organic Solar Cells

The working principles of the solar cell were discussed in section 1.3 briefly. This section discusses in detail the processes associated with generation of charges in the BHJ OSC. The primary yield of photo excitations in organic semiconductors are bound electron – hole pairs (excitons), in contrast to free charge carriers in inorganic semiconductors. This is largely due to their low dielectric constants and the presence of significant electron – lattice interactions relative to the former (Brédas et al, 1996; Gregg & Hanna, 2003). To achieve the dissociation of excitons, a mechanism involving the difference in electronic energy properties of the donor – acceptor materials is required. In the absence of this, exciton will undergo radiative and/or non – radiative recombination (Clarke & Durrant, 2009).

Figure 2.12 illustrates a simplified viewpoint of the process of photo excitation and exciton dissociation at the donor/acceptor interface in a typical BHJ organic solar cell. In the following section, the process of exciton dissociation is discussed in more detail.

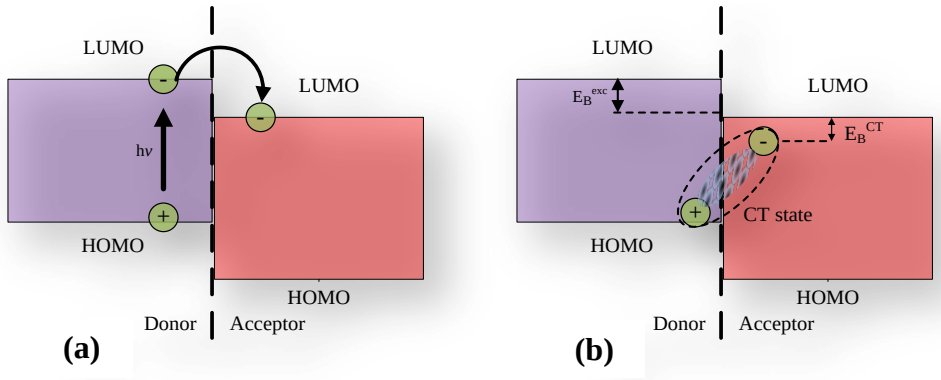

Figure 2.12: (a) Energy level diagram of D/A interface showing the excitation of an electron into the donor LUMO, following photon absorption. (b) Formation of interfacial e-h pairs or charge transfer (CT) states (dashed oval). E_B^{exc} is the exciton binding energy, corresponding to the difference between the optical and electrochemical band gaps, and E_B^{CT} is the charge transfer state binding energy respectively (Adapted from Muntwiler et al, 2008).

2.9.1 Exciton dissociation at Donor/Acceptor interface

The subsequent successful dissociation of photo-generated excitons at the D/A interface to free charge carriers is a critical step in the working process of the organic solar cell. At the D/A interface, excitons do not immediately dissociate into free charge carriers, as a spatial separation of holes and electron occurs first. This spatial separation, an initial electron transfer across D/A interface results in a coulombically bound interfacial electron-hole pair state (Clarke & Durrant, 2009). A few terminologies have been used in literature to describe this electron transfer state, which include germinate pairs, bound polaron pairs, and charge transfer states (Tvingstedt, et al., 2009). The most common is the 'charge transfer' (CT) state, which will be used throughout this work. Essentially, the CT state denotes an intermediate state between excitons and fully dissociated charges. Following the formation of CT states, their subsequent successful dissociation into free charges is very critical to photocurrent generation. The process from CT state to fully dissociated charges is however met by one of two competing recombination process; namely germinate or bimolecular recombination. Germinate recombination involves the recombination of the CT (germinate) state, whilst the latter involves free charges (Clarke & Durrant, 2008). As mentioned earlier, the mechanism at D/A interface required for successful exciton dissociation represents the overcoming of the Coulomb's attractive force between holes and electron, expressed as

$$V = \frac{q^2}{4\pi\varepsilon_r\varepsilon_0 r} \tag{2.16}$$

, where q is the electron's charge, ε_r is the dielectric constant of the conjugated polymer, ε_0 is the permittivity of vacuum, and r is the electron – hole distance of separation.

To achieve the initial charge separation step (see Figure 2.12 (a)), it is generally accepted that there should be a necessary suitable energy difference between the donor and acceptor LUMO levels (Muntwiler et al, 2008). This LUMO offset should be just sufficient to overcome the exciton binding energy (E_B^{exc}). This will enable an initial energetically downhill transfer step of electrons (Bittner, et al., 2005). Since both donor and acceptor molecules at the interface are physically close to each other, this initial electron transfer step only results in the spatial separation between the electron and hole (CT state). The distance of separation concerned is relatively between 0.5 – 1 nm, typically of the order of magnitude as the size of the molecules (Clarke & Durrant, 2008). Applying equation 2.16, the approximate Coulomb's attraction can be estimated to be within the range of 0.1 – 0.5 eV, and this is referred to as the CT state binding energy (E_B^{CT}), as illustrated in Figure 2.12. Comparing the magnitude of the Coulomb attraction with that of the thermal energy i.e., k_BT (0.025 eV), evidently it is significant. Therefore energy that is more than the thermal energy will be required to dissociate excitons. In principle this constitutes a barrier to photo-generation of charges in organic solar cells. Interestingly, in their estimation of V_{OC} from polymer – fullerene BHJ OSCs, Scharber and his group demonstrated that a minimum LUMO offset of 0.3V is just sufficient for efficient exciton dissociation and charge separation (Scharber et al, 2006). Any value above this is considered to be wasted energy. The estimation is given by the Equation

$$V_{OC} = \frac{1}{q}(HOMO_{Donor} - LUMO_{Fullerene}) - 0.3V \qquad (2.17)$$

0.3V in equation 2.17 denotes the minimum LUMO offset.

The process of exciton dissociation at the D/A interfaces in organic solar cells have consistently been described in literature based on the theoretical model of Onsager (Onsager, 1938). Onsager's theory provides a quantitative description of the efficiency of dissociation of excitons under the influence of an electric field. This is discussed in the following section.

2.9.1.1 Onsager Theory

As mentioned previously, exciton dissociation can be difficult primarily due to characteristic low dielectric constants of conjugated polymers. Polymer's low charge carrier mobilities also contribute to this difficulty. Failure for CT state to dissociate within its lifetime, will result in

recombination (germinate). The quantitative description of germinate recombination was first provided by Onsager (Onsager, 1934). Originally designed to describe the probability of recombination of ion – pairs, with an initial separation, the theory has provided a classical framework which have been successfully applied to several conjugated semiconducting systems (Scher & Rachkovsky, 1984; Milhailetchi et al, 2004). For oppositely charge ion – pairs in a weak electrolyte, undergoing a Brownian motion, whilst under the combined influence of their mutual Coulomb attraction and an external field, Onsager was able to calculate the probability of their escape from recombination. The model particularly proposes that a localized hole and a hot electron are generated following photon absorption. Due to the excess thermal energy it possesses, the electron thermalizes after undergoing a rapid motion. This thermalization occurs at a distance *a*, from the localized hole. This distance of separation between the hot electron and the localized hole is referred to as the thermalization length (as shown in Figure 2.13). The resultant electron – hole pair, after initial separation by the thermlization length (*a*), is analogous to the CT state. Depending on the magnitude of the Coulomb's attraction within the CT state; it will either dissociate into free charges or recombine back to the ground state. In addition, the model also proposes a definition for the Coulomb capture radius, alternatively referred to as the Onsager radius, r_c, as the distance at which the Coulomb attraction energy is equivalent to the thermal energy, $k_B T$. The capture radius is given by

$$r_c = \frac{q^2}{4\pi\varepsilon_r\varepsilon_0 k_B T} \tag{2.18}$$

, where q is the charge of an electron, ε_r is the dielectric constant of the surrounding medium, ε_0 is the permittivity of vacuum, k_B the Boltzmann's constant, and T is temperature. In Figure 2.13, the green curve represents the potential energy from Coulomb attraction due to electron – hole (e – h) separation.

According to the Onsager model, the CT state is considered to be fully dissociated if $a > r_c$. In the case where $a < r_c$, the dissociation of the CT state into free charge carriers occurs with an escape probability of $P(E)$. On the other hand germinate recombination occurs with a probability of $1 - P(E)$. $P(E)$ has been demonstrated to depend on the electric field strength, E, the distance at which the charged pair are generated, a, and the temperature, T (Tachiya, 1988). When $E = 0$, $P(E)$ is proportional to the negative reciprocal of the CT state distance of separation, a. The escape probability is given by (Tachiya, 1988)

$$P(E) = \exp\left(\frac{-r_c}{a}\right)\left(1+\frac{qr_c}{2k_BT}E\right) \quad (2.19)$$

, where a is the initial separation distance between two thermalized ions, r_c is the Coulomb capture radius, q is the electron charge, k_B Boltzmann constant, T the temperature, and E is the electric field strength.

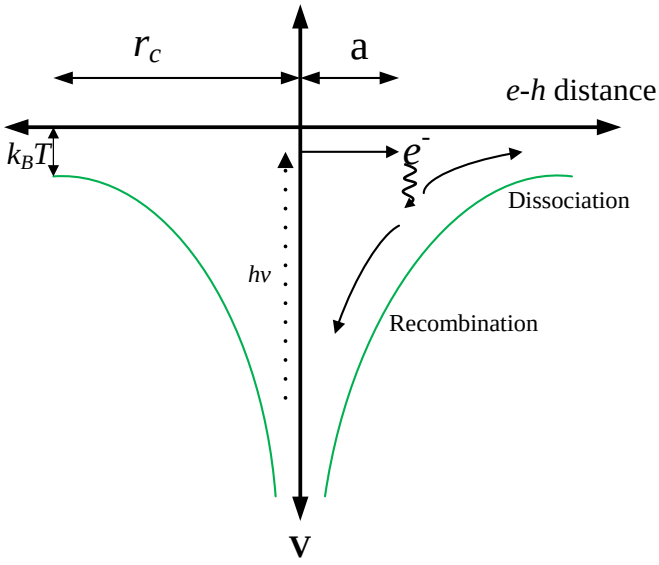

Figure 2.13: Potential energy diagram summarizing the probability that Coulombically bound ion – pair (electron – hole) in a weak electrolyte will escape its Coulomb's attraction and generate free charges according to Onsager theory (Adapted from Clarke & Durrant, 2010).

In 1984, Onsager's work was further modified by Braun, who emphasised the fact that the CT state has a finite lifetime (Braun, 1984). This modification was prompted by the observation that the thermalization lengths, a, obtained, using the Onsager's conventional model, i.e., the electric-field dependence of free charge carriers yield, were in the region of 2.5 – 3.5 nm. However this is larger than lengths typical for the CT state (less than 1 nm). In addition, Onsager's theory has the boundary condition that recombination occurs if the thermalization length approaches zero, and the ion pair irreversibly varnishes. Braun in his modification however stated that the condition for the Onsager's model was inappropriate since the generated CT state has a finite lifetime. This means that the CT state formed at the interface can either undergo one of two processes, namely; recombination to the ground state with a decay constant k_F, or an electric-field dependent separation with a rate constant $k_D(E)$. Once separated, the free charges can again form a bound pair which will eventually

recombine with a rate constant k_R (Blom, et al., 2007). An interesting implication of this (which significantly differentiates Braun's model from Onsager's) is that free charge carriers which happen to be captured into bound pairs may still be able to dissociate again during their lifetime. Therefore Braun's revised model of the electric-field dependent dissociation into free carriers by the rate constant $k_D(E)$, and the germinate recombination to ground state with k_R, at a given electric field E and temperature T and is expressed as

$$P(T,E) = \frac{k_D(E)}{k_F + k_D(E)} = k_D(E)\tau(E) \tag{2.20}$$

Where $P(T, E)$ is the escape probability and $\tau(E)$ is the lifetime of the CT state. On the basis of Onsager's original model for the relative applied electric field – dependent dissociation in a weak electrolyte, $k_D(E)$ is defined as (Braun, 1984)

$$k_D(E) = k_R \frac{3}{4\pi a^3} \exp\left(\frac{-E_B}{k_B T}\right)\left[1 + b + \frac{b^2}{3} + \frac{b^3}{18} + \frac{b^4}{180} + \cdots\right] \tag{2.21}$$

, where a is the initial distance of separation of the CT state (bound electron-hole, $e - h$ pair) at the D/A interface, $b = q^3E/8\pi\varepsilon_0\varepsilon_r k_B{}^2T^2$, and E_B is the $e - h$ pair's binding energy, and $k_R = e\langle\mu\rangle/\varepsilon_0\langle\varepsilon_r\rangle$, where $\langle\varepsilon_r\rangle$ is the spatially averaged dielectric constant and $\langle\mu\rangle$ the spatially averaged sum of electron and hole mobilities (where the symbol $\langle\ \rangle$, denotes the spatial average). Figure 2.14 summarises illustratively the processes involved in the Photogeneration of charges in polymer/fullerene OSCs.

From Figure 2.14; ***hν***: Photo excitation leading to the formation of a singlet exciton, S_1. $\boldsymbol{k_{CT}}$: initial spatial separation of exciton, i.e., exciton dissociation, yielding hot CT state. $\boldsymbol{k_{ISC}}$: Spin mixing of the ^{1}CT and ^{3}CT states, due to weak electronic coupling. $\boldsymbol{K_{triplet}}$: Germinate recombination of ^{3}CT state to the triplet exciton, T_1. $\boldsymbol{k_{GR}}$: Germinate recombination of ^{1}CT state back to the ground state S_0. $\boldsymbol{k_{CS*}}$: Dissociation of hot CT state into a fully charge-separated (CS) state. $\boldsymbol{k_{CS}}$: Dissociation of thermally relaxed CT state into the CS state. $\boldsymbol{k^{CS}_{therm}}$: Thermal relaxation of the CS state and migration away from D/A interface. $\boldsymbol{k^{CT}_{therm}}$: Thermal relaxation of CT state. $\boldsymbol{k_{BR}}$: Bimolecular recombination of the CS state. $\boldsymbol{\Delta G_{CS}}$**:** Difference in energy between singlet exciton and the dissociated CS state. $\boldsymbol{\Delta G_{CT}}$**:** Free energy driving the initial separation of exciton to form the CT state.

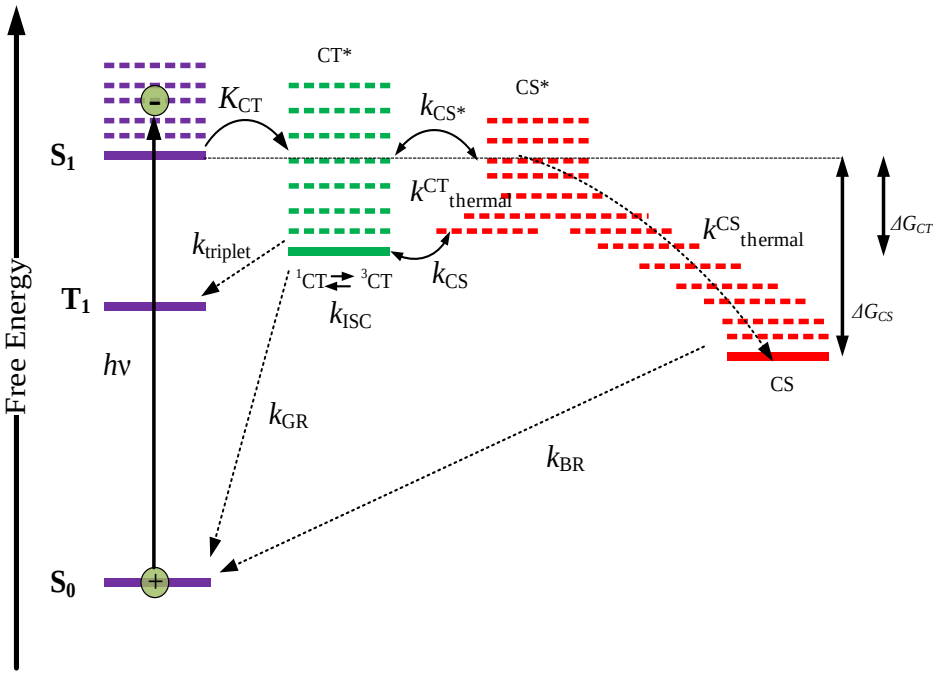

Figure 2.14: A schematic illustration of the energy level diagram depicting a summary of the processes involved in Photogeneration of charges in a typical organic semiconductor based solar cell (Adapted from Clarke & Durrant, 2009).

2.9.2 Germinate and Bimolecular Recombination

Two significant processes were mentioned in the previous section, namely; germinate and bimolecular (or non-germinate) recombination. Between the generation of excitons and free charge carriers, either germinate recombination will occur (i.e., CT state recombining to the ground state, soon after exciton dissociation), or bimolecular recombination (i.e., recombination of free charge carriers). These processes constitute a significant loss mechanism in the BHJ OSC (Koster, et al., 2006). In addition, they are also in competition with charge generation or collection (Nelson, 2011), since they are the inverse of current generation. Therefore its minimisation is beneficial to optimising PCEs in BHJ OSCs. The rate at which bimolecular recombination occurs is given by

$$R = \gamma_L \left(np - n_i p_i \right) \tag{2.22}$$

, where n and p are the free electron and hole density, $n_i p_i = N_{CV} \exp[-E_{gap}/kT] = n_i^2$, where n_i denotes the intrinsic concentration in the material, and γ_L is the Langevin recombination constant. In the case of pristine materials, the Langevin recombination constant is given by (Langevin, 1903)

$$\gamma_{\mathrm{L}} = \frac{q}{\varepsilon}\left(\mu_{\mathrm{e}} + \mu_{\mathrm{h}}\right) \tag{2.23}$$

, where q is the elementary charge, ε is the dielectric constant, and μ_{e} (μ_{h}) is the electron (hole) mobility. The above Equation consists of the sum of both charge carriers, since they are free to move toward each other. This essentially implies that the fastest carrier will dominate, and thereby determine the recombination rate. This can be illustrated schematically in Figure 2.15. It can be seen that in contrast to the pristine semiconductor, the holes and electrons are confined to different phases (donor and acceptor), and recombination occurs mainly across the interface between materials (see Figure 2.15(b)). Furthermore to compensate for any eventual mobility differences in the blend, Braun adapted Equation 2.23 as

$$\gamma_{\mathrm{L}} = \frac{e}{\varepsilon}\langle \mu_e + \mu_h \rangle \tag{2.24}$$

In the case of Equation 2.24, the recombination constant is proportional to the spatial average of the sum of hole and electron mobilities.

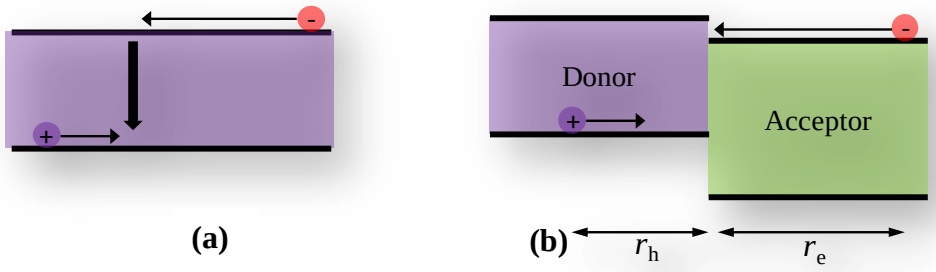

Figure 2.15: Schematic energy band profiles illustrating bimolecular recombination in (a) pristine semiconductor, and (b) donor – acceptor BHJ solar cell (Adapted from Koster et al, 2006).

However, in the situation where the electron and hole are confined to the respective materials at distances indicated in Figure 2.15(b); the carriers will have to travel this distances, to subsequently get to the interface. For example when $\mu_{\mathrm{e}} >> \mu_{\mathrm{h}}$, it implies that the electron will get to the interface faster, and the time taken for both charges to be at the interface will be dominated by the hole. Therefore for BHJ solar cells, recombination will be governed by the slowest charge carrier. Due to this, it is expected that the recombination constant in Equation 2.23 should be close to the value expressed in the following equation:

$$\gamma_{\mathrm{L}} = \frac{q}{\varepsilon}\min\left(\mu_{\mathrm{e}}, \mu_{\mathrm{h}}\right) \tag{2.25}$$

In contrast to the original Langevin results in Equations 2.23 and 2.24, the above Equation indicates the recombination constant is governed by the slowest charge carrier (Koster et al, 2006).

2.9.2.1 Traps and Recombination centres

Within the band gap of semiconductors, there maybe one or more localized energy levels due to the presence of impurities. Exchange of charges can take place between these levels and the valance (or conduction) bands (Petty, 2008). These energy levels can trap electrons (or holes) for example from the conduction (or valence) band respectively. This occurs by attracting an electron (or hole) first and subsequently a hole (or electron) in that order. These levels are considered to act as *traps* (Sze, 1985). The process of trapping a hole or an electron followed by a subsequent attracting of an electron or a hole is referred to as *trap – assisted recombination* (Schokley & Read, 1952). The localized energetic levels (traps) are also termed as *recombination centres*. The presence of defects in semiconductors is often characteristics of recombination centres, which can be a limitation to the performance of many semiconductor devices. The rate of trap – assisted recombination is dependent on the number of sites that act as traps in the material, and how fast the free carrier can find the respective trapped carrier. The model designed originally for inorganic semiconductors also known as the Shockley – Read – Hall (SRH) recombination (Schokley & Read, 1952), is often applied to organic systems, including OSCs (Cowan et al, 2010; Kuik et al, 2011; Nalwa et al, 2011). Figure 2.16 is a schematic illustration of the four basic steps involved in the process of trap – assisted recombination. E_{C}, E_{V}, and E_{t} are the conduction, valence bands, and energy level of the recombination centres. From the illustration in Figure 2.16, we have the following scenarios:

- **a.** An electron can be captured by a neutral centre, and the rate at which this occurs is governed by a capture coefficient, denoted by C_n,
- **b.** The captured electron in (a) can be subsequently excited back to the conduction band, OR,
- **c.** On the other hand, the electron in the trap site can be captured by a hole with a capture coefficient, C_p, thus leaving a neutral centre behind.
- **d.** Electron can be captured from the valence band by a neutral centre.

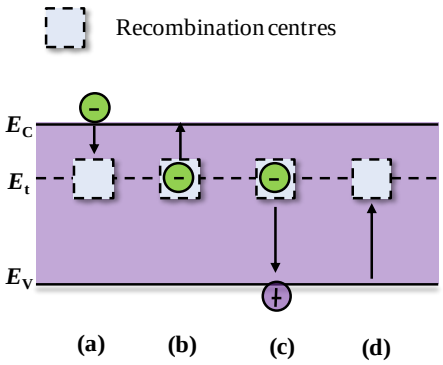

Figure 2.16: Schematic illustration of the basic steps involved in trap – assisted recombination: (a) electron capture, (b) electron emission, (c) hole capture, and (d) hole emission.

Assuming thermal equilibrium between the processes **a** – **b**, above, trap – assisted recombination rate according to SRH is described by

$$R_{\mathrm{SRH}} = B_{\mathrm{SRH}}(np - n_{\mathrm{i}}p_{\mathrm{i}}) \tag{2.26}$$

, where $B_{\mathrm{SRH}} = \frac{C_n C_p N_{\mathrm{t}}}{[C_n(n+n_{\mathrm{i}})+C_p(p+p_{\mathrm{i}})]}$, with C_n denoting the probability per unit time an electron in the conduction band will be captured by a neutral centre (i.e., a trap centre that is empty and able to capture an electron), C_p denotes the probability per unit time that a hole will be captured for the case when a trap is filled with an electron and able to capture the hole, and N_{t} is the density of electron traps.

An effective method of extracting the SRH capture coefficients (i.e., C_n and C_p) has been reported in the work of Kuik et al (2011). In their work, they employed the light – intensity dependence of the open circuit voltage (V_{OC}) of a light – emitting diode. The V_{OC} response to light – intensity variation follows the relation (i.e., in the absence of traps, where Langevin recombination is considered to be dominant)

$$V_{\mathrm{OC}} = \frac{E_{\mathrm{gap}}}{q} - \frac{k\mathrm{T}}{q}\ln\left(\frac{(1\text{-}P)B_{\mathrm{L}}N_{\mathrm{CV}}^2}{P\mathrm{G}}\right) \tag{2.27}$$

, where P is the dissociation probability, E_{gap} is the energy gap, N_{CV} the effective density of states, B_{L} the bimolecular recombination strength. G is the generation rate of excitons, directly proportional to the light – intensity and thus establishing the correlation between V_{OC} and light – intensity.

When V_{OC} is plotted against the natural logarithm of light – intensity, the expected slope is kT/e (see Equation 2.27). This is in the case where Langevin recombination process is dominant. However, where trap – assisted recombination process is present, it has been established that that the slope exceeds that in Equation 2.27 (Kuik et al, 2011). Consequently the relation between V_{OC} and light – intensity can be well described by incorporating the SRH recombination strength (B_{SRH}) in Equation 2.27, (i.e., $B = B_L + B_{SRH}$), to account for the trap – assisted recombination processes (Nalwa et al, 2011).

2.10 Summary

In this chapter, an overview of the basic theory and current understanding underpinning organic semiconductor materials and their application in OSCs was presented. These include brief descriptions of the formation of energy bands in organic semiconductor materials on the basis of the interaction of molecular orbitals. The energy bands are associated with the $\pi - \pi^*$ molecular orbitals. These are the highest occupied and lowest unoccupied molecular orbitals (HOMO and LUMO) in terms of molecular physics. They are also synonymous to the valence and conduction bands respectively in semiconductor physics. Charge carrier transport in organic semiconductor materials is via hopping mechanism, primarily due to the delocalisation of π – orbitals. This is in contrast to highly localized bands in inorganic semiconductors, wherein charge transport is via band transition.

Descriptions of the metal – semiconductor junction was also presented, as this was significant in explaining the electrical processes in a complete OSC device. The underlying theoretical understanding of experimental methods for determining significant device parameters such as series and shunt resistances were also highlighted. Furthermore, the current understanding of the working principles of the OSC, from a theoretical standpoint was discussed. These include steps in the mechanisms of exciton generation and dissociation, ultimately yielding free charge carriers. The so called 'unwanted' challenges associated with this process, such as recombinations are also discussed. These recombination processes (either bimolecular or germinate) are crucial as they constitute the unwanted source of power loss in OSC devices. The significance of understanding and minimising these processes is critical to improved OSCs.

Chapter 3

Organic solar cell materials

"Especially, OPVs (organic photovoltaics) have recently made rapid progress for recent years, and they are definitely one of the most promising technologies in the field of next-generation photovoltaics" .

— Researchandmarkets.com

3.1 Introduction

Their advantage of ease of fabrication is one of the reasons for the growing attractiveness of the BHJ organic solar cell. The active layer of devices is mostly fabricated from solution – processable materials. These mostly include conjugated polymers and fullerene derivatives in a blend. Amongst materials used today, electron donating poly (3-hexylthiophene) (P3HT), and electron – accepting [6, 6] phenyl-C_{61}-butyric acid methyl ester, (PCBM) have proven to be promising materials. This chapter provides a review of these materials and others in light of their applications in solar cells.

3.2 Conjugated Polymers

Conjugated polymers are organic materials consisting of alternating single and double bonds. In general they are often regarded as "intrinsic wide band gap organic semiconductors", with energy gaps typically above 1.4 *eV* (Günes et al, 2007). In 1977, it was found out by Shirakawa and co – workers that by doping polyacetylene (simplest form of conjugated polymer), the conductivity was observed to increase by several orders of magnitude (Shirakawa et al, 1997). Following their work, researches in organic electronics have rapidly been expanding. Examples of some of the conjugated polymers that are widely used in photovoltaic applications include; derivatives of poly(phenylenevinylene), PPVs, polyanilines (PANIs), and polythiophenes (PTs) (Mao et al. 1993; McCullough et al. 1993;

Tan et al. 2004; Krebs, 2008). The chemical structures of some of these conjugated polymers are shown in Figure 3.1.

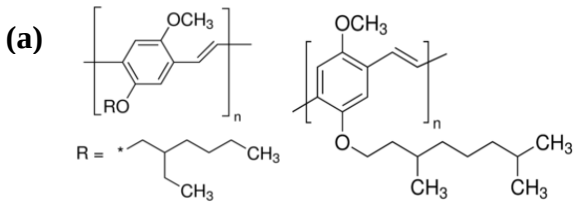

MEH-PPV MDMO-PPV

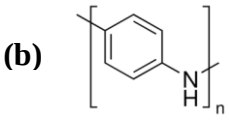

Polyaniline

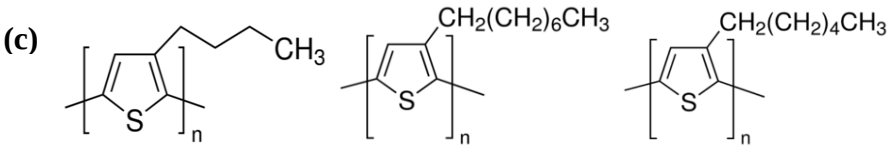

P3BT P3OT P3HT

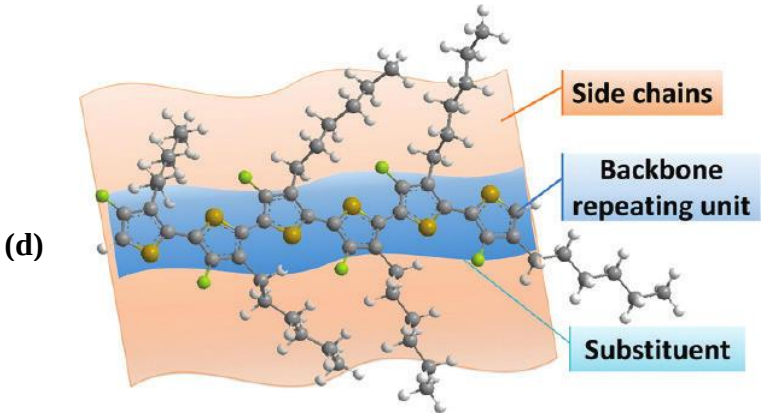

Figure 3.1: Chemical structures of a range of conjugated polymers (a) PPVs, (b) PANIs, and (c) PTs, and (d) a schematic illustration of a typical conjugated polymer, depicting repeating units of thiophene units (backbone), and hexyl side chains, $CH_2(CH_2)_4CH_3$ (Zhou et al, 2012).

Previous studies focused on PPV – based BHJ solar cells, such as MEH-PPV and MDMO-PPV with fullerenes, demonstrated efficiencies of 1.5 – 3.3% (Yu et al. 1995; Brabec et al.

2002). However it was shown that due to large band gaps (>2 eV), current was significantly limited in devices based on PPV polymers (Brabec et al. 2002). The PT derivative, P3HT on the other hand with a narrower band gap (1.9 eV), has the potential of higher achievable current densities. In Figure 3.1 (d), it can be seen that the backbone and side chains, are features that characterises a typical conjugated polymer. The backbone is a repeating unit (hence conjugated), forming the polymer chain. The side chain on the other hand is responsible for imparting solubility to the polymer (eds. Brabec et al. 2008). In addition, it also plays a significant role in improving the molecular weight and processability of the conjugated polymer. The following sections review some important properties of conjugated polymers (particularly PTs), and their influence in solar cells.

3.3 Properties of Conjugated Polymers for Solar Cells Applications

Thiophene – based conjugated polymers were typically designed to be efficient photon absorbers, electron donors, and hole – transporting materials in solar cell applications. The electronic properties of conjugated polymers can be described generally in terms of semiconductor physics, particularly discussed in section 2.1.1. Typically electron rich, PT polymer chains are lamellar microstructures, exhibiting closely packed π – stacked backbones. Such molecular conformation is advantageous for charge transport, as intermolecular interaction increases, thereby improving charge hopping processes. For the purposes of this work, the polymer P3HT, a good example of PTs will be discussed in this review. Widely available, and easy to process from solution; P3HT exhibits good crystalline microstructures in thin films. These attribute contributes to its promising electrical properties. To further understand this, first it is important to consider the molecular properties of PTs. These include their degree of regioregularity, and molecular weights in general. Significant attributes such as charge transport, and optical absorption have been shown to have their origins in the nature of these properties.

3.3.1 Regioregularity and Molecular weights in polymers

Regioregularity simply refers to the regular structuring of head – head, head – tail, and tail – tail isomers in the polymer chain (Mao et al. 1993). The ‘head’ and ‘tail’ are usually designated by the alphabets ‘H’ and ‘T’. The property of regioregularity in conjugated polymers has a significant influence on the behaviour of the polymer. Depending on the percentage of regioregularity or the lack thereof in the material, a variation in a number of its characteristics will be evidenced (McCullough et al. 1993). Conjugated polymers are

essentially obtained from the polymerisation of their monomer units, for example, the polymerisation of 3-substituted thiophene units, with three possible couplings via the 2- and 5- positions (Barbarella et al. 1994). These couplings, notably; head-to-head (HH), head-to-tail (HT), and tail-to-tail (TT) have formations, which are responsible for the different degrees of regioregularity of the polymer. Figure 3.2 shows an illustration of the three possible couplings (or diads). In view of the regiochemistry of PTs, two main classifications are commonly presented in literature, namely; regioregular and regioirregular (or regiorandom), with prefixes "rr" or "rR" and "rIR" or "ran" (eds. Brabec et al. 2008). This classification primarily arises from the percentage of the proportion of coupling sequences in the polymer chain (Chen et al. 1995; eds. Brabec et al. 2008). For example, a PT, following synthesis, with a >90% HT dimmer (or coupling) content is regarded as regioregular. The regioregularity obviously increases as the percentage value increases, whilst with <90% it is regiorandom. The impact of regioregularity on molecular structure and hence overall material characteristics shall be briefly discussed in the next section.

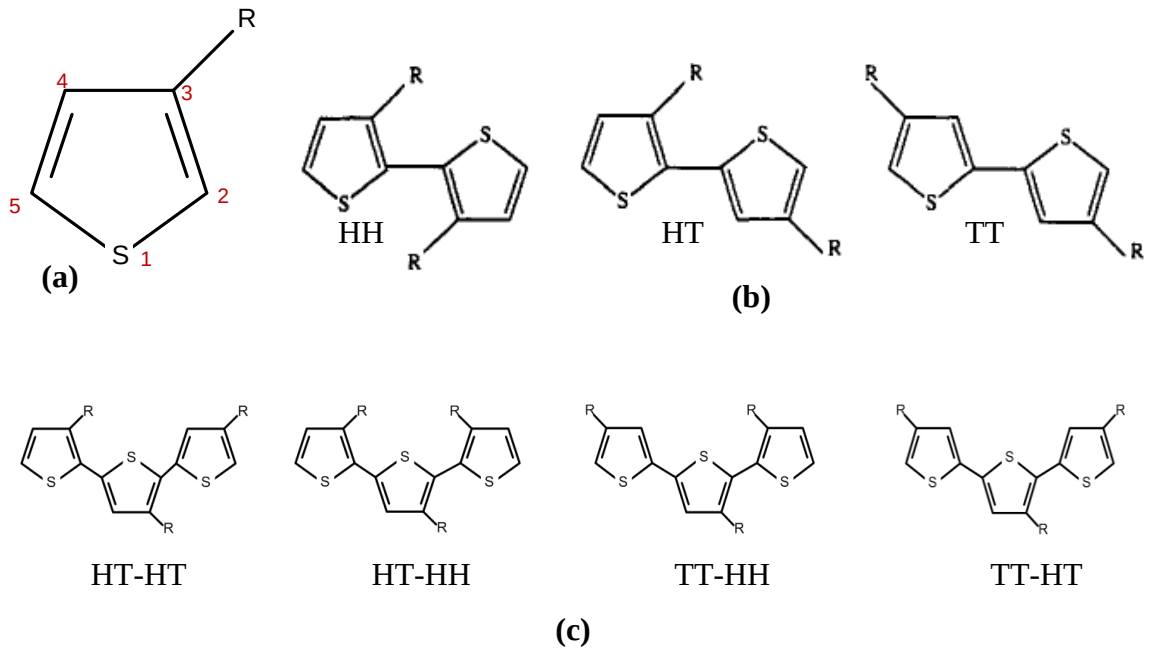

Figure 3.2: (a) 3-subtituted thiophene, where the 2- and 5- positions are designated as the head and tail (eds. Brabec et al. 2008); (b) three possible couplings formed between two 3-substituted monomer thiophene unit, and (c) the four distinct configurational triads that can be formed from coupling 3-substituted thiophene units.

The molecular weights and processing conditions both have a significant influence on optical properties, film morphologies, energy levels, and charge carrier mobility (Wang et al, 2010).

It has been shown that for different molecular weights of a conjugated polymer (e.g. P3HT), the measured charge carrier mobility differs (Ballantyne et al, 2008). Mobility can be improved by orders of magnitude as the molecular packing is optimised. In their work, Ballantyne and co – workers showed decreased mobility in P3HT: PCBM solar cells, for polymer with molecular weights > 30kDa (kilodaltons, molecular weight). A possible explanation given for this is that the polymer chains tend to tangle for higher molecular weights, thereby distorting the polymer backbone, decreasing intra-chain transport, and/or also reducing inter-chain charge hopping due to less overlap of conjugated segments.

Owing to these molecular attributes found particularly in P3HT, they are increasingly been employed for studying a range of optoelectronic devices such as organic light emitting diodes (OLEDs) (Li et al. 2002; Shrotriya & Yang, 2005; Perepichka et al. 2005), thin film field-effect transistors (TFT's) (Sirringhaus et al. 1999; Zen et al. 2004), and even more so in OSCs (Kim et al. 2007; Oklobia & Shafai, 2013).

3.3.1.1 Properties of P3HT

UV-visible spectroscopic studies of rrP3HT thin film show maximum absorption occurring at ~ 550 nm (Chen et al, 1995). Additionally, there are other well resolved features present. Two peaks at around 525 and 595 nm, and a well – defined shoulder – like feature at ~610 nm. The distinct shoulder on the long – wavelength of the absorption spectrum is generally accepted to be indicative of inter-chain interaction. A more pronounced shoulder is indicative of improved inter-chain interaction, as opposed to a weak or missing one. Contrastingly, these notable features are blue shifted in ranP3HT, since they differ in their molecular conformation owing to different regiochemistry. Barbarella et al (1994) in their report showed that P3HT with different percentages of regiochemistry displayed different optical and electrical properties. A maximised regioregularity eliminates out – of – plane twists along the backbone of the polymer, otherwise the planarity of the molecule is disrupted, decreasing its effective conjugation. This is reflected by the shifts in the optical absorption spectrum as the regioregularity decreases. Kim et al (2006) demonstrated the correlation between polymer regioregularity and device performance. In their work, they reported a strong influence of regioregularity on solar cell performance. This was attributed to enhanced optical absorption and charge transport for maximised regioregular P3HT polymer chains and crystalline domains. It is evident from several studies that the degree of regioregularity of the polymer is critical in view of device applications (Kim et al. 2006; Woo et al. 2008).

Charge carrier mobility on the other hand can be systematically improved by maximising the regioregularity and molecular weight of the polymer (Hagen, 2012). Achieving highly ordered polymer chains within the BHJ structure is therefore desirable, as it promises efficient absorption and charge transport properties.

Furthermore photoluminescence (PL) spectra studies have also shown that higher rrP3HT tend to exhibit an increase in PL intensity, suggesting that in the more ordered polymer, non – radiative quenching pathways are reduced (Kim et al, 2006). This information is significant in light of recombination processes, discussed in section 2.6.2.

Diffraction techniques such as grazing-incidence X-ray diffraction (GIXRD) have revealed that the structure of regioregular polymer films consists of microcrystalline domains in an amorphous matrix (Mao et al. 1993). The XRD data show peaks interpreted as polymer chain stacking in a particular orientation, forming a lamella structure (Mao et al. 1993; Sirringhaus et al. 1999, Brown et al. 2003). These reflection peaks in the case of a regiorandom polymer, are absent. In P3HT thin films, three significant reflection peaks associated with highly regioregular polymer has been reported in literature (Mao et al. 1993, Chen et al. 1995). These are termed 1^{st}, 2^{nd} and 3^{rd} order reflections. They are associated with in-plane stacking of polymer chains, with an interlayer *d*-spacing of ~16.4 Å. The orientation of the π – stacked polymer chains have been reported to have a significant impact on the electrical properties of corresponding polymer – based devices (Sirringhaus et al. 1999; Kim et al, 2006). Employing thin film field effect transistor structures, Sirringhaus and co – workers (1999) were able to probe the dependence of transport properties on molecular orientations of P3HT polymer chains. It was found that depending on processing conditions, the polymer chain can adopt two different orientations, namely edge – on or face – on with respect to the substrate. It was also shown that their mobilities differ by more than a factor of 100.

An enhanced intraplane chain, stacking perpendicular to the substrate (edge – on) is favourable for improved electrical properties of solar cells. This is because the edge – on orientation in OSC architectures is beneficial for inter – chain transport by hopping (Kim et al, 2006).

Complimentary structural studies, employing atomic force microscopy (AFM), have also been performed to probe the surface structures of the polymer thin film (Shrotriya et al. 2006; Ayzner et al. 2009). These revealed regular "spaghetti-like" structures in an amorphous matrix (Shrotriya et al. 2006). Such studies have shown that it is possible to estimate the

polymer mean crystal size using AFM. This was found to be approximately between 10-50 nm (Shrotriya et al. 2006), which is comparable to that from reported X-ray diffraction data (Erb et al. 2005).

Figure 3.3 is an illustration of the edge – on orientation exhibited in polymer P3HT thin film. In the Figure, **a**, denotes the lamella spacing (separated by alkyl side chain) indicated by the (100) reflection, whereas **b**, indicated by the (010) reflection denotes the polymer chain length-independent spacing, perpendicular to the thiophene ring plane.

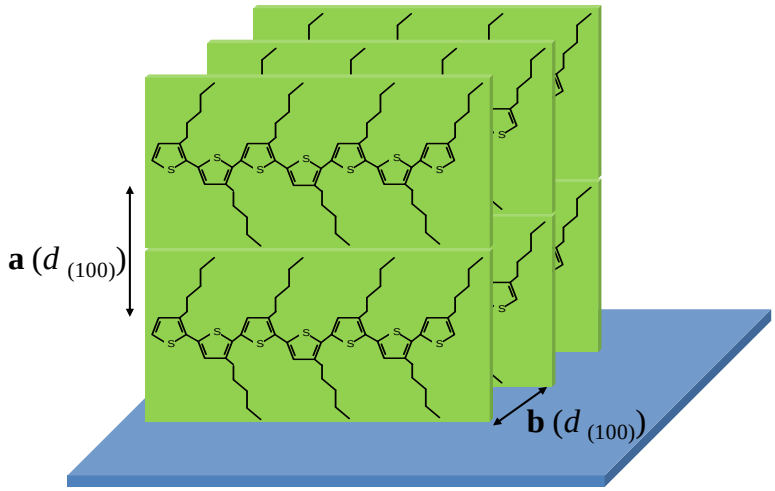

Figure 3.3: Schematic illustration of the molecular orientation of microcrystalline regioregular P3HT with respect to the substrate (Adapted from Sirringhaus et al. 1999).

Raman spectroscopy studies also show the characteristic semi crystalline structures in regioregular P3HT polymer (Nalwa et al. 2011). The Raman spectra of rrP3HT thin film consists of peaks at around 1440-1450 and another at 1380 cm^{-1}. These have been associated with the crystallinity of the polymer. These peaks are attributed to the –C=C– stretching vibrations of the 3-substituted thiophene ring and the C–C skeletal stretching, respectively (Baibarac et al. 1998). Furthermore, Klimov et al. (2006) has shown from their Raman spectroscopy studies that the polymer (i.e., P3HT) is more crystalline when the thiophene rings are averagely more closely stacked. This information on crystallinity can be deduced from the full width half maximum (FWHM) of the Raman spectra peaks. A decrease in this value after the film has been subjected to any particular treatment (e.g. thermal annealing), suggests an improvement in crystallinity.

In the next section, a brief overview of the characteristics of acceptor materials used in conjunction with polymers in OSC applications is presented.

3.4 Acceptor Materials

The efficiency of an organic solar cell employing the conjugated polymer (in a homojunction) is significantly improved when the polymer is used in a blend with another nano-material in a heterojunction. The heterojunction concept (previously discussed in section 1.2) produced a 15% improvement in the external quantum efficiency over a bilayer heterojunction device (Tang, 1985). The improvement was interpreted to have originated from exciton dissociation at the interface of the organic semiconductors. These investigations are evidences that support the beneficial need for an interface between the conjugated polymer and the acceptor material, necessitating efficient exciton dissociation. The conjugated polymer is blended with a solubilized form of buckminsterfullerene (C_{60}) in the BHJ structure (Yu et al. 1995). This has resulted in dramatic improvements in OSC efficiencies, as previously discussed. The use of the conjugated polymer-fullerene derivative based BHJ is currently considered the most efficient conjugated polymer-based PV device. Generally, in OSCs, the C_{60} or its derivative (PCBM) has been mostly used as the electron accepting material. This is mostly because fullerenes have a high electron affinity, making them suitable materials utilised in conjunction with polymers. In the next section, a brief overview is presented on what have now become the most successfully used acceptor material in OSCs, namely [6, 6] phenyl-C_{60}-butyric acid methyl ester, PCBM.

3.4.1 [6, 6] phenyl-C_{61}-butyric acid methyl ester, [60] PCBM

In addition to having high electron affinities, organic materials mostly used as electron acceptors typically provide a transport medium for electrons within the active layer of OSCs. One of such material, as mentioned earlier is the fullerene, C_{60} and its derivative, [60] PCBM. Figure 3.4 shows the chemical structure of the fullerene (which resembles that of a soccer ball, hence also referred to as 'bucky-ball'), and its derivative.

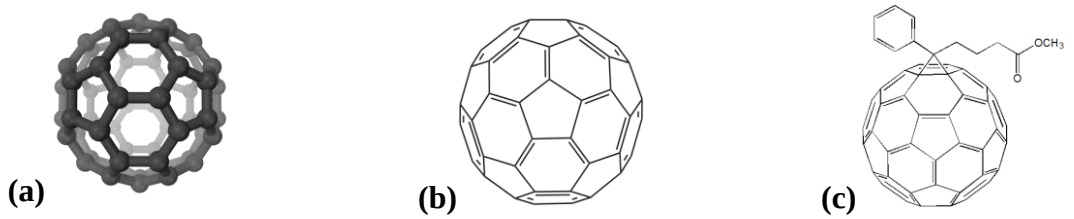

Figure 3.4: (a) 3-D illustration of the Buckminsterfullerene (b) Buckminsterfullerene, C_{60}, (c) [6, 6]-phenyl butyric acid methyl ester.

The Buckminsterfullerene is a molecule consisting of 60 carbon atoms, arranged into twelve pentagons and twenty hexagons (Yadav & Kumar, 2008). First reported in 1985 by Kroto and co – workers, it is in itself not readily soluble in solvents used for dissolving most conjugated polymers. It was successfully employed in the development of the bilayer heterojunction together with a *p* – type semiconducting material (Sariciftci et al, 1993; Roman et al, 1998). By adding a functional group to the C_{60} molecule (see Figure 3.4 (c)), Hummelen et al (1995) were able to demonstrate a solubilized derivative of the Buckminsterfullerene, [6, 6] phenyl-C_{61}-butyric acid methyl ester, [60] PCBM.

3.4.1.1 Properties of [60] PCBM

In BHJ OSC, [60] PCBM does not usually absorb photons significantly in visible region of the solar spectrum. Rather it mainly facilitates exciton dissociation, charge separation and subsequently transport of electrons to the electrode respectively (Tvingstedt et al. 2009). The pristine [60] PCBM thin film shows a strong characteristic absorption in the ultraviolet region, mostly in the wavelength range of 200 – 400 nm (ed. Choy, 2013). This is a relatively low-optical absorption in the solar spectral range.

Optical microscopy studies (Jo et al. 2009), have shown that within the bulk heterojunction blend, [60] PCBM molecules exhibit the unique property of self assembly and crystallization. This typically occurs as a function of processing conditions. This phenomenon has been demonstrated to occur strongly following thermal annealing (Swinnen et al. 2006). In OSC applications, the crystallization of [60] PCBM molecules has significant implications on charge carrier mobility (eds. Brabec et al, 2008). Analogues to conjugated polymers, it is known that charge carrier mobility also exhibits a dependence on the crystallinity of the acceptor molecules. This was demonstrated when the crystal structures of [60] PCBM was crystallized from chlorobenzene by Rispen et al. (2003); it was found to have a ball-to-ball (i.e., fullerene-fullerene centre-to-centre) distance of ~0.1 nm. This configuration happens to be similar to that in C_{60} as well. The study provided an indication of the sensitivity of charge carrier mobility to the slight variation in ball-to-ball distances in view of different organic solvents used in crystallizing different [60] PCBM crystal structures. Additionally, it also implies that in the BHJ thin film, different structures are precipitated due to different solvents. This will ultimately yield varying molecular configurations and nanomorphological structures. For an optimised BHJ nanomorphology, one with favourable D/A interfaces,

percolating pathways for charge transport, the controlled aggregation and crystallisation of acceptor molecules is critical (Chirvase et al. 2004; Jamieson et al. 2012).

Other properties such as the dielectric constant of [60] PCBM is somewhat similar to that of C_{60}, which is essentially at the core of the derivatized fullerene (Mihailetchi et al. 2003). Having a value of 3.9, is a relatively high dielectric constant, which has a positive implication on charge carrier formation in blends with donor polymers in OSCs.

3.5 ITO – coated substrates and Buffer layer materials

OSCs are fabricated starting with the substrate, which is typically a glass slide coated with a thin layer of electrically conductive and optically transparent indium tin oxide (ITO) (Krebs, 2008). ITO – coated substrates also have been and are still extensively employed in a variety of applications beside OSCs. Such applications include: organic light emitting diodes (OLEDs), and liquid crystal displays (LCDs), due to their good transmittance in the visible region of the solar spectrum and low electrical resistivity (Breen et al, 2002; Minami, 2008; Tan et al, 2014; Alvarez-Fraga et al, 2015). In a typical OSC application, the ITO – coated substrate used, serves as the anode of the device, usually needs to be patterned to avoid short circuiting in the completed device. When making connections to the evaporated metal electrode (e.g. Al) of the OSC device, there is the risk of short – circuiting the device. Patterning of the ITO – coated substrate thus prevents this from happening. This is achieved by etching and will be discussed further in the next chapter.

Other materials also used in the fabrication of OSCs include what are generally referred to as electrode interfacial of buffer layer materials (Yin et al, 2016). One of such materials is poly (3, 4-ethylenedioxythiophene) polystyrene sulfonate, PEDOT: PSS; which is available in an aqueous dispersion (eds. Sun & Sariciftci, 2005). It became prominent when the stability and performance of polymer LED was found to improve as a result of using it as a buffer layer between ITO and the polymer active layer (Cao et al, 1997; Carter et al, 1997). Figure 3.5 shows the molecular structure of PEDOT: PSS. In the fabrication of OSCs, a thin transparent layer of PEDOT: PSS is formed on a pre-cleaned ITO – coated substrate by spin coating. The important properties of PEDOT: PSS thin films in OSC applications are high electrical conductivity and a smooth surface (eds. Sun & Sariciftci, 2005). A hole conducting layer, it improves the surface roughness of ITO – coated substrate, and stabilizes the electrical contact between the anode and the active layer (Krebs, 2008). This stabilization is achieved due to its

desirable work function, as it decreases the energy barrier at the interface between the anode and the active, and ensuring effective collection of holes (eds. Sun & Sariciftci, 2005).

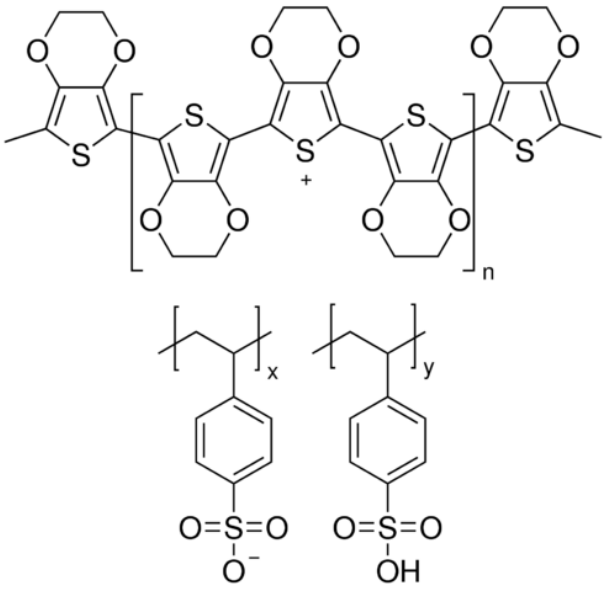

Figure 3.5: Molecular structure of PEDOT: PSS (eds. Sun & Sariciftci, 2005).

Since they are hole conducting, the PEDOT: PSS is between the active layer and the anode (the hole collecting anode), as such they are also considered as anode interfacial layers. Similarly, at the cathode, where electrons are collected, they are materials that can be used as buffer or interfacial layers. Examples of these include calcium (Ca) (Li et al, 2007), lithium fluoride (LiF) (Wang et al, 2013). Due to their low work function, they similarly provide stable electrical contact between the cathode and the active layer. Both Ca and LiF are deposited by thermal deposition.

For single – charge carrier devices (in a diode configuration) used for experimental measurement of charge carrier mobilities, it is necessary for the device to conduct only one type of charge (holes or electrons) (Coropceanu et al, 2007). To fabricate such a device, the active layer is sandwiched between buffer layer materials which will block one type of charge. For example, PEDOT: PSS a hole conducting material cannot be employed in an electron-only device, thus it is replaced with another material. Caesium carbonate (Cs_2CO_3) is a good replacement material (Shrotriya et al, 2006); as its work function low compared to PEDOT: PSS, thus increasing the energy barrier, which will block the injection of holes. This will be discussed later in chapter 5.

3.6 Summary

In this chapter, a brief overview of the constituent materials for an OSC device was presented. Particularly with respect to the work of this thesis, only the materials used in fabricating OSCs investigated here, were considered in detail. P3HT and PCBM are available from a number of suppliers. They are weighed and dissolved in solvents such as dichlorobenzene or chlorobenzene in the required ratio to form a blend solution. The active layer of the OSC is applied to the substrate by spin coating, which will be discussed in detail in the next chapter. Important material properties were highlighted as they pertain to their application in OSCs. One of which is the compatibility of donor and acceptor materials; the difference between the LUMO levels of the two materials should be sufficient to overcome the exciton binding energy. This is to ensure that exciton created is subsequently dissociated successfully. The importance of other properties such as solubility of the materials in solvents, charge carrier mobility, to OSCs, was also highlighted. The role and importance of OSC components other than the active layer composite materials such as ITO – coated substrates and buffer layer materials were discussed.

Chapter 4

Methods and Background of Experimental Approach

"... The scientific method itself would not have led anywhere; it would not even have been born without a passionate striving for clear understanding."

— Albert Einstein

4.1 Introduction

Details of materials and methods, including the respective instrumentations employed for this thesis is presented in this chapter. In addition, discussions on the background of the experimental approaches taken are also outlined. These include measurement principles underlying thin film characterisation techniques employed. Table 4.1 summarises the list of materials used in this thesis.

Table 4.1: Summary of materials used in this work

Active layer materials	Poly(3-hexylthiophene), P3HT (96.6% RR), and acceptor material, [6, 6] phenyl-C61-butyric methyl ester, $PC_{61}BM$
Buffer layer materials	Poly (3, 4-ethylenedioxythiophene): poly (styrenesulfonate) (PEDOT: PSS), Calcium (Ca), Lithium fluoride (LiF), Caesium carbonate ($CsCO_3$)
Electrode contact material	Aluminium, Al (cathode), Indium tin oxide, ITO (anode), Gold (Au)
Substrates	ITO – coated, and quartz glass substrates
Solvents	Dichlorobenzene, chlorobenzene, acetone, isopropyl

4.2 Thin Film Deposition and Device Fabrication

Thin films of materials can be obtained by a number of techniques. Some of these include, spin coating, doctor blading, spray coating, printing, thermal deposition, etc. (Krebs, 2009). Depending on which technique is employed, thin films of materials are either fabricated from their solutions or their solid forms respectively. Spin coating and thermal deposition are the two techniques used in this thesis. Prior to thin film deposition and device fabrication, all substrates (ITO – coated or quartz) were first prepared according to the procedures outlined in the following sections.

4.2.1 Quartz glass substrates

All the quartz glass substrates used in this work were cleaned in three sequential steps, using an ultrasonic bath. Three different solvents are used in each step, namely; deionised water, acetone, and isopropyl alcohol (IPA). First the substrates were immersed in a beaker of deionised water and then placed in an ultrasonic bath for ten minutes. The same procedure was repeated, this time with acetone and subsequently IPA. The substrates were subsequently dried, kept in a Petri dish, and transferred to nitrogen – filled glove box (< 1 ppm of O_2 and H_2O).

Quartz glass substrates here are mainly used for fabricating thin films of a pristine P3HT, PCBM or their blend for absorption, Raman, photoluminescence spectroscopy, AFM, and x-ray diffraction studies. However, where they are used for fabricating devices with a diode configuration, metal/thin film/metal, the cleaned quartz glass was first coated with a thin film of metal electrode (Al).

4.2.2 ITO-coated glass substrates

The procedure for cleaning ITO-coated substrate is the same as that outlined in section 4.2.1. Before cleaning however, the substrates were pre-patterned. Patterning of the substrates by etching was important in order to avoid short circuits when making connections to the completed OSC device. By etching, a region of the ITO-coated substrate is stripped of ITO coating. Etching methods that can be utilized to pattern ITO – coated substrates include sputter etching, and acid etching. Sputter etching process involves bombarding the ITO – coated substrate with argon ions, resulting in a controlled removal of the ITO coating. In this thesis, all ITO – coated substrates were patterned using the acid etching process. The process involves the use of an acid solution (concentrated hydrochloric acid, HCL) to strip away the

ITO coating from the substrate. First the portion on the substrate that does not require etching is taped over with a masking tape. The substrate is then immersed in a solution of HCl in a beaker, and left for 20 minutes. Following successful etching, the substrates (without the masking tape) are subsequently cleaned, following the procedure described in section 4.2.1. Figure 4.1 schematically summarises the procedure from substrate patterning to fabrication of the completed organic solar cell device.

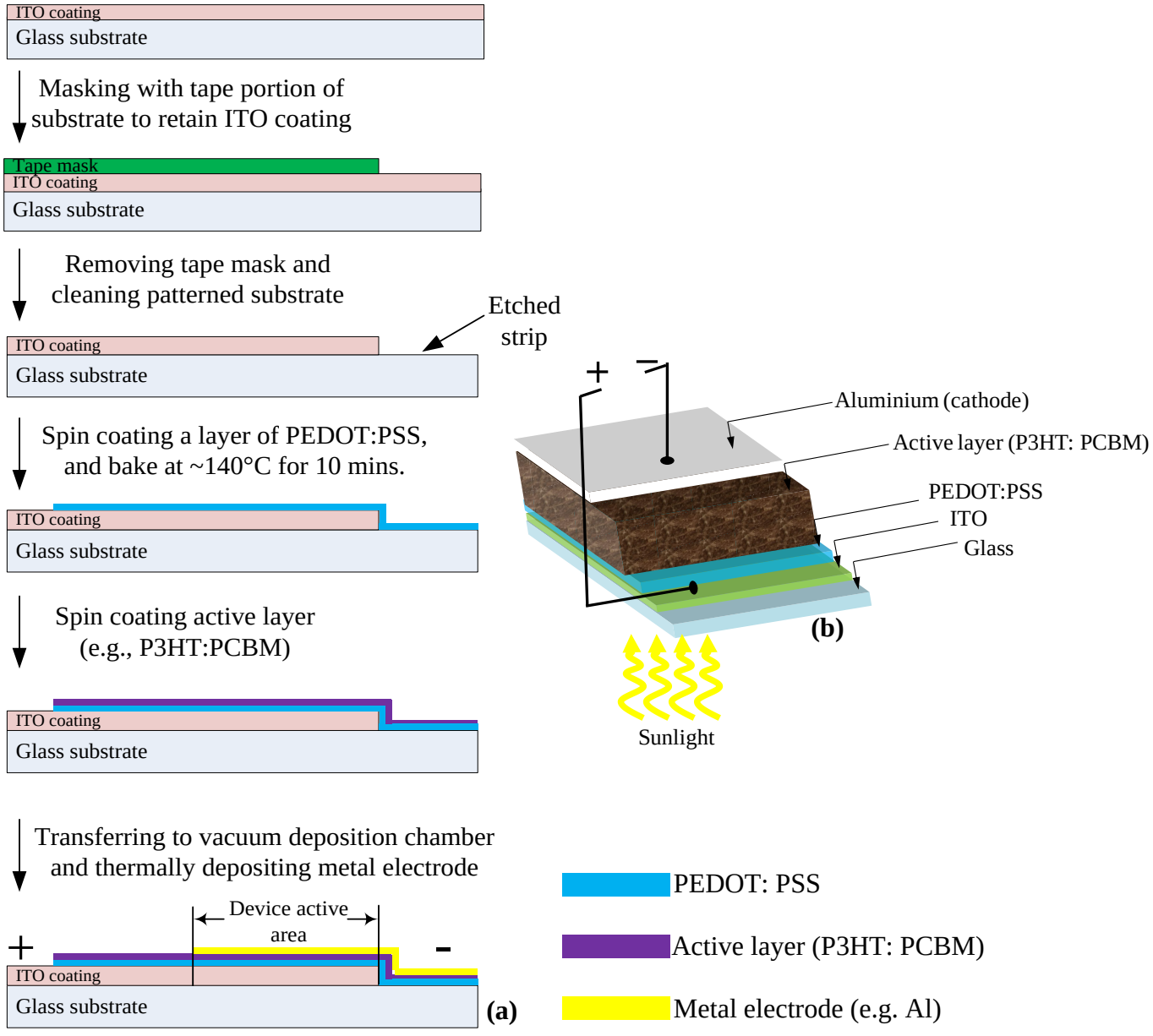

Figure 4.1: (a) A flow diagram illustrating the procedure from ITO – coated patterning, through depositing the buffer layer (PEDOT: PSS) and active layer to the completed organic solar cell device (b) 3-dimensional view of a completed organic solar cell.

All thin film depositions, were performed in nitrogen – filled glovebox. The vacuum deposition chamber wherein electrode contacts were deposited is housed in the glovebox. Thus samples are not exposed to the ambient at any time during the device fabricating process. The device's active area is defined by a shadow mask, and the overlap of the top and back electrodes (see Figure 4.1).

4.2.3 Spin casting method

Spin casting is a widely used method for depositing thin films from solution. This is performed by employing a spin coater. In this thesis, the KW – 4A spin coater (Chemat Technologies Inc) was used. The process of spin casting typically involves dispensing a solution on to the surface of the substrate. This substrate, firmly fixed on the spin coater's stage, will be subsequently spun at a speed and duration, set by an operator. Due to the effect of the centripetal force associated with the spinning action, the solution will evenly spread over the surface of the substrate. Figure 4.2 depicts a summary of the spin casting procedure, including an illustrative example of a typical spin curve.

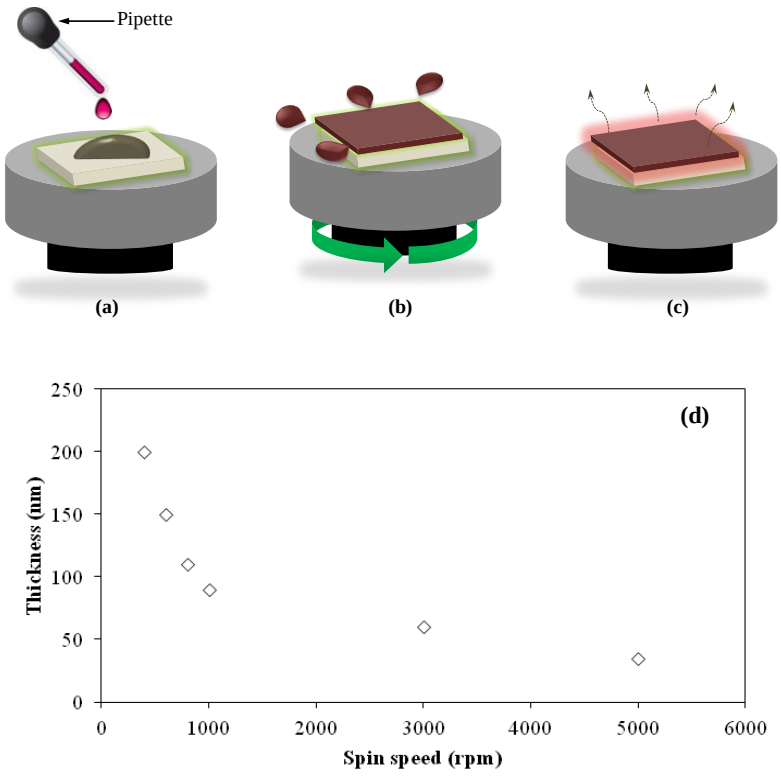

Figure 4.2: (a) Dispensing the solution on to the substrate, (b) Solution thin out, as substrate spins, (c) Film formed at end of spin, residual solvent evaporates, (d) Typical spin curve for a P3HT: PCBM blend solution of 2 wt %.

At the end of the spin, the solution would have undergone a shear thinning out. This is accompanied with the evaporation of the solvent, leaving an almost homogeneous film on the substrate. It should be noted that the thickness of the deposited film varies with spin speeds and concentration of solution. It has been shown that the film thickness is proportional to the rotational speed (Norman et al, 2005), according to relation $d = k\omega^{\alpha}$. d is film thickness, ω is the angular velocity, and k and α, are empirical constants, which are related to the physical properties of the solution (e.g. viscosity) and substrate (e.g. surface energy). In the case where low boiling solvents, such as chlorobenzene is used, the resulting thin film is usually dried at the end of the spinning process. On the other hand, depending on spin duration, the films may still be wet in the case of high boiling point solvents (e.g. 1, 2 – dichlorobenzene).

4.2.4 Thermal Deposition method

Thermal deposition is also another commonly used method for thin film deposition in the field of organic solar cells. For the deposition of metal electrodes, buffer layers (such as Ca, LiF), the Auto 500 vacuum deposition system (HHV Ltd) was employed in this work. Figure 4.3 is a schematic illustration of a vacuum deposition system for thin film fabrication employing the thermal deposition method.

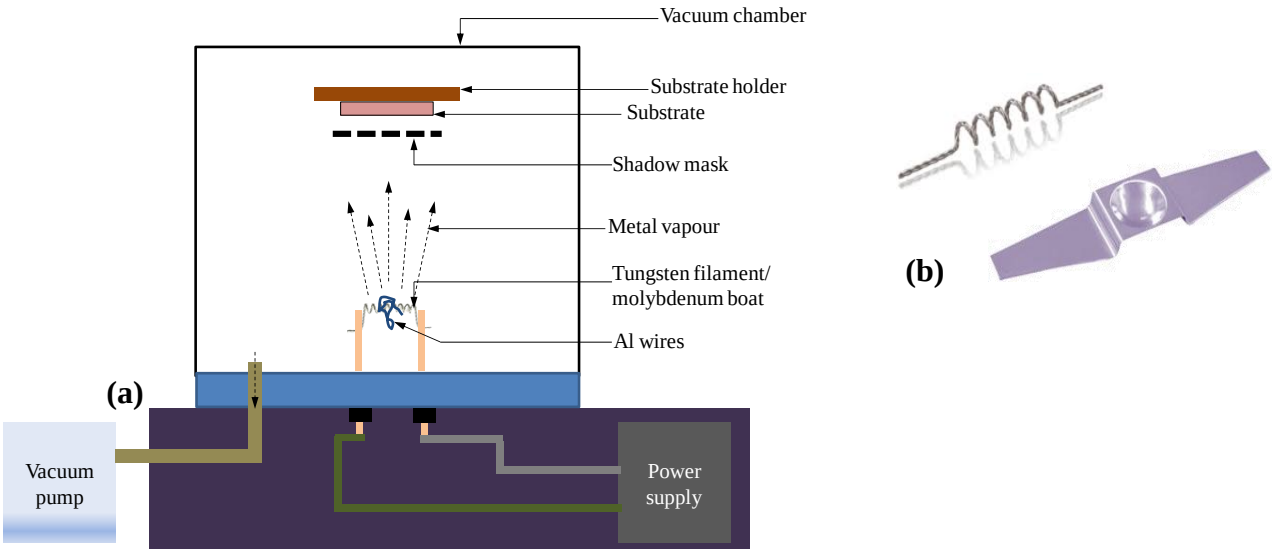

Figure 4.3: (a) A schematic illustration of the thermal evaporation method of thin film deposition, (b) Pictures of evaporation sources; a tungsten filament and a molybdenum boat.

The process of thermal deposition requires that the source material to be deposited is heated to high temperatures under vacuum (~10^{-6} mbar). Consequently it evaporates, with its vapour transported to and deposited on the surface of the substrate. On the substrate surface, located

at a distance from the source material, the evaporant vapour condenses, forming a thin film. To evaporate Al and Ca, tungsten filament was used as the evaporation source, whilst molybdenum boats were employed for depositing LiF and Au. To ensure that deposition is generally consistent, producing uniform films, it was imperative that the deposition process was performed at base pressures aforementioned (i.e. ~ 10^{-6} mbar or less).

4.3 Thin Film property characterisation methods

The methods used in studying the spectroscopic, structural and electrical properties of thin films fabricated in this thesis are presented in this section. All spectroscopy characterisation techniques are on the basis of measuring processes associated with the interaction of electromagnetic radiation with the respective thin film material (Yacobi, 2002). These processes include (not limited to) ultraviolet-visible (UV-Vis) absorption, reflection, transmission, scattering (Raman) or emission (Photoluminescence) of light of a particular wavelength range by the material medium. These processes are summarised illustratively in Figure 4.4.

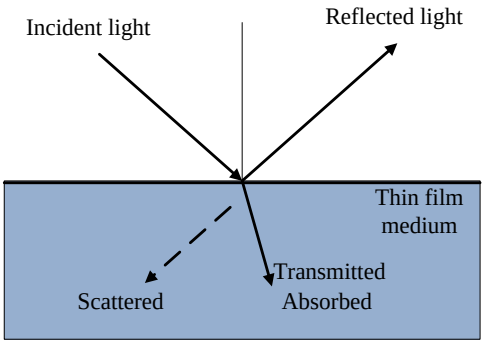

Figure 4.4: Schematic representation of the various optical processes as a result of interaction between electromagnetic radiation and material medium.

Structural methods involve measurements which provide useful information regarding the orientation of nanodomains of composites within and on surfaces of thin films. From these measurements, it is possible to elucidate the impact of processing parameters on the nano – morphology of pristine, and BHJ thin films. In this work, X-ray diffraction (XRD) and atomic force microscopy (AFM) were used for the structural characterisation of thin films. These methods have been demonstrated to be very useful in thin film characterisation in organic solar cells (Erb et al. 2006; Shrotriya et al. 2006; Nguyen et al. 2007). In the

following sections, the aforementioned methods as employed in this work shall be presented in detail.

4.3.1 UV-Vis absorption spectra measurement

UV-Vis absorption spectra measurements of thin films have been extensively used as a spectroscopic technique for the characterisation of materials and thin films for OSC applications (Oklobia & Shafai, 2013; Erb et al. 2006; Shrotriya et al. 2005). The measured UV-Vis spectrum of thin films can also be used to extract significant physical information on the composite material in the film. This information includes the optical and electronic properties of the thin film material(s). The optical band gap is a good example of an electronic property that can be extracted from thin film absorption spectra. This is because the absorption of light of particular wavelength range by materials is attributed to electronic transitions (Zhong, 2009). According to Beer's law, the characteristic absorption, A is a function of incident light, I_0 and transmitted light, I, intensities, as expressed in Equation 4.1.

$$A = \log\left(I_0/I\right) = -\log_{10} T \tag{4.1}$$

,where T is the transmittance (I/I_0). The plot of A as a function of light wavelength represents the absorption spectrum. Varian Cary 50 UV – Vis spectrophotometer was used to obtain all the absorption spectra of thin films in this thesis. This mainly consists of a light source, and detector optics. Figure 4.5 is a schematic illustration of the key components and set – up of the instrument.

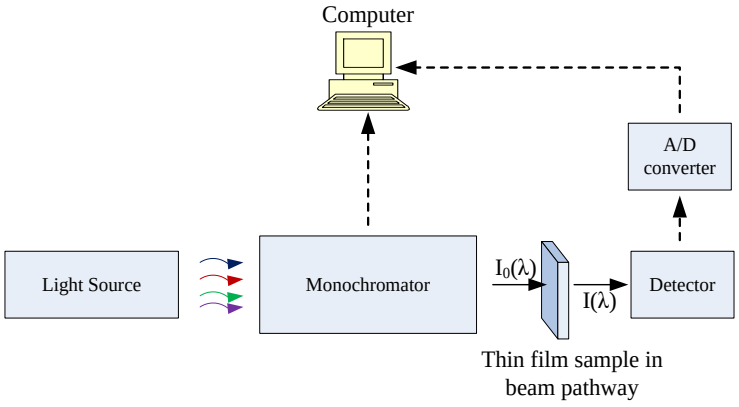

Figure 4.5: Schematic illustration of the main instrumentation components of a typical UV-Vis spectrophotometer.

Additionally UV-Vis absorption spectra measurements can also probe the nanoscale structural properties in thin films, such as polymer conjugation and interchain interaction (Li et al, 2006). As well as being a spectroscopic technique, it can also to an extent be applied for probing the nature of phase separations in composite thin films (Oklobia & Shafai, 2013).

4.3.2 Raman and Photoluminescence spectra measurement

The other spectroscopic techniques for thin film characterisation are Raman and Photoluminescence (PL) spectroscopy. These methods are effective and widely used as non-destructive techniques for the characterisation of thin films and nanoscale structures in the field of OSCs (Guo et al. 2008; Campoy-Quiles et al. 2008, Nalwa et al. 2011). Raman spectroscopy is discussed first, followed by PL spectra measurements.

The principle of operation of Raman spectroscopy is based on the measurement of the shift in frequency (or energy) of the scattered light following its incidence on a sample (thin film) under investigation (Yacobi, 2002; Ferraro et al. 2003). As illustrated in Figure 4.4, scattering is one of the processes that results from the interaction of electromagnetic waves (usually monochromatic light) with the molecules of the sample material. The frequency of most of the scattered light is similar to that of the incident light. But a fraction of the scattered light is at a different frequency. This shift in frequency gives rise to the effect referred to as Raman scattering (Mayo et al. 2003). The difference in frequency between the incident and scattered light is termed Raman shift. This corresponds to the energy of vibration of the scattering molecule (Yacobi, 2002). The Raman spectra from a sample under investigation are commonly regarded as both unique spectral and molecular "fingerprints". A number of significant information can be obtained from the Raman spectra, which are both qualitative and quantitative in nature. In examining composite materials commonly used in organic electronics, for example blends of polymers/polymers or polymers/fullerenes for light emitting diodes (LEDs) or solar cells, their identification and characterisation are important. The qualitative analysis of Raman spectra can also be used to map composite materials. The intensities of peaks (or bands) observed in P3HT thin films, for example, have been shown to correlate with the concentrations of the functional groups yielding them, therefore allowing for quantitative analysis (Socrates, 2001; Klimov et al, 2006). Probing the nature of conformation of nanodomains of composite materials within thin films can also be achieved using Raman spectroscopy. Such knowledge is useful for understanding the impact of thin film nanodomains on the performance of OSCs. Raman spectra analysis of thin films have

been reported, correlating the full width at half maximum (FWHM) of Raman peaks with polymer self – organisation and crystallinity respectively (Nalwa et al. 2011).

Raman spectra of thin films studied in this thesis were all obtained using the InVia Raman microscope (Renishaw Inc.). The instrument consists of an optical microscope coupled to a Raman system. Thin film samples are illuminated through the microscope coupled with a monochromator. The instrument set – up is illustrated in Figure 4.6. It should be noted that one of the advantages of this set – up is that it allows for obtaining spatially resolved Raman spectra with about a 1 µm resolution (Yacobi, 200). Laser with an excitation wavelength of 514 nm was employed.

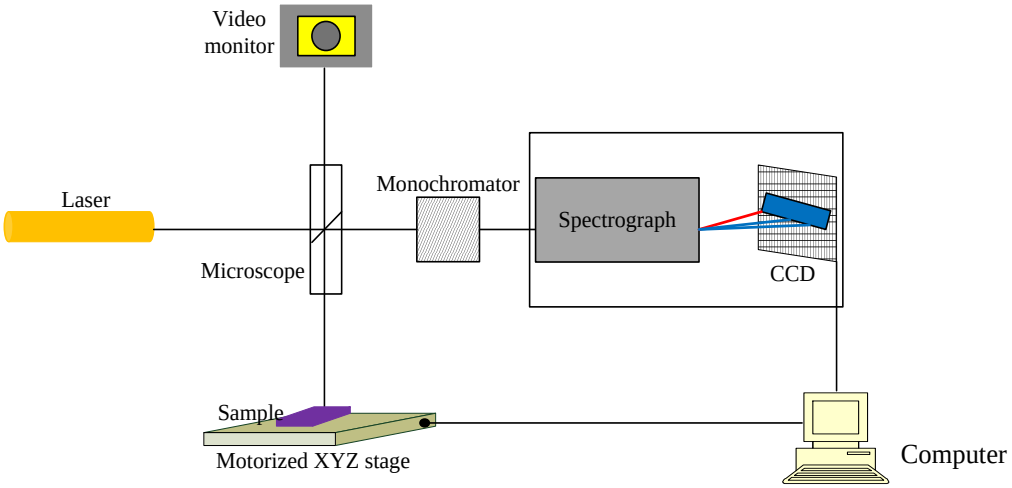

Figure 4.6: Principle of a conventional micro Raman spectrometer (Adapted from Gouadec & Colomban, 2007).

PL spectroscopy on the other hand can also be a useful technique. It is often used to compliment Raman and UV – Vis spectra measurements. Photoluminescence is the spontaneous emission of light following the photo excitation of a material. Analysis of PL spectra involves comparing the emission counts from a pristine polymer thin film and that from a thin film comprising a blend of the pristine and a small molecule for example. An observed quenching of the spectra in the case of the blend of donor/acceptor materials is indicative of charge transfer from polymer to the small molecule. For an efficient OSC, complete PL quenching is ideal. In addition to probing charge transfer dynamics in blend thin film, the method can be used to evaluate how well composite materials in thin films are intermixed (phase separation) (Chirvase et al. 2003; Tsoi et al. 2011). The typical experimental set-up for PL measurements include a laser with a specified wavelength

(excitation wavelength), which is used to excite the sample surface. The sample emits its characteristic photoluminescence, which, through a lens is measured by a spectrometer. The InVia Raman microscope used for obtaining Raman spectra was also used in PL mode to measure all PL spectra of thin films studied in this work. In the PL mode however, a different laser power density is employed and sample exposure times are longer in contrast to Raman spectra measurements. In addition to charge transfer dynamics, PL spectroscopy can also provide important information relating to recombination processes in active layer of OSCs (Campoy-quiles et al. 2008; Tvingstedt et al. 2009). Figure 4.7 shows a typical experimental set-up for PL spectrum measurements.

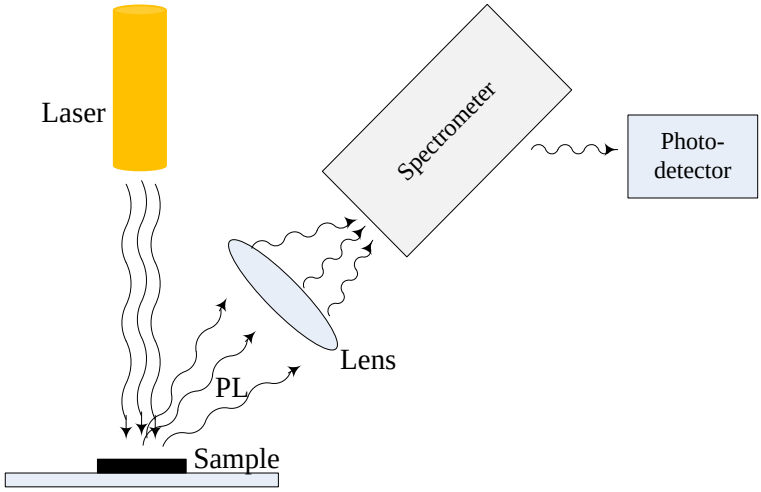

Figure 4.7: A typical experimental set-up for PL spectrum measurements.

4.3.3 Atomic Force Microscopy

Active layer/cathode interfaces play a significant role in influencing the electrical properties of BHJ solar cells (Li et al. 2005). For this reason, it is significant to probe the surface topographies of thin films which form interfaces with the cathode. Scanning probe microscopy (SPM) is generally the technique employed for imaging thin film surfaces. An example of SPM is the atomic force microscopy (AFM), which is capable of probing surface topographies down to the nanometre scale. AFM have been demonstrated to be invaluable in the investigation of thin film surfaces and how they correlate with PV performances of polymer – based solar cells respectively (Li et al. 2007; Ma et al. 2005; Karagiannidis et al. 2011). In principle, the surface probing technique images the topography and surface composition by observing changes in the dynamic properties of a vibrating cantilevered tip interacting with the surface (García & Pérez, 2002). This interaction is characterised by interatomic forces between the tip and sample surface (Petty, 2008). Figure 4.8 shows the

basic principle of an AFM. A schematic illustration of three distance – dependent regimes describing the interaction between oscillating cantilever/tip and a sample surface (Haugstad & Jones, 1999) is also included in Figure 4.8.

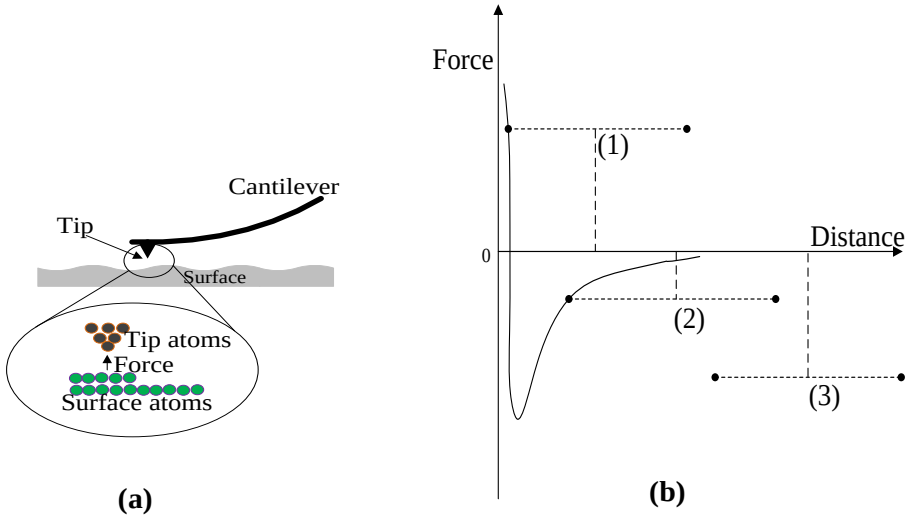

Figure 4.8: (a) AFM cantilever/tip interaction with sample surface, (b) Schematic representation of three distance-dependent regimes of oscillating cantilever/tip and a sample surface interaction. Dashed horizontal line segments indicate distance intervals between tip and sample surface at three mean distances (vertical dashed lines). These are labelled (1) intermittent contact (repulsion dominant), (2) non – contact (attraction dominant), and (3) free oscillation (no interaction) (Adapted from Haugstad & Jones, 1999).

The AFM essentially consists of a tip attached to a cantilever (AFM probe), which can operate in two modes, namely: contact, and tapping mode. All the AFM images presented in this work were obtained in the tapping mode (TM), using an Agilent 5500 surface probing microscope AFM. Tapping mode was employed because AFM imaging in contact mode can modify or damage most organic samples, as they are soft. In the tapping mode the cantilever is oscillated at a frequency in the range of 100-400 kHz by a piezoelectric transducer, with amplitude of ~20 nm. In this mode, the tip is just touching (tapping) the surface of the sample, which essentially acts a damper. The operating principle of the AFM in the tapping mode uses a feedback system to control and maintain constant amplitude of the cantilever. A change in the oscillation of the cantilever as a result of its interaction with the sample surface is sensed by a four – position – sensitive photodiode. The photodiode monitors this change by means of a reflected laser beam from the back of the cantilever head. The resulting signal from the detector is the 'Deflection' measured in volts. The difference between the

'Deflection' and a user-specified set point is referred to as the "error signal". This "error signal" is fed back via the feedback electronics to correct the difference. Figure 4.9 shows a schematic illustration of the principle of operation of the AFM.

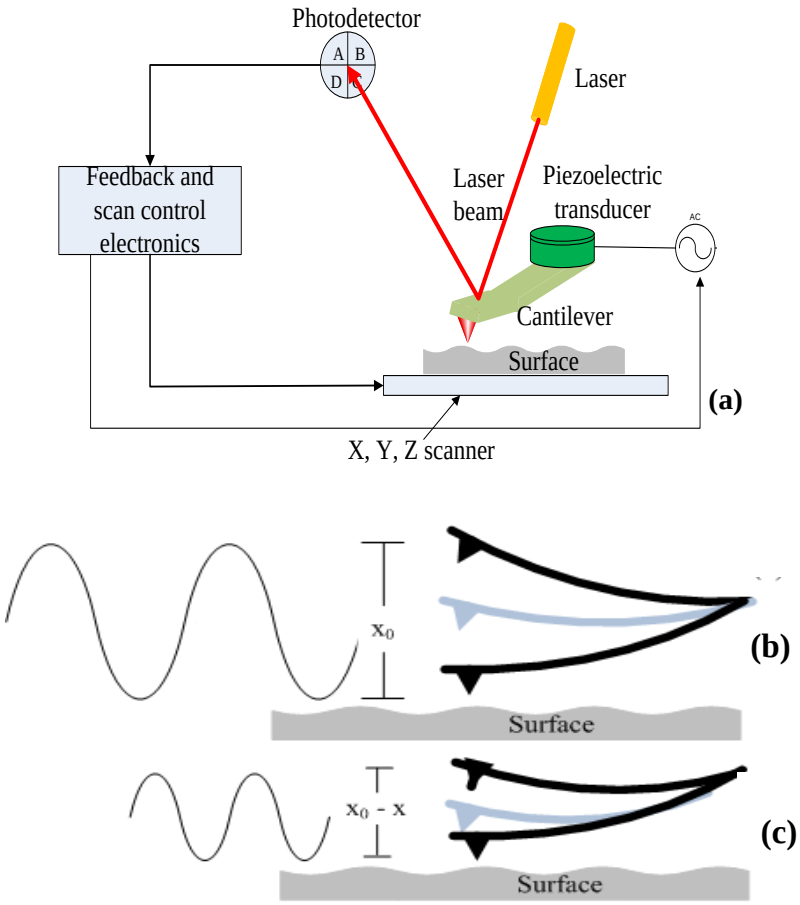

Figure 4.9: (a) A schematic representation of an AFM's principle of operation in tapping mode, (b) free amplitude before contact (c) and amplitude damping arising from tip-surface interaction.

The topographic variation of a sample surface is mapped from the analysis of the feedback signal. In addition to topography (height) images, the phase image of the sample can also be obtained. This is particularly useful for differentiating between composite materials in a thin film sample. The phase image in AFM is obtained from monitoring the phase lag of the cantilever oscillation due to amplitude damping, relative to the piezoelectric transducer signal (Haugstad, 2012). Since the measured phase lag is sensitive to varying material properties such as adhesion and viscoelasticity, it can be used to perform a compositional mapping of a sample. Figure 4.10 illustrates this principle.

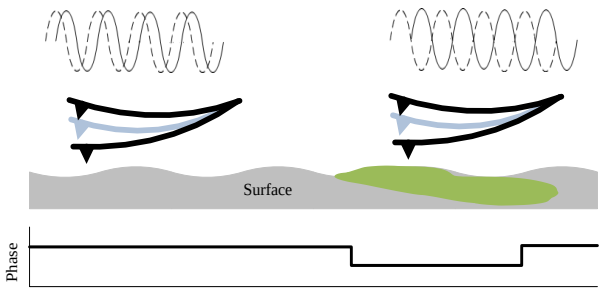

Figure 4.10: Schematic diagram illustrating the principle of phase imaging.

4.3.4 X-ray Diffraction (XRD) measurement

The performance of organic electronic materials is closely related to their thin film morphology and molecular conformation (DeLongchamp et al. 2011). For example, a highly improved crystalline polymer implies a regular structural order. This means an improved creation of regular overlap of π orbitals (ed. Klauk, 2012). These overlaps of π orbitals are involved in the transport of charges (holes and electrons). Therefore their regularity is desirable as it ensures efficient charge transport throughout the materials (as previously discussed in Chapter 3). To characterise details of the crystallographic structure and microstructure in thin films, XRD is a widely used method. In thin films nanotechnologies, particularly for BHJ OSC applications, XRD methods have been extensively employed for structural characterisations (Li et al. 2007; Guo et al. 2008). In contrast to AFM, the XRD technique has a unique advantage of probing the molecular or crystalline structures of materials (e.g., semiconducting polymers) in a thin film. The AFM surface probing technique is mechanical and confined only to the surface of the material, whilst with an XRD; further insight can be gained into the structure and orientation of molecules in thin film composites.

In XRD, a collimated X-ray beam directed from a source is incident on the plane of a sample such as a thin film at an angle of θ, which is reflected specularly (i.e., angle of reflected beam is equal to the angle of incidence). In addition, the incident beam also undergoes diffraction by the crystalline or microcrystalline phases within the sample. This condition occurs according to Bragg's law (Cutility, 1956)

$$n\lambda = 2d \sin\theta \tag{4.2}$$

,where λ is the incident X-ray wavelength, d is the interplanar spacing (i.e., spacing between layers), θ the angle of incidence, and the integer n is the interference order (1, 2, 3, ...). The intensity of the measured X-rays is a function of the diffraction angle 2θ and

crystalline/microcrystalline phase orientation (Guozhong, 2004). For polymers such as P3HT, thin film XRD has shown that there are three possible orientations: a- (100), b- (010) and c- (001) axis orientations, with their respective *d*-spacing (Erb et al. 2005; Kim et al. 2006). Figure 4.11 shows a representation of the three possible orientations found in P3HT thin film.

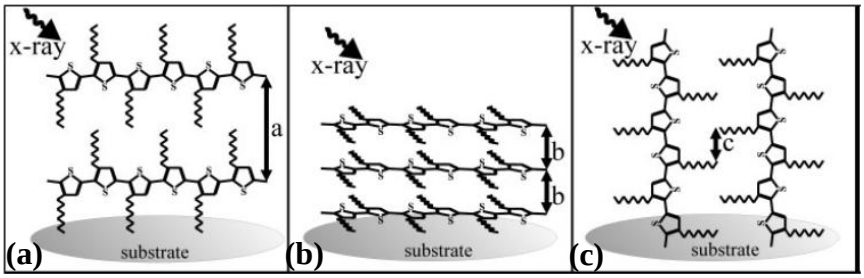

Figure 4.11: Possible crystalline orientations of P3HT crystallites with respect to the substrate: (a) *a*-axis (100), due to lamella layer structure, i.e., stacks of planar thiophene chains uniformly spaced by the alkyl side chains (b) *b*-axis (010), due to π – π interchain stacking, i.e., with spacing independent of alkyl side-chain length (c) *c*-axis (001), due to thiophene chains oriented normal to the substrate, and with alkyl side chain parallel to the substrate (Adapted from Adapted from Erb et al. 2005; Sirringhaus et al. 1999; Chen et al. 1995).

Figure 4.12 is a schematic representation of the geometry of a thin film XRD set up, where *k* and *k'* are the incident and diffracted wave vectors.

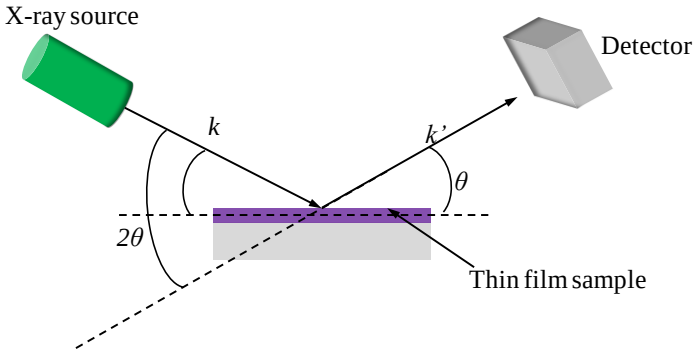

Figure 4.12: Thin film XRD geometry.

In addition, the sizes, *L*, of crystals or grains can be estimated using the Scherrer's relation (Scherrer, 1918).

$$L \sim \frac{0.9\lambda}{\Delta_{2\theta} \cos\theta} \tag{4.3}$$

,where $\Delta_{2\theta}$ is the full width at half maximum (FWHM) of the diffraction peak. All XRD spectra in this work were measured using D8 ADVANCE with DAVINCI (BRUKER, Germany), with LYNEYE detector (2 theta = 3 – 40°). The instrument was operated at a generating power of 1600 W (40kV and 40 mA tube voltage and current).

4.3.5 Thin film thickness measurement

In characterising thin films for organic solar cell application, the knowledge of the thickness of such films is important. The thicknesses of thin films in this work were measured using two types of techniques; stylus surface Profilometry and microbalance quartz crystal monitoring techniques.

4.3.5.1 Stylus Surface Profilometry technique

The DektakXT stylus surface profiler (BRUKER, Germany) is used in measuring the thicknesses of thin film samples. The instrument simply measures the thickness of thin films by a stylus tip in contact with the sample film surface. The stylus tip-surface contact force is as low as 30 nN, and this is required to access a film edge as it is traced across the sample surface. Figure 4.13 is a screen shot of a step height profile obtained using the DektakXT. As the tip makes its motion across the sample surface, a trace is collected, and converted by the analogue/digital converter electronics to a step profile shown in the Figure.

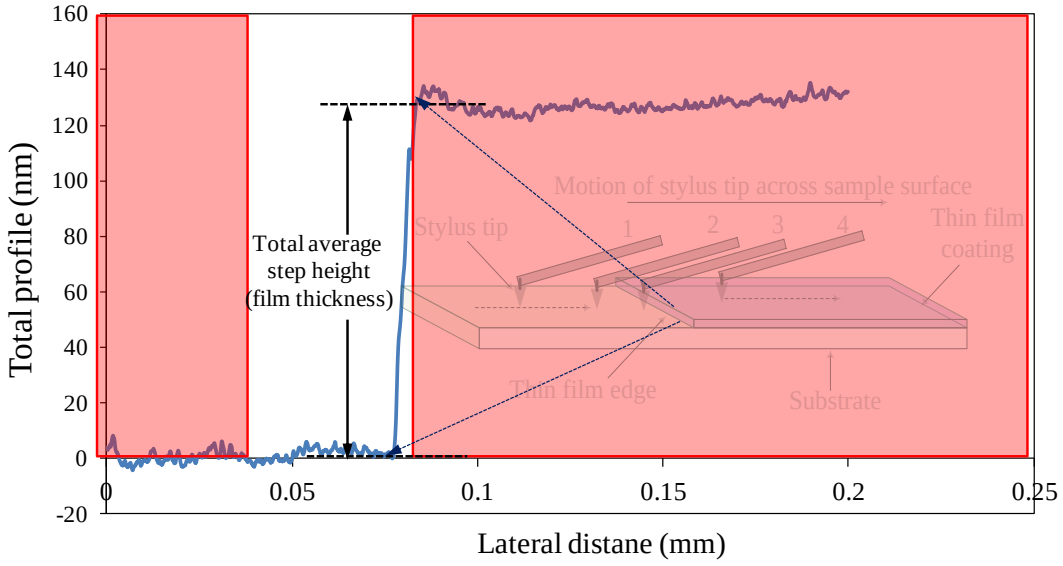

Figure 4.13: A measured step height profile of a thin film based on polymer/fullerene blend (Inset: schematic illustration of stylus tip motion).

The DektakXT surface profiler is capable of providing a step height repeatability of < 0.6 nm.

4.3.5.2 Microbalance Quartz Crystal monitoring

For thin films fabricated via spin coating, the surface profilometer can be easily employed to determine the film thickness. However for physical vapour-deposited thin films, particularly for systems under vacuum conditions, it is necessary to monitor the growth of films on the substrate during deposition. By monitoring the growth of films on the substrate, the desired thickness can be readily obtained. To achieve this, a microbalance quartz crystal monitor, IL150 thickness monitor (Intellemetrics) was used to control the thickness of thermally deposited thin films. It is useful for *in situ* monitoring of deposition rates and film thickness, during deposition under vacuum. In principle, the quartz crystal monitor operates by setting a quartz crystal oscillator (a homogeneous elastic plate) into mechanical vibration (Milton, 2001). The resonant frequency of the quartz crystal oscillator is a function of its dimension, elastic modulus and density. The crystal's properties vary as a result of the presence of additional mass in the form of deposited material during the deposition process (Milton, 2001). The change in the resonant frequency noted to vary linearly with the change in mass of deposited thin film. Using both the IL150 thickness monitor and the DektakXT, deposition rates were calibrated between 0.1-0.2Å/s for ultra thin films (e.g., LiF as buffer layers) and 2-10Å/s for the other film deposition (i.e., aluminium or gold for electrode contacts).

4.4 Electrical Characterisation Methods

The main electrical characterisation methods performed in this work include direct current (DC) current – voltage ($I - V$), capacitance – voltage ($C - V$), and alternating voltage (AC) impedance measurements. Details of these measurements are discussed in the following sections, highlighting the respective parameters that are readily studied.

4.4.1 DC Current – voltage (I–V) measurements

I–V measurements are the most commonly used method for characterising the photovoltaic performance of OSCs (ed. Krebs, 2008). From such method, key photovoltaic parameters can be evaluated. These include; the device's short circuit current density, J_{SC}, open circuit voltage, V_{OC}, current density and voltage at maximum power point (J_M and V_M). The power conversion efficiency is subsequently determined from Equation 2.21.

All I–V characteristics of fabricated devices in this work were obtained using a Keithley 2400 source measure unit. For photocurrent measurements, a 150 – W Xenon lamp solar simulator

(L.O.T – Oriel) was used to provide illumination (AM 1.5G, 100 mW/cm^2). The intensity of the solar simulator was determined and calibrated using a silicon (Si) reference solar cell (Newport Spectra Physics). Fabricated OSC devices were mounted in a custom built device holder shown in Figure 4.14.

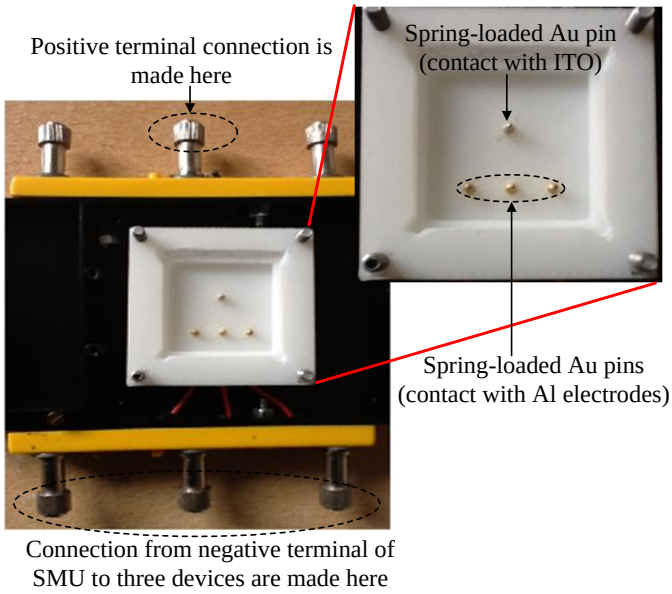

Figure 4.14: A picture of a custom built device holder for measurement of *I–V* characteristics.

Other important device parameters such as the series and shunt resistances are also determined from the obtained *I–V* characteristics (under illumination and in the dark). The calculated series resistances include the contact and bulk resistance. The series resistance can be extracted from the slope of *I–V* curve at higher voltages (Chirvase et al. 2004). From the measured current density – voltage curves of devices under light; it is also possible to obtain values of the series resistances from a linear fit around the point where current density is zero (Aernouts et al. 2002). To extract values of shunt resistances, similar fittings (as in the case for series resistance) were performed at approximately V = 0V. These are illustrated in figure 4.15.

Similarly the series resistance in the dark were extracted from *I–V* characteristics measured in the dark. As previously discussed, typically the current – voltage characteristics of solar cells can be described by Equation 2.22. In the dark, J_{SC} = 0 and it is assumed that shunt resistance is sufficiently high such that Equation 2.22 can be expressed as:

$$J = J_S \left[\exp\left(\frac{q(V - JR_S)}{nk_BT}\right) - 1\right] \tag{4.5}$$

Expressing voltage, V (expressed in volts) as a function of current, Equation 4.5 can be expressed as follows

$$V = \frac{nk_BT}{q}\ln\left(\frac{J}{J_S}+1\right)+JR_S \tag{4.6}$$

Differentiating V with respect to current density, J, Equation 4.6 can be expressed as

$$\frac{dV}{dJ} = \frac{nk_BT}{q}\frac{1}{J/J_S+1}\frac{1}{J_S}+R_S \tag{4.7}$$

In the region of high current, the total current is higher than the reverse saturation current (i.e., $J >> J_S$). Equation 4.7 then becomes

$$J\frac{dV}{dJ} = \frac{nk_BT}{q}+JR_S \tag{4.8}$$

From Equation 4.8, it follows that $J\frac{dV}{dJ}$ is linearly dependent on J. As such the series resistance can be easily extracted from the slope by a linear fit in the high current region. A typical $J - J\frac{dV}{dJ}$ characteristic plot is shown in Figure 4.15 (a). R_S and R_{SH} are both expressed in Ohms - square centimetre (Ωcm^2).

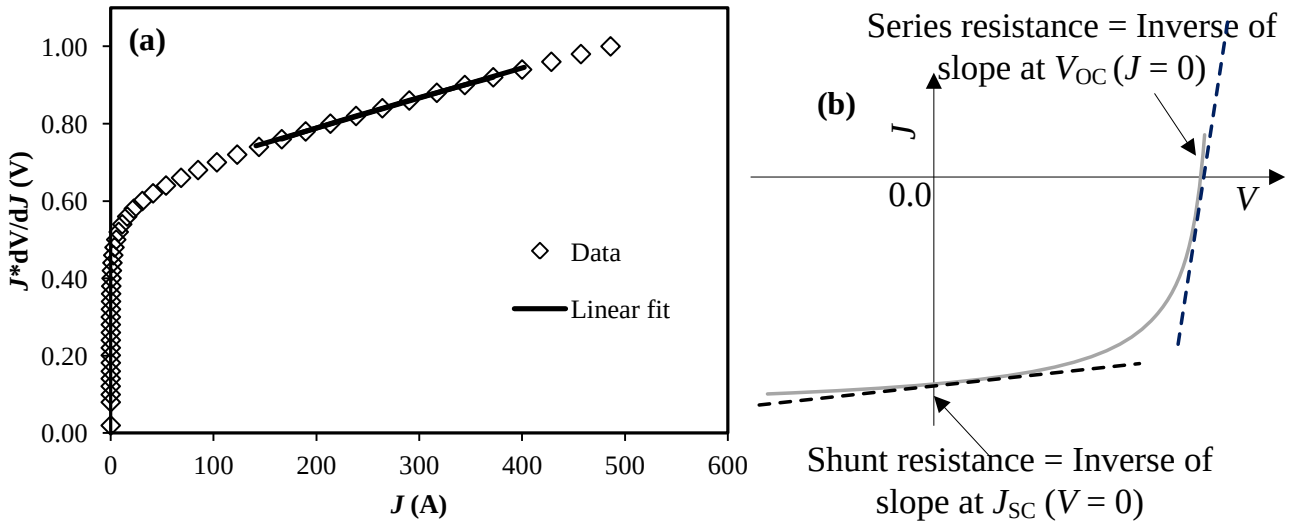

Figure 4.15: (a) $J - J\frac{dV}{dJ}$ characteristic plot of a typical OSC. (b) How to determine series and shunt resistances from the *I–V* curve under illumination.

4.4.1.1 Charge carrier mobility measurements

In polymer/fullerene BHJ solar cells an important factor in determining the efficiency of charge collection is the carrier transport in the active layer (Shrotriya et al. 2006). As previously discussed in section 1.3.3 and 2.6.2, improvement of transport properties implies increased crystalline domains, and optimised percolation pathways in the active layer. This will particularly have a positive impact on minimising losses due to bimolecular recombination. Techniques employed for studying transport properties of materials include; Time of Flight (TOF) (Li et al. 2005; Kokil et al. 2012), Photo induced charge extraction by linearly increasing voltage (Photo-CELIV) (Sariciftci et al. 2005), and space charge limited current (SCLC) model fitting (Shrotriya et al. 2006; Mihailetchi et al. 2006; Kim et al. 2011). In this work, charge carrier mobilities were determined by fitting the current density – voltage characteristics (in the dark) to the SCLC model (see Equation 2.17). This method requires that devices are single charge carrier devices (either electrons or holes). As such hole – or electron – only devices are fabricated in a simple diode structure (e.g., anode/organic layer/cathode). Figure 4.16 is an illustration of the device architecture of single charge carrier devices from which charge carrier mobilities were determined.

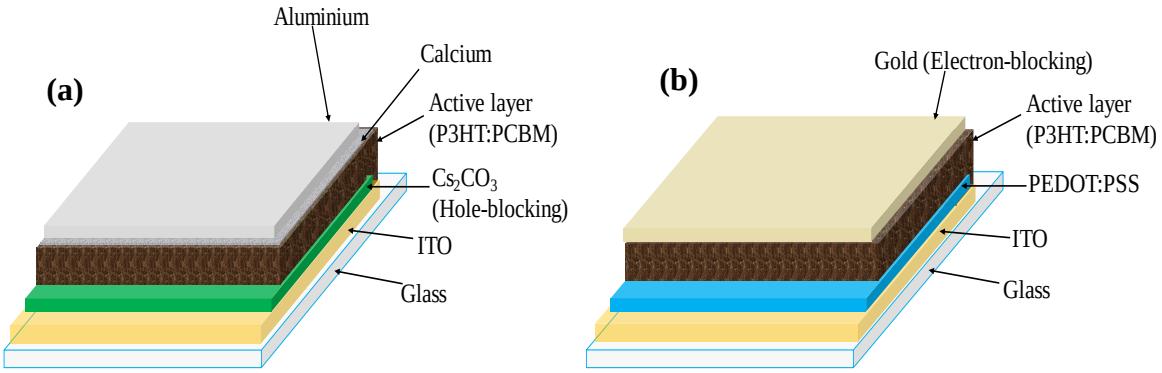

Figure 4.16: Device architecture of electron – only (a), and hole – only (b) devices, used for charge carrier mobility measurements.

To make electron – only devices, caesium carbonate (Cs_2CO_3) layer was spin casted on ITO – coated substrate instead of PEDOT: PSS. Due to its work function, Cs_2CO_3 serves as a hole blocking layer. In the case of hole – only devices, the Al and Ca back electrodes in an OSC device is replaced with Au (an electron blocking contact). The electronic structure of these single charge carrier devices in terms of their energy bands will be discussed further in Chapter 5.

4.4.2 Capacitance – Voltage (*C* – *V*) Measurements

C –*V* measurement is a useful technique that can be used to further provide interpretation of the fundamental transport and recombination mechanisms in OSC devices (Garcia et al. 2008). In addition, other valuable information on metal/organic interface properties can be gained from *C*–*V* measurements. They have been employed in semiconductor device analysis involving diode structures such as: *p*-*n* junctions, Schottky barrier or metal – insulator – semiconductor diodes. Such analysis includes the determination of charge distributions within the depletion region of the semiconductor (Yacobi, 2002). It is known that the width of the depletion region varies with applied voltage (Garcia et al. 2008). Hence measuring capacitance as a function of applied voltage is useful for determining doping concentration levels in semiconductors. This relationship is expressed in the Mott – Schottky relation (Equation 2.15), previously discussed in section 2.3. In this work, values of built – in potential (V_{bi}) in fabricated devices were numerically extracted from the fit to $C^{-2} – V$ plots. Impurity concentration (N_A) can be measured from the slope of the straight line fit. Figure 4.17 is a typical $C^{-2} – V$ plot, showing the intercept (V_{bi}) of a straight line fit.

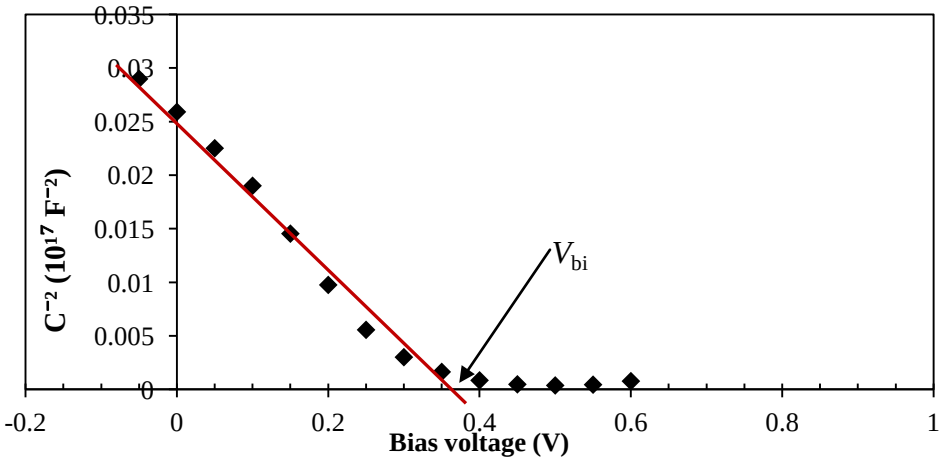

Figure 4.17: A typical plot of the dependence of C^{-2} on applied voltage.

All *C*–*V* measurements in this in work were performed using a Hewlett Packard 4284A Precision LCR meter (impedance analyser). The measurements were obtained at a fixed frequency of 1 kHz, with AC oscillating amplitude of 50 mV.

4.4.3 AC Impedance spectroscopy measurements

AC impedance spectroscopy is a non-destructive technique commonly employed for the analysis of a wide range of electrical devices. Over recent years, it has become an established method for determining charge carrier lifetimes in dye sensitized solar cells (DSSC) (Longo

et al. 2002; Wang et al. 2005; Bisquert et al. 2009). In addition to previously mentioned methods, impedance spectroscopy can also be useful in providing insights to improving the performance of organic electronic devices (Jaiswal et al. 2006; Hsiao et al. 2008). Although not widespread, it is used for probing the electric properties of interfaces and the bulk of devices, which cannot be observed by DC measurement methods alone (Garcia-Belmonte et al. 2008; Kuwabara et al. 2009; Garcia-Belmonte et al. 2010; Zhang et al. 2013). Numerous reports have shown that impedance spectroscopy measurements can also be applied reliably to OSCs for their characterisation. In principle, impedance spectroscopy measurements involves applying an electrical stimuli (usually an ac signal), to an electronic material via electrodes and observe the response accordingly (Barsoukov & Macdonald, 2005). Its working principle is based on the variation of a measured alternating current as a function of frequency. In principle, the impedance (Z) is the overall opposition a circuit offers to the flow of an alternating current at a given frequency (Petty, 2008). It is made up of two components; a real and an imaginary component, expressed as:

$$Z = R_S + jX = |Z| \angle \theta \tag{4.9}$$

,where R_S, is the series resistance in Ohms, X, is the reactance (j denoting the imaginary component of the impedance) in Ohms, $|Z|$ is the impedance magnitude in Ohms, and $\angle\theta$ the phase angle in degrees or radians. Figure 4.18 is an illustration of a typical impedance plot (in vector representation) on an Argand diagram, and the instrumentation set – up.

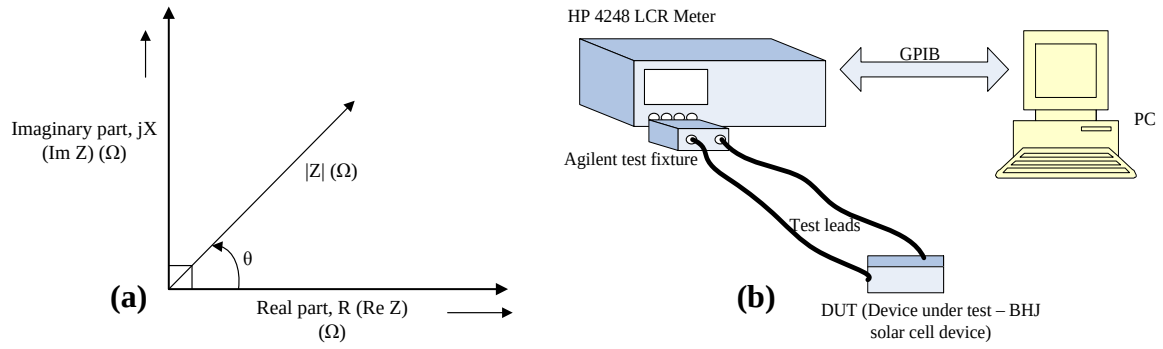

Figure 4.18: (a) Vector representation of impedance, (b) Instrumentation set – up for impedance spectroscopy measurement.

On the LCR meter, the measurements were performed in the frequency range of 20 Hz to 1 MHz, with an oscillation voltage between 20 – 50 mV. The parameters obtained are $|Z|$, the impedance magnitude in Ohms, and $\angle\theta$ the phase angle in degrees. The calculated

parameters Im *Z*, and Re Z are subsequently presented in a Cole – Cole plot. Real impedances, Re Z (Ω) $=|Z| \times \cos\theta$, and Imaginary impedances, –Im Z (Ω) $=-|Z| \times \sin\theta$. Figure 4.19 shows an example of a typical Cole – Cole plot for impedance data obtained in a frequency range of 20 Hz – 1MHz.

Impedance spectra and *C–V* data were all acquired by using a LABVIEW® program, used to control the LCR meter via GPIB interface.

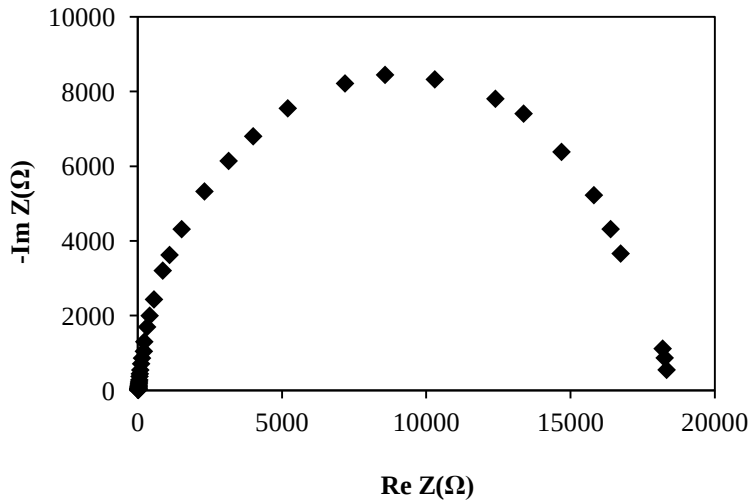

Figure 4.19: A typical Cole – Cole plot of an impedance spectroscopy data.

4.4.4 Cyclic Voltammetery Measurements

Cyclic Voltammetery (CV) measurements were performed in this work to determine the energy levels corresponding to the HOMO and LUMO levels of P3HT and PCBM. It has been previously used to provide direct information on the electrochemical *p* – and *n* – doping potentials (ϕ_p and ϕ_n) of organic materials (Li et al. 1999). ϕ_p and ϕ_n are also regarded as the reduction and oxidation potentials of the material. The CV measurement is based on an electrochemical process. This encompasses both charge – transfer and transport processes between an electrode and the material under investigation. It is therefore a suitable method for studying electroactive materials (Kissinger & Heineman, 1983). Since most organic materials are recognised as electroactive, CV measurements have been shown to be an effective approach in evaluating their energy levels (Holt et al. 2005; Dissanayake et al. 2008; Hou et al. 2009; Yoo et al. 2011). In electrochemical terms, *p*-doping corresponds to the removal of electrons from the HOMO energy level. On the other hand *n*-doping corresponds to the addition of electrons to the LUMO energy level of the organic material (Misra et al.

2005). The HOMO and LUMO energy levels of the organic materials were evaluated from the onset potential of the *p*-doping (ϕ_p^{ons}), and the onset potential of the *n*-doping (ϕ_n^{ons}), respectively, according to the method reported by Li et al. (1999). The potential difference, i.e., $\Delta\phi = \phi_p^{ons} - \phi_n^{ons}$, can be used to estimate the electrochemical energy gap of the material. According to Leeuw et al. (1997), the HOMO and LUMO energy levels (in electron volts, e*V*), can be calculated using the formulae:

$$E_{HOMO} = -e(\phi_p^{ons} + 4.4) \tag{4.10a}$$

$$E_{LUMO} = -e(\phi_n^{ons} + 4.4) \tag{4.10b}$$

All electrode potential values are vs. saturated calomel electrode (SCE) a reference electrode. This is the case, since CV measurement involves controlling the potential at a working electrode with respect to a reference electrode. Controlling the potential at a working electrode involves performing forward and reverse voltage scans. The value 4.4 in Equation 4.10 is a scale factor in volts relating SCE to vacuum level (Brédas et al. 1983). Figure 4.20 is an illustration of a typical electrochemistry setup, consisting of three electrodes, in an electrolytic medium.

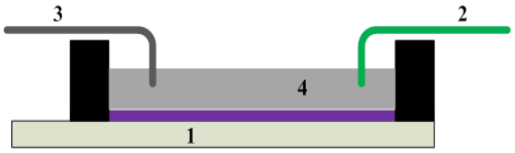

Figure 4.20: Schematic of the electrochemistry experiment set – up: working electrode (1), reference electrode (2), counter electrode (3), and electrolyte (4).

In this work, silver (Ag) wire was employed as a quasi – reference electrode. Adopting a similar method as Leeuw et al. (1999), Ag was calibrated to be – 0.01 vs. SCE. Therefore Equation 4.10 (a) and (b) can be expressed as follows:

$$E_{HOMO} = -e(\phi_p^{ons} + 4.39) \tag{4.11a}$$

$$E_{LUMO} = -e(\phi_n^{ons} + 4.39) \tag{4.11b}$$

A platinum wire was used as the counter electrode, and polymer or fullerene/ITO as the working electrode. The electrolyte used in this work consisted of salts of lithium

trifluormethanesulfonate (Li trifilate), tetrabutylammonium tetrafluoroborate (TBA BF_4), in acetonitrile at 0.01*M*.

All CV measurements were performed on an Agilent 5500 AFM, equipped with an electrochemistry work station. The measurements were obtained at a scan rate of 50 mV/s. Also included in the Agilent 5500 AFM is a potentiostat and a galvanostat. Both are for the control of voltage and measurement of the corresponding current arising from the electron transfer processes. The set – up of the Agilent 5500 AFM electrochemistry work station is shown in Figure 4.21.

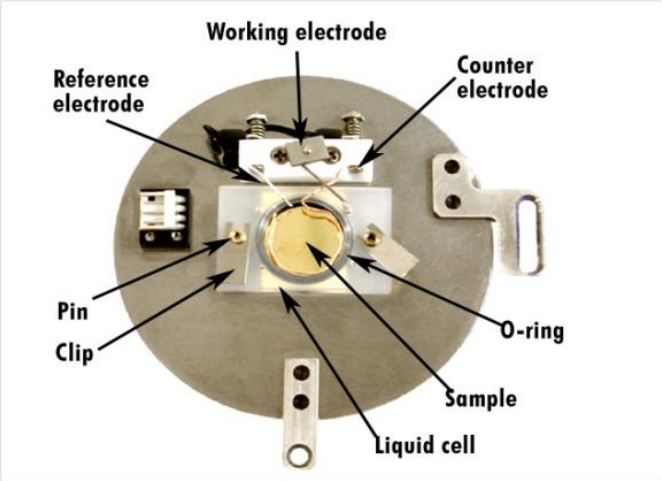

Figure 4.21: Agilent 5500 AFM electrochemistry workstation set – up.

4.5 Locations of Measurement Instrumentations

D8 ADVANCE XRD is located at the X-Ray Diffraction laboratory (R026). InVia Raman microscope at Forensic and Criminalistic Methods laboratory (R328). The rest of instrumentations used for this work are located at the Thin Film Technology Laboratory (R117). All the laboratories are at the Science Centre, Staffordshire University, where this work was carried out.

4.6 Summary

The various experimental methods (including appropriate instrumentations) employed in the work of this thesis has been reviewed and presented in this chapter. This mainly involved their use for the characterisation of thin films for OSC applications and the corresponding device characterisation. Additionally, the discussions of the underlying working principles of the aforementioned methods were also presented respectively.

Chapter 5

Material and Thin Film Characterisation

"Anybody who has been seriously engaged in scientific work of any kind realizes that over the entrance to the gates of the temple of science are written these words: 'Ye must have faith'."

— Max Planck

5.1 Introduction

The importance of thin film characterisation for OSC application is well established in literature. In the field of thin film technologies, the main constituents in electronic devices (particularly OSCs) are thin films of organic semiconductor materials. Understanding the various properties of these thin films is crucial to the optimisation of devices based on them. An important aspect of characterising thin films for devices is the determination of their optical spectroscopic properties. Most organic semiconducting materials are often referred to as "intrinsic wide band gap" semiconductors. This means their absorption band tends to be relatively narrow (Nicholson & Castro, 2010). The measurement of their absorption spectra properties is important as this can provide useful information regarding the materials, such as structure, and electronic energy levels. In this chapter, the results of absorption spectra characterisation of thin films in the work of this thesis are presented. In addition, structural characterisations of thin films were undertaken and the corresponding findings are presented and discussed respectively.

It is important to point out that details of the experimental methods have been covered in Chapter 4. However, in some occasions, where it is deemed necessary additional information are provided for purposes of clarity.

5.2 Absorption Spectra of Thin Films

Optical absorption spectroscopy measurements have been shown to be an effective technique for providing insight into the structural characteristics of thin films of organic materials (Kim et al. 2005; Erb et al. 2006). In this section, the impact on the optical absorption of thin films due to the structural changes in pristine PH3T, PCBM and P3HT: PCBM blends upon thermal annealing are investigated. Optical absorption spectroscopy is used to identify the nature of molecular ordering of P3HT or PCBM within fabricated thin films. The absorption spectra of pristine P3HT and PCBM are shown in Figure 5.1.

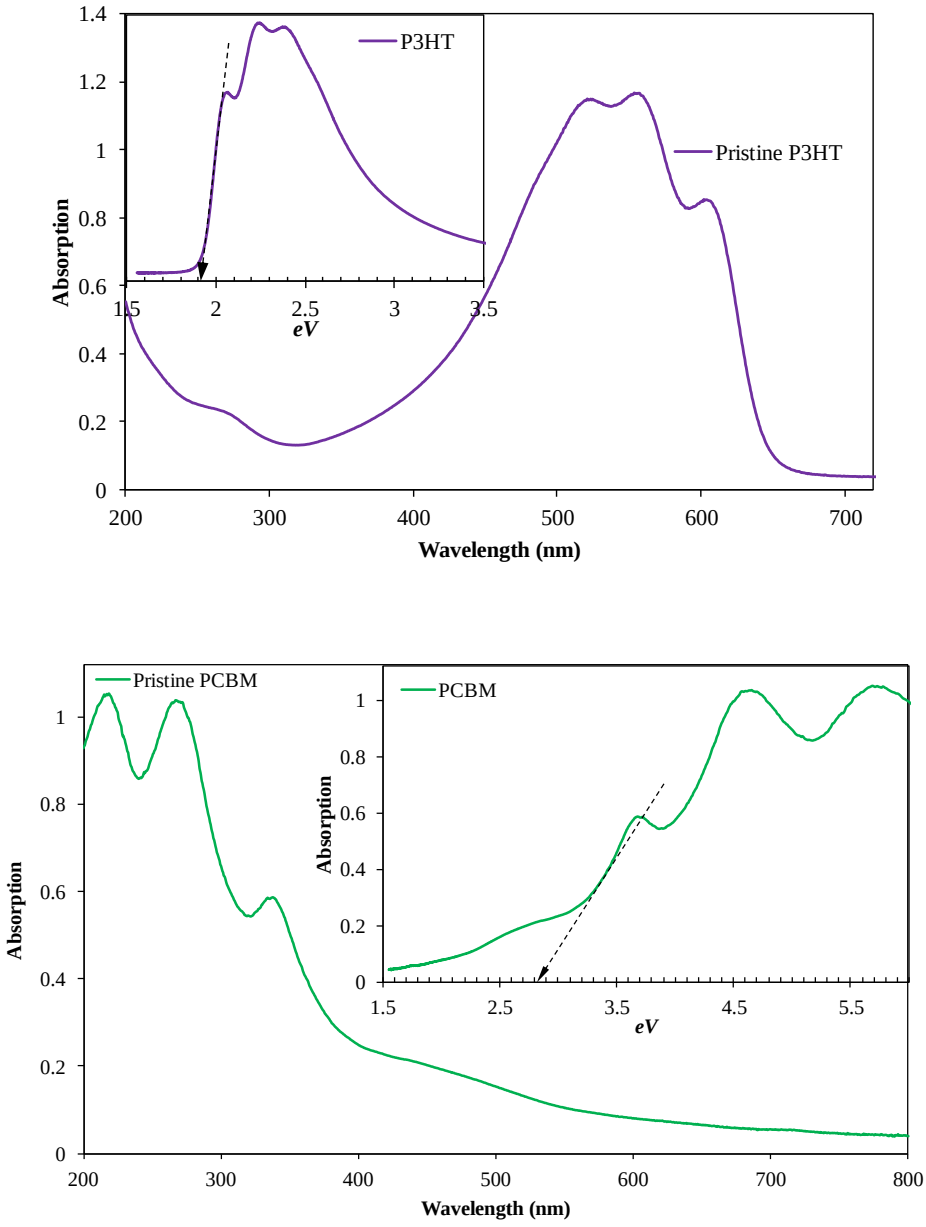

Figure 5.1: UV-visible absorption spectra of pristine (a) P3HT and (b) PCBM.

In Figure 5.1, the insets are plots of absorption vs. photon energy in electron volts (eV). The values of the photon energy were determined from the inverse relationship between energy (in electron volts) and wavelength of the UV-visible spectrum, as follows:

$$E = \frac{hc}{q\lambda} \tag{5.1}$$

Where h is the Planck's constant (6.626×10^{-34} J.s), c is the speed of light (2.998×10^{8}), λ is the wavelength in nanometres, q is the electronic charge (1.6×10^{-19} C), and E is the energy in electron volt. 1 electron volt is the energy gained by an electron moving through a potential difference of 1 volt (i.e., 1 eV = 1.6×10^{-19} J). The value on the photon energy axis, indicated by the arrows in the insets of Figure 5.1 is an estimate of the optical band gap (E_g) of P3HT and PCBM respectively. This corresponds to the wavelength of the onset of absorption of the materials, which is the photon energy required to excite an electron from the HOMO of the materials (Peter, 2009). For the P3HT and PCBM used in this work, the determined values of E_g from the insets of Figure 5.1 are ~1.9 eV and ~2.8 eV. It will be shown later in this chapter that band gap values determined from other methods such cyclic voltammetery differ from the optical band gap.

5.2.1 Thermal Annealing Effects

The thermal annealing effects on the optical absorption properties of polymers and fullerenes for OSCs have been reasonably documented (Chirvase et al. 2004; Erb et al. 2006; Zhokhavets et al. 2006). In most of these reports, the interpretation of the optical absorption properties of the polymer/fullerene system (P3HT/PCBM in particular) have mostly focused on the wavelength region (450 – 650 nm) associated particularly with P3HT absorption (Li et al. 2005; Chen et al. 2010). The observations and discussions reported have mostly included improvements in the crystallinity of P3HT molecules, ordering, conjugation length in the polymer chain, etc, deduced from P3HT absorption maximum, vibronic features (at around 620-650 nm), and shift in its absorption spectra (Li et al. 2007). It is recognised however, that there has been somewhat less attention paid to the region of spectrum associated with PCBM, and its interpretation in light of morphological variation due to thermal annealing. It is against this backdrop, that this section will seek to demonstrate optical absorption spectra measurements as a simple yet effective tool for controlling, as well as monitoring the morphology evolution in P3HT/PCBM blend thin films.

Solutions of pristine P3HT, and PCBM were prepared separately, from 1, 2-dichlorobenzene (DCB), with total concentration of 25 mg/L. Three different compositional ratios were prepared for composite P3HT: PCBM blend solutions; i.e., 1: 1, 1: 0.8, and 1: 0.6. Following their dissolution in DCB, solutions (pristine and blend) were left to stir overnight at room temperature. All films were spun cast on to quartz glass substrates (Knight Optical), having a characteristic transmission in the range of 200 – 2500 nm. Spin casting of all thin films were performed in ambient air. Details of UV-Vis absorption spectra measurement method and instrument used can be found in section 4.3.1.

First, optical absorption spectroscopy of pristine thin films are considered. Figure 5.2 represents the UV-Vis absorption spectra of as casted and thermally annealed thin film of pristine PCBM.

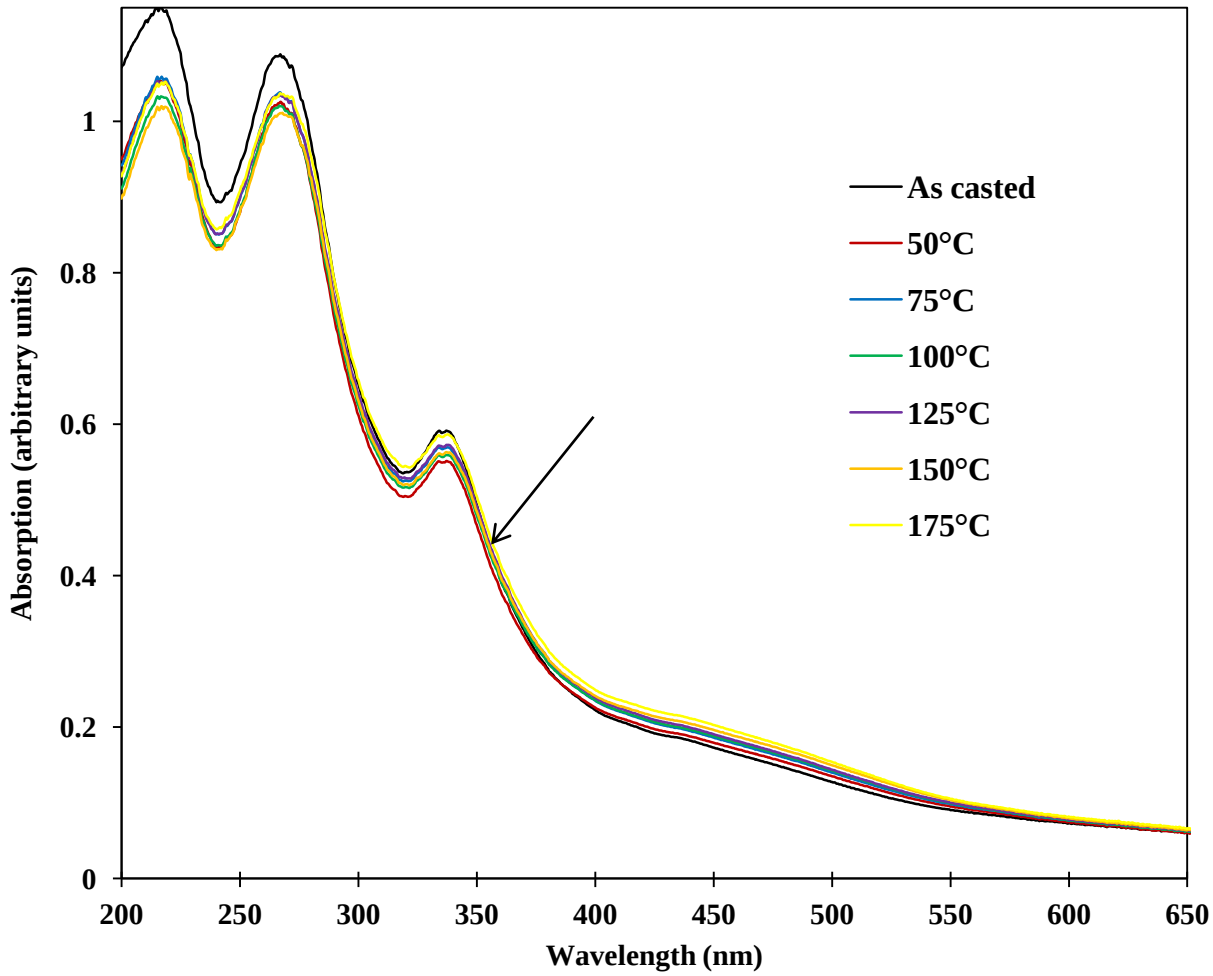

Figure 5.2: UV-Vis absorption spectra for pristine PCBM film, as casted and annealed at various temperatures.

Three distinct absorption peaks are observed at 216.5, 267, and 337 nm. These have been identified as corresponding to electronic transitions from singlet ground state to higher excited states (Harris & Bertolucci, 1978; Karagiannidis et al. 2011). A weak absorption detected in the range of 400 to 550 nm is associated with intermolecular interactions between fullerenes (Cook et al. 2007). Upon thermal annealing there are no noticeable shifts in wavelengths and only slight reduction in peak absorption intensity is observed. It is believed that this may be attributed to the diffusion of PCBM and the gradual formation of nano crystals, which subsequently forms aggregates at higher temperatures (Karagiannidis et al. 2011). At wavelengths above 350 nm this role is however reversed and the absorption intensity slightly increases with annealing temperatures. The region of this observation is indicated by an arrow in Figure 5.2. One possible explanation could be the effect of temperature on interactions between fullerenes, resulting in charge transfer transitions of intermolecular excitons (Karagiannidis et al. 2011). Figure 5.3 shows the comparison of the spectra on either side of 350 nm, showing the reversal of trends upon thermal annealing.

Figure 5.4 shows the UV – Vis absorption spectra of pristine P3HT films; as casted and thermally annealed at several temperatures. Two distinct peak intensities at 521 and 553 nm corresponds to the electronic transitions in P3HT polymer chains, and associated with the generation of excitons (Karagiannidis et al. 2011). Furthermore a shoulder at 602 nm corresponds to what is referred to as vibronic feature (Li et al. 2007), indicative of orderly P3HT polymer chains stacking. As is evident in Figure 5.4 only a slight increase in peak intensities is observed. Using dichlorobenzene with a relatively higher boiling point as the casting solvent allows favourable crystal growth during slow drying and therefore no further significant crystal growth was observed upon subsequent thermal annealing. This is in contrast to chlorobenzene-casted films for which absorption improves with annealing temperatures (Dang et al. 2011). This suggests that depending on processing conditions, i.e., casting solvents, the morphology evolution trends are expected to vary.

The UV-Vis absorption spectra for the blend of P3HT: PCBM with three different PCBM percentage loadings were also measured. This is shown in Figure 5.5. As can be seen, the peak absorption associated with PCBM decreases with reduced percentage loadings. Upon thermally annealing at 175°C, it is noted that the blend with the highest concentration of PCBM (50% weight ratio 1:1) showed the greater reduction in intensity. Other annealing temperatures are not shown here for the purpose of clarity.

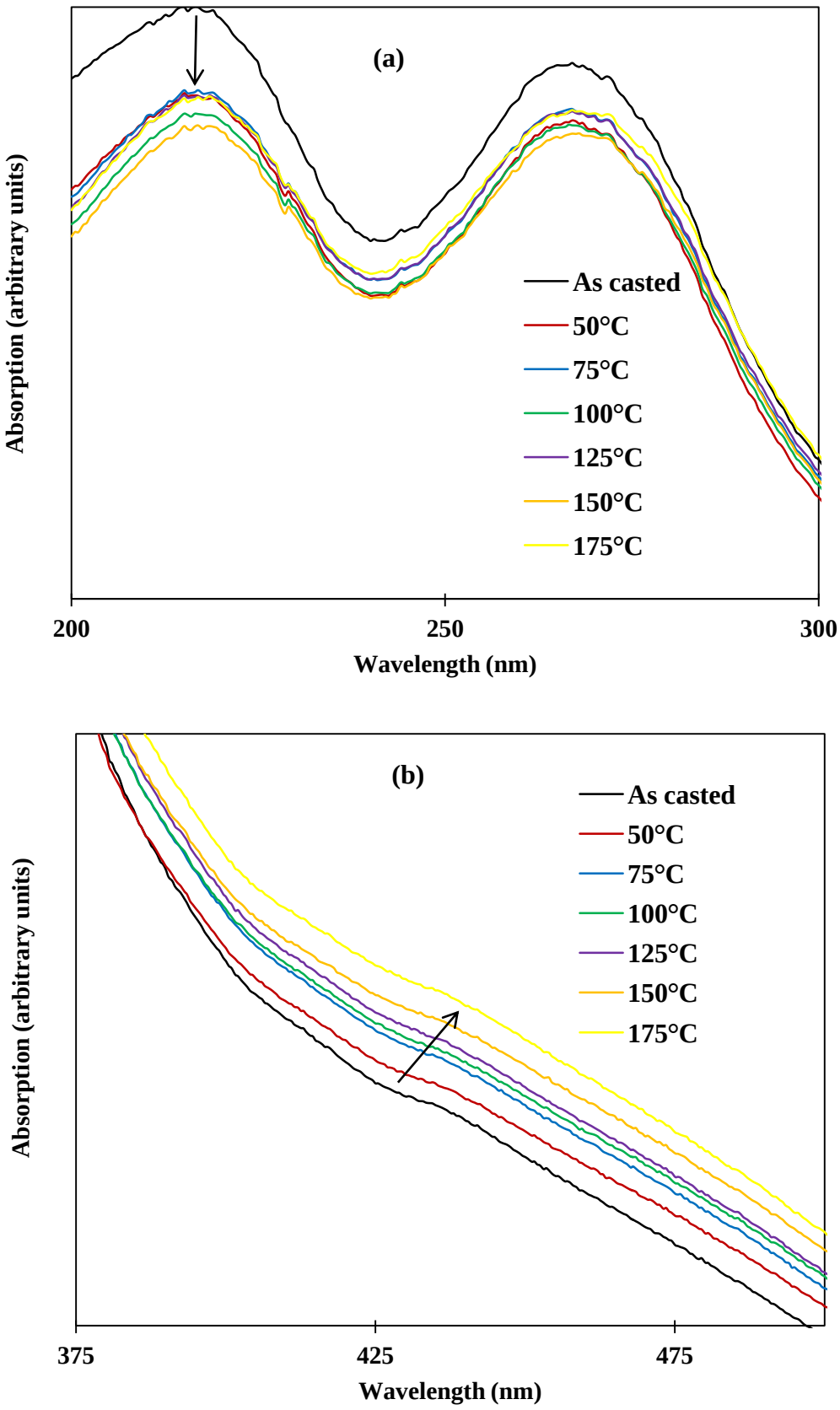

Figure 5.3: Comparison between the spectra below (a) and above (b) 350 nm for PCBM absorption spectra.

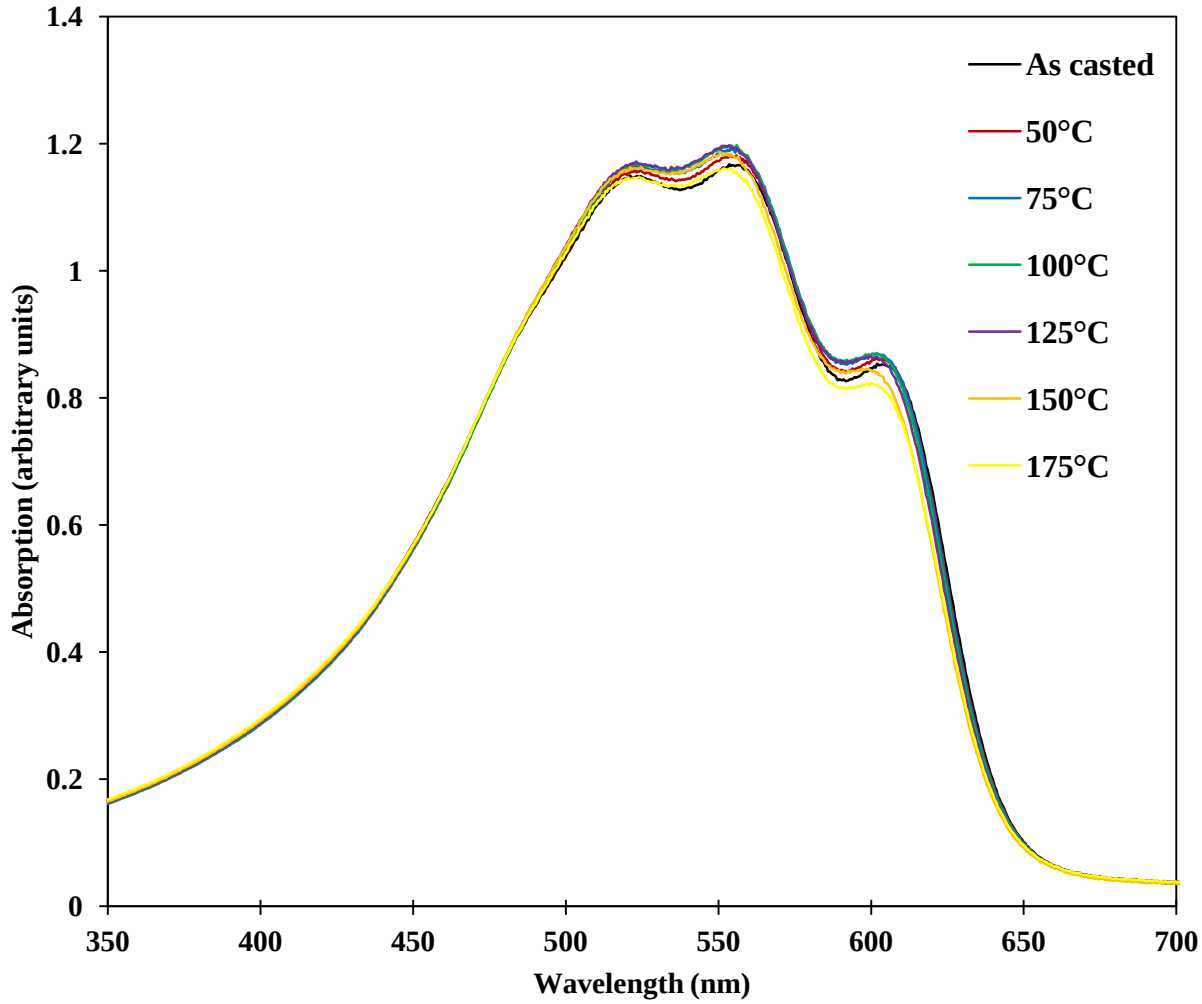

Figure 5.4: UV-Vis absorption spectra of pristine P3HT film; as casted and thermally annealed at various temperatures.

The percentage change (%Δ) of the peak intensities in the 250 – 350 nm wavelength range after thermal annealing was determined and are presented in Table 5.1. From Table 5.1, it can be noted that the quantity, %Δ is greatest for the 1:1 P3HT: PCBM ratio, and reduces as the PCBM content reduces. This is likely to be an indication of the degree of vertical segregation events within the bulk of the film, where it is more pronounced in the case of 1:1. This is consistent with the work of Kokubu and Yang (2012), which demonstrated that the increased PCBM – rich region at the surface of the film may contribute to light reflection, hence a reduction in absorption. Seeing that the spectrometer only measures transmitted light, the reflection from PCBM – rich regions in the 1:1 ratio is expected to be more in contrast to that of 1: 0.6. This is suggested to be evidenced in the reduced absorption spectra (indicated by the corresponding arrows in the insert of Figure 5.5).

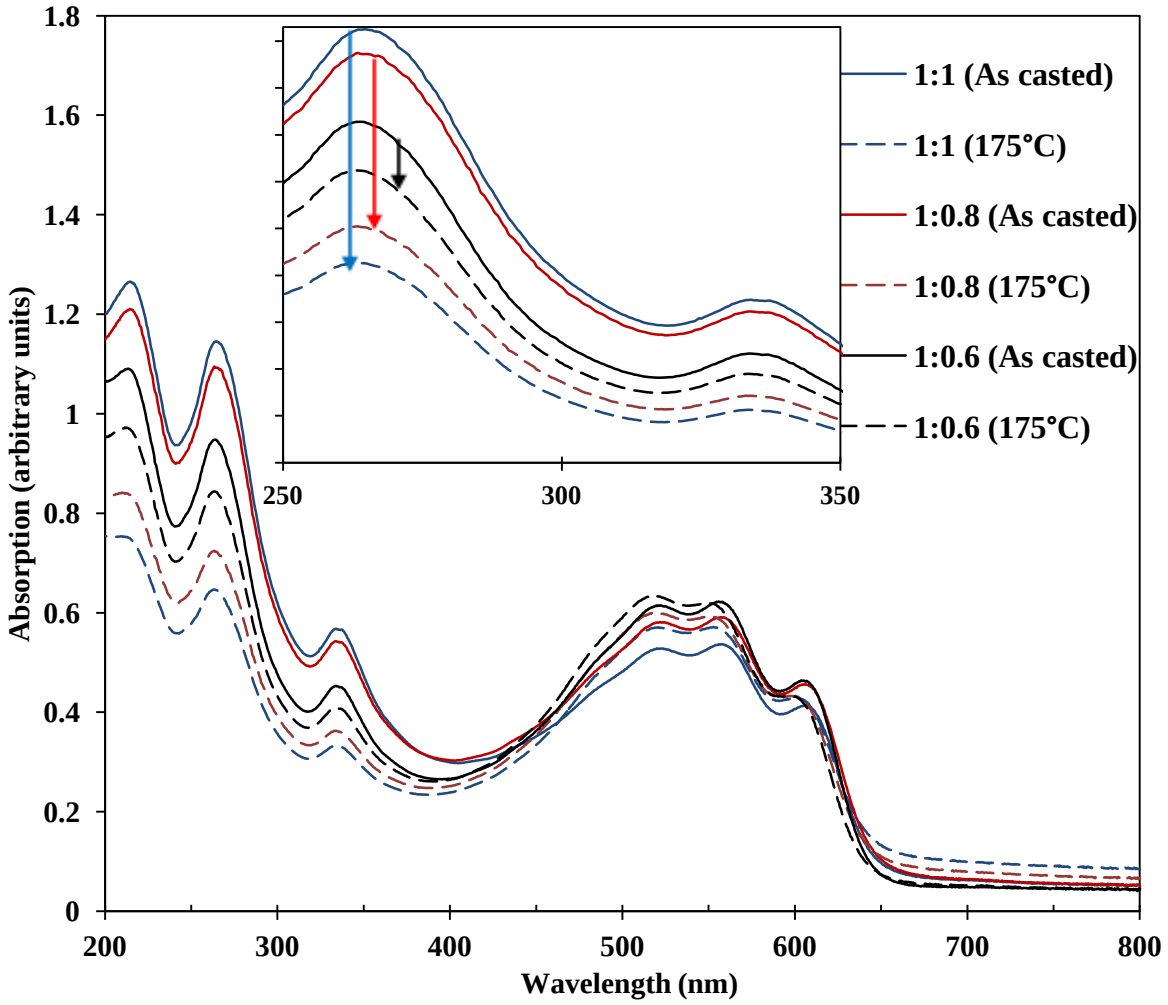

Figure 5.5: UV-Vis absorption spectra of P3HT: PCBM films, with three PCBM wt% loadings (1:1, 1:0.8, and 1:0.6), as casted and annealed at 175°C.

Table 5.1: Variation in the peak intensities of PCBM associated spectra after thermal annealing.

	P3HT:PCBM Ratios	Percentage reduction in absorption maxima		
		As cast	175°C	%Δ
250-280 nm	1:1	1.15	0.65	43.5
	1:0.8	1.10	0.72	34.6
	1:0.6	0.95	0.84	11.6
320-350 nm	1:1	0.57	0.33	42.1
	1:0.8	0.54	0.36	33.3
	1:0.6	0.45	0.41	8.9

In addition, the peak intensities corresponding to P3HT show a small but noticeable increase and shift towards lower wavelength. The vibronic shoulders also appear to be more pronounced for as casted films. However at higher annealing temperatures this shoulder tends to smooth out. This is believed to be indicative of a disruption in interaction of P3HT polymer chains by the segregated PCBM molecules (Huang et al. 2009).

5.2.1.1 Thermal Annealing Impact on PCBM cluster formation

Numerous studies on the effects of thermal annealing on the nanomorphology of blended polymer/fullerene thin films have been reported (Chirvase et al. 2004; Kim et al. 2005; Li et al. 2005; Karagiannidis et al. 2011). It has also been shown that besides thermal annealing, other processing conditions such as solvent choice (Park et al. 2009; Dang et al. 2011), solvent vapour annealing or spin coating parameters (Zhao et al. 2007; Li et al. 2007), can significantly influence the nanomorphology of blended thin films. The influences of modifying processes are evidenced in the optical absorption properties of thin films (Kim et al. 2005), and photovoltaic properties (Ma et al. 2005). Swinnen and co – workers (2006), in their work, found that different thin films structures can be obtained as a function of varying thermal annealing conditions and composition ratios. In a similar vein, Huang et al (2009) reported the growth of PCBM aggregates or clusters in the P3HT: PCBM blend with annealing time. It was suggested that depending on aggregates sizes, the bi-continuous network within the thin film can be disrupted, leading to poor solar cell efficiencies. It has been noted that for example, some of these previous reports have indicated that there are no significant changes to the PCBM part of the optical absorption spectrum upon thermal annealing at around 120°C-140°C (Shrotriya et al. 2005; Heejoo et al. 2006; Jung et al. 2010). By employing different thermal annealing strategies (annealing temperatures and times were varied accordingly), for a blend ratio of 1:1 (P3HT: PCBM), interesting structural changes have been observed. The impact of these structural changes as revealed in optical absorption spectra properties are discussed here. Their corresponding photovoltaic properties will also be discussed the next chapter.

The details of the method of preparation of blend solution and fabrication of thin films has been discussed in section 5.2.1. All thin films in this section however were fabricated in nitrogen – filled glovebox.

Figure 5.6 shows the UV-Vis absorption spectra for thin films of P3HT: PCBM blend of ratio 1:1, and approximately 150 nm thick.

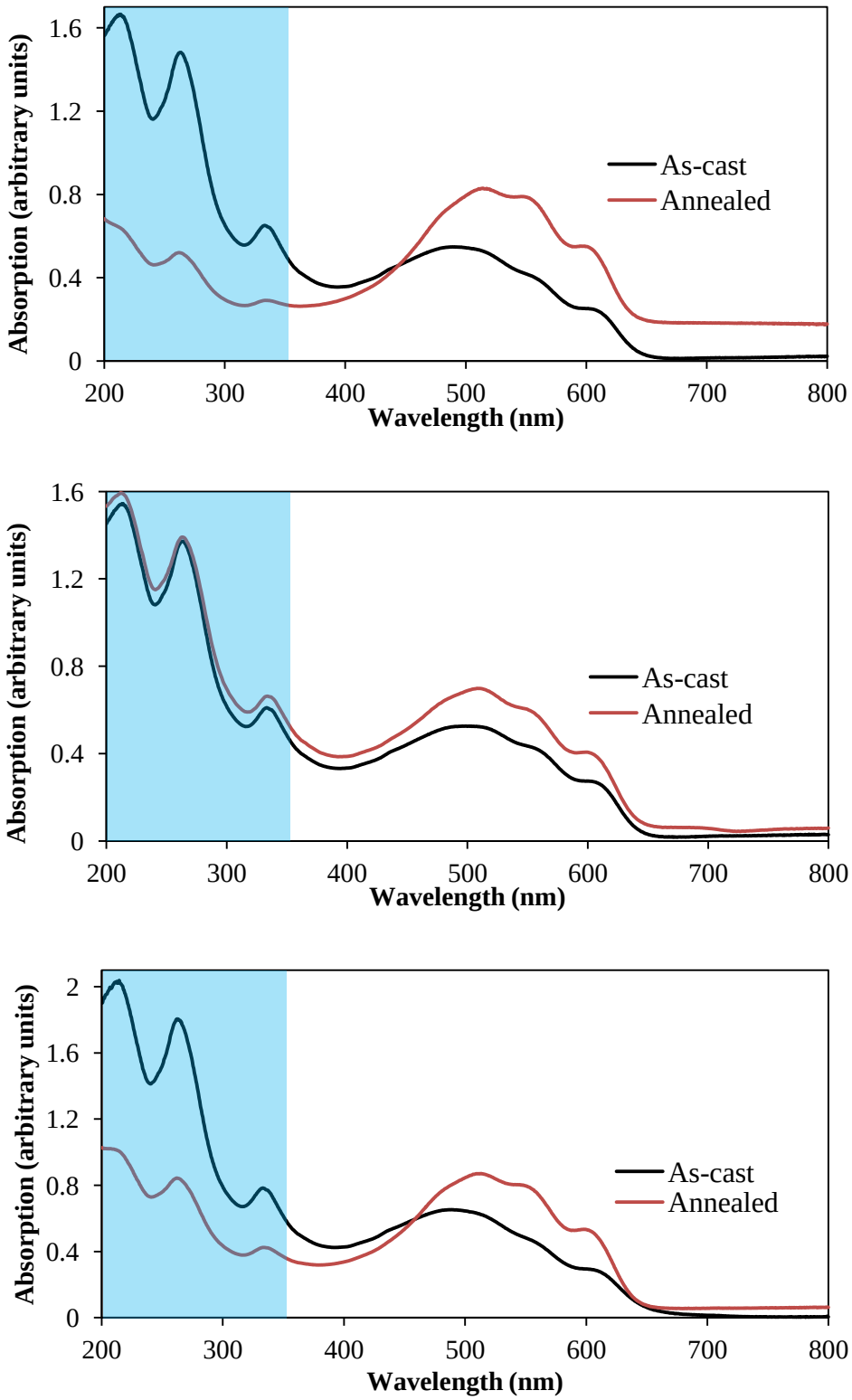

Figure 5.6: UV-Vis absorption spectra of P3HT: PCBM (1:1) thin films of thickness ~150 nm (a) as-cast and after gradual thermal annealing from 50°C to 175°C in intervals of 25°C, for 10 minutes, (b) as-cast and after thermal annealing at a constant temperature of 175°C, for 10 minutes, (c) as-cast and after thermal annealing at a constant temperature of 175°C, for 60 minutes.

Three different thermal annealing strategies have been employed for the structural characterization in this study, namely: (*i*) annealing at temperatures of 50 - 175°C, in intervals of 25°C, for 10 minutes, (*ii*) annealing at 175°C for 10 minutes, and (*iii*) annealing at 175°C for 60 minutes.

As can be seen, the peak absorption intensity of P3HT (~500-600 nm) increases upon thermal annealing. This increase in peak intensity is attributed to the orderly stacking of the polymer chains upon gradual increase in annealing temperature as previously reported (Kim et al. 2005). Therefore an increase in peak optical absorption intensity of P3HT with annealing temperature may initiate an increase in short circuit current density. This would be discussed later in the next chapter. Observations of the PCBM part of the spectrum (~200-350nm) reveals some interesting features. Contrary to P3HT, the peak absorption intensity of PCBM reduces upon thermal annealing. As is evident in Figure 5.6, interestingly the level of this reduction depends on the strategies employed. Thin film annealed at temperatures of 50 to 175°C, in intervals of 25°C, for a period of 10 minutes, revealed highest peak intensity reduction in comparison to the film annealed at a temperature of 175°C for 60 minutes, and at 175°C for 10 minutes respectively (see Figures 5.6 (c) and (b)). Upon thermal annealing, diffusion of PCBM molecules is believed to result in segregation of PCBM clusters.

Additionally, due to the differences in the surface energies of the components of the BHJ blend, and the interaction between the organic materials and substrate, the direction of vertical segregation is expected to be strongly affected. For example, the surface energy associated with PCBM, P3HT, quartz substrate, PEDOT: PSS and Al are given as 37.8, 26.9, 11.5, 45.7, and 42.9 mN/m^2 (Germack et al. 2009; Orimo et al. 2010). Having used quartz glass substrates for absorption measurements, the minimum free energy requires that P3HT to reside at the glass/film boundary and PCBM at the film/air boundary (Germack et al. 2009). However, when considering an actual completed organic solar cell device, i.e., one having aluminium as top electrode; the minimum free energy will in this case require that a PCBM-rich region be formed at the cathode/film boundary owing to its higher surface energy compared to the organic material (Orimo et al. 2010). This type of distribution between electrodes is favourable for electrode selectivity, and should result in improved short current densities upon thermal annealing, as shall be observed later in chapter 6, where detailed discussions on the photovoltaic properties are presented. Optical microscopy images were obtained of surfaces of the thin films subjected to the three different thermal annealing strategies. These are summarised in Figure 5.8.

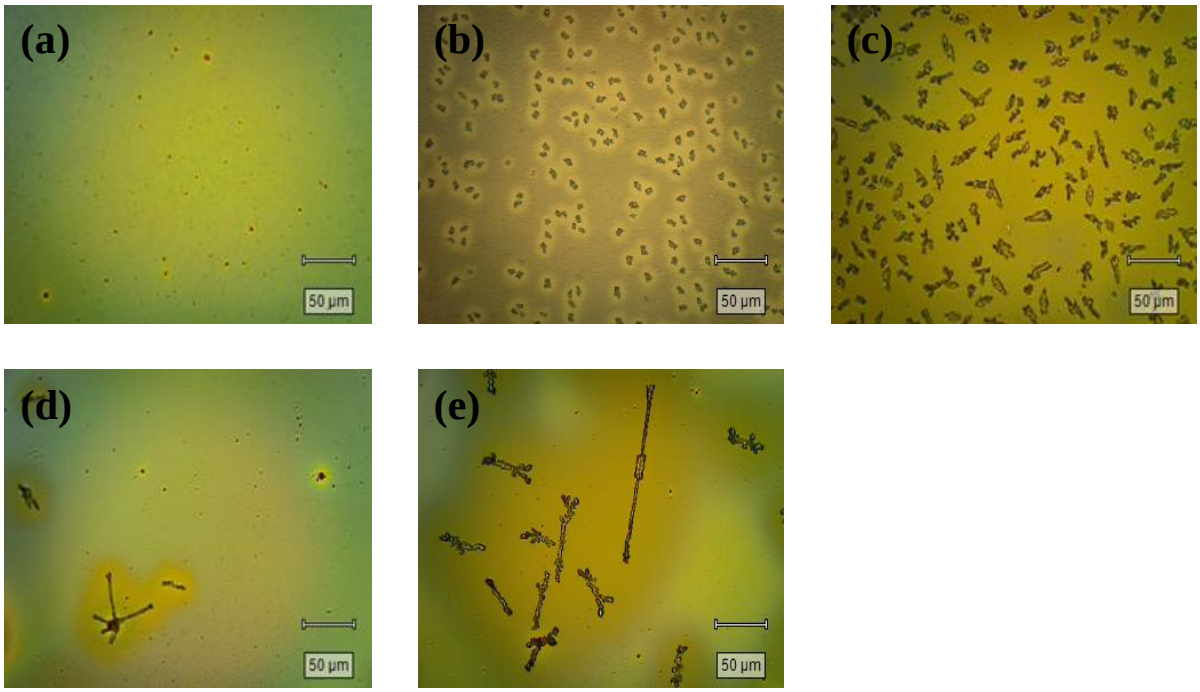

Figure 5.7: Optical microscopy images of P3HT: PCBM blend thin films: (a) as cast, (b) after thermal annealing at temperatures; of 50 - 150°C, in intervals of 25°C, (c) 50 - 175°C, in intervals of 25°C, (d) 175°C for 10 minutes, and (e) 175°C for 60 minutes.

As is evident in Figures 5.7 (b) and (c), there is a large distribution of networks of PCBM aggregates formed as a result of gradual thermal annealing, this is in contrast to Figures 5.7 (d) and (e) having needle – shaped PCBM clusters formed as result of high temperature-induced diffusion of PCBM aggregates.

By using the relation given in equation 5.2 (Jang et al. 2009), the density (d_{PCBM}) of PCBM clusters in the area of optical micrographs (see Figure 5.7) were estimated.

$$d_{\mathrm{PCBM}}(\%) = \frac{N_{\mathrm{PCBM}} \times 100}{N_{\mathrm{P_{total}}}} \tag{5.2}$$

In equation 5.2, N_{PCBM} denotes the number of pixels occupied by PCBM clusters, and N_{Ptotal} is the total number of pixels in the image. The PCBM cluster density measured was found to be 21.35% for P3HT: PCBM blend films annealed gradually (i.e., 50 - 175°C, in intervals of 25°C). Similar calculations for fast thermal annealing i.e. 175°C for 10 and 60 minutes revealed a PCBM cluster density of 2.4% and 3.78% respectively.

Figure 5.8 is a graphical summary illustrating the influence of the different thermal annealing strategies, outlined in the work of this thesis.

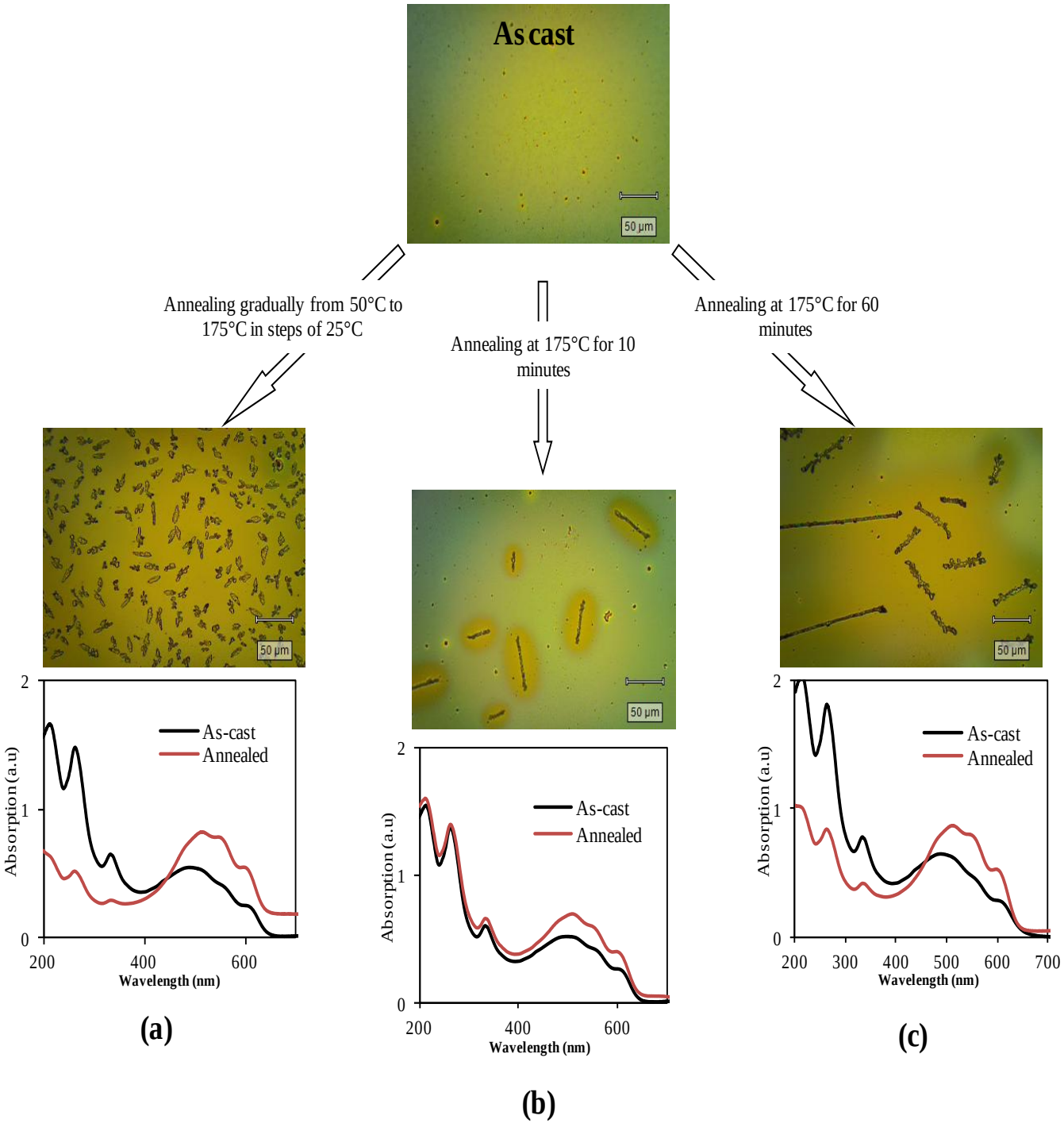

Figure 5.8: Illustration of the three different thermal annealing strategies with optical microscopy images and optical absorption properties respectively: (a) 50 - 175°C, in intervals of 25°C, (b) 175°C, for 10 minutes and (c) 175°C, for 60 minutes.

2D line profiles of the surface morphologies of these P3HT: PCBM blend thin films after thermal annealing (for the three different strategies) were also obtained. This was achieved

using the DektakXT stylus profiler. Details of the use of the stylus profiler can also be found in section 4.3.5.1. These are presented in Figure 5.9.

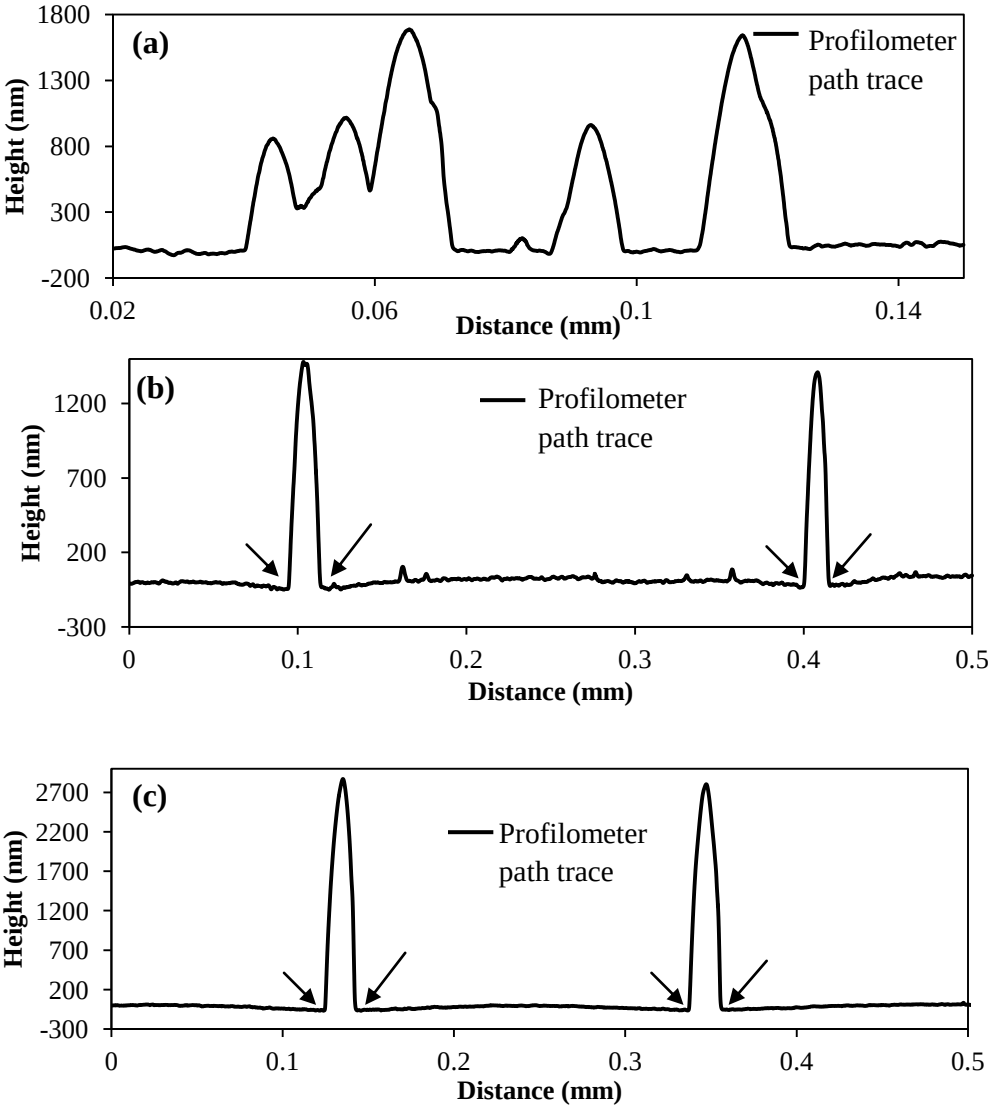

Figure 5.9: 2-D profile of PCBM clusters or needles of thin films annealed (a) gradually from 50°C - 175°C in intervals of 25°C, for 10 minutes, (b) at 175°C for 10 minutes, and (c) at 175°C for 60 minutes.

In Figure 5.9 (b) and (c), the regions indicated by the arrows were observed to be depleted, around the aggregated PCBM clusters.

5.2.2 Raman and PL spectroscopy of Thin Films

The underlying measurement principles in both Raman and PL spectroscopy for thin film characterisations have been previously discussed in detail in section 4.3.2. Figure 5.10 (a) shows a typical Raman spectrum of pristine P3HT thin film excited at 514 nm.

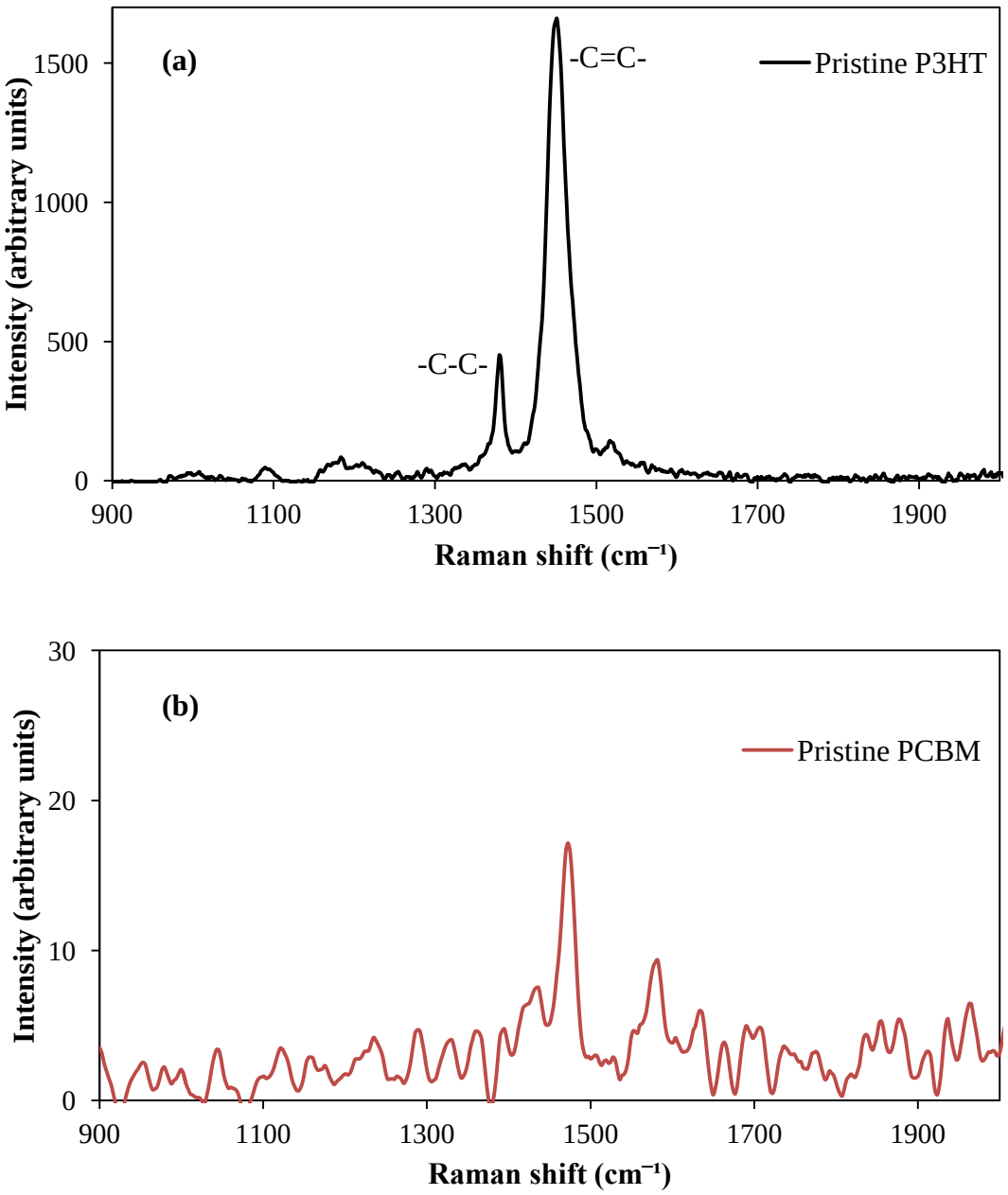

Figure 5.10: Raman spectrum of pristine (a) P3HT and (b) PCBM under 514 nm excitation.

In Figure 5.10 (a), various Raman modes can be observed between 900 – 1600 cm^{-1} (Baibarac et al. 1998; Campoy – Quiles et al. 2008; Ballantyne et al. 2010; Tsoi et al. 2011): with main vibrational modes at 1450 cm^{-1} and 1380 cm^{-1} corresponding to symmetric –C=C–, and –C–C– stretching modes. These two stretch modes are of significance as they are believed to be sensitive to the conjugation length of P3HT molecules (Gao & Gery, 2009). It should be noted however, that –C=C– stretch mode at 1450 cm^{-1} may differ from other reported values in literature, depending on the excitation wavelength under which the Raman spectra is obtained (Tsoi et al. 2011). Note in the case of pristine PCBM, the Raman spectrum

is not as well defined as in the case of pristine P3HT. This is attributed to the wavelength of excitation used (514 nm). Because the excitation wavelength is within the maximum absorption wavelength range of pristine P3HT in contrast to PCBM (compare Figure 5.2 and 5.4), Raman signals obtained from pristine P3HT will be more pronounced (Campoy-Quiles et al. 2008). When a 325 nm excitation was employed, Campoy-Quiles and co-workers (2008) reported Raman spectrum of pristine PCBM with well defined peaks.

Raman spectroscopy was employed in this section to probe the influence of the different thermal annealing strategies on the crystallization of P3HT polymer chains within blend films. Raman spectra measurements were taken of P3HT: PCBM blend films as a function of thermal annealing. It is known that thermal annealing induces crystallization in P3HT polymer chains within the blend thin film (Li et al. 2005). This crystallization however has been shown in many cases to have an impact on the short circuit current densities, for organic PV devices (Li et al. 2005; Gong et al. 2010). The measured Raman spectra of P3HT: PCBM blend thin films; as cast and after thermal annealing are presented in Figure 5.11.

The Raman peak of the P3HT –C=C– mode can be observed in P3HT: PCBM blend film at the same position (1450 cm^{-1}) as in pristine P3HT (compare with Figure 5.10). In addition to P3HT conjugation length, the –C=C– peak is also sensitive to the degree of molecular order of P3HT (Tsoi et al. 2011). It should be noted that no Raman modes of PCBM molecules were observed under the 514 nm excitation.

The narrowing of this Raman band associated with –C=C– symmetric stretching mode of P3HT molecules is related to an enhancement in the crystallinity of the P3HT polymer chains (Nalwa et al. 2011). From the Raman spectra in Figure 5.11, with particular focus on the nature of the width of the –C=C– peak, the molecular order of P3HT induced by thermal annealing can be understood. To do so, the values of the full width half maximum (FWHM) were determined from performing fits to the measured Raman spectra. These are summarized in Table 5.2. FWHM refers to the measured average width of the Raman band of the –C=C– peak. The observed reduction in the FWHM after thermally annealing at 50 - 150°C, in intervals of 25°C, and 175°C for 60 minutes, both suggest a better self-organized and crystalline structure of P3HT within the blend. Although the FWHM measured from the Raman spectra of films from these two thermal annealing strategies are reduced, the degree of crystallinity indicated in the latter is very small. However, after thermal annealing at

175°C for 10 minutes, the FWHM measured from the Raman spectra of the films did not indicate an improvement in the crystallinity of P3HT.

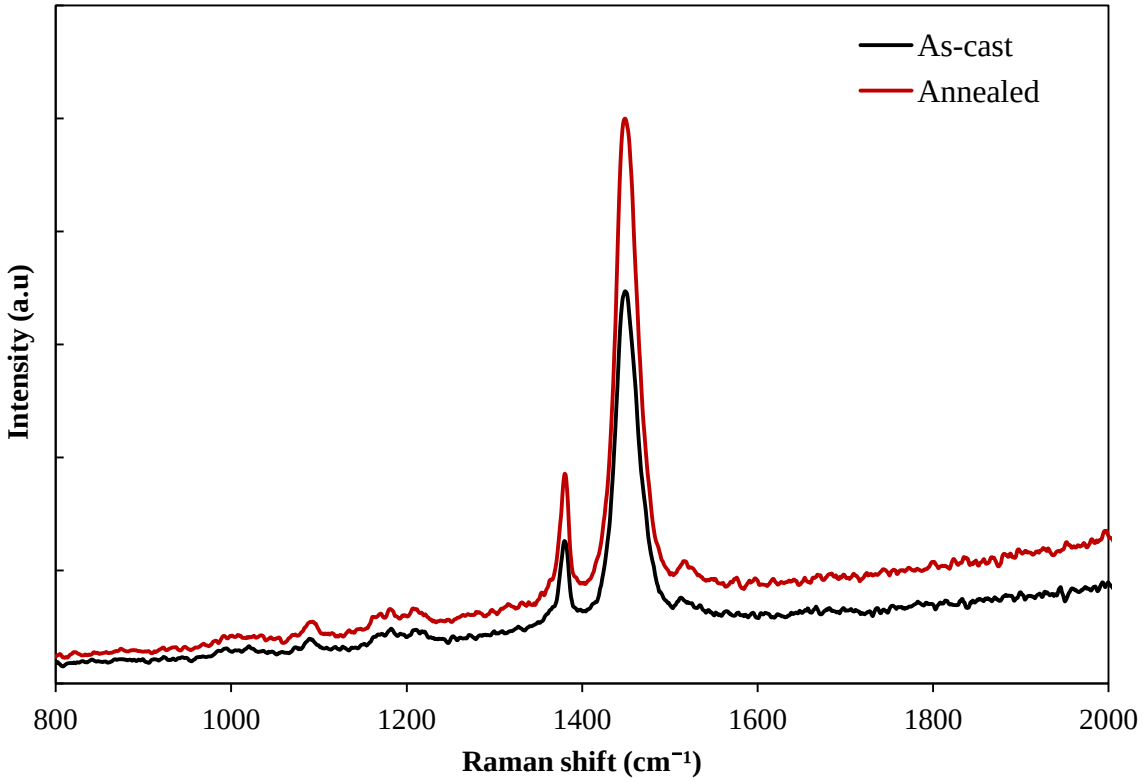

Figure 5.11: Raman spectra of P3HT: PCBM blend thin film; as-cast and gradually annealed from 50°C to 150°C in intervals of 25°C, for 10 minutes.

Table 5.2: Summary of FWHM of the –C=C– mode for P3HT: PCBM blend thin films; as cast, and as a function of the three different thermal annealing strategies.

	FWHM (cm^{-1})			
Sample	**As cast**	**50-150°C**	**175°C (10 min)**	**175°C (60 min)**
P3HT: PCBM	30.00	28.40	31.40	29.60

Nevertheless, the results in Table 5.2 implies that thermal annealing at 175°C (10 min.) yielded a less crystalline and disordered P3HT phase, compared to the other two strategies. These results are in agreement with the optical absorption spectra results, discussed previously in section 5.2.1.1 (see Figure 5.6). A reduction in the Raman intensity signal for thermally annealed blend films can be observed in Figure 5.11. A possible explanation for this is that the region from which the Raman spectrum was taken has a slight depletion of

P3HT. This observation is consistent with previously reported Raman spectroscopy studies (Campoy-Quiles et al. 2011).

Previously in section 5.2.1.1, optical microscopy images of blended film from various thermal annealing strategies were presented (see Figure 5.7). In order to confirm that the clusters, as seen in the images are rich in PCBM aggregates, a Raman spectroscopy mapping technique was employed. As previously highlighted, a laser source with excitation wavelength of 514 nm will be more suitable for observing P3HT rather than PCBM Raman signal. Therefore it is expected that a reduction in signal intensity associated with P3HT will be indicative of P3HT – depleted regions. P3HT: PCBM blend film was therefore imaged using micro – Raman spectroscopy mapping, in order to probe the microstructure and phase separation. Figure 5.12 shows the Raman spectra map for P3HT: PCBM blend thin film thermally annealed gradually from 50 °C to 175 °C in intervals of 25 °C for 10 minutes.

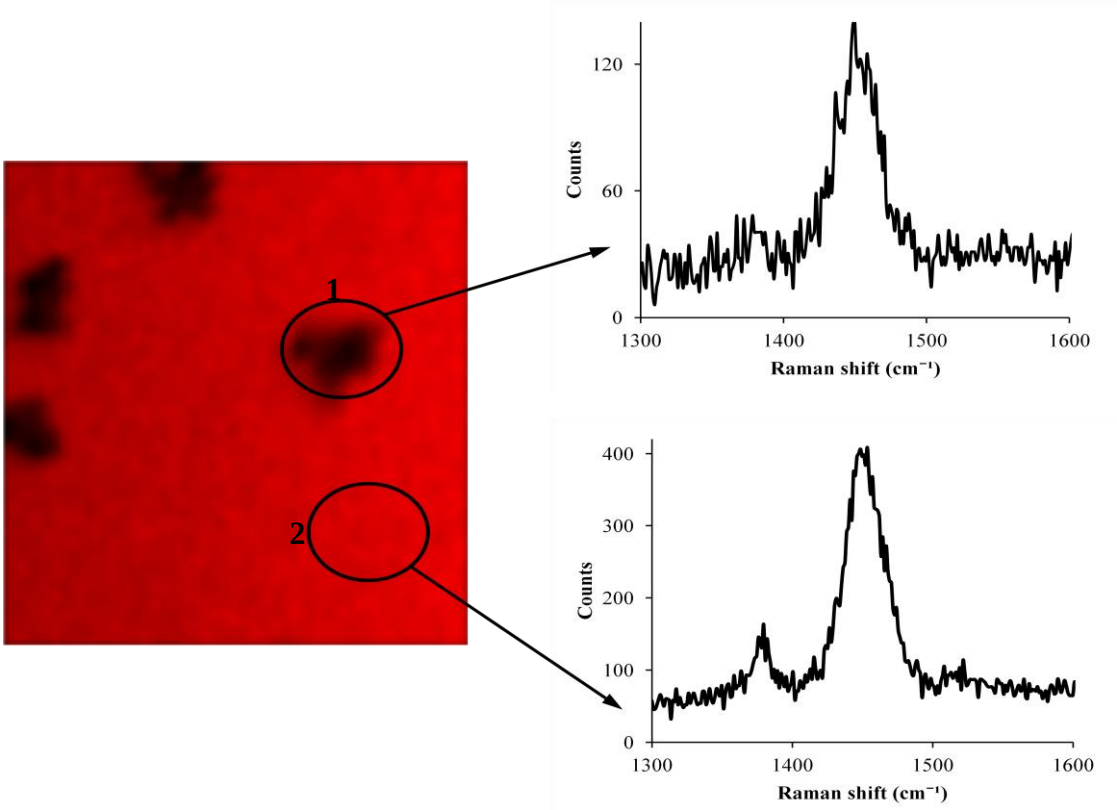

Figure 5.12: Raman spectra map for a thermally annealed thin film (P3HT: PCBM, 1:1). This was taken from two points; (1) at a point containing PCBM aggregates, showing a weak Raman signal for P3HT (a), (2) at a uniform region, showing strong Raman signal for P3HT (b), indicating a P3HT-rich region.

In Figure 5.12, the circle indicated (1) identifies PCBM cluster region, where as the circle (2) identifies P3HT rich region. This is evidenced by the reduction in Raman signal intensity for P3HT (about 400 to 130 counts). This is consistent with observations made by Campoy-Quiles et al. (2008).

Furthermore, PL spectroscopic studies were also undertaken, in order to elucidate the nature of charge transfer processes taking place within the P3HT: PCBM blend film. Details of the mechanism of charge transfer processes have been previously discussed in section 2.9. This is with particular focus on the impact of the different thermal annealing strategies.

Figure 5.13 shows the PL spectra of thin films (pristine P3HT and P3HT: PCBM blend). In all cases, a reduction in the PL intensity is observed (comparing pristine P3HT and the blend film). This PL quenching is interpreted as originating from charge transfer processes between P3HT and PCBM phases in the blend film (Tvingstedt et al. 2009; van Bavel et al. 2010). However, upon thermal annealing the PL intensity increases indicating less efficient charge transfer processes. This effect is also supported by the segregation of ordered P3HT domains, and change in phase separation initiated by the clustering of PCBM molecules. This is consistent with optical microscopy images in Figure 5.7. Although the exciton generation rates are expected to increase with thermal annealing, their dissociation may be hindered by the diffusion of PCBM molecules (Mihailetchi et al. 2006). Therefore this results in creating a nano-structure with phase separations exceeding typical exciton diffusion lengths (10 – 20 nm). It is also important to remark, that this increase in PL intensities may also be as a result of the removal of non-radiative recombination centres upon thermal annealing, in light of the work of Kim and co-workers (2006). Thus its influence should not be completely ruled out. It can also be deduced that all three thermal annealing strategies have different impacts on the charge transfer events within the bulk of the film. This is attributed to the fact that the annealing strategies induce different nanostructuring of blend film morphologies. This consequently has an impact on the nature of donor/acceptor interfaces in the different blend films. From previous reports, it is known that depending on donor/acceptor interface separation, the efficiency of charge transfer events will be affected (Tvingstedt et al. 2009).

To further explore the nature of morphologies in P3HT: PCBM blend film, after thermal annealing, X-ray diffraction is employed. X-ray diffraction studies on thin films are able to provide insight in to the molecular conformation of thin film composite materials (Erb et al. 2006; Kim et al. 2006). These are discussed in the following section.

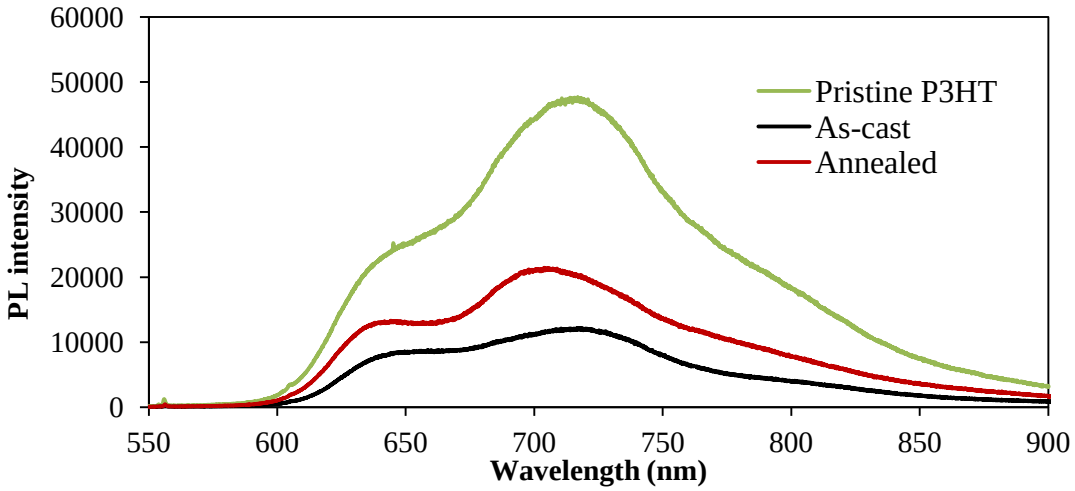

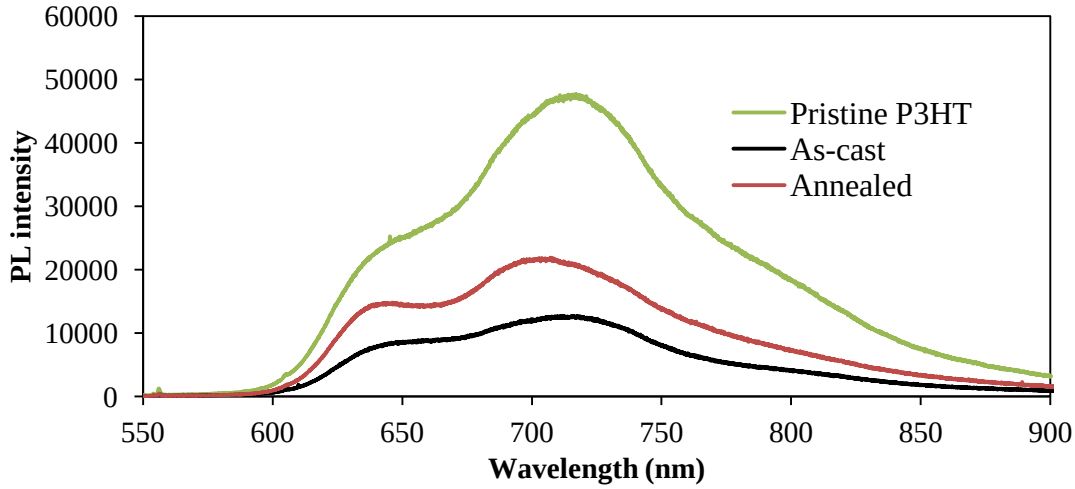

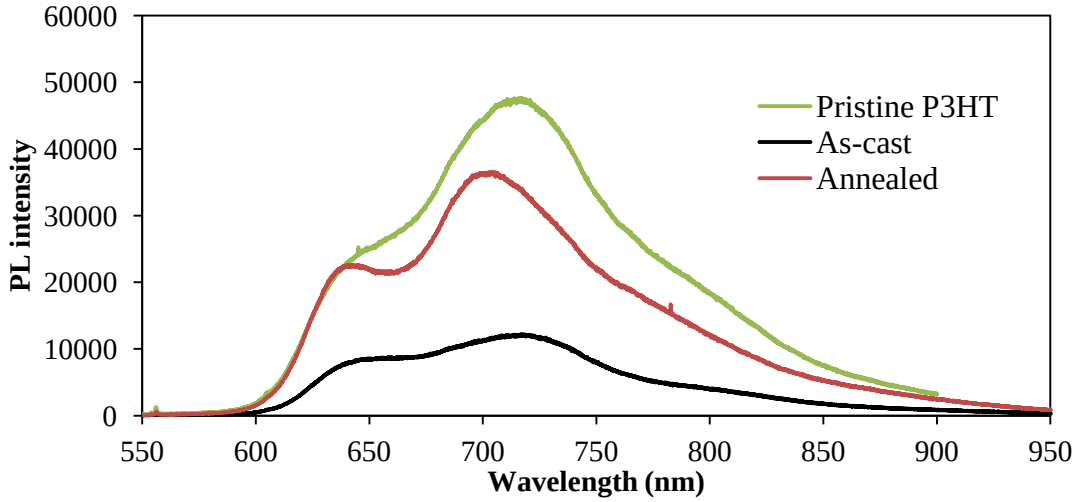

Figure 5.13: PL spectra of pristine P3HT, P3HT: PCBM (1:1) thin films; as-cast and (a) after gradually annealing from 50°C to 175°C in steps of 25°C, for 10 minutes, (b) after annealing at 175°C for 10 minutes, (c) after annealing at 175°C for 60 minutes. Thickness of film is ~150 nm.

5.3 X-ray Diffraction Studies of Thin Films

In probing the structural ordering of thin films of semiconducting material, Grazing Incidence X-ray Diffraction (GIXRD) has been shown to be an effective tool (Li et al, 2007). Particularly for applications in OSCs, information regarding factors such as crystallinity, grain sizes, *d*-spacing, etc. are relevant, as these pertain to carrier mobility, the degree of intermolecular interactions and preferential orientations (Erb et al, 2005; Kim et al, 2006).

Figure 5.14 shows the GIXRD of P3HT: PCBM thin films; as cast and after thermal annealing.

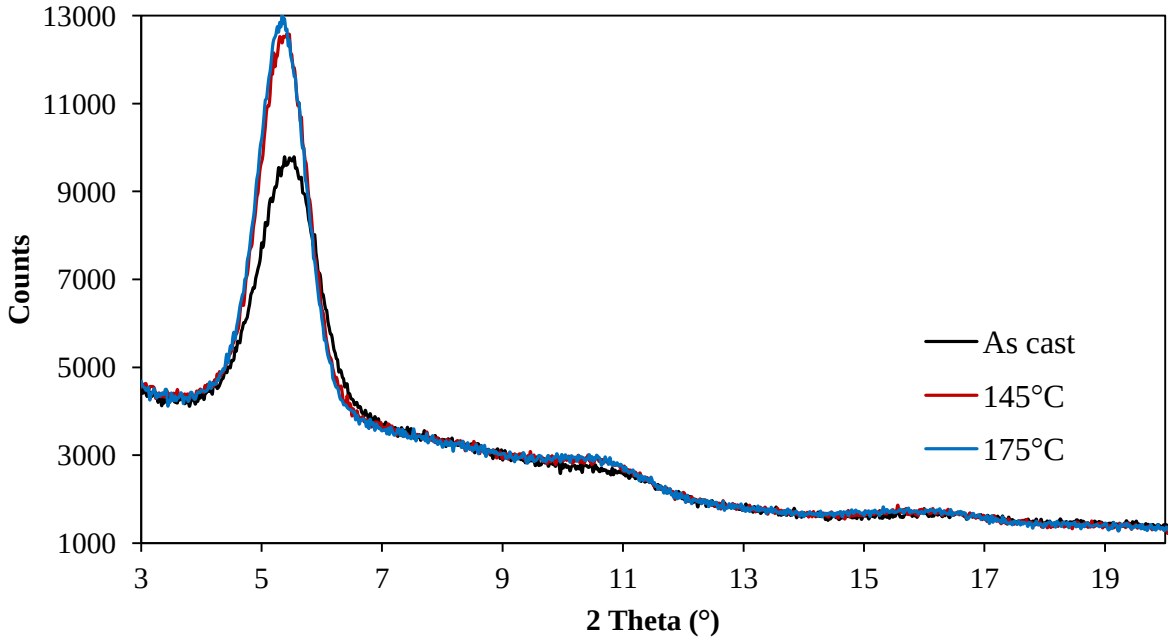

Figure 5.14: GIXRD (with incident X-ray angle = 0.3°) of P3HT: PCBM blend thin films; as cast and after thermal annealing.

As is evident, the GIXRD data of P3HT: PCBM blend film shows a diffraction peak at 2θ = 5.41°, corresponding to a *d* – spacing value of 1.635 nm. Using equation 4.3, the crystal or grain size was calculated to be 7.36 nm. Upon thermal annealing it slightly increased to 8.55 and 8.83 nm (145°C and 175°C). This trend in crystal growth is consistent with the absorption spectroscopy results (see section 5.2.1.1). It was noted that upon thermal annealing, the absorption spectra in the wavelength region of 500 – 600 nm increased. This is indicative of increased conjugation and stacking of polymer chains. Consequently it is believed to be correlated to the increase of the grain size of polymer molecules within the blend film.

As have been suggested from the previous discussions, i.e., in section 5.2.1.1, supported by optical microscopy images (Figure 5.7) and 2-D height profiles (Figure 5.9); that thermal annealing of thin films possibly induces a vertical segregation, one with PCBM molecules segregated towards the film/air boundary. To shed more light on this morphological evolution upon thermal annealing, GIXRD spectra was measured for the structural characterisation of P3HT: PCBM thin film at the near surface. This was achieved by adapting the method reported in literature (Chabinyc, 2008) of obtaining X-ray diffractograms with varying incident angles on either side of the critical angle. The following equation summarises the method employed.

$$R_{\alpha_i} = \frac{\text{Intensity}_{(\text{P3HT})}}{\text{Intensity}_{(\text{PCBM})}} \tag{5.3}$$

The empirical quantity, R is the ratio of the diffraction peak intensities of P3HT to PCBM, assuming they are arising distinctly from P3HT and PCBM molecular phases within the blend film. It is also assumed that these intensities are proportional to the amounts of P3HT or PCBM crystals. From equation 5.3, α_i denotes the angle of incidence of the incident X-ray beam.

By varying the X-ray beam incident angles in the range below and above the critical angle ($\alpha_c \approx 0.12°$). That is, $\alpha_i < \alpha_c$, the X-rays can just probe the top surface properties of the thin film (~ 10 nm), and higher incidence angles above the critical angle i.e., $\alpha_i > \alpha_c$, probes within the film's bulk (Agostinelli et al, 2011; Karagiannidis et al, 2011; Chabinyc, 2008). Another important relationship used for this evaluation is given in equation

$$r = \frac{R(\text{bulk}_{\alpha_i=0.2,\,0.3,\,0.4,\,0.5°})}{R(\text{surface}_{\alpha_i=0.05°})} \tag{5.4}$$

The quantity, $\boldsymbol{r}$ in equation 5.4, is the ratio of R (for $\alpha_i > \alpha_c$, i.e., bulk of the film) to R (for $\alpha_i < \alpha_c$, i.e., probing the near surface of the film). By monitoring this quantity as a function of thermal annealing some useful insight can be gained into the vertical segregation of PCBM molecules in the blend film. It can be observed from Figure 5.14, that the diffraction peak intensities arising from P3HT is very obvious in contrast to that from PCBM molecular phase. Reports in literature have indicated that typical peak intensities arising from PCBM in a P3HT: PCBM blend thin film can be found around $2\theta \approx 20°$ (Agostinelli et al, 2011; Karagiannidis et al, 2011). In the case of this study, peak intensities associated with PCBM

were able to be resolved when thicker blend films were employed. This is clearly illustrated in Figure 5.15.

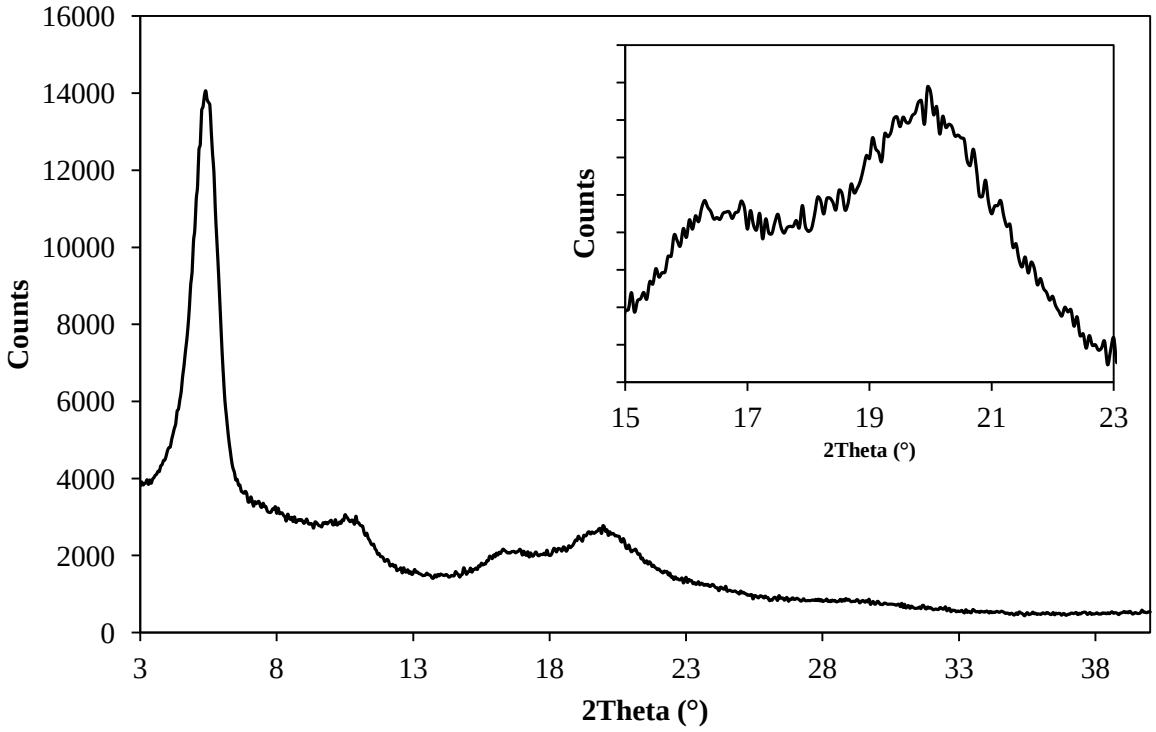

Figure 5.15: GIXRD of very thick P3HT: PCBM blend film, after annealing at 150°C (X-ray incident angle = 0.3°). Inset showing peak arising from PCBM molecular phase.

To confirm that the observed diffraction peak noted in Figure 5.15, at $2\theta = 20°$ really arises from PCBM; a GIXRD of pristine PCBM was obtained. Figure 5.16 shows the GIXRD of pristine PCBM spin casted on quartz substrate. As can be observed the characteristics peak intensity found at $2\theta = 20°$ is similar to that in Figure 5.15 above, confirming that the peak is associated with PCBM molecules in blend thin film.

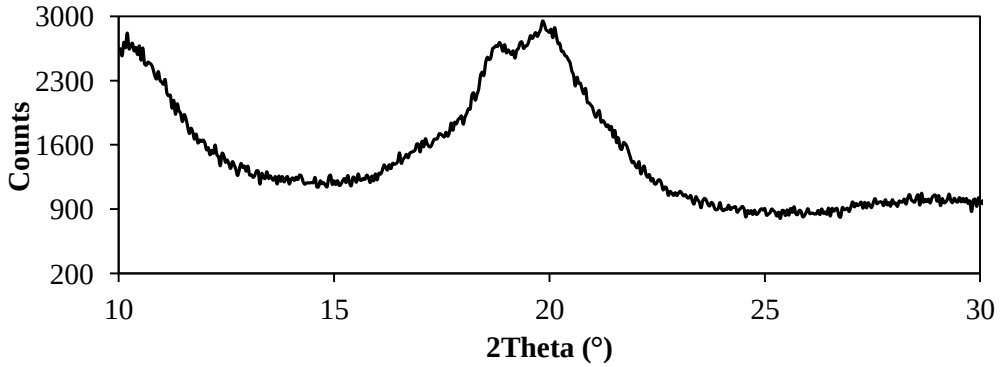

Figure 5.16: GIXRD of pristine PCBM thin film. X-ray incident angle of 0.12°.

Figure 5.17 shows a plot of ***r*** as a function of thermal annealing. It is evident that upon thermal annealing, ***r*** increases steadily and significantly at higher annealing temperatures (above 125°C). This observation is similar to that reported by Agostinelli and co-workers (2011), and is believed to be indicative of vertical segregation of PCBM molecules in the blend thin film. Together with the optical microscopy images obtained (see Figure 5.7), this strongly suggests that vertical segregation of PCBM molecules occurs as a result of thermal annealing. Since after annealing at 150°C, the surface of thin film samples in this work revealed an increased presence of PCBM clusters.

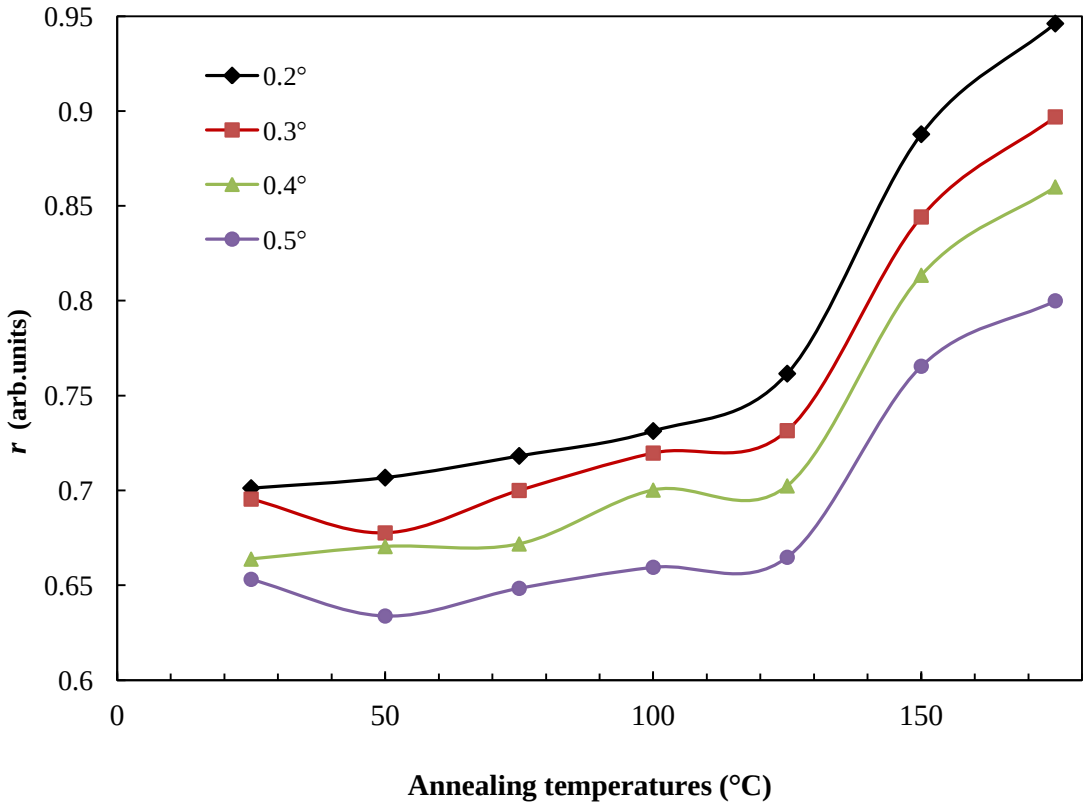

Figure 5.17: A plot of the measured quantity ***r*** (as determined from equation 5.3) as a function of thermal annealing.

Table 5.3 shows a summary of the percentage changes in ***r*** for the various depth probed (i.e., for different α_i) as a function of thermal annealing. These follow the logical path that for X-rays with incident grazing angles $\alpha_i > \alpha_c$, varying depths within the bulk are probed. This also suggests that the change in PCBM concentration as evaluated by the quantity, ***r***, is confined only to the depth probed as a result of the incident angles. Upon thermal annealing at 150°C, the measured percentage change in the values of ***r*** suggests a vertical diffusion of PCBM molecules toward the surface of the film is taking place. However when the glancing angle

was increased to 0.5°, as such the X-rays probing a deeper depth of the film, a lower value of %Δ was measured (suggesting the percentage change at that depth is relatively less). A possible reason for this observation could be that as a majority of PCBM molecules residing at the glass surface boundary make an upward migration, the measure of the percentage change at this depth will be less compared to the case of the depth probed by an X-ray with an incident angle of 0.2°.

Table 5.3: Estimated values of ***r*** and the corresponding percentage changes as a result of thermal annealing, for different probing depths.

	0.2°/0.05°		**0.3°/0.05°**		**0.4°/0.05°**		**0.5°/0.05°**	
P3HT:PCBM	***r***	%Δ	***r***	%Δ	***r***	%Δ	***r***	%Δ
As cast	0.70	0.00	0.70	0.00	0.66	0.00	0.65	0.00
50°C	0.71	0.79	0.68	-2.56	0.67	0.99	0.63	-2.96
75°C	0.72	2.42	0.70	0.65	0.67	1.20	0.65	-0.73
100°C	0.73	4.29	0.72	3.49	0.70	5.48	0.66	0.97
125°C	0.76	8.60	0.73	5.19	0.70	5.81	0.66	1.78
150°C	0.89	26.60	0.84	21.38	0.81	22.54	0.77	17.20
175°C	0.95	34.92	0.90	28.97	0.86	29.55	0.80	22.48

5.4 HOMO and LUMO Energy Levels of P3HT and PCBM

The HOMO and LUMO energy levels of P3HT and PCBM, in this work were estimated from electrochemistry methods. An Agilent 5500 SPM, equipped with an electrochemistry work station was used to perform the measurements in this section. Details of the electrochemistry experimental method, cyclic voltammetery measurements, instruments and setup used have been previously discussed in section 4.4.4. It was necessary that the energy levels of these materials were determined in the laboratory, as they were purchased without this information. Nevertheless, the knowledge of the HOMO and LUMO would be required for an accurate evaluation of mobility measurements based on the SCLC method, which shall be discussed later. The following section will be looking at the cyclic voltammetery method employed for the determination of the HOMO and LUMO energy levels of P3HT and PCBM materials respectively.

5.4.1 Reduction – oxidation potentials of P3HT and PCBM

The electrochemical reduction-oxidation potentials of both P3HT polymer and fullerene, PCBM were measured by cyclic voltammetery. The cyclic voltammograms for these materials are presented in Figure 5.18.

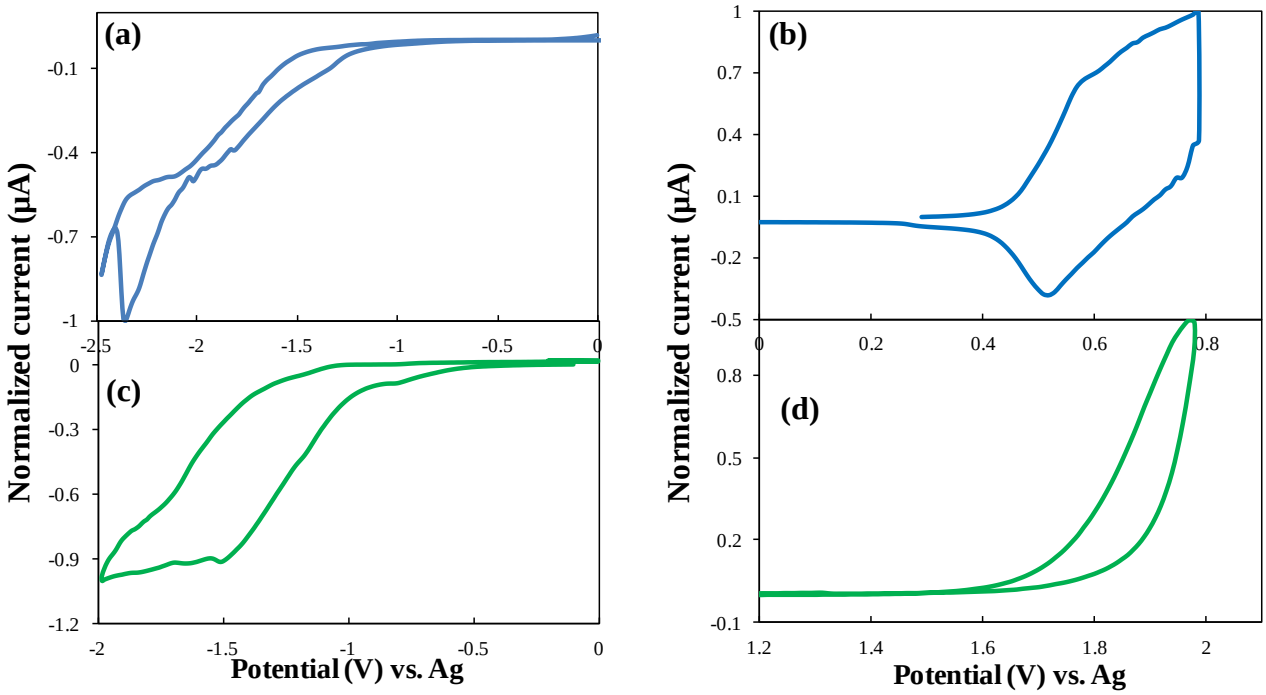

Figure 5.18: Cyclic voltammograms of pristine P3HT and PCBM; oxidation and reduction potentials of pristine P3HT (a) and (b), and pristine PCBM (c) and (d).

Details of how to calculate the HOMO and LUMO energy levels respectively have also been covered in section 4.4.4. The estimated HOMO and LUMO energy levels for pristine P3HT and PCBM are presented in Table 5.4.

Table 5.4: Doping (reduction and oxidation) onset potentials, and calculated HOMO and LUMO levels for pristine P3HT and PCBM.

	Doping potentials (V)		Energy levels (eV)	
	ϕ_n^{ons}	ϕ_p^{ons}	LUMO	HOMO
P3HT	-1.25	0.45	-3.14	-4.84
PCBM	-0.56	1.70	-3.83	-6.09

From the discussions in section 4.4.4, the electrochemical energy band gap for P3HT and PCBM are ~ 1.7 eV and ~2.26 eV. These values indicate that values for energy band gap determined using electrochemical methods are different from the optical band gap (in section 5.2).

Using the onset potentials of *n*-doping (ϕ_n^{ons}), and *p*-doping (ϕ_p^{ons}), from the cyclic voltammograms in Figure 5.18, in Equation 4.10 (a) and (b) (see section 4.4.4), HOMO and LUMO energy levels have been estimated. The onset potentials (i.e., either *n*- or *p*-doping) were determined from the intersection of the two tangents drawn at the rising current (oxidation or reduction) and background current in the cyclic voltammograms (Li et al. 1999). The energy levels obtained in this work, summarised in Table 5.4, all fall within the range of previously reported values, determined by other techniques (Lof et al. 1992).

5.5 Morphological Properties of Thin Films

The nanoscale morphology of pristine P3HT and P3HT: PCBM blend films in this work were studied with AFM. The AFM surface topography images were obtained using the Agilent 5500 SPM, in tapping mode, in ambient air. Details of method and the working principle of the AFM for this work have already been discussed under section 4.3.3. Figure 5.19 shows the AFM topography images of pristine P3HT and P3HT: PCBM (in 1:1, 1:0.8 and 1:0.6 blend ratios). The image of the surface of a film of pristine P3HT shown in Figure 5.19 (a) seem to be composed of spaghetti – like nanoscale crystallites. These distinct features are believed to be self-organised P3HT polymer chains within the film, and will be further discussed later. Similar observations have been previously reported in literature (Shrotriya et al. 2006). Note that on the other hand, these features are not readily obvious in the case of the 1:1 blend ratio, and similarly for 1:0.8 P3HT: PCBM blend. As is evident from Figure 5.19 (d), i.e., topography for 1:0.6 blend ratio film; these features become more prominent.

Because the PCBM weight content is less in the case of Figure 5.19 (d), there would be some relatively P3HT – rich regions. However, this will be less in comparison to the case of pristine P3HT film. Consequently, in view of a completed OSC based on a 1:0.6 blend ratio, there is expected to be an undesired distribution of P3HT at the active layer/cathode interface. This configuration may not offer the advantages for efficient charge transport and electrode selectivity (Campoy-Quiles et al, 2008). This could possibly be one of the reasons why PV devices based on 1:0.6 ratio, have been reported to exhibit low current densities as will be discussed later, compared to the other two ratios. This is expected to result in unfavourable

D/A distributions within the bulk, which in turn would be detrimental to the efficiency of exciton dissociations (Kim et al. 2005).

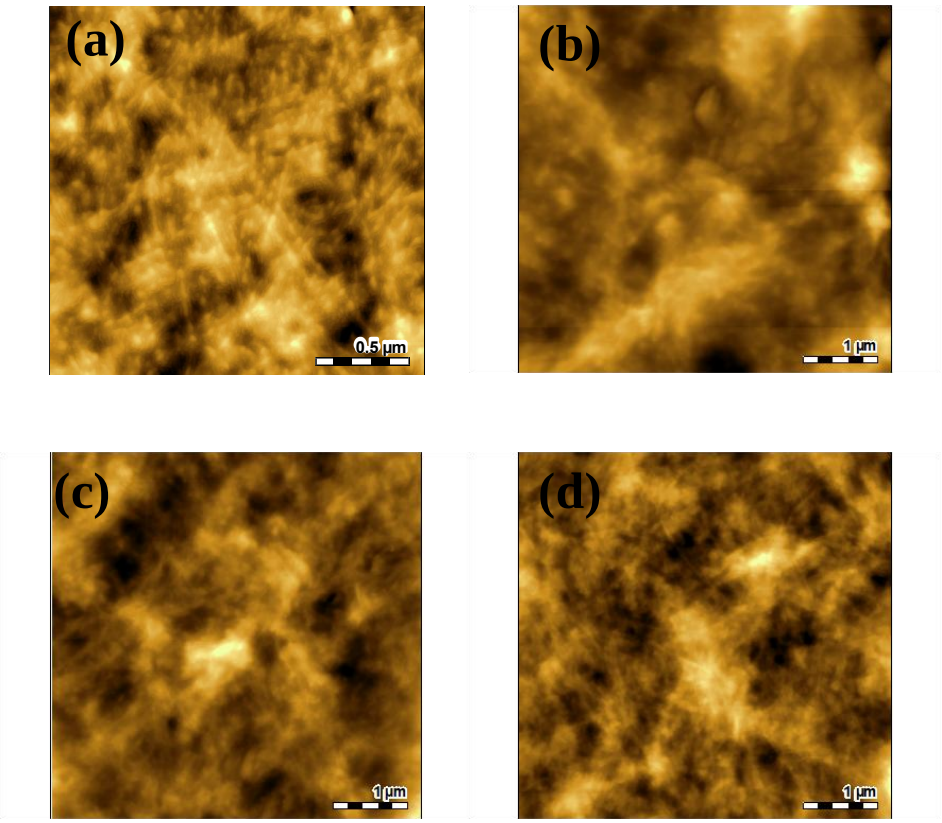

Figure 5.19: AFM topography images of (a) pristine P3HT film, and P3HT: PCBM blend thin films, in weight ratios of; (b) 1:1, (c) 1:0.8, and (d) 1:0.6.

Figure 5.20 shows the AFM phase image of pristine P3HT thin film. In the AFM phase image, the crystalline domains can be clearly observed. From the AFM phase image, a 2-D line profile analysis can be performed between two points (B and A), as shown in Figure 5.20 (b). By employing the horizontal distance function in the surface analysis software (Pico Image Basic, v. 6.0) (see Figure 5.20 (c)), the thickness of what appears to be grains of crystalline P3HT chains can be estimated. The value estimated from this method was in the range of 18 – 35 nm, which is consistent with values reported in literature (Shrotriya et al. 2006).

5.5.1 Evolution of Morphology with Thermal Annealing

Figure 5.21 shows the AFM topography images of as cast thin films of P3HT: PCBM and after they have been thermally annealed according to the three different strategies outlined in section 5.2.1.1, namely: 50 - 175°C (in steps of 25°C for 10 min each), 175°C for 10 min and

60 min. These measurements were performed in order to probe the impact of different thermal annealing approaches on the surface morphologies of the blend film.

It has been found that the surface topography of thin films thermally annealed at 175°C (10 min.) appears much smoother in comparison to blend films annealed at the same temperature but for a longer time (i.e., 60 min.). By comparing these with the optical microscopy images presented in Figure 5.7, it is interesting to note that the films annealed for the shortest time (i.e., 175°C for 10 min), showed the lowest reduction in absorption intensity associated with PCBM. This also supports the quantitative analysis results of PCBM cluster densities, discussed in the section 5.2.1.1: which showed that a cluster density of only 2.4% resulted from annealing at 175°C for 10 min. compared to the other two annealing approaches. S_q is the estimated root mean square (rms) surface roughness.

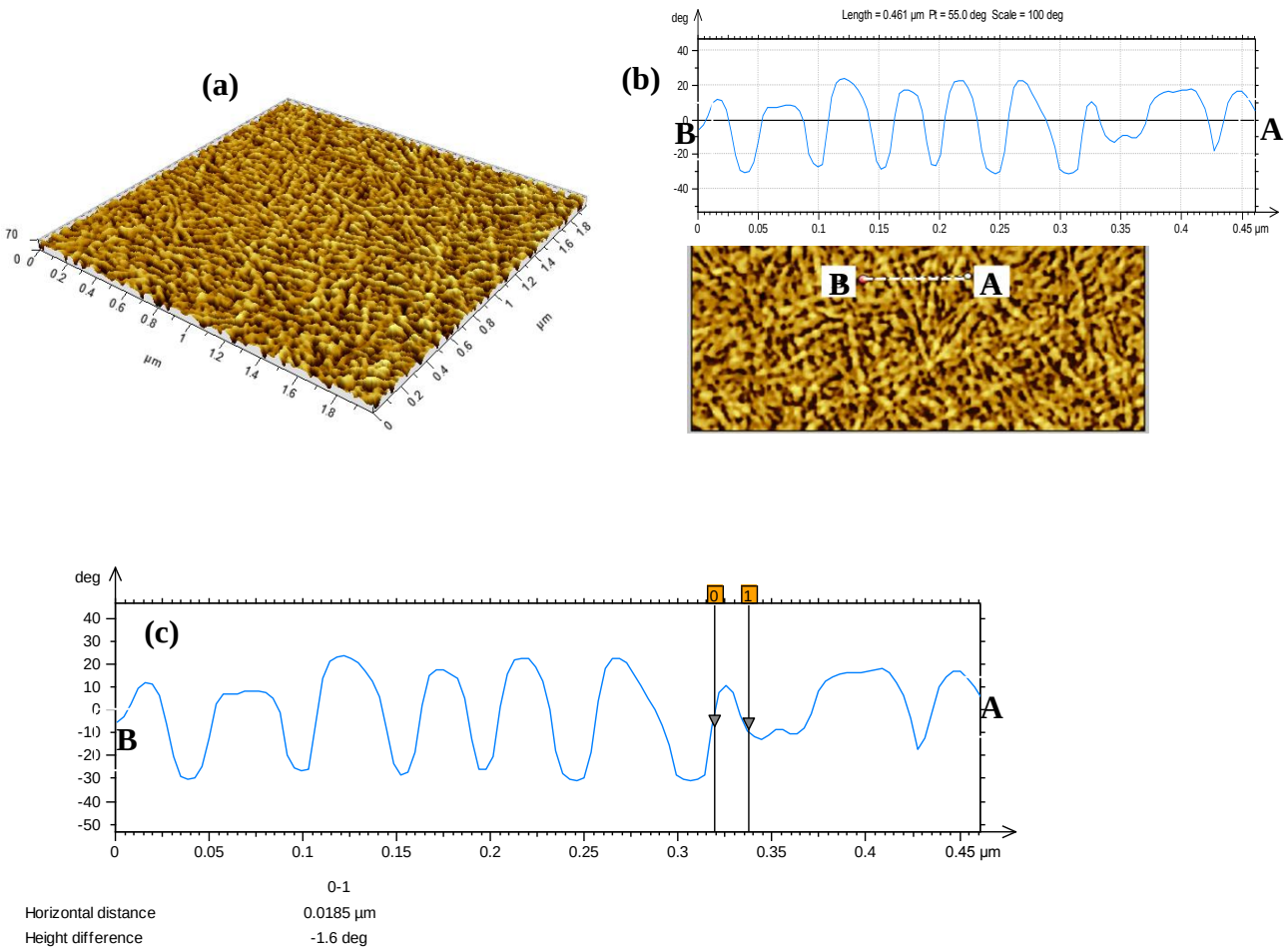

Figure 5.20: AFM phase image of pristine (a) P3HT film (b) 2-D line profile, (c) Horizontal distance measurement profile.

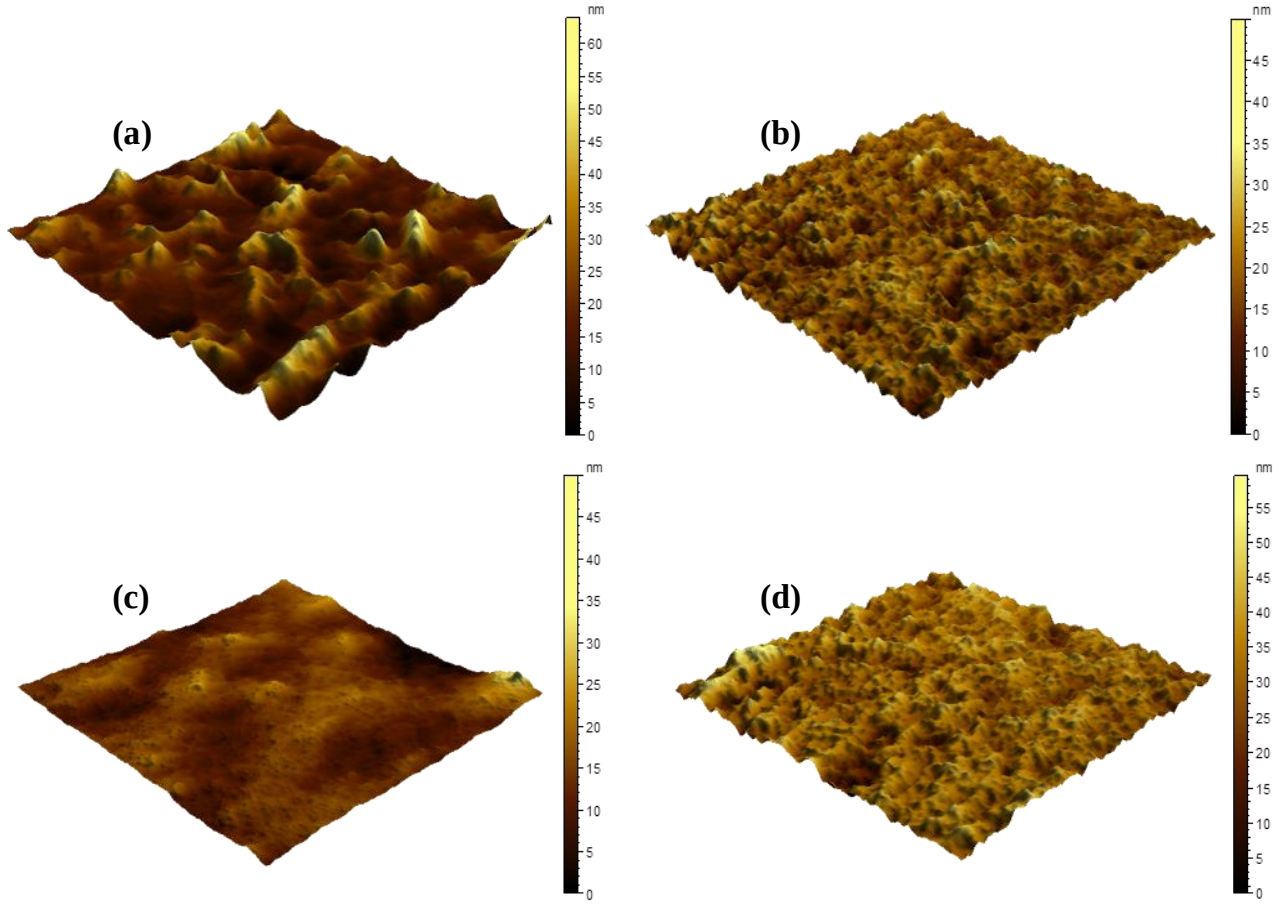

Figure 5.21: AFM topography images (5 µm x 5 µm) of thin films (P3HT: PCBM) of weight ratio 1:1, and thickness ~150 nm; (a) as-cast, S_q = 4.64 nm, and after annealing at (b) 50°C to 175°C, in steps of 25°C; S_q = 9.5 nm, for 10 minutes each, (c) 175°C for 10 minutes; S_q = 3.76 nm, and (d) 175°C for 60 minutes; S_q = 6.16 nm.

5.6 Summary

In this chapter, the results of employing a number of characterisation methods to investigate significant properties of organic semiconductor materials and thin films were presented. A correlation between thermally induced morphological variations in P3HT: PCBM blend thin films and their corresponding optical absorption spectra properties were demonstrated. The method of UV-visible absorption spectroscopy can be effectively used as a tool for evaluating PCBM aggregation in P3HT: PCBM blend thin films. The importance of including the far UV region of the spectrum for analysis of P3HT: PCBM blend thin films were clearly highlighted. Depending on the thermal annealing strategy employed, PCBM aggregate dimension tuning differs accordingly. Proof of PCBM cluster formation was presented with optical micrographs. Furthermore, the underlying mechanism of the process of aggregation and P3HT polymer crystallization as a result of thermal annealing were probed using Raman

and PL spectroscopy, X-ray diffraction and atomic force microscopy methods. From the foregoing, it has been demonstrated that the gradual thermal annealing strategy (i.e., 50 - 175°C, in steps of 25°C) exhibited a more stable and controlled tuning of thin film morphology.

In the following chapter, the various impacts of processing conditions such as composition, and thermal annealing, on PV properties will be presented with detailed discussions.

Chapter 6

Photovoltaic Properties of OSCs

"Efficiency is the essential parameter for solar cells with respect to energy production and cost."

— Christoph J. Brabec

6.1 Introduction

The results from the electrical characterisation of devices based on P3HT: PCBM blend films (current-voltage properties, both in the dark and under illumination) are presented and discussed here. Details of the experimental methods and instrumentation with respect to the measurements of current – voltage characteristics of devices have been previously discussed in section 4.4.

6.2 Dependence of Dark *J – V* properties of P3HT: PCBM Blend Thin Films

To determine the dependence of dark current – voltage characteristics on thermal annealing, solar cells with the structure ITO/PEDOT: PSS/Blend film/Al was investigated. Three different P3HT: PCBM blend ratios, with 50, 44.4, and 37.5% of PCBM, were used respectively. Figure 6.1 shows the dark current – voltage characteristics of the fabricated devices.

Comparing the dark *J – V* characteristics of the three blend ratios in Figure 6.1 (a), the leakage current (current measured at -1V) was observed to be highest for 1:0.6 blend. It is expected that such a high leakage will have a negative impact on solar cell performance based on 1:0.6, compared to the other two ratios. The comparison between the solar cell performances for these blends will be further explored later on. When these BHJ devices where thermally annealed, it was observed that the measured leakage currents for all three

blends increased respectively. In addition, the leakage currents are comparable between the three blends.

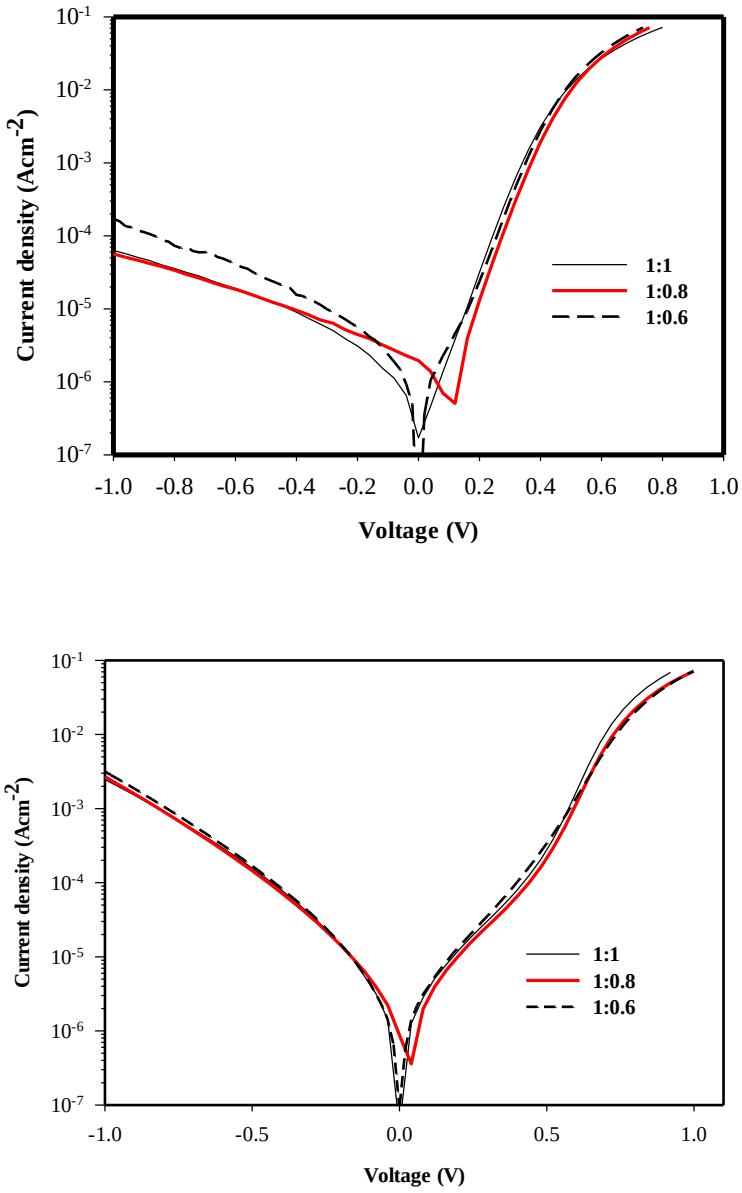

Figure 6.1: Dark *J* – *V* plots of P3HT: PCBM BHJ solar cells: (a) as cast and (b) annealed.

Between blend films as cast and thermally annealed; 1:1 and 1:0.8 blend ratios increased by two orders of magnitude, whilst 1:0.6 blend by only one order of magnitude. Recalling the observed change in peak absorption intensities associated with PCBM absorption in section 5.2.1., between the three blend ratios, 1:0.6 had the lowest percentage change in absorption intensities after thermal annealing at 175°C. Exactly how this is related to the dark *J* – *V* characteristics is not very clear. However what is interesting though is that the two trends

(i.e., leakage currents and absorption intensities) seem to follow the same direction. It could be that the compositional ratios together with their corresponding morphology evolution following thermal annealing (as revealed in their impact upon optical absorption), may also be connected to the leakage current trend observed here.

Another interesting point is with respect to the comparable leakage currents mention above for all three blends after thermal annealing. This trend, as will be seen in following sections, may likely be related to the V_{OC} of devices, seeing that this was observed to be similarly comparable after thermal annealing. Therefore it can be suggested that the nature of leakage currents following thermal annealing is related to the measured V_{OC}s of devices under illumination. In other words both parameters might have their origins in the same mechanism.

6.3 Photovoltaic (PV) Performance Measurements

In this section, the results and discussions of PV measurements obtained from fabricated P3HT: PCBM BHJ solar cells are presented. To measure the PV performance of the devices discussed in the previous section (6.2), current – voltage characteristics were obtained under illumination provided by a solar simulator. The details of the method for device characterisation under illumination have been covered in section 4.4.1. PV properties discussed in this section with respect to composition and thermal annealing impact are based on devices fabricated in ambient air, with an active area of 0.14 cm^2. $J - V$ characteristics of P3HT: PCBM BHJ solar cells based on blend ratios of 1:1, 1:0.8 and 1:0.6 respectively are shown in Figure 6.2.

The short circuit current density J_{SC} is observed to increase with increasing PCBM percentage weight ratio. To explain this increase in current density, Figure 5.5 is referred to with particular focus on only as cast devices. It can be observed from the absorption spectroscopy results that the absorption spectrum peak intensity for P3HT is reduced upon increasing PCBM percentage weight ratio while PCBM absorption followed the opposite trend. It is believed that increasing the PCBM content, as in the blend of 1:1 ratio, the interfaces between donor and acceptor material within the bulk are enhanced (Kim et al. 2005). Consequently this results in better exciton dissociation which is critical to photocurrent generation. Therefore it can be argued that the donor/acceptor (D/A) interface distribution within the active layer based on 1:1 is more favourable, but decreases in 1:0.8, and 1:0.6 respectively. Furthermore the PCBM content in the P3HT: PCBM blend ratio of 1:1 supports better charge transport pathways to the respective electrodes. The increased leakage

current previously highlighted in the case of 1:0.6 could also be a contributing factor to the low current density measured in devices based on this ratio.

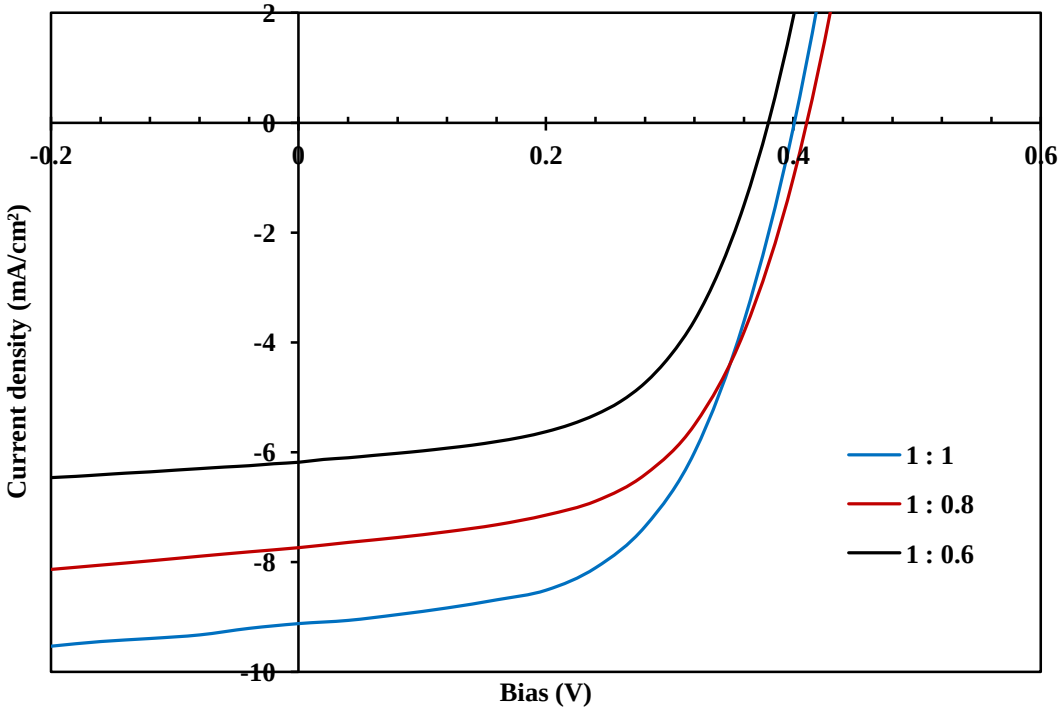

Figure 6.2: *J-V* curves under illumination for devices based on P3HT: PCBM blend films: P3HT: PCBM (weight ratio; = 1:1, 1:0.8, and 1:0.6).

6.3.1 Thermal Annealing Effects on D/A interfaces in P3HT: PCBM solar cells

P3HT: PCBM BHJ solar cells discussed in the previous section were subsequently thermally annealed. Current – voltage characteristics under illumination were measured for these annealed devices in ambient air. The PV performance parameters of these devices were studied in light of the impact of thermal annealing on D/A interfaces within the active layer. Thermal annealing was performed on a hotplate at 50, 75, 100, 125, 150, and 175°C (for 10 minutes each). It is important to remark here that the current – voltage characteristics obtained under illumination, were done without applying a spectral mismatch correction factor.

Figure 6.3 shows the *J – V* characteristics under illumination of the three OSC devices (i.e., with three different PCBM percentage loadings); as cast and after thermal annealing at

several temperatures. Table 6.1 is a summary of the experimental PV parameters measured for all devices from the *J* – *V* curves in Figure 6.3.

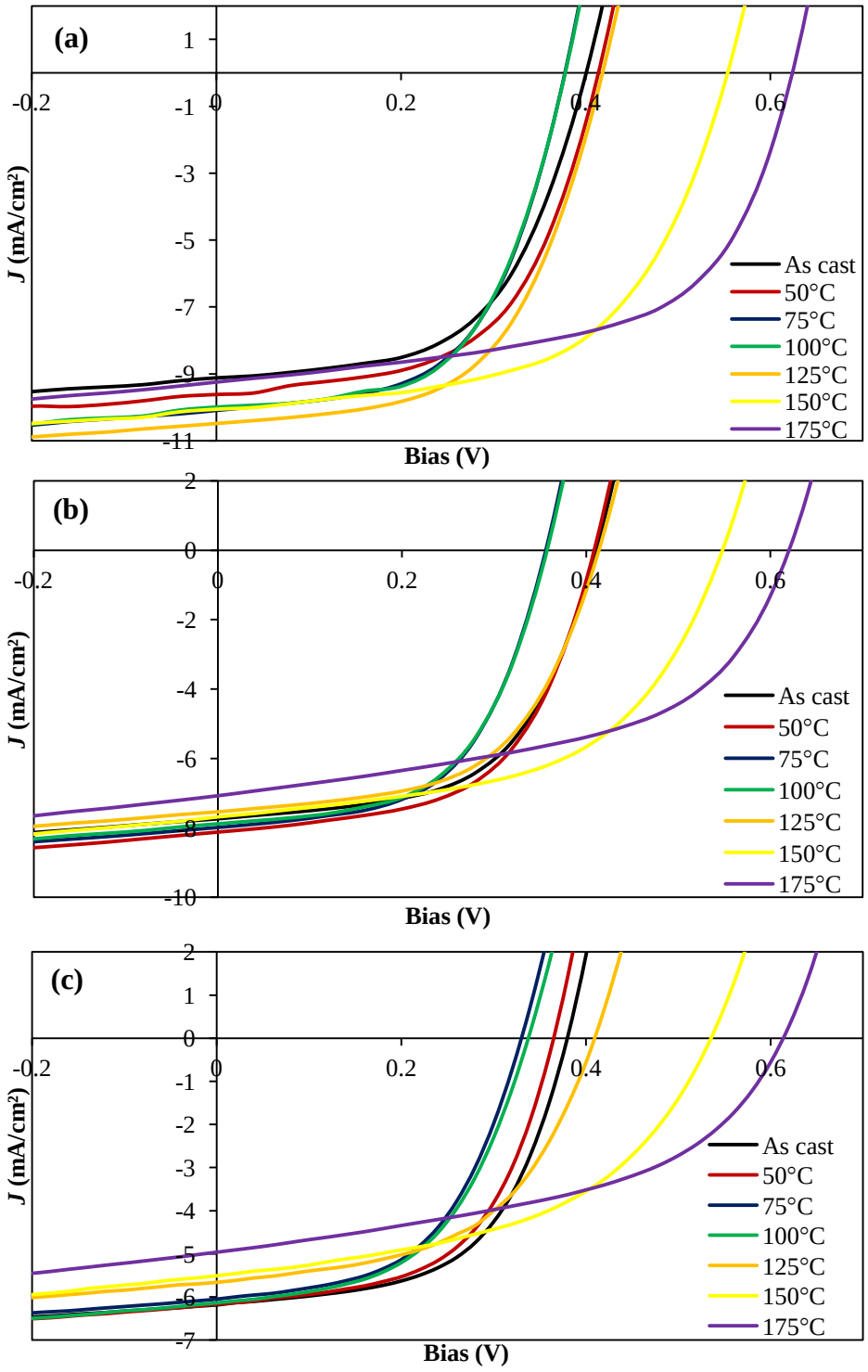

Figure 6.3: *J* – *V* characteristics of P3HT: PCBM BHJ solar cells based on (a) 1:1, (b) 1:0.8, and (c) 1:0.6 blend ratios; as – cast and after thermal annealing.

Table 6.1: Summary of PV performance parameters for devices based on P3HT: PCBM (1:1, 1:0.8, and 1:0.6).

	1:1				1:0.8				1:0.6			
Annealing temperatures	***J*sc (mA/cm²)**	***V*oc (V)**	**FF (%)**	**PCE (%)**	***J*sc (mA/cm²)**	***V*oc (V)**	**FF (%)**	**PCE (%)**	***J*sc (mA/cm²)**	***V*oc (V)**	**FF (%)**	**PCE (%)**
As casted	9.12	0.40	56.34	2.06	7.74	0.41	56.63	1.79	6.18	0.38	56.49	1.33
50°C	9.62	0.41	55.95	2.22	8.12	0.41	56.39	1.87	6.17	0.36	56.02	1.26
75°C	10.09	0.38	56.24	2.13	7.99	0.36	55.87	1.59	6.05	0.33	53.04	1.06
100°C	9.99	0.38	56.80	2.14	7.88	0.36	55.67	1.56	6.14	0.34	52.17	1.08
125°C	10.49	0.42	56.00	2.45	7.54	0.41	55.82	1.74	5.66	0.41	52.51	1.21
150°C	10.06	0.55	56.97	3.17	7.69	0.55	53.97	2.27	5.51	0.53	48.79	1.44
175°C	9.25	0.62	58.76	3.38	7.08	0.62	51.59	2.26	4.96	0.61	47.20	1.43

It is evident from Table 6.1, that for OSC devices with higher PCBM loadings, J_{SC} improves with annealing temperatures. For example, in device based on 1:1 blend ratio, J_{SC} peaks at 125°C, whilst the same trend occurs at 50°C for 1:0.8. For the device based on the blend ratio of 1:0.6 on the other hand, the parameter J_{SC} deteriorates with annealing temperatures. Previous publications on the influence of thermal annealing have also reported such deterioration in J_{SC} after annealing at certain temperatures (Chirvase et al. 2004; Parlak, 2012). In addition, it is clear from Table 6.1 that devices with PCBM content of 50 and 44.4% exhibited a relative thermal stability by utilizing the optimisation procedure. The experimental PV performance results also suggest that the nature of PCBM molecular clustering is sensitive to the PCBM content, diffusion time and temperatures (Erb et al. 2005; Jo et al. 2009). The resulting nanostructure within the active layer is a D/A interpenetrating network which will support better charge transport as seen in the case of P3HT: PCBM (1:1) blend ratio. However for PCBM content of 37.5% or less, the thermal anneal induced clustering may result in disrupted pathways for electron transport. The implication of this will be a lower current density upon thermal annealing.

Figure 6.4 summarises the variation in short circuit current density and open circuit voltage with annealing temperatures. The open circuit voltage V_{OC} remains almost constant up to around 100°C and upon further increase in annealing temperature (upper limit of temperature used, 175°C) increases to around 0.62V. This increase in V_{OC} is believed to be due to vertical segregation of PCBM, disrupting shunt paths between the two electrodes (Sirringhaus et al. 1999). Table 6.2 summarises the values of series and shunt resistances (R_S and R_{SH}), extracted from the $J - V$ curves in Figure 6.3.

Table 6.2: Summary of measured R_S and R_{SH} as a function of PCBM loadings and thermal annealing (values determined using the method outlined in section 4.4.1)

Annealing Temperatures (°C)	R_S (Ω.cm^2)			R_{SH} (Ω.cm^2)		
	1:1	**1:0.8**	**1:0.6**	**1:1**	**1:0.8**	**1:0.6**
As casted	4.9	4.9	4.6	498.0	449.8	588.7
50	4.7	4.6	4.6	507.0	320.2	519.9
75	4.6	4.9	6.7	483.8	283.6	507.2
100	4.6	5.0	6.9	505.2	299.6	475.3
125	5.0	5.2	5.9	492.2	483.4	580.9
150	4.6	5.3	5.5	456.0	415.0	459.7
175	4.2	5.2	5.4	355.7	314.1	379.9

This may be attributed to the observed decrease in the calculated shunt resistances R_{SH}, for all three different blend ratios. R_{SH} decreased from 498 Ω.cm^2 to ~356 Ω.cm^2 after thermal annealing at 175°C, for devices based on 1:1 blend ratio. This downward trend was similarly observed for the other two blend ratios, i.e., ~450 Ω.cm^2 to ~314 Ω.cm^2 (1:0.8) and ~589 Ω.cm^2 to ~380 Ω.cm^2 (1:0.6). This is also consistent with the optical absorption data presented in Figure 5.5, with emphasis on the PCBM associated absorption spectra, i.e., 250 – 350 nm wavelength range.

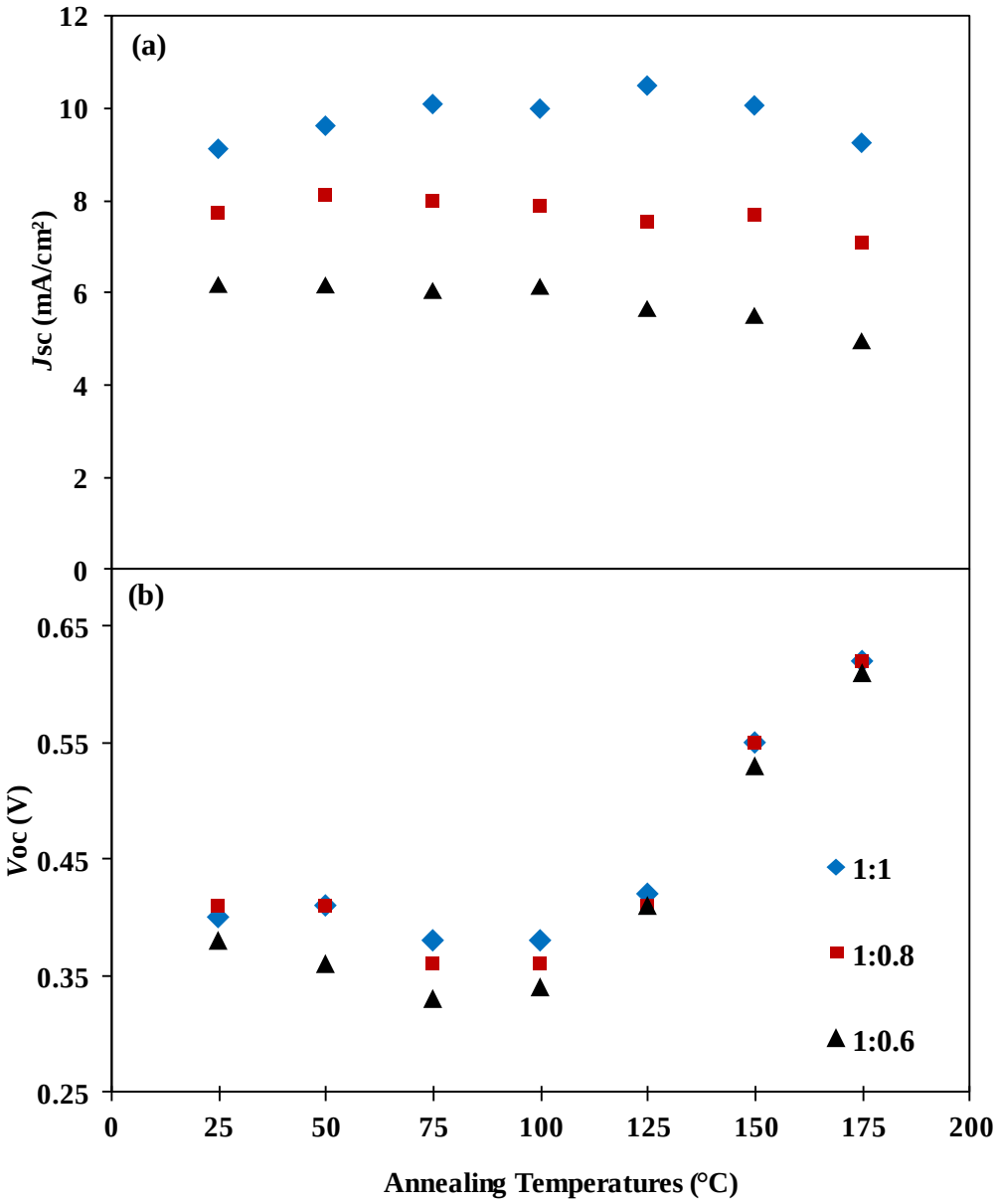

Figure 6.4: J_{SC} (a) and V_{OC} (b) as a function of thermal annealing temperatures for P3HT: PCBM solar cell devices.

It is clear that the devices with highest PCBM content i.e., 1:1 ratio upon thermal annealing show greatest peak optical absorption intensity reduction. This is due to the segregation of the PCBM aggregates to the film air boundary and hence reduction in optical absorption (Campoy-Quiles et al. 2008). Other possible reasons for this observed increase in V_{OC} could be associated with increase in built in potential at higher temperatures resulting from traps generated within the bulk of the active layer. The device power conversion efficiency tends to increase with PCBM loading. This is attributed to higher short circuit currents resulting from efficient charge transfer. Also it is noted that the devices annealed at temperatures of above 125°C shows improved power conversion efficiencies with highest PCE of 3.38% recorded for 1:1 ratio at 175°C. On the other hand, for blend ratios of 1:0.8, and 1:0.6, the best PCE was determined to be 2.27% and 1.44% at 150°C. In all cases, the improved PCEs are considered to be due to the improved V_{OC} at these temperatures respectively. As far as the fill factor is concerned there is no significant variation for this parameter at room temperature upon variation of PCBM loading. However above 125°C it has been observed that the fill factor increases with PCBM loading. The mechanism responsible for this is likely to be the same resulting in the increase in open circuit voltage with temperature rather than improved short circuit current density.

6.3.2 Influence of PCBM cluster dimension tuning on the Photovoltaic properties of P3HT: PCBM solar cells

In section 5.2.1.1, the discussions on the influence of thermally induced PCBM cluster dimension tuning, on the optical properties of P3HT: PCBM blend thin films were presented. This section however, focuses on the PV characteristics of P3HT: PCBM BHJ solar cells, as a function thermal annealing strategies and how it influences the dimension tuning of PCBM clusters. The controlled formation of PCBM aggregates within the blend structure, undoubtedly affects charge transport to respective electrodes (Jo et al. 2009). In addition, the balancing of electron/hole mobilities to avoid space charges are all significant parameters in maximizing PCEs (Mihailetchi et al. 2006). Previous works on thermal annealing of bulk heterojunction solar cells mainly focus on analysis of as cast, post-processed devices at optimum temperatures and its implications on device physical parameters such as V_{OC}, J_{SC} and subsequently PCEs (Mihailetchi et al. 2006; Jeong et al. 2011). However it is of interest to study the effect of higher annealing temperatures on device performance. It is herein suggested that, only at such high thermal annealing temperatures, significant structural changes taking place can be observed. The case study at this point, in this section is such that

under different thermal annealing strategies (outlined previously in section 5.2.1.1), and at temperatures above 150°C the aforementioned observations were being investigated. To gain insight in to the properties of the D/A phase separations due to PCBM dimension tuning, particular emphasis is placed on the photocurrent generation measurements. Photocurrent generation measurement is a very useful tool for studying the effects of thermal annealing processes on device performance (Mihailetchi et al. 2006). This is particularly the case in terms of physical parameters such as PCBM molecular aggregation, for example. It is in view of this that the measurement is being employed herein to quantify PCBM dimension tuning as a function of thermal annealing processes. The implications of the thermal annealing processes on D/A phase separations and in particular photocurrent generation, can shed light on the solar cell device performance characteristics.

To study this effect within the active layer on the photocurrent generation in the P3HT: PCBM BHJ device, $J - V$ properties were measured in reverse bias under 100 mW/cm^2 simulated AM 1.5 conditions. The structure of fabricated devices is the same as those described previously in section 6.2. In this section, all device fabrication and characterisations were done in nitrogen – filled glovebox.

The $J - V$ curves under illumination of P3HT: PCBM BHJ solar cells, with an active layer thickness of ~150 nm, are presented in Figure 6.5. The summary of PV performance parameters, exciton generation rates, G_{max}, and exciton dissociation probability, P (E, T), are presented in Table 6.3. Details of how G_{max} and P (E, T) were determined will be discussed in subsequent sections.

It is important to note at this point that the summary of data in Table 6.3 included annealing temperatures between 120 - 145°C (in steps of 5°C). Thermal annealing at this temperature ranges was necessitated in order to carefully probe gradual changes leading to the optimised condition (i.e. 150°C). These data were however not included in Figure 6.5 (a) for purposes of clarity.

Focusing particularly on devices thermally annealed at 50 - 175°C (in intervals of 25°C), it is evident from Table 6.3, that the short circuit current density J_{SC} improves with annealing temperature up to around 150°C after which deterioration in J_{SC} is observed. In contrast, the V_{OC} tends to reduce upon thermal annealing up to 100°C and remains almost constant up to around 130°C, there after it increases with further thermal annealing.

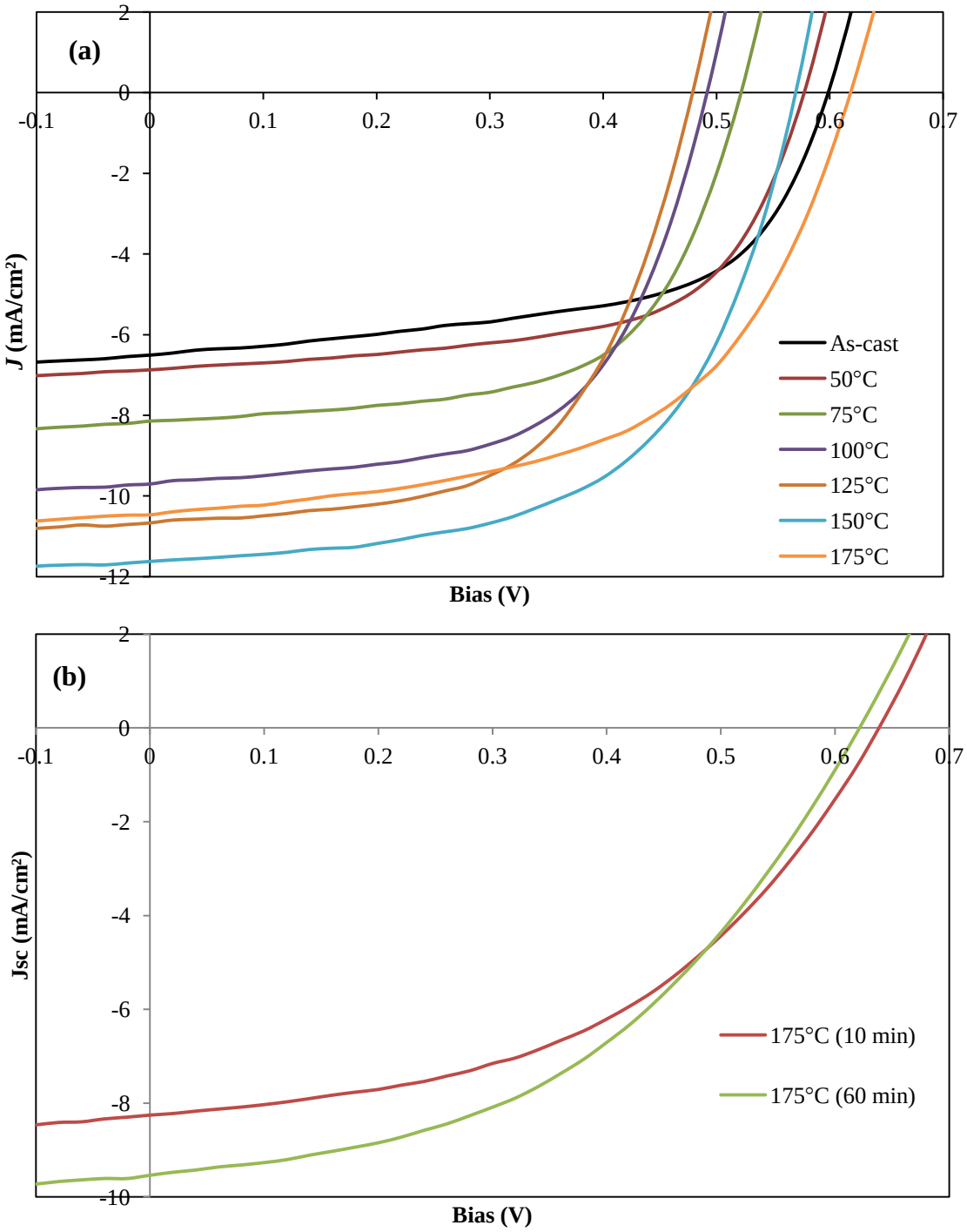

Figure 6.5: *J – V* characteristics of P3HT: PCBM – based BHJ devices: (a) as cast and after thermal annealing from 50 - 175°C (in steps of 25°C, 10 min.) (b) After thermal annealing at 175°C for 10 and 60 min.

Table 6.3: Summary of PV parameters: short circuit current density (J_{SC}), open circuit voltage (V_{OC}), fill factor (*FF*), power conversion efficiency (PCE), and exciton generation rate (G_{max}), and probability of exciton dissociation ($P(T, E)$), all as a function of thermal annealing (50 - 175°C).

	***J*sc (mA/cm²)**	***V*oc (V)**	***FF***	**PCE (%)**	***G*max ($m^{-3}s^{-1}$)**	***P* (*T*,*E*)**
As-cast	6.51	0.60	0.58	2.26	3.37×10^{27}	0.80
50°C	6.87	0.58	0.61	2.42	3.66×10^{27}	0.78
75°C	8.14	0.52	0.61	2.60	4.21×10^{27}	0.81
100°C	9.70	0.49	0.60	2.84	4.75×10^{27}	0.85
120°C	10.20	0.48	0.59	2.90	4.79×10^{27}	0.89
125°C	10.67	0.48	0.59	3.00	5.00×10^{27}	0.89
130°C	10.04	0.48	0.58	2.79	4.67×10^{27}	0.89
135°C	10.90	0.49	0.58	3.07	5.04×10^{27}	0.90
140°C	11.21	0.52	0.57	3.31	5.08×10^{27}	0.93
145°C	11.33	0.53	0.57	3.39	5.21×10^{27}	0.90
150°C	11.62	0.57	0.58	3.84	5.78×10^{27}	0.90
175°C	10.46	0.62	0.55	3.56	5.33×10^{27}	0.82

In all cases the power conversion efficiencies tend to follow the same trend as the short circuit current density, with the highest PCE recorded at 150 °C. A possible reason for this observed trend in J_{SC} as a function of the thermal annealing processes was briefly highlighted in sections 5.2.1.1, and 5.2.2, which has to do with improved crystallinity, and favourable D/A separation. Another explanation is associated with a number of factors, namely: better exciton generation rates, improved exciton dissociation, improved charge carrier mobilities and transport of charges to the respective electrodes.

Details of the relationship of D/A interfaces within the active layer of BHJ solar cells and efficient exciton dissociation have been previously discussed in 2.9.1. Improved crystallinity in the donor phase would ensure efficient exciton generation (Milhailetchi et al. 2006). D/A phase separations have a significant impact on exciton dissociations and subsequently charge carrier generations (Tvingstedt et al. 2009; Guo et al. 2010). Whilst the peak optical

absorption intensity of the PCBM has little to do with the current density, its cluster formation i.e. size, distribution, orientations, etc., may or may not result in more efficient exciton dissociation. Therefore exciton generation rate and dissociation probability at D/A interfaces as a function of thermal annealing must be investigated to support this idea.

6.3.2.1 Analysis of G_{max} and $P(T, E)$

A double logarithmic plot of photocurrent ($J_{ph} = J_{light} - J_{dark}$) versus the effective applied voltage (V_0-V) is presented in Figure 6.6, where V_0 is the bias at $J_{light} = J_{dark}$.

The maximum generation rates, G_{max} is given as $J_{sat} = qG_{max}d$, where J_{sat} is the saturation current density, q is the electronic charge and d is the device active layer thickness. In the low effective field region (V_0-V < 0.1V), J_{ph} is observed to increase linearly with voltage (see Figure 6.6). A similar behaviour has also been previously reported (Milhailetchi et al. 2006). It is also evident that at a higher reverse electric field (V_0-V >1V), J_{ph} saturates. This is indicated as the saturation region in Figure 6.6. Assuming at this region, all the excitons (electron – hole pairs) have dissociated to the respective electronic charges and taking the active layer device thickness as 150nm, G_{max} was deduced for as casted and after gradual thermal annealing up to 175°C. Only a certain fraction of photogenerated excitons will dissociate into free charges with the probability, $P(T, E)$, at any given electric field (Shrotriya et al. 2006). Generation of free charge carriers $G(T, E)$ is very much dependent on both temperature and electric field (Mihailetchi et al. 2006) and is given by

$$G(T,E) = G_{max} P(T,E) \tag{6.1}$$

The probability of exciton dissociation can also be obtained given that:

$$J_{ph} = eG_{max}P(T,E)d \tag{6.2}$$

Using equations 6.1 and 6.2, G_{max} and $P(T, E)$ were determined from experimental results. The summary of the exciton generation rates, probability of exciton dissociation at $V = V_0$ as a function of thermal annealing are included in Table 6.3. As can be seen the exciton generation rate increases with annealing temperatures up to 150°C. It follows the same trend as J_{SC} and furthermore the onset of its deterioration correlates well with the observed reduction in short circuit current density. The increase in exciton generation rates presented in Table 5.6 further verifies the interpretation of the increase in optical absorption of P3HT as a result of recrystallization (see Figure 5.5). It is also important to point out that the probability

of exciton dissociation at $V = V_0$ remains almost constant at ~ 80% in response to increasing annealing temperatures of up to 75°C.

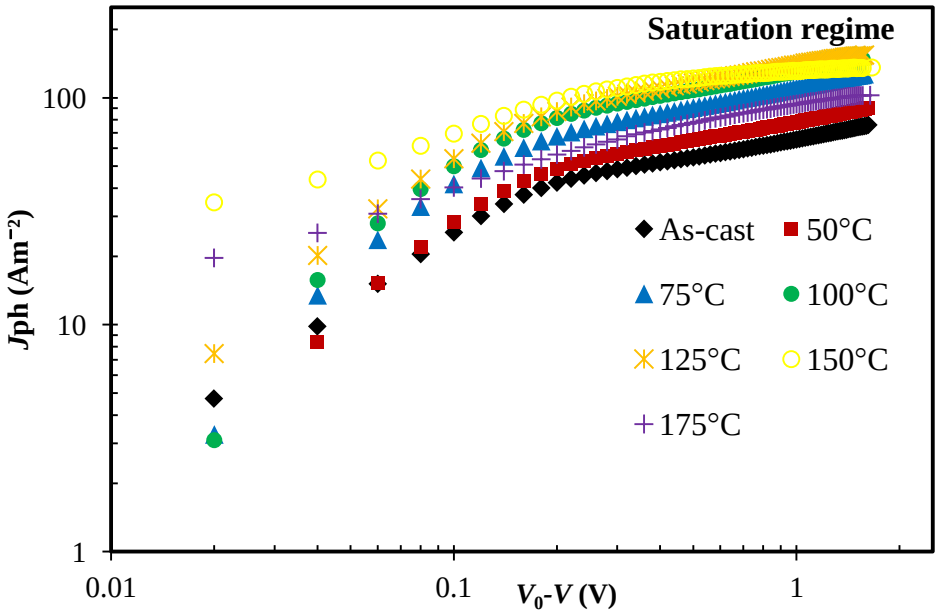

Figure 6.6: Double logarithmic plot of photocurrent ($J_{ph} = J_{light} - J_{dark}$) versus effective applied voltage (V_0-V) for P3HT: PCBM devices (active layer thickness ~ 150 nm) gradually annealed from 50°C to 175°C in steps of 25°C, for 10 min each.

This is in contrast to the observed increase in short circuit current density with thermal annealing. Above 100°C dissociation probability increases to 93% at 140°C, above which both V_{oc} and J_{SC} increases with thermal annealing, whilst exciton probability reduces, indicating that not all the excitons dissociated have successfully been collected.

Figure 6.7 summarises the correlation of the short circuit current density and maximum exciton generation rates of the BHJ device, as a function of thermal annealing.

6.3.3 Influence of nanomorphology and charge carrier mobility in P3HT: PCBM BHJ solar cell

Whilst there have been extensive research based on the P3HT: PCBM BHJ solar cell (Campoy-Quiles et al. 2008; Chen et al. 2010; Kalita et al. 2010; Nalwa et al. 2011), no breakthrough in PCEs above 10% has yet been realised. As previously highlighted in Chapter 1, the external quantum efficiency, given by $\eta = \eta_A \eta_D \eta_{CT} \eta_{CC}$ (Forrest, 2005), is a product of four efficiencies, namely: η_A the efficiency associated with photon absorption, η_D efficiency

associated with exciton dissociation, η_{CT} efficiency associated with charge transfer and η_{CC} that associated with charge collections at respective electrodes. Enhancing η_A is significantly material – dependent (Forrest, 2005).

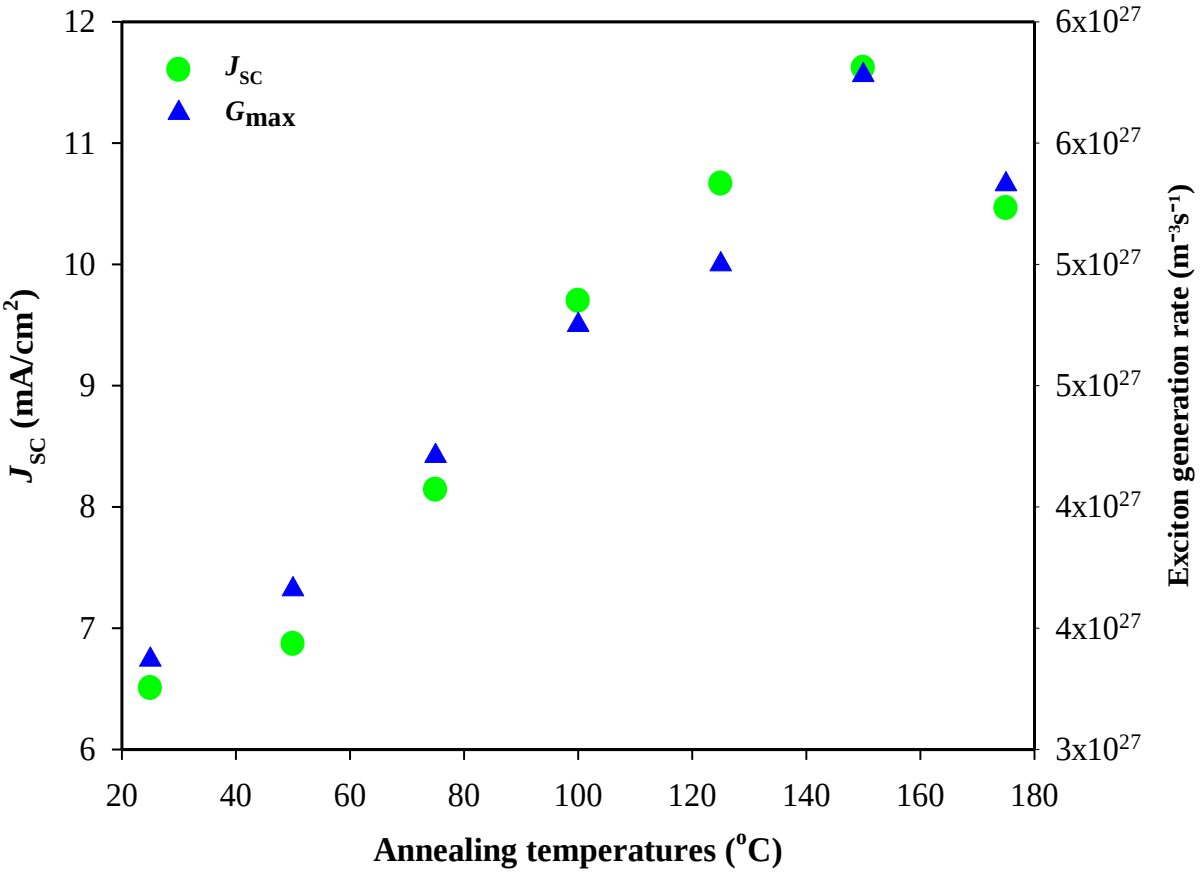

Figure 6.7: Short circuit current density, J_{SC}, and the maximum exciton generation rate (G_{max}) of P3HT: PCBM device, as-cast and as a function of thermal annealing temperature.

P3HT is known to have a relatively high degree of crystallinity and absorption extending in the region of 650 nm of the solar spectrum (Shrotriya et al, 2005; Erb et al, 2006). In addition, it also possesses suitable electronic band gap favouring efficient charge transfer (Scharber & Sariciftci, 2013). When considering η_D and η_{CC}, again material choice is a significant factor, as the difference in their LUMOs is somewhat critical to efficient exciton dissociation and also charge transport properties of the blended materials. Furthermore D/A interfaces, transport pathways (within the bulk of the active layer) to the respective electrodes, charge carrier mobilities, loss mechanisms via recombination etc. all have an impact on the overall device's PCEs (Hoppe et al, 2004; Koster et al, 2006; Milhailetchi et al,

2006; Kim et al, 2007; Pivrikas et al, 2011). Owing to the influence of the bulk morphology of these blends, PCEs can remarkably improve upon subjecting the device to various physical and chemical processes (Peet et al, 2007; Miller et al, 2008; Zhuo et al, 2011; Sun et al, 2013). In the previous section, investigations on PCBM cluster formation resulting from different thermal annealing strategies and its impact on photocurrent generation were discussed. Nano-structuring of the photo active layer (due to PCBM cluster formation) significantly influences charge carrier mobilities, charge separation and recombination processes, all of which have a direct impact on PCEs. It is known that the charge carrier mobilities enhances exciton dissociations and charge carrier recombination which are both believed to be a competing process (Clarke & Durrant, 2010). This parameter can improve or deteriorate upon thermal annealing. To also address the influence of trap density on charge carrier mobility, this case study was designed with a suggested range of thermal annealing temperatures above the glass transition temperature of P3HT, for which this phenomenon was studied. It is widely suggested that the best device efficiency reported for P3HT: PCBM blend is at the annealing temperature in the range of ~140 – 150°C (Kim et al, 2005); which is consistent with results reported here in the previous sections. However, thermal annealing at this temperature results in restructuring of nanodomains which consequently has a direct impact on exciton dissociation as well as recombination processes, as a consequence of overall changes in the polymer/fullerene interfaces. The case study herein therefore is focused on the effects of thermal annealing on transport properties of solar cell devices based on blended materials (P3HT: PCBM) as well as probing and establishing the processes that impact recombination mechanisms. In the following subsections, the nanomorphology-bulk transport property relationship and impact of thermal annealing will be discussed in details.

6.3.3.1 Implications of thermal annealing on the bulk network transport properties

The materials and methods for the fabrication of OSC are the same as outlined previously in section 6.3.2. In addition, single charge carrier devices, i.e., hole – and electron – only devices were fabricated, following a similar procedure for OSCs (although using charge blocking layers accordingly). Details of the fabrication of these devices can be found in section 4.4.1.1, where the corresponding device structures are depicted in Figure 4.16. In addition the energy band diagram representations of these devices are shown in Figure 6.8. The measured dark current density – voltage characteristics of the hole – and electron – only devices are shown in Figure 6.9.

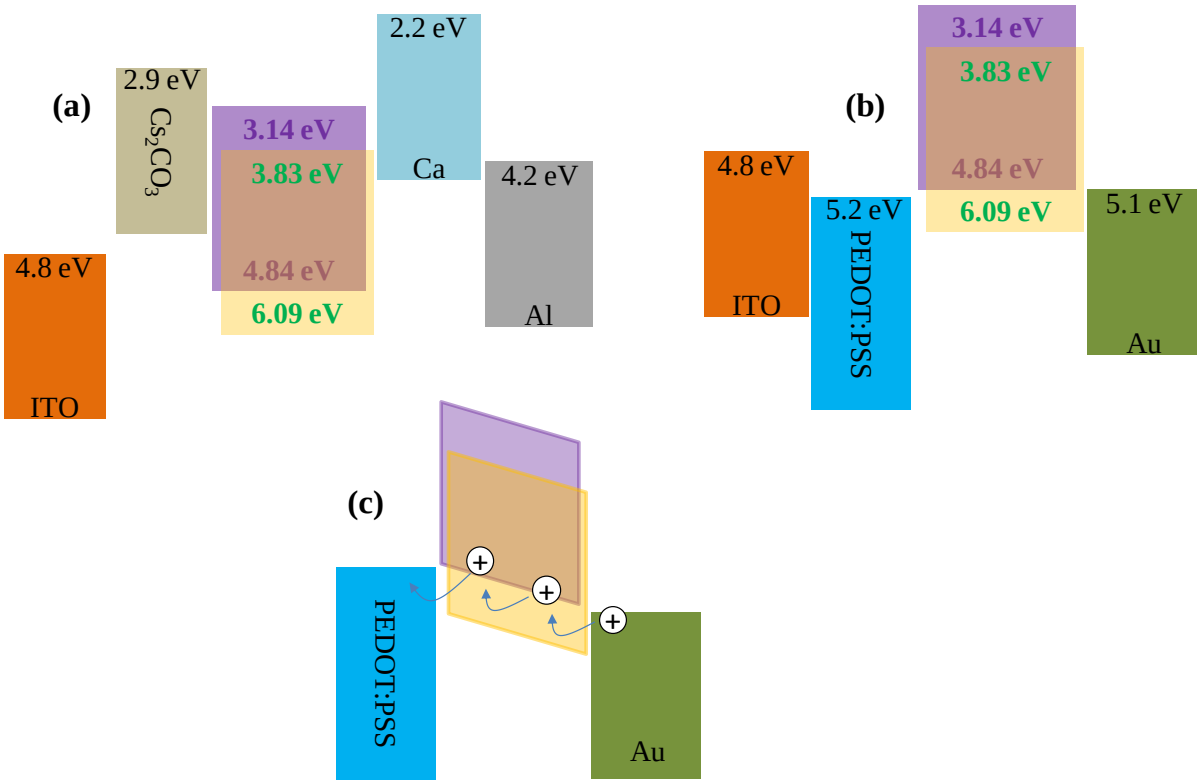

Figure 6.8: Energy band diagrams of (a) electron – only device, (b) hole – only device. (c) Energy band diagram of hole – only device in reverse bias showing hole injection.

Upon positively biasing Au contact with respect to PEDOT: PSS, there is no potential barrier and holes are injected from Au into the highest occupied molecular orbital (HOMO) of P3HT (reverse bias condition) (see Figure 6.8 (c)). In the voltage range of 0.2V $< V_{eff} <$ 0.7V (V_{eff} being the applied bias corrected for the built-in potential arising from the difference between the work-function of contacts).

It was found that the current density–voltage property obeys Ohm's law (see equation 2.7). At higher effective applied field 3.5V $< V_{eff} <$ 4.4V the current density – voltage relationship was observed to depart from Ohmic behaviour and followed the space charge limited current (SCLC) behaviour (see equation 2.8). For P3HT: PCBM blend film, the dielectric constant was assumed to ~3.4 in equation 2.8, and thickness of the active was measured to be ~150 nm. Using the slope corresponding to the square law in Figure 6.9 (a) and appropriate parameters, equation 2.8 yields a value of the hole mobility for as cast device as μ_h = 1.15×10^{-9} m^2 V^{-1} s^{-1}. This is in close agreement with reported data for this parameter (Shrotriya et al, 2006; Nalwa et al, 2011).

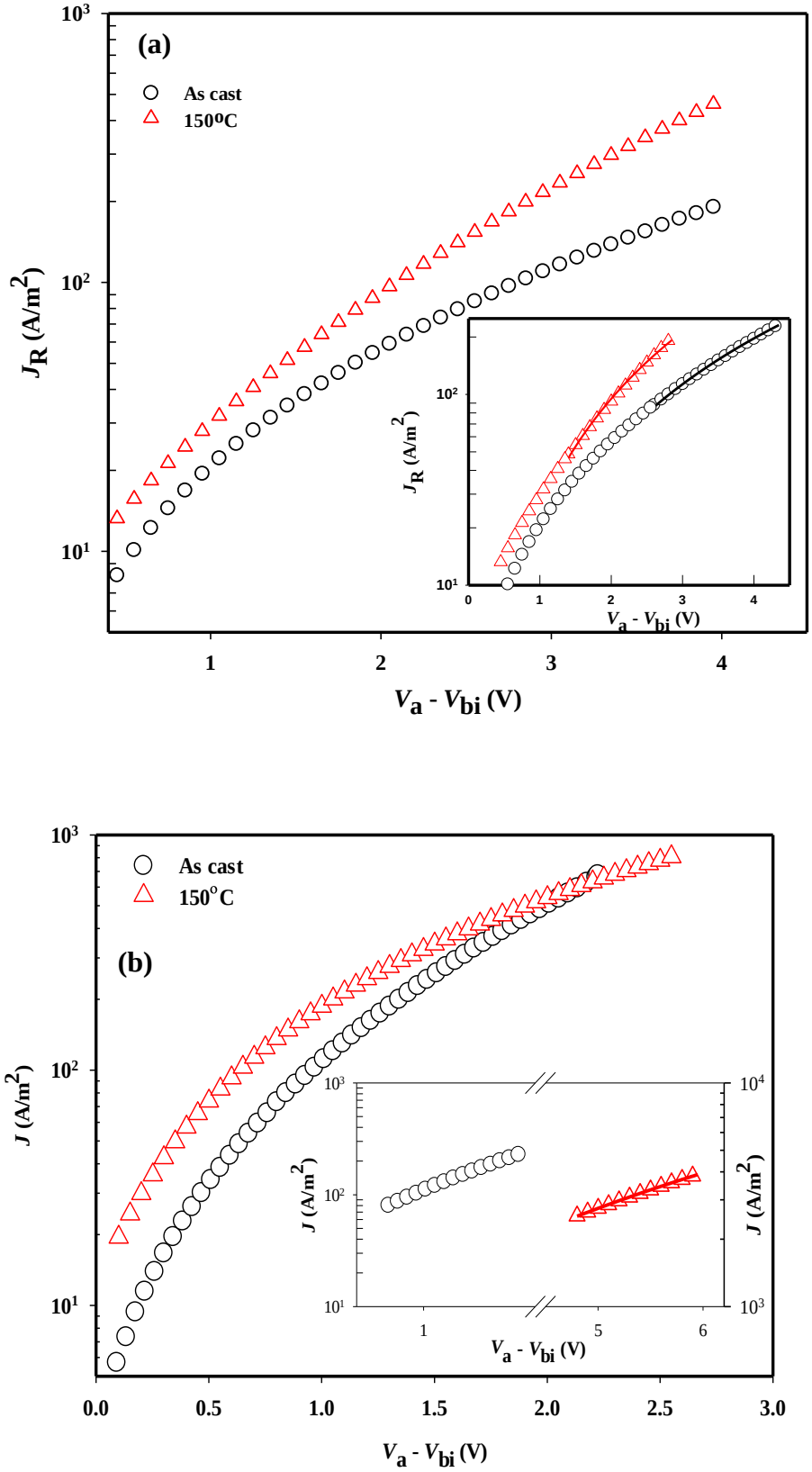

Figure 6.9: Dark *J* – *V* plots of P3HT: PCBM based single charge carrier devices; (a) hole – only (reverse biased) and (b) electron – only. The insets show the best fits (solid lines) of the experimental data to the SCLC model.

Similarly the Ohmic region of Figure 6.9 (a) together with appropriate parameters in equation 2.7 leads to a hole carrier concentration of $1.49\times10^{22}\mathrm{m}^{-3}$ which is of the same order of magnitude reported in the literature (Nalwa et al, 2011).

It was noted that at higher applied field V_{eff} > 5V, the current density-voltage relationship is indicative of trap-filling states associated with exponent greater than 2 namely power law (Lampert & Mark, 1970), which is given by:

$$J = \left(\frac{\mu_{e(h)}N_{\mathrm{CV}}}{q}\right)\left(\frac{\varepsilon_0\varepsilon_r}{N_{T_{e(h)}}}\frac{1}{l+1}\right)^{l}\left(\frac{2l+1}{l+1}\right)^{l+1}\frac{V^{l+1}}{d^{2l+1}} \tag{6.3}$$

where N_{CV} is the effective density of states in the conduction or valence band, $N_{T_{e(h)}}$ is the trap density for electrons (holes). Employing equation 6.3 yields N_{T_h} of $2.98\times10^{25}\mathrm{m}^{-3}$, for as cast device.

Similarly, for electron mobility measurements, the range corresponding to the trap filled SCLC regime (0.842V<V_{eff}<1.43V) yields a value of electron mobility, μ_e =1.1x10^{-8} m^{2}V^{-1}s^{-1}. For the sake of clarity the voltage regions for which the parameters are extracted have been included in Table 6.4. It is worth noting that the Ohmic region for both electron – and hole – only devices are in the range 0-1 V whereas for space charge limited conductivity the range varies, suggesting the influence of associated deep or shallow trap levels within the bulk material (Nam et al, 2009). The region associated with higher exponents is analysed using equation 6.3 for exponential trap distribution. Initially the hole mobility reduces upon thermal annealing as is evident from Table 6.4. However above 50°C it is observed that it begins to increase, with its maximum value measured at 175°C. Mihailetchi et al (2006) have previously reported a similar observation of an increase in the hole mobility in the P3HT phase upon thermal annealing, with mobility values consistent with values measured in pristine P3HT (~10^{-8} m^{2}V^{-1}s^{-1}), i.e., in the absence of PCBM molecules. According to the work of Yang and co-workers (2005), it can suggested that at such high temperatures as shown here, the crystallization of P3HT would have occurred thus resulting in the measured enhanced transport of holes. However in the case of the electron mobility, a reduction in this property at annealing temperature above 150°C was measured. The reason for this is somewhat unclear at this stage, although it maybe suggested that this might be due to the increased formation of PCBM aggregates, and also the extensive depletion regions around them, previously shown in Figure 5.7 (c).

Table 6.4: Summary of parameters determined from experimental data.

	As cast	**50°C**	**100°C**	**125°C**	**150°C**	**175°C**
μ_h ($m^2V^{-1}s^{-1}$)	$1.15x10^{-9}$	$6.68x10^{-10}$	$8.53x10^{-10}$	$2.14x10^{-9}$	$2.30x10^{-9}$	$1.06x10^{-8}$
μ_e ($m^2V^{-1}s^{-1}$)	$1.1x10^{-8}$	$5.93x10^{-9}$	$8.51x10^{-9}$	$1.31x10^{-8}$	$1.1x10^{-8}$	$3.78x10^{-9}$
μ_e/μ_h	9.56	8.88	9.98	6.12	4.78	0.357
n (m^{-3})	$4.9x10^{21}$	$4.74x10^{21}$	$7.09x10^{22}$	$6.37x10^{22}$	$6.05x10^{22}$	$2.65x10^{21}$
p (m^{-3})	$1.49\ x10^{22}$	$1.06x10^{22}$	$9.68x10^{21}$	$1.08x10^{22}$	$1.17x10^{22}$	$6.22x10^{22}$
N_{Th} (m^{-3})	$2.98x10^{25}$	$6.79x10^{24}$	$2.22x10^{24}$	$7.72x10^{24}$	$1.36x10^{23}$	$1.14x10^{26}$
N_{Te} (m^{-3})	$2.51x10^{24}$	$6.76x10^{24}$	$2.54x10^{26}$	$3.79x10^{26}$	$1.14x10^{26}$	$4.30x10^{24}$
Ohmic region* (V)	0.20-0.70	0.25-0.60	0.35-0.80	0.45-0.95	0.45-0.95	0.50-1.00
SCLC region* (V)	3.45-4.35	1.85-3.00	1.25-2.20	1.45-2.45	1.70-2.40	2.30-3.15
Trap-limited region* (V)	5.25-6.75	5.00-6.15	4.50-5.95	3.00-6.45	4.60-6.90	3.50-6.45
Ohmic region† (V)	0.10-0.43	0.1-0.39	0.15-0.38	0.10-0.70	0.15-0.65	0.10-0.55
SCLC region† (V)	0.84-1.43	0.78-1.21	2.00-2.48	2.80-3.90	4.80-5.95	1.88-2.72
Trap-limited region† (V)	1.51-2.22	1.76-2.21	2.48-2.73	3.85-4.45	5.80-6.45	3.13-4.13

Voltage ranges: * Hole – only devices, † Electron – only devices.

In other words, at very high annealing temperatures (i.e., above 150°C), the resulting change in morphology, with its corresponding phase separation characterised by highly isolated PCBM aggregates (in this study) was noted to have not facilitated electron transport.

It is known that the charge transport in organic semiconductors is mainly due to hopping mechanism from site to site (Peter, 2009). The increased separation between isolated clusters as shown in Figure 5.7 (c) may impede the hopping mechanism. Therefore this probably could explain the reduction in the electron mobility as measured in this study. In addition,

the maximum PCE for devices in this study was measured after thermal annealing at 150°C and upon increasing the annealing temperature to 175°C, a reduction in this parameter is observed (see Table 6.3).

At 150°C where the maximum PCE was measured, the ratio of electron to hole mobility (μ_e/μ_h) was determined to be 4.78 (see Table 6.4). This observed trend where μ_e/μ_h reduces with thermal annealing is consistent with previous works (Li et al. 2005; Shrotriya et al. 2006), suggesting an improved balance in carrier transport is advantageous for PCE improvement. However, after thermal annealing at 175°C, a lesser than unity for this ratio ($\mu_e/\mu_h \sim 0.357$) was measured. It is suspected here that the reason for this may be due to the disruption of electron transport pathways to the respective electrode as a result of an undesirable clustering of PCBM molecule, leading to lower electron mobility.

Exciton dissociation and recombination (either bimolecular or germinate), are competing processes which increases as a result of improved charge carrier mobilities (Clarke & Durrant, 2010). Due to the nature of fast charge transfer, which is prior to exciton dissociation, it was found that the PL measurements (section 5.2.2) are unable to adequately probe recombination processes. Because of this the nature of the relationship between exciton dissociation and recombination processes will be further explored in the following section.

6.3.4 Exciton Dissociation and Recombination Mechanisms

Excitons created as a result of absorption of photons by polymer phase, may or may not result in dissociation of free charge carriers depending on the probability that these bound electron – hole pairs overcome their columbic attraction given by the capture radius proposed by Onsager (Onsager, 1938). The expression for the capture radius is given in equation 2.18. Due to low values of ε_r associated with organic semiconductors; the capture radius is relatively larger than their inorganic counterparts. Furthermore this model suggests that a hot electron will impart its thermal energy by rapid motion settling at a distance *a*, from the hole, known as the thermalization length. The values of *a* calculated on the basis of Onsager model is around 2.5 – 3.5 nm which is larger than expected for nearest neighbouring charge transfer states (1nm) (Clarke & Durrant, 2010). Taking into account the relatively larger values of thermalization lengths, Braun (1983) modified the Onsager's model with the view that charge transfer states have a finite life time τ_{CT} which depends on the two competing mechanisms of dissociation and recombination as given by equation 2.20. The details of the modification of Onsager's model have been discussed in section 2.9.1.1. It follows that the probability of

exciton dissociation is dependent on the dissociation rate constant k_d and the rate constant k_f associated with geminate recombination rate back to the ground state.

It is important to note that when $k_d >> k_f$, the probability approaches unity and the charge transfer state life time is described by the dissociation rate, while on the other hand when $k_f >> k_d$ the probability approaches zero and the charge transfer states life time will approach the geminate recombination life time back to the ground state. The dissociation rate k_d can be evaluated from the expression given in equation 2.21. k_r in equation 2.21 is the recombination constant. This could either be equivalent to Langevin recombination (discussed in section 2.9.2) or trap assisted recombination (Schokley & Read, 1952).

To investigate the impact of recombination mechanisms, first the Braun's modified model is estimated on the basis of Langevin recombination (B_L). B_L can be expressed as (Kuik et al. 2011);

$$B_L = \frac{\langle \mu \rangle q}{\varepsilon_r \varepsilon_0} \tag{6.4}$$

,where $\langle \mu \rangle$ is the average sum of the electron and hole mobilities.

Using the calculated values of electron and hole mobilities in section 6.3.3.1, the rate constant, k_f associated with germinate recombination to the ground state was found to be $1.0\times10^4 s^{-1}$, with $B_L = 6.11\times10^{-18}\mathrm{m^3s^{-1}}$ respectively. These results are consistent with the report of Koster and co-workers (2006). Following the thermal annealing at 150°C however, k_f increases to $2.0\times10^4 s^{-1}$ ($B_L = 1.22\times10^{-17}\mathrm{m^3s^{-1}}$). This parameter continued to increase (i.e., $k_f = 8.0\times10^4 s^{-1}$, where $B_L = 5.64\times10^{-17}\mathrm{m^3s^{-1}}$), after thermal annealing at 175°C. It is suggested here that this measured increase in the decay rate is attributed to the increase in hole carrier mobility, resulting in a higher value of Langevin constant B_L and faster geminate recombination back to the ground state. This will therefore be reflected in a shorter charge transfer state life time.

On the other hand, if one assumes only bimolecular recombination mechanism, on the basis of trap –assisted (or Shockley Read Hall) recombination model, expressed as

$$B_{\mathrm{SRH}} = \frac{C_n C_p N_{T_e}}{\left[C_n (n + n_1) + C_p (p + p_1) \right]} \tag{6.5}$$

where C_n is defined as the probability per unit time that an electron in PCBM phase is captured by an empty trap. Similarly C_p is defined as the probability per unit time that a hole is captured by an electron – occupied trap site, N_{T_e} is the density of the electron traps, n and p are the electron and hole density in the conduction and valence band respectively, and $n_1p_1=n_i^2$ the intrinsic carrier concentrations. Since intrinsic carrier concentrations are much lower than electron and hole densities, equation 6.5 can therefore be reduced to

$$B_{\mathrm{SRH}} = \frac{C_n C_p N_{T_e}}{\left[C_n(n) + C_p(p)\right]} \tag{6.6}$$

Assuming $C_n = C_p$, equation 6.6 can be further simplified as

$$B_{\mathrm{SRH}} = \frac{C_n N_{T_e}}{[n+p]} \tag{6.7}$$

Figure 6.10 shows the plot of experimental photocurrent versus the effective reverse applied voltage; for as cast and after thermal annealing at 150°C. Included in these plots are calculated photocurrents incorporating either Langevin (B_L) or SRH (B_{SRH}) recombination models. The data in Table 6.4 were used, and the value of C_n was assumed to be $1.6\times10^{-18}\mathrm{m^3s^{-1}}$. Equation 6.7 yields a B_{SRH} value of $2.0\times10^{-16}\mathrm{m^3s^{-1}}$, with a computed k_f of $2.3\times10^{5}s^{-1}$ for as cast device. Whereas after thermal annealing at 150°C, B_{SRH} was calculated to be $2.5\times10^{-15}\mathrm{m^3s^{-1}}$, with a corresponding $k_f = 2.0\times10^{6}\,s^{-1}$ respectively.

The higher recombination constant B_{SRH} in comparison to B_{L} is an indication that the trap assisted recombination is dominant in comparison to its Langevin counterpart. The highest PCEs measured in the present work correspond to a thermal annealing at 150°C. Therefore on the basis of this, a lower recombination rate should be expected. On the contrary this is not so, as the results indicates higher recombination constant with higher geminate recombination rate back to the ground state k_f. Referring again to Table 6.4 it is noticed that the trap concentration has increased by almost 2 orders of magnitude which resulted in a higher value of B_{SRH}. However, the improved μ_e/μ_h ratio upon thermal annealing plays an important role in charge transport to the respective electrodes, hence improving PCE. In order to further verify the dominant process considered above, the relationship between light intensity and open circuit voltage (V_{OC}) given by Koster et al. (2006), is explored.

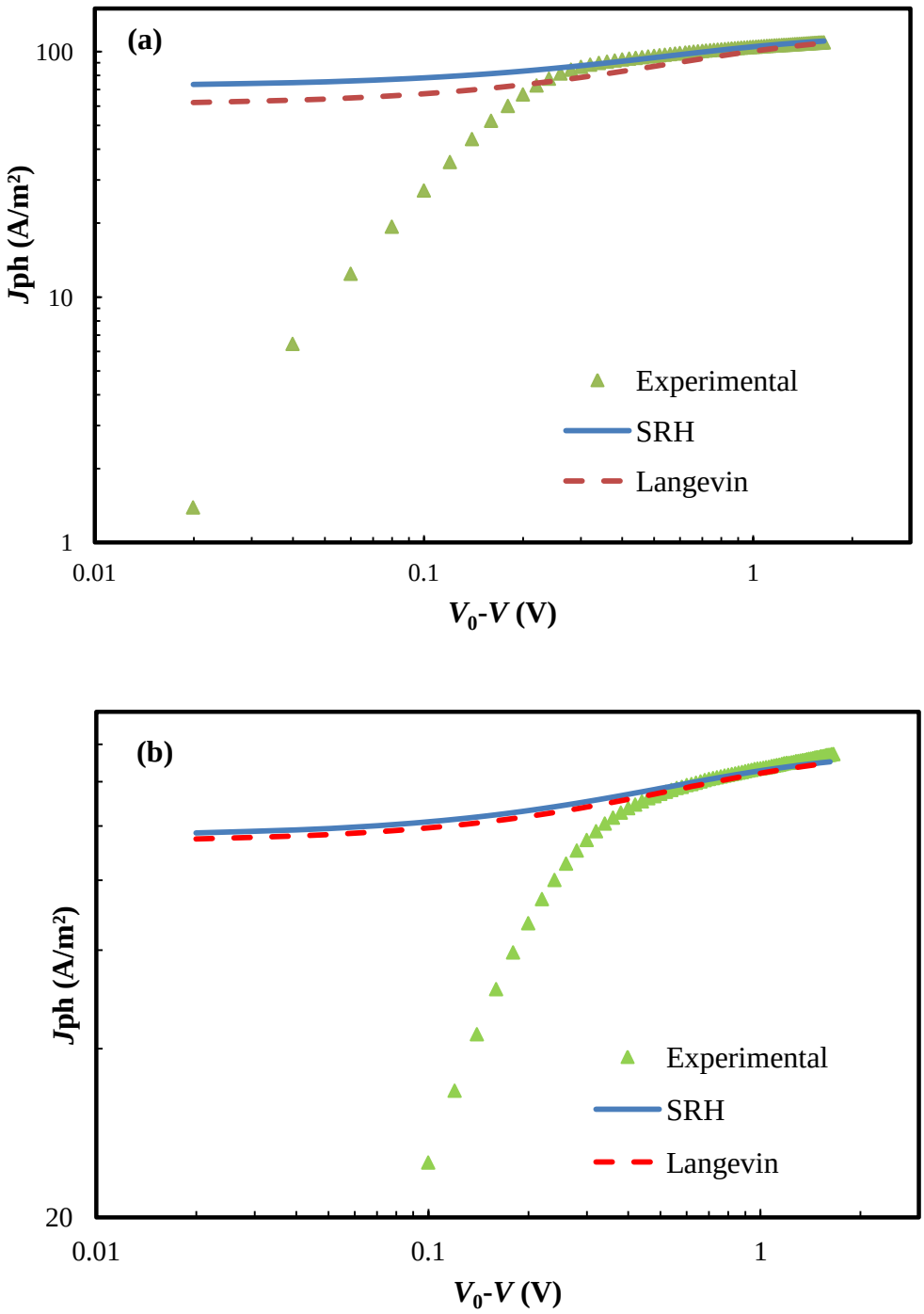

Figure 6.10: Photocurrent density (J_{ph}) as a function of effective reverse applied voltage (V_0-V) for P3HT: PCBM based solar cell device; (a) as-cast and (b) after thermal annealing at 150°C. The solid lines represent numerical calculations based on Shockley-Read-Hall (blue), and Langevin (broken, red) recombination.

Refer to 2.9.2.1 for details of discussions on the relation between V_{OC} and light intensity. From equation 2.27, the energy gap, E_{gap} is taken to be the difference between the LUMO and

HOMO levels of PCBM and P3HT. In the event were traps are absent in the bulk of the active layer, equation 2.27 holds with a slope, S, equalling k_BT/q (eV), when V_{OC} is plotted as a function of the logarithm of light intensity. It has been shown that values of S higher than k_BT/q is indicative of a trap-assisted recombination mechanism (Kwuik et al. 2011). Thus a measured increase in this quantity is considered to be evidence of an increase in the strength of the trap-assisted recombination. To perform the voltage dependence on light intensity measurements, illumination intensity of the solar simulator was varied by varying the power output of the lamp's power supply. The intensity of the illumination was checked every time before each measurement with a calibrated Si reference solar cell and meter (Newport and Oriel Instruments). Figure 6.11 shows a semi log plot of V_{OC} versus the light intensity.

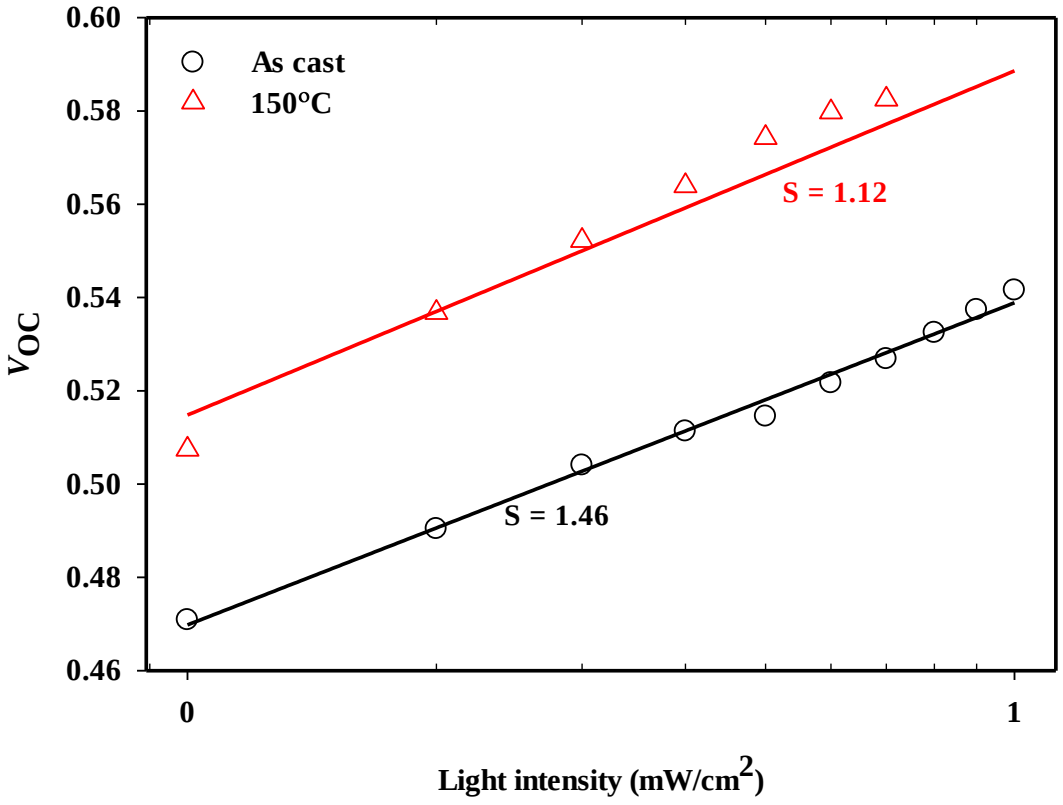

Figure 6.11: V_{OC} as a function of light intensity for P3HT: PCBM based solar cell device; as-cast and annealed at 150°C, solid lines are linear fits used to determine the slopes.

As is evident, the slope of 1.12 (k_BT/q) is indicative of trap assisted recombination. Upon thermal annealing at 150°C the value of this slope increased to 1.46 (k_BT/q) indicating an increase in the strength of the trap assisted recombination. This is consistent with the calculated increase in trap density presented in see Table 6.4.

6.3.5 Recombination Losses: Impact of PCBM weight ratio

In section 5.2.1, the compositional studies of BHJ active layers based on P3HT: PCBM for organic solar cells were presented. In that section, optical absorption spectroscopy was employed to elucidate the nature the PCBM molecular clustering as a function of both composition and thermal annealing.

Herein in this section, for didactic purposes, 50 and 37.5 wt% PCBM content in the blend film are being considered. Single charge carrier devices, i.e., hole – and electron – only, were employed in order to measure their respective charge carrier mobilities. The impact of composition on bimolecular recombination for the two different percentage weights of PCBM has been investigated and is presented here.

The comparison between these two systems mentioned above under thermal annealing conditions is also of interest. It has already been established from the foregoing that thermal annealing induces a nano-restructuring of the morphology of the active layer bulk. This restructuring in turn have an effect on the D/A interface separation, which also influences the efficiencies of exciton dissociation. Depending on whether an optimised network within the bulk is achieved as a result of thermal annealing, charge transport and collection at the respective electrodes are influenced. It has been shown that the charge carriers' mobility is a significant factor in the estimation of bimolecular recombination (Koster et al, 2006, Oklobia & Shafai, 2014). The desired highly efficient organic solar cell would be one with recombination at the very minimum, therefore allowing for efficient and maximum collection of charges at the respective electrodes. The investigations presented in this section seek to probe the effect of PCBM content on charge carrier mobilities and its impact on bimolecular recombination and PCEs as well. All fabrications of thin films and devices for direct current measurements were done following the same methods described previously in section 4.2.2. The structure of the fabricated single charge carrier devices are as illustrated in Figure 4.17.

Referring again to the optical absorption spectroscopy results in Figure 5.5, to provide a backdrop for the ongoing discussion, with emphasis on 1:1 and 1:0.6 ratios, for: as cast and after thermal annealing at 175°C. 175°C in particular was chosen for the purposes of clarity. As previously highlighted, the increase in peak absorption intensity (see Figure 5.5) may translate to an improvement in the current density. The trend showed by the absorption spectra associated with PCBM is also believed to have some bearing on the nature of the internal nanostructuring within the photoactive layer bulk. Both of these were regarded as a

function of PCBM content and thermal annealing approaches. These observations together with the optical microscopy images (Figure 5.7) strongly support this idea.

The variation in the bulk re-structuring evidenced in optical absorption spectroscopy results is expected to have some degree of impact on charge carrier mobility in devices based on the two blend ratios. In addition, it is also of interest to investigate the nature of losses via recombination in these two systems. Firstly, to study the impact of recombination losses in these systems, the method of measuring the photocurrent generation as was employed in section 6.3.2.1 is similarly adapted here. Shown in Figure 6.12 are the photocurrents (J_{ph}) as a function of the effective applied bias (V_{eff}) under illumination, for P3HT: PCBM (1:1 and 1:0.6) blend ratios (after thermal annealing at 175°C). Using $J_{sat} = eG_{max}d$ also, the maximum generation rates were found to be 5.33×10^{27} $m^{-3}s^{-1}$ and 4.54×10^{27} $m^{-3}s^{-1}$, for 1:1 and 1:0.6 P3HT: PCBM blend ratios respectively.

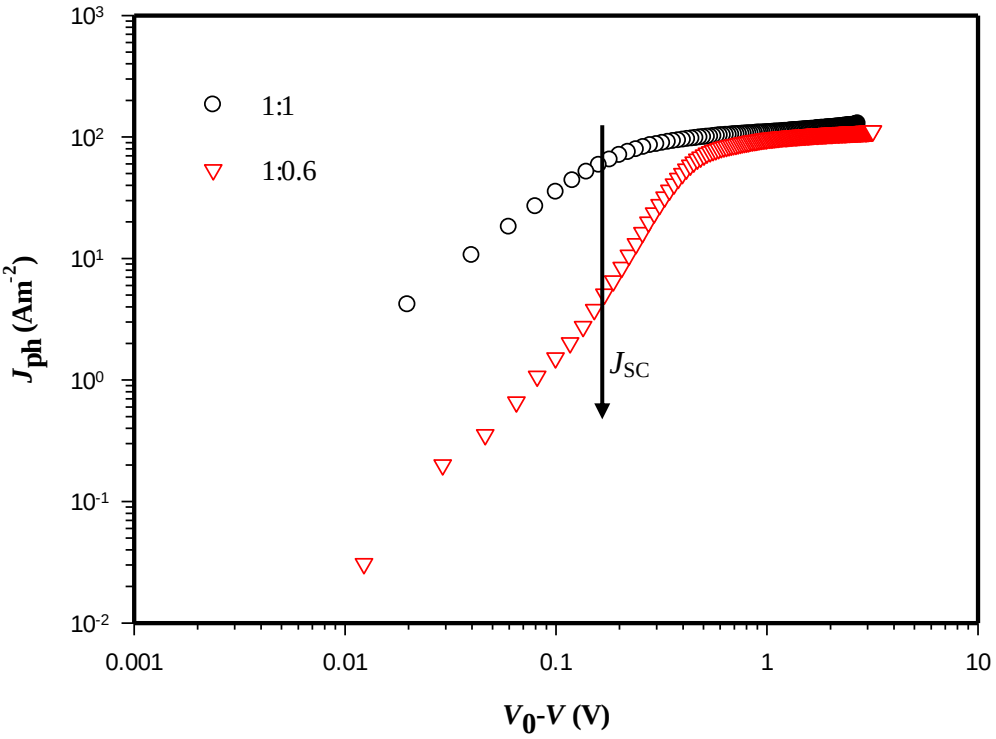

Figure 6.12: Measured photocurrents as a function of effective applied voltage bias for 1:1 (black open circles) and 1:0.6 (red open triangles), after thermal annealing at 175°C.

When the PCBM content was increased from 37.4% (in 1:0.6) to 50% (in 1:1), the maximum generation rates was determined to increase by 15%. A somewhat similar observation was

made by Shrotriya and co-workers (2006). In their work, they compared maximum generation rates between 'fast' and 'slow' grown films. It was reported that the slow grown films which had an increased absorption in the active layer yielded a much higher maximum generation rate. By comparing the probabilities of excitons dissociated at short circuit conditions ($V_{eff} = V_0$), and at the maximum power output point (at $V_{eff} = V_{max}$), it is possible to gain some qualitative insight into the role of recombination. At $V_{eff} = V_0$, about 82% of the total photogenerated *e-h* pairs dissociate to free charges in the case of 1:1. This was further reduced to 75.4% at the maximum power output point (V = 0.44V). Similarly for the blend ratio of 1:0.6, about 78% of the total photogenerated *e-h* pair dissociate to free charges. This however was significantly reduced to 23% at maximum power point (V = 0.25V). According to the work of Shrotriya et al. (2006), these values suggest that there is a higher loss due to recombination in the devices based on 1:0.6 ratio, since more than half of the photogenerated *e-h* pairs are lost. This could probably be the reason for the reduction in short circuit current density measured in this device after thermal annealing at 175°C (see Table 6.1).

6.3.5.1 Investigation of Recombination rates

Figure 6.13 shows the dark current density – voltage characteristics for both an electron – and hole – only device, based on P3HT: PCBM bulk heterojunction with blend ratios of 1:1 and 1:0.6.

At low applied effective voltage, the current density – voltage (J – V) relations similarly obeyed the Ohm's law, following the relationship given by equation 2.7. According to the same procedure as previously described, at higher effective applied voltage J – V relationship departs from Ohmic behaviour and is consistent with the SCLC behaviour (equation 2.8). By fitting the dark J – V curves to SCLC model for single charge carrier devices, the electron and hole mobilities were measured for P3HT: PCBM (1:1 and 1:0.6). The results, including calculated bimolecular recombination constants and recombination rates respectively are summarised in Table 6.5.

Having calculated the charge carrier mobilities, the electron and hole density can be determined using the slope of the Ohmic region together with values of the parameters in equation 2.7. B_L was similarly calculated according to previously discussed method, using equation 6.4. The recombination rates, R_L in Table 6.5 were calculated using the relationship expressed in the following equation.

$$R_L = B_L n_{\mathrm{e}}.n_{\mathrm{h}} \tag{6.8}$$

Where n_{e} and n_{h} are the electron and hole charge carrier densities, and B_L is the Langevin (bimolecular) recombination, determined from equation 6.4.

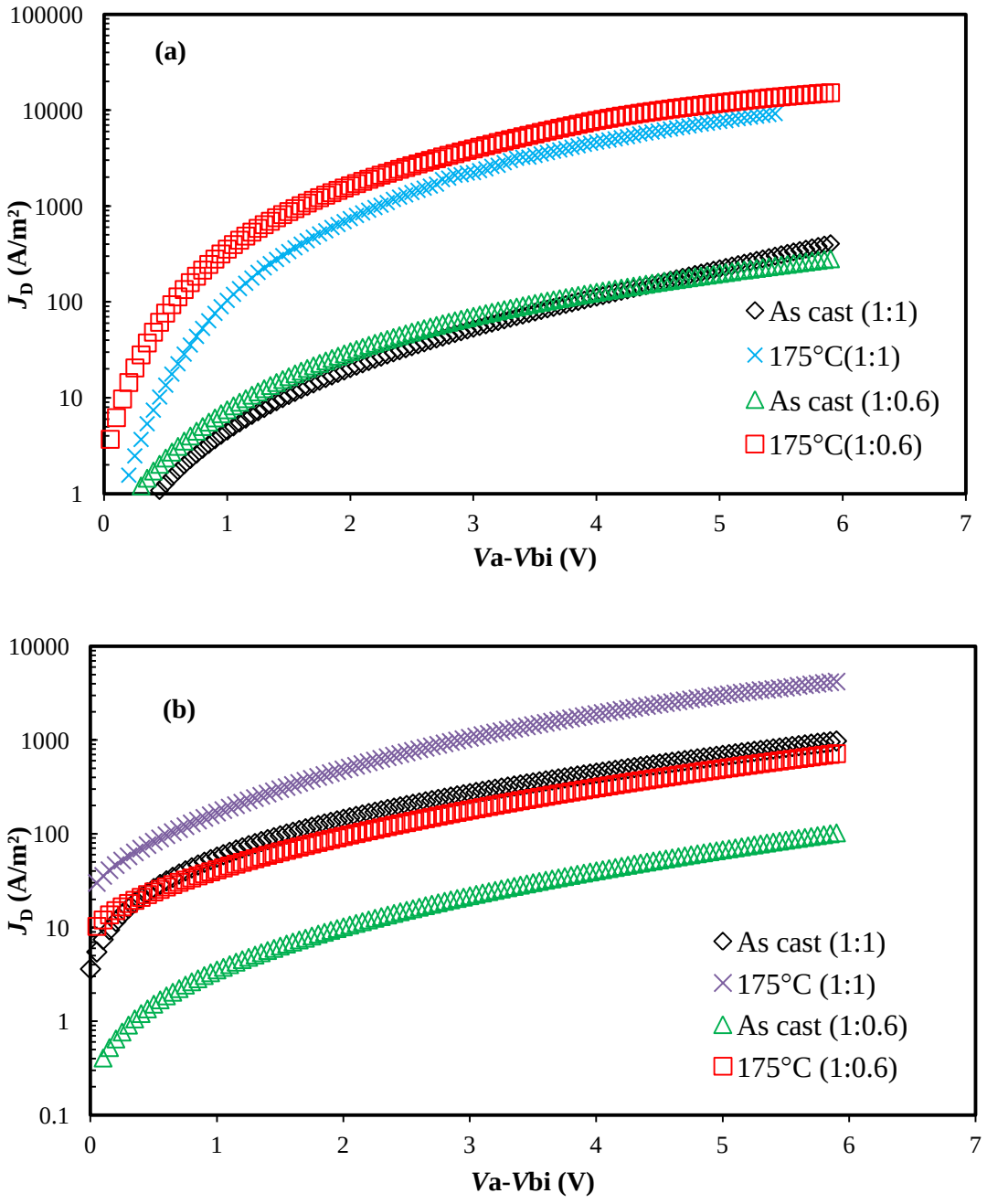

Figure 6.13: Dark *J* – V characteristics for (a) electron – only and (b) hole – only devices based on P3HT: PCBM blend of ratios, 1:1 and 1:0.6; as cast and after annealing at 175°C.

Up to a thermal annealing temperature of 150°C a continuous improvement in electron mobility is observed for both PCBM percentage loadings. However above this temperature

deterioration of this parameter was measured. In the case of the blend ratio 1:1, for hole - only device, the hole mobility tend to remain almost constant up to a temperature of 150°C after which a sharp increase above this temperature is recorded.

Table 6.5: Summary of charge carrier mobilities (μ_e: electron mobility, and μ_h: hole mobility), electron (n_e) and hole (n_h) density, bimolecular recombination constant, B_L, and recombination rate, R_L for P3HT: PCBM solar cells of ratios; (a) 1:1, and (a)1:0.6, as a function of thermal annealing.

(a)	**1:1**					
Temperature	μ_e	μ_h	n_e	n_h	B_L	R_L
As cast	1.46×10^{-9}	1.54×10^{-9}	1.30×10^{21}	3.22×10^{22}	7.77×10^{-18}	3.25×10^{26}
50°C	4.31×10^{-9}	1.33×10^{-9}	4.92×10^{21}	3.12×10^{22}	7.08×10^{-18}	1.09×10^{27}
75°C	3.06×10^{-8}	1.27×10^{-9}	4.38×10^{21}	2.70×10^{22}	6.76×10^{-18}	7.99×10^{26}
100°C	8.96×10^{-8}	1.56×10^{-9}	4.22×10^{21}	2.16×10^{22}	8.30×10^{-18}	7.57×10^{26}
125°C	5.39×10^{-8}	2.59×10^{-9}	2.82×10^{21}	1.69×10^{22}	1.37×10^{-17}	6.53×10^{26}
150°C	5.71×10^{-8}	2.57×10^{-9}	1.42×10^{21}	1.46×10^{22}	1.37×10^{-17}	2.84×10^{26}
175°C	3.98×10^{-8}	9.10×10^{-9}	7.24×10^{20}	1.66×10^{22}	4.84×10^{-17}	5.82×10^{26}

(b)	**1:0.6**					
Temperature	μ_e	μ_h	n_e	n_h	B_L	R_L
As cast	8.39×10^{-10}	4.8×10^{-10}	4.76×10^{21}	1.17×10^{22}	2.55×10^{-18}	1.42×10^{26}
50°C	1.84×10^{-9}	5.31×10^{-10}	6.55×10^{21}	1.15×10^{22}	2.82×10^{-18}	2.12×10^{26}
75°C	1.61×10^{-8}	5.00×10^{-10}	8.56×10^{21}	4.93×10^{22}	2.66×10^{-18}	1.12×10^{27}
100°C	4.38×10^{-8}	6.75×10^{-10}	2.08×10^{22}	7.52×10^{21}	3.59×10^{-18}	5.62×10^{26}
125°C	5.00×10^{-8}	1.72×10^{-9}	7.27×10^{21}	1.07×10^{22}	9.15×10^{-18}	7.12×10^{26}
150°C	3.87×10^{-8}	1.95×10^{-9}	5.29×10^{21}	1.21×10^{22}	1.04×10^{-17}	6.66×10^{26}
175°C	2.96×10^{-8}	3.19×10^{-9}	1.90×10^{21}	1.22×10^{22}	1.70×10^{-17}	3.94×10^{26}

A similar observation for devices based on the blend ratio of 1:0.6 is also observed, although with the onset of this increase being at the lower annealing temperature of 125°C.

As is evident, for devices based on the blend ratio of 1:1 the recombination rates decreases with increasing thermal annealing temperatures up to 150°C. This supports the notion that bimolecular recombination may not have a dominant role to play as compared to the trap assisted recombination, as have been previously shown. In contrast to the device based on 1:1 blend ratio, no noticeable correlation has been observed for that of 1:0.6, between thermal annealing and recombination rates.

6.4 AC Measurements: Impedance spectroscopy and Capacitance – voltage measurements as a tool for characterizing P3HT: PCBM – based OSCs

In the following sections, studies involving the use of impedance spectroscopy and also capacitance – voltage measurements for the characterization of OSCs are presented.

In section 4.4.2, and 4.4.3, a brief overview of the methods of CV and impedance spectroscopy (IS) was presented. From the foregoing discussions, it has been shown in this work so far that a number of experimental techniques have been useful in characterising thin films and OSCs based on P3HT: PCBM. These include the combination of both UV-Vis absorption spectroscopy and optical microscopy in elucidating information on the molecular segregation and D/A phase separation within the photoactive bulk. Charge transfer dynamics as revealed by PL studies. Current – voltage measurements as well, which is a frequently used technique in evaluating significant PV parameters and most importantly device PCEs. In probing the impact of thermal annealing on the nanoscale morphology of BHJ OSC, these aforementioned tools have undoubtedly provided useful insights in better understanding correlations between significant parameters. These include morphological variations and photon absorption, exciton generation and dissociations, charge generation and their subsequent collection. However, as much as these tools have been proven to be informative it is important to note that they are not exhaustive in themselves. For this reason, it can be argued that the relationships between nanoscale morphology, underlying electrical properties, and device performance have not been fully exhausted yet.

6.4.1 Impedance Spectroscopy measurements studies of P3HT: PCBM – based devices

Impedance spectroscopy is known to be an effective tool in characterising the electrical properties of electronic devices (Mora-Seró et al, 2008; Kuwabara et al, 2009; Leever et al, 2012). It is primarily based on the measurement of the current response to an AC voltage

applied as a function of frequency. Unlike DC methods, with IS measurements, it is possible to evaluate the roles of interfaces within the bulk of the photoactive layer of OSCs (Leever et al, 2011). The method has been proven to be effective in characterising a variety of electrical devices such as the dye sensitized solar cells (DSSC). OSC parameters such as charge carrier lifetimes have been successfully determined under a range of operating biases and illumination intensities (Bisquert, 2003; Wang et al, 2005; Bisquert et al, 2009). Wu and co-workers (2010) in their report have shown that the analysis framework established for DSSC can be extended to the BHJ OSC in order to evaluate average charge carrier lifetimes as a function of the device's processing history (for example, thermal annealing). Similarly in this section, a study of the impedance responses of BHJ OSC based on P3HT: PCBM, are presented. It investigates the impact of thermal annealing on nanomorphology evolution in typical BHJ blend film for OSC applications. From the analysis of the impedance responses of devices and their dependence on illumination intensity, bias conditions, and thermal annealing conditions, discussions on the characteristics of P3HT: PCBM – based devices studied here are presented.

The IS responses for BHJ devices with the structure ITO/PEDOT: PSS/Active layer (P3HT: PCBM)/Al are summarised in Figure 6.14. The ratio P3HT: PCBM in the blend used is 1:1.

Leever and co-workers (2011) demonstrated that the larger response of the semi-circle of the Cole-Cole plots (Figure 6.14) for a P3HT: PCBM device compared to that of a P3HT – only device was mainly due to charge transfer processes at D/A interfaces in the bulk active layer. In Figure 6.14 (b), the AC response of the device was found to be approaching the shunt resistance extracted from the $J - V$ curve of as cast device under 1 sun illumination (2500 Ω). This observation is consistent with other reported studies (Leever et al, 2011). Among the number of equivalent circuit models employed for modelling impedance responses, the one used by Yoon et al (2014) has been applied here. This is represented in Figure 6.15, where R_S corresponds to the intersection of the impedance spectra with the real axis on the Cole – Cole plot, indicated by Re Z (in Ohms) at high frequencies. This has been attributed to the resistive losses at the ITO/PEDOT: PSS interface. As is evident, it is almost constant under varied illumination and sample bias. Two semicircular arcs can almost be seen from the AC impedance response (see inset of Figure 6.14 (b)). These are accounted for in the equivalent circuit as; a high frequency arc, represented by the $R_1||C_1$ combination, whereas the low frequency arc is represented by the $R_2||$CPE. The $R_1||C_1$ is associated with the bulk resistance and capacitance (Leever et al, 2011; Yoon et al, 2014).

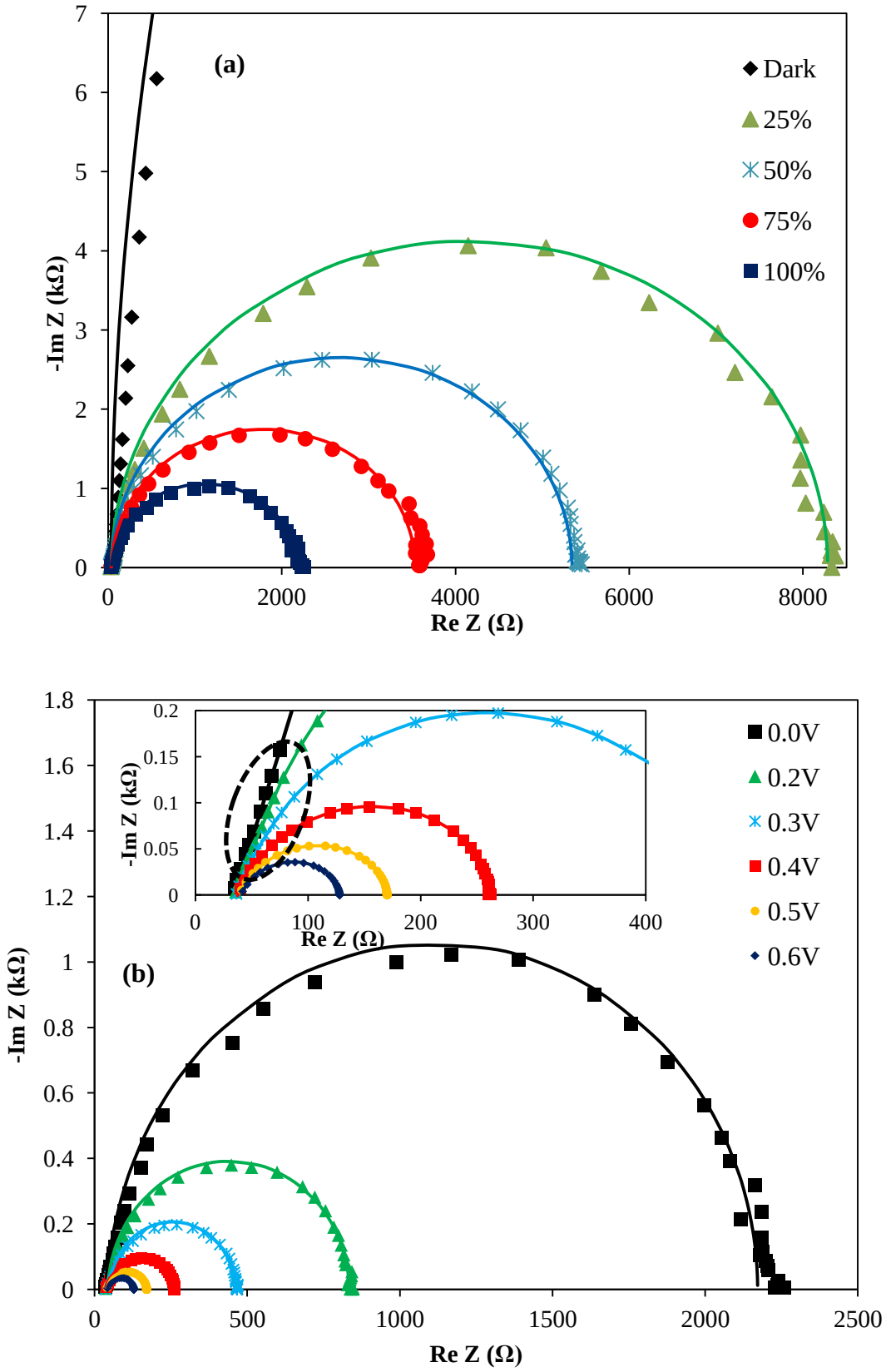

Figure 6.14: Impedance spectra of P3HT: PCBM (1:1) solar cell (as cast): (a) at 0.0 V and under varied illumination intensities, (b) under 1 sun (100%) illumination intensity and varied bias.

Figure 6.15 shows the equivalent circuit representing P3HT: PCBM BHJ solar cell.

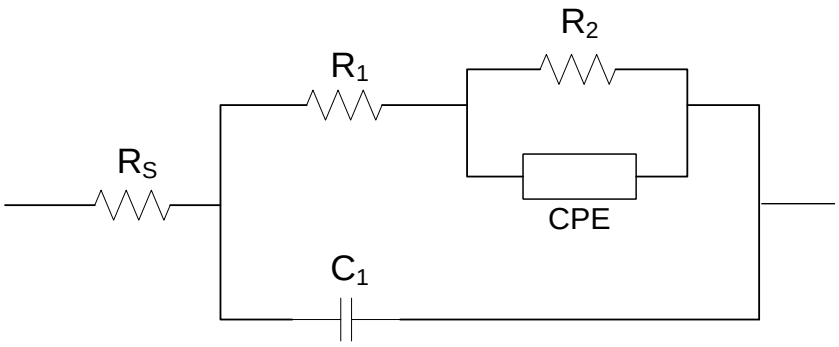

Figure 6.15: Equivalent circuit representing P3HT: PCBM BHJ solar cell.

Whilst in the R_2||CPE combination, R_2 corresponds to a recombination resistance and CPE (constant phase element) a chemical capacitance, having an equivalent capacitance, C_{eq}; both of which are believed to be associated with charge transfer processes at D/A interfaces (Leever et al, 2011).

The impedance responses of devices as a function of thermal annealing are shown in Figure 6.16.

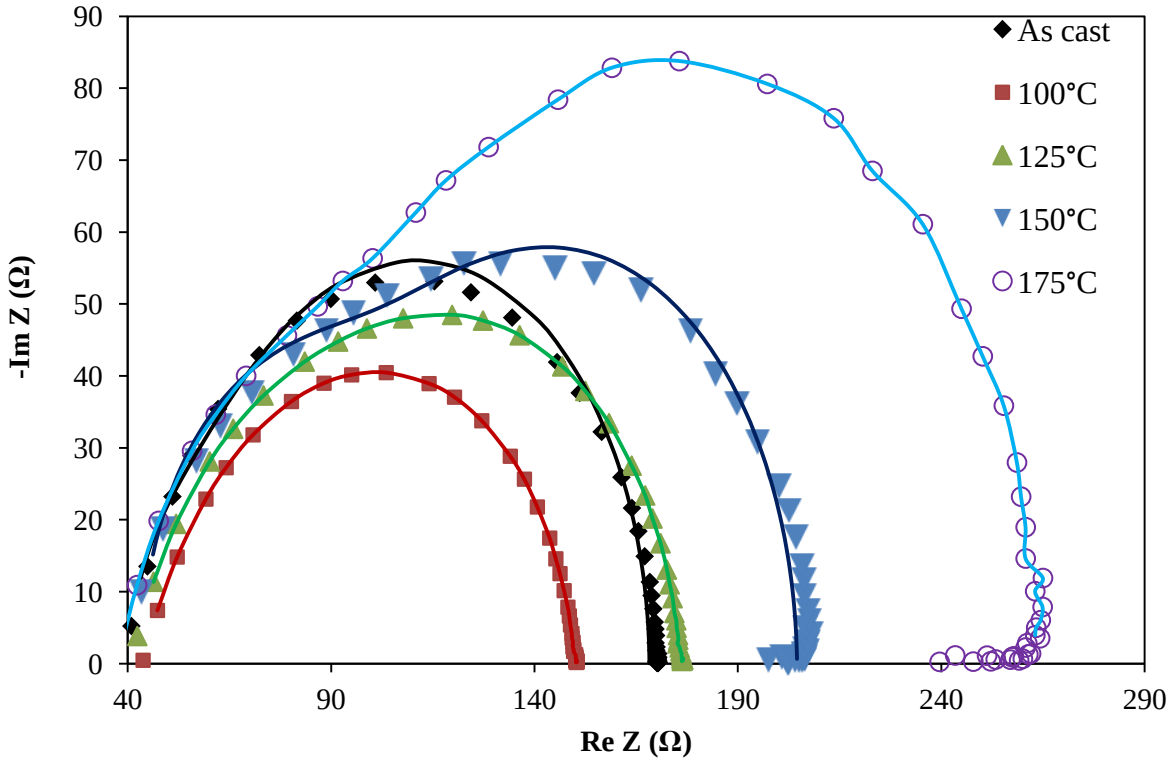

Figure 6.16: Impedance response of P3HT: PCBM solar cell; as cast and thermally annealed a various temperatures, at a sample bias of 0.5V (i.e., around *V*oc) and 1 sun illumination.

From the fits to the impedance data, respective values of R_1, R_2, C_1, and C_{eq} were determined. The average charge carrier lifetimes (τ_{avg}) were calculated using the following equation:

$$\tau_{avg} = R_2 C_{eq} \tag{6.9}$$

The solid lines represent the fits to equivalent circuit model. The equivalent circuit model fit was performed using the EIS Spectrum Analyser software (Bondarenko & Ragoisha, 2011).

Figure 6.17 shows the relationship between the carrier lifetimes and the annealing temperatures.

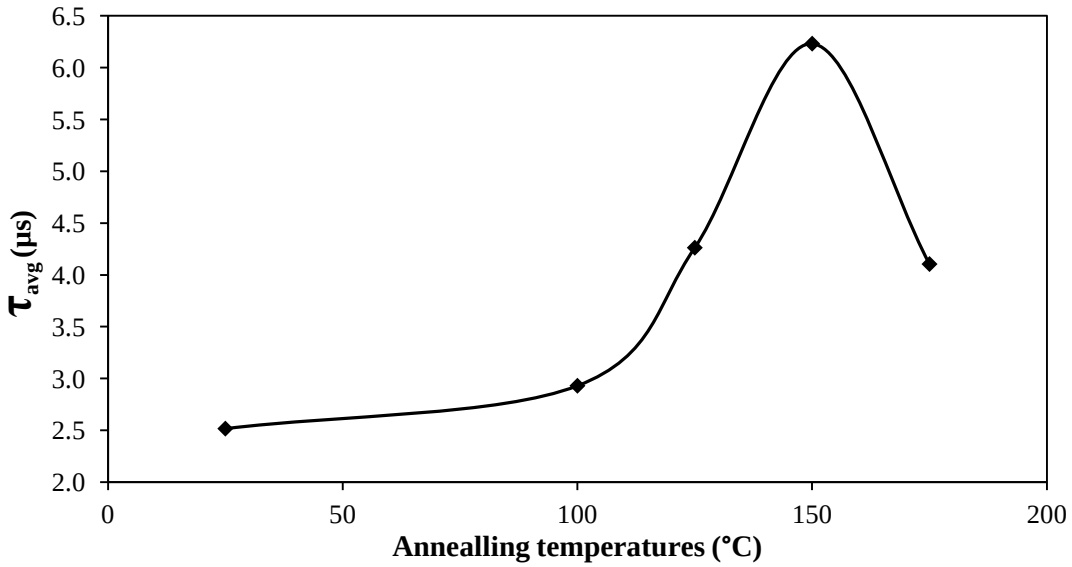

Figure 6.17: A plot of carrier lifetimes as a function of thermal annealing temperatures.

The extracted parameters from the equivalent circuit model fit are summarised in Table 6.6.

Table 6.6: A summary of the equivalent circuit parameters, extracted from the model fit to AC IS response.

1 sun (0.5V)	**R_1 (Ω)**	**R_2 (Ω)**	**C_1**	**C_{eq}**
As cast	56.532	71.132	1.25×10^{-8}	3.54×10^{-8}
100°C	51.87	48.041	1.22×10^{-8}	6.10×10^{-8}
125°C	67.87	60.041	1.18×10^{-8}	7.10×10^{-8}
150°C	85.88	75.2	1.01×10^{-8}	8.29×10^{-8}
175°C	97.87	120.741	6.30×10^{-9}	3.40×10^{-8}

It is interesting to note from Figure 6.17 that as thermal annealing temperature was increased, the charge carrier lifetimes improved, having a highest value at 150°C, after which it deteriorates. Recall from previous section that it is at this temperature that the best PCE was measured. With such an improved lifetime for charge carriers, it is expected that the charge collection will become more efficient, hence more than likely resulting in improved current densities in the device. This together with improved short circuit current density after thermal annealing at 150°C reported previously strongly suggest that the induced morphology at this temperature is one with an optimised D/A interface and efficient transport pathways to respective electrodes (Leever et al. 2011).

6.4.2 Capacitance – voltage (*C – V*) measurements of P3HT: PCBM – based devices

In addition to IS measurements, *C – V* measurements were performed to characterise the P3HT: PCBM PV device. With this technique, the nature of the interfacial interaction between the back electrode and P3HT: PCBM blend can be investigated. Recently it has been reported that with the use of *C – V* measurements techniques, the degree of fullerene coverage (or concentration) on or towards the film surface of active layers for OSCs can be probed (Guerrero et al. 2013). In their work, Guerrero and co-workers (2013) showed that the degree of the accumulation of particular specie of the composite blend material (either electron donor or acceptor material) plays a significant role in carrier selectivity at respective electrodes. In this chapter 5, the explanation for the probable vertical segregation of PCBM molecular aggregates towards the film surface as result of thermal annealing was presented in view of the optical absorption spectra, microscopy image, and GIXRD results. To further provide additional experimental evidence on this nanomorphology evolution, *C – V* measurements have been performed. It is known that *C – V* measurements is somewhat sensitive to interfacial materials, and their relative concentration, at interfaces such as in OSCs (Zhao et al. 2013).

The *C – V* characteristics of P3HT: PCBM device was obtained at 1 kHz, and an AC oscillating amplitude of 50 mV; for as cast and after thermal annealing at several temperatures. The active layer thickness of the device is ~ 150 nm. A brief overview of the characterisation method and the instrumentation employed has been provided in section 4.4.2. From the *C – V* characteristics of the devices under this study, the Mott-Schottky plot (i.e., C^{-2} vs. applied bias voltage, *V*) was obtained. Figure 6.18 shows the Mott-Schottky curve of

P3HT: PCBM BHJ solar cell: as cast and after annealing at 150°C. These two are shown here for the purposes of clarity.

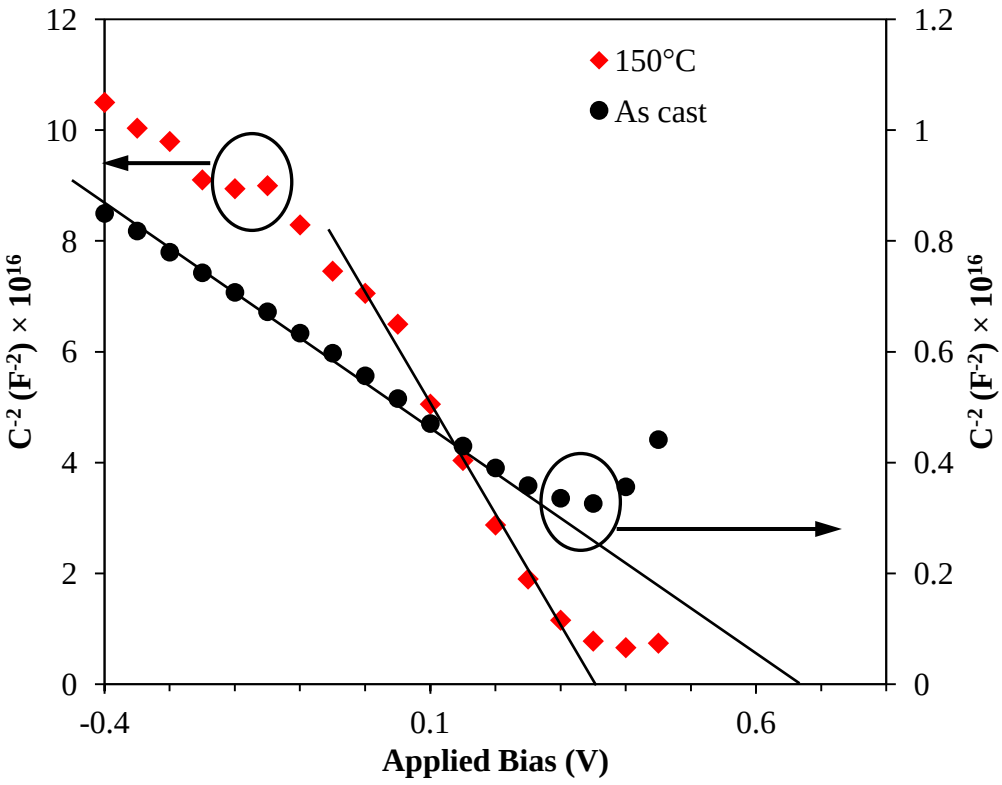

Figure 6.18: Mott-Schottky curve of ITO/PEDOT: PSS/P3HT: PCBM/Al device; as cast and after thermal annealing at 150°C.

Table 6.7: Summary of parameters extracted from the Mott-Schottky curve (shown in Figure 5.38).

	V_{bi} (V)	N_A (cm^{-3})
As cast	0.68	3.05×10^{15}
100°C	0.50	5.33×10^{14}
125°C	0.39	2.31×10^{14}
150°C	0.34	1.18×10^{14}
175°C	0.35	1.02×10^{14}

As is evident, the experimental results follow equation 4.11, i.e., $C^{-2} = 2(V_{bi} - V)/A^2 q\varepsilon\varepsilon_0 N_A$, from which the built – in potential, V_{bi}, and the concentration of impurities, N_A were determined. From Figure 6.18, it can be noted that the $C^{-2} - V$ curve exhibits a straight line

over a wide applied voltage range. The built – in potential, V_{bi}, can be extracted from the intercept in the linear region, shown in Figure 6.18. The extracted V_{bi} and estimated N_A for devices: as cast and after thermal annealing at different temperatures are summarised in Table 6.7.

The estimated values of N_A here are within the range of reported values in literature (Li et al. 2011; Wang et al. 2013). It is interesting to also note that the built – in potential reduces as annealing temperature increases, which then seem to become steady at 150°C. In their work, Guerrero et al (2013) and Kovalenko et al (2014) demonstrated the use of $C - V$ measurement techniques in establishing a correlation between the built – in potential and concentration of acceptor material at the interface of the back electrode (i.e., Al). It was demonstrated that devices with higher concentration of the acceptor material, in this case PCBM, at the cathode, showed a lower built – in potential, compared to a device without PCBM. In view of this, the observed trend in this study can be explained in the light of vertical segregation. Since these observations are consistent with other reports in literature, it can be suggested that thermal annealing of the P3HT: PCBM device, particularly above temperatures of 100°C, induces the vertical segregation of PCBM molecular aggregates. This yields a bulk morphology that consists of a higher concentration of the acceptor material at the cathode interface, hence the observed reduced V_{bi}. This process is summarised graphically in the schematic shown in Figure 6.19.

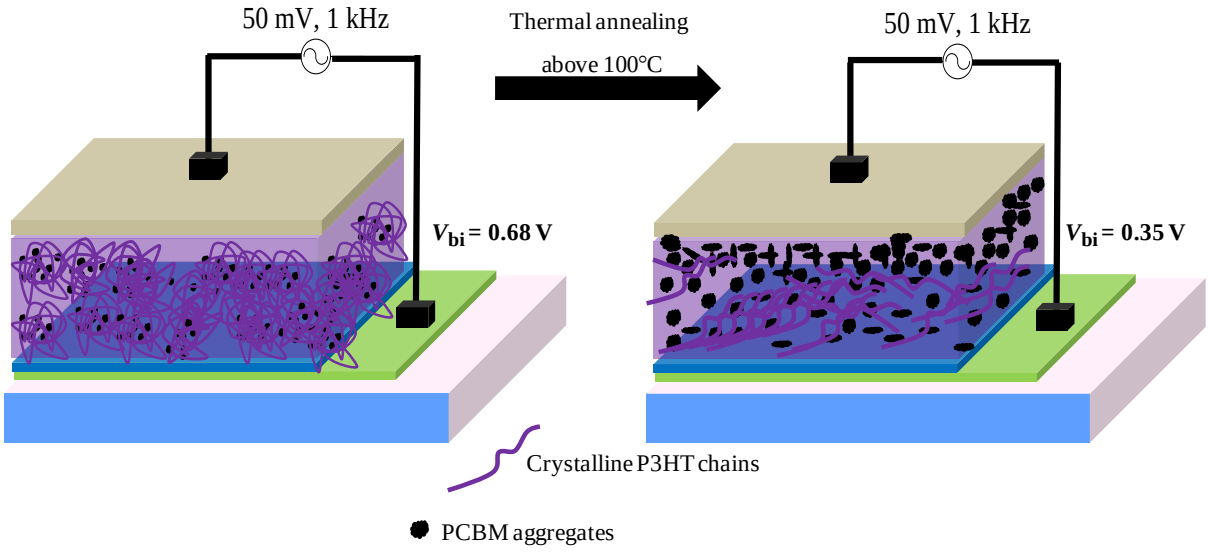

Figure 6.19: A graphical schematic illustrating vertical segregation process following thermal annealing of P3HT: PCBM bulk heterojunction solar cell.

6.5 Summary

In view of the results and discussions on the characteristics of P3HT, PCBM and P3HT: PCBM thin films, presented previously in chapter 5, this chapter has considered the photovoltaic properties of OSCs based on thin films of P3HT: PCBM. The discussions herein were presented in view of the impact of thermal annealing on thin film properties in their application in P3HT – based solar cell.

A direct correlation was demonstrated between absorption spectra properties of PCBM – compositionally different thin films, thermal annealing procedure and photovoltaic properties of P3HT: PCBM bulk heterojunction devices. A number of significant factors were revealed from the electrical characterisation of fabricated OSC devices in the work of this thesis. One of which is the dependence of the device's short circuit current density and open circuit on the thermal annealing strategy adopted. This was shown to be a useful method that can be used to control PCBM molecular cluster arrangements within the active layer structures of devices.

Furthermore, with the use of impedance spectroscopy, complemented with capacitance – voltage measurements, the impact of thermal annealing on charge carrier lifetimes, and vertical segregation of PCBM aggregates in P3HT:PCBM bulk heterojunction solar cells was shown.

Chapter 7

Conclusions and Future Work Recommendations

"The science of today is the technology of tomorrow."

— Edward Teller

7.1 Introduction

In this chapter, the conclusions drawn from the experimental results and discussions, summarising key points of this work are presented. Following the conclusions, a brief outlook is provided. This will be an outlined recommendation of future works in a number of areas significant for the improvement of the performance of OSC.

7.2 PCBM aggregation: A key driver of morphology evolution

The effect of PCBM percentage loading on optical absorption, structural and electrical properties has shown several interesting features. These are believed to be instrumental for better designing highly optimised photovoltaic devices with corresponding improved PCEs. It is clearly evident that the dissociation of excitons is very much dependent on the nature of interfaces between P3HT – PCBM. The nature of the interfaces between P3HT – PCBM donor – acceptor material within the thin film is very much a function of the weight ratio of the composite materials. The loading of the acceptor material, PCBM, in the blend is critical to the resulting P3HT – PCBM phase segregation which in turn influences the exciton dissociation efficiency. Therefore a very important factor in designing devices for optimized performance is demonstrated on account of these observations. It was deduced that the largest reduction in peak absorption intensity of PCBM upon annealing at 175°C is associated with

the highest concentration of PCBM loading. It can be concluded that this reduction is attributed to the diffusion and aggregation of PCBM molecules towards the film air boundary. This explanation was strongly supported by the evidence provided from the capacitance – voltage characterisations of P3HT: PCBM – based photovoltaic devices. Analysis of $C - V$ measurement revealed that the measured built – in potential reduced from 0.68V to 0.35V, with a corresponding reduction noted in the concentration of impurities. This was interpreted as indicative of having an increased concentration of the acceptor material (i.e., PCBM), segregated towards the cathode interface. This is believed to be evidence of vertical segregation induced by thermal annealing, which becomes more prominent at temperatures above 125°C. In view of the morphology evolution and subsequent device performance, it is significant for there to be a preferred segregation direction for typical OSC. This is to ensure the selectivity of electrodes towards one type of charge carrier. Based on the range of PCBM loading used in this investigation the largest PCBM ratio resulted in higher current density (50 wt%). This is attributed to the optimised interfaces between electron donor and acceptor materials and better charge transfer and their subsequent transport to the respective electrodes. The effect of PCBM loading is not as significant on open circuit voltage V_{OC} as in the case for short current density. Furthermore V_{OC} was noted to remain constant upon thermal annealing, till at the annealing temperature of around 100°C after which a significant increase was observed resulting from further annealing temperatures. It is believed however that this is possibly connected to the vertical segregation of PCBM, disrupting shunt paths between the two electrodes. This trend also noticed in V_{OC}s for all the different PCBM weight percentage could be associated with the dark saturation currents observed in the device's respective diodes characteristics.

Furthermore the electrical characterisation for thin film blends of P3HT: PCBM revealed some important factors. The short circuit current density and open circuit voltage dependence on thermal annealing strategies could be used as the controlling factor in PCBM cluster arrangements or tuning within the active layer structures. Optical absorption spectroscopy together with microscopic images presented in Figures 5.4 and 5.6 supports the view that the nature of PCBM cluster formation varies as a result of thermal annealing strategies. In other words, depending on which thermal annealing approach undertaken (be it gradually, or to subjecting the film to a 'shock' annealing treatment), the resulting outcome of aggregated PCBM cluster will differ. Due to its higher surface energy, PCBM cluster nucleation starts at the glass/film boundary. In order to have more efficient charge transport process, PCBM is

required to reside at the boundary with aluminium metal electrode. Additional evidence supporting vertical segregations of PCBM upon thermal annealing was also provided by the 2-D surface profiles (see Figure 5.8), which interestingly correlates with Raman mapping image of the PCBM rich cluster region. From this study it was also deduced that the exciton generation rate is very much dependent on annealing temperatures as indicated in the results.

7.3 Optical absorption spectroscopy

A system consisting of P3HT: PCBM with different percentage weigh ratios showing differing nanomorphology restructuring in response to thermal annealing was also investigated. In this study, a quantitative estimation of the optical absorption and optical images obtained from thin film surfaces, established that cluster formation increases with thermal annealing. Furthermore it was also established that the optical absorption intensity for the PCBM part of the spectrum reduces with annealing temperatures and the absorption intensity reduction is highest for blend thin films with the largest PCBM percentage weight ratio (i.e., 1:1). This can be utilised as a simple yet effective method for evaluating the formation of PCBM aggregates within composite thin films. In addition, phase separation is not only governed by PCBM concentration itself, but is also strongly influenced by thermal annealing too. Absorption of light by P3HT: PCBM blend film, followed by exciton generation, charge transfer and their subsequent transport within the bulk heterojunction is sensitive to the amount and size of PCBM clusters. A low PCBM concentration (37.5%) does not enable the formation of the required percolating pathways for efficient transport of free charge carriers within the photoactive layer of devices.

7.4 Charge carrier recombination in P3HT: PCBM BHJ organic solar cells

Previously it was reported that a system consisting of a highly intermixed blend of P3HT: PCBM could result in additional disorder and formations of traps. The results presented in this work support this view in the light of high trap densities measured. Furthermore the increase in electron trap density upon thermal annealing correlates with temperatures above the glass transition temperature for P3HT phase initiating traps formation in the heterojunction device. From the charge carrier mobility studies in this work, it was found that the ratio of electron to hole mobility improves with annealing temperature up to 150°C above which the hole mobility overtakes electron mobility. This is believed to be most likely as a result of molecular segregation of PCBM and formation of clusters, thereby leading to the disruption of transport pathways for electrons and subsequently the deterioration of device

PCEs. The higher recombination constant B_{SRH} measured in this investigation in comparison to B_L is an indication that the trap assisted recombination is dominant in comparison to its Langevin counterpart. The presence of high density of traps in the blended material further supports the Shockley-Read-Hall trap assisted recombination with further evidence of the dependence of open circuit voltage on light intensity also demonstrated. To further highlight the significance of recombination in the P3HT: PCBM BHJ organic solar cells, it was also demonstrated from photocurrent generation studies that the extent to which free charge carriers are lost due to recombination is very much dependent on the PCBM weight percentage in the blend. The study in this work showed that a high percentage of photo generated charge carriers were lost because of the low PCBM content in the devices based on the ratio of 1:1.6, as compared to that based on 1:1. This also suggests that recombination mechanisms are likely related to the PCBM loading within the bulk of the active layer.

Measurements for charge carriers' mobility with thermal annealing temperatures in this work, proved instrumental in establishing the dependence of bimolecular recombination rate on thermal annealing. Whilst a direct correlation between bimolecular recombination and short circuit current density is observed for 1:1 device, it was rather unclear at this stage at to how the trend applies to the 1:0.6 percentage weight ratios.

With the use of impedance spectroscopy, it was possible to also provide an in – depth understanding into recombination events at donor – acceptor interfaces for photovoltaic devices. These studies revealed that one of the mechanisms contributing the best device PCEs recorded at the optimum thermal annealing temperature of about 150°C could be the measured extended lifetime of charges after thermal annealing at the said temperature. This is in addition to all the other aforementioned factors. These show that to have a system with efficient charge collection, extending lifetimes of free charges is critical to optimum device performance.

The best power conversion efficiency measured for the P3HT: PCBM organic solar cells in this study, was 3.84%, obtained from the blend ratio of 1:1, and at an optimum thermal annealing temperature of 150°C.

7.5 Future Work Recommendations

Thermal annealing amongst other morphology controlling techniques (such as solvent vapour annealing) is considered and as being employed here in this work, a very effective method for

morphology optimisation in P3HT – based OSCs. Application of the established protocols here in this work, for effective nanostructuring in P3HT: PCBM OSCs should be further explored in newly developed low band gap polymers. The impact of thermal annealing on the variation of the open circuit voltage parameter of OSC devices is not fully understood. Although generally considered to be influenced by the physical properties of the active layer, its dependence on the electronic energy levels of materials, as shown by Scharber and co – workers (2006) in view of thermal annealing has not been studied yet. This will require further work to understand the impact of thermal annealing on the HOMO and LUMO of the donor and acceptor material (in this case, P3HT and PCBM).

The thermally induced vertical segregation of PCBM clusters, as revealed by capacitance – voltage measurements, demonstrated the significance of having a gradient active layer distribution. This means having higher concentration of materials at the respective electrodes, favouring selective transport and collection of charge carriers. Hence to manually fabricate such an active layer with favourable electrode selectivity would be ideal, however this is difficult, as the active layer is processed from solution. There is therefore the need to investigate novel, yet low cost fabrication techniques to achieve such an active layer structure.

It is moreover evident that there is the need for research investigation and development of novel concepts for further improvement of efficiencies of organic solar cells, bringing it close to achieving its potential for low-cost energy conversion. In as much as this is significant, it is also important to note that, it is not only about having favourable nanoscale morphology control for improved efficiencies, but also for devices that are stable in time and temperature, thus it will be interesting to study this, and to also understand the influence of a strategy of nanomorphology control on efficiency and stability of large area devices too.

REFERENCES

Aernouts, T. Geens, W. Poortmans, J. Hermans, P. Borghs, S. Mertens, R. (2002). Extraction of bulk and contact components of the series resistance in organic bulk donor-acceptor-heterojunctions. *Thin Solid Films*, 403-404, 297-301.

Agostinelli, T. Lilliu, S. Labram, J. G. Campoy-Quiles, M, Hampton, M. Pires, E. Rawle, J. Bikondoa, O. Bradley, D. D. C. Anthopoulos, T. D. Nelson, J. Macdonald, J. E. (2011). Real-Time Investigation of Crystallization and Phase Segregation Dynamics in P3HT: PCBM Solar Cells During Thermal Annealing. *Advanced Functional Materials*, 21, p.1701-1708.

Alvarez-Fraga, L. Jiménez-Villacorta, F. Sanchez-Marcos, J. deAndres, A. Prieto, C. (2015). Indium-tin oxide thin films deposited at room temperature on glass and PET substrates: Optical and electrical properties variation with the H_2–Ar sputtering gas mixture. *Applied Surface Science*, 344, p. 217–222.

Ayzner, A. L. Tassone, C. J. Tolbert, S. H. Schwartz, B. J. (2009). Reappraising the Need for Bulk Heterojunctions in Polymer-Fullerene Photovoltaics: The Role of Carrier Transport in All-Solution-Processed P3HT/PCBM Bilayer Solar Cells. *Journal of Physical Chemistry C*. 113, p. 20050-20060.

Baibarac, M. Lapkowski, M. Pron, A. Lefrant, S. Baltog, I. (1998). SERS Spectra of Poly (3-Hexylthiophene) in Oxidized and Unoxidized States. *Journal of Raman Spectroscopy*, 29, 825–832.

Ballantyne, A. M. Chen, L. Dane, J. Hammant, T. Braun, F. M. Heeney, M. Duffy, W. McCulloch, I. Bradley, D. D.C. Nelson, J. (2008). The Effect of Poly(3-hexylthiophene) Molecular Weight on Charge Transport and the Performance of Polymer: Fullerene Solar Cells. *Advanced Functional Materials*, 18, p. 2373-2380

Ballantyne, A. M. Ferenczi, T. A. M. Campoy – Quiles, M. Clarke, T. M. Maurano, M. Wong, K. H. Zhang, W. Stingelin-Stutzmann, N. Kim, J.-S. Bradley, D. D. C. Durrant, J. R. McCulloch, I. Heeney, M. Nelson, J. (2010). Understanding the Influence of Morphology on Poly (3-hexylselenothiophene): PCBM Solar Cells. *Macromolecules*, 43, 1169-1174.

Bao, Z. Dobabalapur, A. Lovinger, A. J. (1996). Soluble and processable regioregular poly (3-hexylthiophene) for thin film field-effect transistor application with high mobility. *Applied Physics Letters*, 69, p. 1-3.

Bar – Lev, A. (1993). *Semiconductor and Electronic Devices.* Prentice Hall: UK

Barbarella, G. Bongini, A. Zambianchi, M. (1994). Regiochemistry and Conformation of Poly (3-hexylthiophene) via the Synthesis and the Spectroscopic Characterization of the Model Configurational Triads. *Macromolecules*, 27, p. 3039-3045.

Barth, S. Bassler, H. (1997). Intrinsinc photoconduction in PPV-type conjugated polymers. *Physical Review Letters*, 79, p. 4445-4448.

Basak, T. K. (2012). *Electrical Engineering Materials*. New Academic Science: Kent, GBR

Bässler, H. (1993). Charge Transport in Disordered Organic Photoconductors a Monte Carlo Simulation Study. *Physica Status Solidi*, 175, p. 15-56.

Bisquert, J. (2002). Theory of the Impedance of Electron Diffusion and Recombination in a Thin Layer. *Journal of Physical Chemistry B.* 106, p. 325-333.

Bisquert, J. (2003). Chemical capacitance of nanostructured semiconductors: its origin and significance for nanocomposite solar cells. *Physical Chemistry Chemical Physics*, 5, p. 5360-5364.

Bisquert, J. Fabregat-Santiago, F. Mora-Sero, I. Garcia-Belmonte, G. Gimenez, S. (2009). Electron Lifetime in Dye-Sensitized Solar Cells: Theory and Interpretation of Measurements. *Journal of Physical Chemistry C*, 113 (40), 17278-17290.

Blom, P. W. M. Mihailetchi, V. D. Koster, L. J. N. Markov, D. E. (2007). Device Physics of Polymer: Fullerene Bulk Heterojunction Solar Cells. *Advanced Materials*, 19, p. 1551-1566.

Bondarenko, A. S. Ragoisha, G. A. (2011). *EIS Spectrum Analyser*, http://www.abc.chemistry.bsu.by/vi/analyser/.

Bozano, L. Carter, S. A. Scott, J. C. Malliaras, G.G. Brock, P. J. (1999). Temperature- and field-dependent electron and hole mobilities in polymer light-emitting diodes. *Applied Physics Letters*, 74, p. 1-3.

Brabec, C. Dyakonov, V. Scherf, U. (eds.) (2008). *Organic Photovoltaics: Materials, Device Physics, and Manufacturing Technologies.* Weinheim: Wiley-VCH.

Brabec, C. J. Shaheen, S. E. Winder, C. Sariciftci, N. S. (2002). Effect of LiF/metal electrodes on the performance of plastic solar cells. *Applied Physics Letters*, 80 (7), 1288-1290.

Brabec, C.J. (2004). Organic Photovoltaics: technology and market. *Solar Energy Materials and Solar Cells*, 83, p.273-292.

Brabec, C.J. Sariciftci, N. S. Hummelen, J. C. (2001). Plastic Solar Cells. *Advanced Functional Materials*, 11, p. 15-26.

Bradley, D. D. C. (1991), Characterisation of polymers for semiconductor applications. *Polymer International*, 26, p. 3-16.

Bradley, D. D. C. (1998). Conjugated Electroluminescence. *Synthetic Metals*, 54, p. 401-415.

Bradley, D. D. C. Grell, M. Grice, A. Tajbakhsh, A. R. O'Brien, D. F. Bleyer, A. (1998), Polymer light emission: control of properties through chemical structure and morphology. *Optical Materials*, 9, p. 1-11.

Braun, C. L. (1984). Electric field assisted dissociation of charge transfer states as a mechanism of photocarrier production. *The Journal of Chemical Physics*, 80, 4157.

Brédas, J. L. Silbey, R. Boudreaux, D. S. Chance, R. R. (1983). Chain – Length Dependence of Electronic and Electrochemical Propertis of Conjugated Systems: Polyacetylene, Polyphenylene, Polythiophene and Polypyrrole. *Journal of American Chemical Society*, 105, 6555-6559.

Breen, T. L. Fryer, P. M. Nunes, R. W. Rothwell, M. E. (2002). Patterning indium tin oxideand indium zinc oxide using microcontact printing and wet etching. *Langmuir*, 18, p. 194–197.

Brown, P. J. Thomas, D. S. Köhler, A. Wilson, J. S. Kim, J-S. Ramsdale, C. M. Sirringhaus, H. Friend, R. H. (2003). Effect of interchain interactions on the absorption and emission of poly (3-hexylthiophene). *Physical Review*. 67, 064203, p. 1-16.

Brütting, W. Adachi, C. (eds.). (2012). *Physics of Organic Semiconductors*. Wiley-VCH.

Burroughes, J. H. Bradley, D. D. C. Brown, A. R. Marks, R. N. Mackay, K, Friend, R. H. Burns, P. L. Holms, A. B. (1990). Light-emitting diodes based on conjugated polymers. *Nature*. 347, p.539-541.

Campoy-Quiles, M. Ferenczi, T. Agostenilli, T. Etchegoin, P. G. Kim, Y. Anthapoulos, T. D. Stavrinou, P. N. Bradley, D. D. C. Nelson, J. (2008). Morphology evolution via self-organisation and lateral and vertical diffusion in polymer: fullerene solar cell blends. *Nature Materials.* 7, p. 158-164.

Cao, Y. Yu, G. Zhang, C. Menon, R. Heeger, A. J. (1997). Polymer light-emitting diodes with polyethylene dioxythiophene–polystyrene sulfonate as the transparent anode. *Synthetic Metals*, 87, p. 171-174.

Carter, S. A. Angelopoulos, M. Karg, S. Brock, P. J. Scott, J. C. (1997). Polymeric anodes for improved polymer light-emitting diode performance. *Applied Physics Letters*, 70, p. 2067.

Chabinyc, M. L. (2008). X-ray Scattering from Films of Semiconducting Polymers. *Polymer Reviews*, 48, p. 463-492.

Chen, C. J. (2011), *Physics of Solar Energy*, John Wiley & Sons, New Jersey.

Chen, F.-C. Ko, C.-J. Wu, J.-L. Chen, W.-C. (2010). Morphological study of P3HT: PCBM blend films prepared through solvent annealing for solar cell applications. *Solar Energy Materials and Solar Cells*, 94, p. 2426-2430.

Chen, J. Cao, Y. (2009). Development of Novel Conjugated Donor Polymers for High-Efficiency Bulk Heterojunction Photovoltaic Devices. *Accounts of Chemical Research*, 42, p. 1709-1718.

Chen, L.-M. Hong, Z. Li, G. Yang, Y. (2009). Recent Progress in Polymer Solar Cells: Manipulation of Polymer:Fullerene Morphology and the Formation of Efficient Inverted Polymer Solar Cells. *Advanced Materials*, 21, p. 1434-1449.

Chen, T-A. Wu, X. Rieke, R. D. (1995). Regiocontrolled Synthesis of Poly (3-akylthiophene) Mediated by Rieke Zinc: Their Characterization and Solid-State Properties. *Journal of American Chemical Society*, 117, p. 233-244.

Chiang, C. K. Fischer, C. R. Park, Y. W. Heeger, A. J. Shirakawa, H. Lious, E. J. Gau, S. C. McDiarmid, A. G. (1977). Electrical Conductivity in Doped Polyacetylene. *Physical Review Letters*, 39, p. 1098.

Chirvase, D. Chiguvare, Z. Knipper, M. Parisi, J. Dyakonov, V. Hummelen, J. C. (2003). Electrical and optical design and characterisation of regioregular poly (3-hexylthiophene-2, 5 diyl)/fullerene-based heterojunction polymer solar cells. *Synthetic Metals.* 138, p. 299-304.

Choy, W. C. H. (ed.) (2013). *Organic Solar Cells: Materials and Device Physics*. London: Springer-Verlag.

Christopher, M. P. Martijn, K. Thuc-Quyen, N. (2013). Charge carrier recombination in organic solar cells. *Progress in Polymer Science*, 38, p. 1941-1960

Clarke, T. M. Durrant, J. R. (2010). Charge Photogeneration in Organic Solar Cells. *Chemical Reviews*. 110, p. 6736-6767.

Coropceanu, V. Cornil, J. da Salvia Filho, D. A. Olivier, Y. Silbey, R. Brédas, J-L. (2007). Charge Transport in Organic Semiconductors. *Chemical Reviews*, 107, p. 926-952

Cowan, S. R. Roy, A. Heeger, A. J. (2010). Recombination in polymer – fullerene bulk heterojunction solar cells. *Physical Review B*, 82, 245207, p. 1-10

Cutility, B. D. (1956). *Elements of X-ray Diffraction.* Reading, MA: Addision-Wesley.

Dang, M. T. Wantz, G. Bejbouji, H. Urien, M. Dautel, O. J. Vignau, L. Hirsch, L. (2011). Polymeric solar cells based on P3HT: PCBM: Role of the casting solvent. *Solar Energy Materials and Solar Cells*, 95, p. 3408-3418.

de Leeuw, D. M. Simenon, M. M. J. Brown, A. R. Einerhand, R. E. F. (1997). Stability of n – type doped conducting polymers and consequences for polymeric microelectronic devices. *Synthetic Metals*, 87, 53-59.

Deibel, C. Dyakonov, V. Brabec, C. J. (2010). Organic Bulk-Heterojunction Solar Cells. *IEEE Journal of Selected Topics in Quantum Electronics*, 16, p. 1517-1527.

DeLongchamp, D. M. Kline, R. J. Fischer, D. A. Richter, L. J. Toney, M. F. (2011). Molecular Characterisation of Organic Electronic Films. *Advanced Materials*, 23, 319-337

Ecker, B. Nolasco, J. C. Pallarés, J. Marsal, L. F. Posdorfer, J. Parisi, J. von Hauff, E. (2011). Degradation Effects Related to the Hole Transport Layer in Organic Solar Cells. *Advanced Functional Materials.* 21 (14), p. 2705-2711.

Erb, T. Zhokhavets, U. Hoppe, H. Gobsch, G. Al-Ibrahim, M. Ambacher, O. (2006). Absorption and crystallinity of poly(3-hexylthiophene)/fullerene blends in dependence on annealing temperature. *Thin Solid Films*. 511-512, p. 483-485.

Ferraro, J. R. Nakamoto, K. Brown, C. W. (2003). Introductory Raman Spectroscopy. Academic Press, San Diego, CA.

Forrest, S.R. (2005). The Limits to Organic Photovoltaic Cell Efficiency, *MRS Bulletin*, 30, p. 28-32.

Gao, Y. Gery, J. K. (2009). Resonance Chemical Imaging of Polythiophene/Fullerene Photovoltaic Thin Films: Mapping Morphology-Dependent Aggregated and Unaggregated C═C Species. *Journal of American Chemical Society*, 131, 9654–9662.

Garcia-Belmonte, G. Boix, P. P. Bisquert, J. Sessolo, M. Bolink, H. J. (2010). Simultaneous determination of carrier lifetime and electron density-of-states in P3HT: PCBM organic solar cells under illumination by impedance spectroscopy. *Solar Energy Materials and Solar Cells*. 94, p. 366-375.

Garcia-Belmonte, G. Munar, A. Barea, E. M. Bisquert, J. Ugarte, I. Pacios, R. (2008). Charge carrier mobility and lifetime of organic bulk heterojunctions analyzed by impedance spectroscopy. *Organic Electronics.* 9, p. 847-851.

Geens, W. Aernouts, T. Poortmans, J. Hadziionannou, G. (2002). Organic co – evaporated films of a PPV – pentamer and C60. *Thin Solid Films*, 403, p. 438.

George, S. (2001). *Infrared and Raman characteristic group frequencies: tables and charts.* 3rd ed. Chichester: Wiley.

Germack, D. S. Chan, C. K. Hamadani, B. H. Richter, L. J. Fischer, D. A. Gundlach, D. J. DeLongchamp, D. M. (2009). Substrate-dependent interface composition and charge transport in films for organic photovoltaics. *Applied Physics Letters*. 94, 233303, p. 1-3.

Gong, S. E. Jang, S. K. Ryu, S. U. Jeon, H. Park, H.-H. Chang, H. J. (2010). Post annealing effect of flexible polymer solar cells to improve their electrical properties. *Current Applied Physics*. 10, p. e192-e196.

Gouadec, G. Colomban, P. (2007). Raman Spectroscopy of nanomaterials: How spectra relate to disorder, particle size and mechanical properties. *Progress in Crystal Growth and Characterisation of Materials.* 53, p. 1-56.

Green, M. A. Emery, K. Hishikawa, Y. Warta, W. (2011). Solar cell efficiency tables (version 37). *Progress in Photovoltaics: Research and Applications*, 19, p. 84-92.

Gregg, B. (2003). Excitonic Solar Cells. *Journal of Physical Chemistry B*, 107, p. 4688-4698.

Gregg, B. A. Hanna, M. C. (2003). Comparing organic to inorganic photovoltaic cells: Theory, experiment, and simulation. *Journal of Applied Physics*, 93, p. 3605-3614.

Guerrero, A. Dörling, B. Ripolles-Sanchis, T. Aghamohammadi, M. Barrena, E. Campoy-Quiles, M. Garcia-Belmonte, G. (2013). Interplay between Fullerene Surface Coverage and Contact Selectivity of Cathode Interfaces in Organic Solar Cells. *ACS Nano*, 7, p. 4637-4646.

Günes, S., Neugebauer, H., and Sariciftci, N.S. (2007) Conjugated Polymer-Based Solar Cells. *Chemical Review,* 107, p. 1324-1338.

Guo, J. Ohkita, H. Benten, H. Ito, S. (2010). Charge Generation and Recombination Dynamics in Poly(3-hexylthiophe)/Fullerene Blend Films with Different Regioregularrities and Morphologies. *Journal of American Chemical Society*, 132, 6154-6164.

Guo, T-F. Wen, T-C. Pakhomov, G. L. Chin, X-G. Liou, S-H. Yeh, P-H. Yang, C-H. (2008). Effects of film treatment on the performance of poly(3-hexylthiophene)soluble fullerene-based organic solar cells. *Thin Solid Films.* 516, p. 3138-3142.

Guozhong, C. (2004). *Nanostructures and Nanomaterials.* Singapore: World Scientific Publishing Co.

Halls, J. J. M. Pichler, K. Friend, R. H. Moratti, S. C. Holmes, A. B. (1996). Exciton diffusion and dissociation in poly (*p*-phenylenevinylene)/C_{60} heterojunction photovoltaic cell. *Applied Physics Letters*. 68, p. 3120-3122.

Halls, J. J. M. Walsh, C. A. Greenham, N. C. Marseglia, E. A. Friend, R. H. Moratti, S. C. Holmes, A. B. (1995). Efficient photodiodes from interpenetrating polymer networks. *Nature*. 376, p. 498-500.

Haugeneder, A. Neges, M. Kallinger, C. Spirkl, W. Lemmer, U. Fledmann, J. Scherf, U. Harth, E. Gügel, A. Müllen, K. (1999). Exciton diffusion and dissociation in conjugated polymer/fullerene blends and heterostructures. *Physical Review B*, 59, 15346.

Haugstad, G. (2012). *Atomic Force Microscopy: Understanding Basic Modes and Advanced Applications.* USA: Wiley.

Haugstad, G. Jones, R. R. (1999). Mechanisms of dynamic force microscopy on polyvinyl alcohol: region-specific non-contact and intermittent and contact regimes. *Ultramicroscopy.* 76, p. 77-86.

Heejo, K. Won-Wook, S. Sang-Jin, M. (2006). Effect of thermal annealing on the performance of P3HT/PCBM polymer photovoltaic cells. *Journal of the Korean Physical Society*. 48, p. 441-445.

Heremans, P. Cheyns, D. Rand, B.P. (2009). Strategies for Increasing the Efficiency of Heterojunction Organic Solar: Material Selection and Device Architecture, *Accounts of Chemical Research*, 42, p.1740-1747.

Hoppe, H. Niggemann, M. Winder, C. Kraut, J. Hiesgen, R. Hinsch, A. Meissner, D. Saciciftci, N. S. (2004). Nanoscale Morphology of Conjugated Polymer/Fullerene-Based Bulk-Heterojunction Solar Cells. *Advanced Functional Materials*, 14, p. 1005-1011.

Hoppe, H. Sariciftci, N. S. (2004). Organic solar cells: An overview. *Journal of Materialss Research*, 19, p. 1924-1945.

Hsiao, C. – C. Hsiao, A. – E. Chen, S. – A. (2008). Design of Hole Blocking Layer with Electron Transport Channels for High Performance Polymer Light-Emitting Diodes. *Advanced Materials*, 20, 1982.

Huang, Y.-C. Liao, Y.-C. Li, S.-S. Wu, M.-C. Chen, C.-W. Su, W.-F. (2009). Study of the effect of annealing process on the performance of P3HT/PCBM photovoltaic devices using scanning-probe microscopy. *Solar Energy Materials and Solar Cells*, 93, p. 888-892.

Hummelen, J. C. Knight, B. W. LePeq, F. Wudl, F. (1995). Preparation and Characterisation of Fulleroid and Methanofullerene Derivatives. *Journal of Organic Chemistry*. 60, p. 532-538.

Jaiswal, R. Menon, M. (2006). Equivalent circuit for an organic field-effect transistor from impedance measurements under dc bias. *Applied Physics Letters*, 88, 123504.

Jaiswal, R. Menon, M. (2006). "Polymer electronic materials: a review of charge transport," *Polymer International*, 55, p. 1371–1384.

Jamieson, F. C. Domingo, E. B. McCarthy-Ward, T. Heeney, M. Stingelin, N. Durrant, J. R. (2012). Fullerene crystallisation as a key driver of charge separation in polymer/fullerene bulk heterojunction solar cells. *Chemical Science*, 3, 485-492.

Jang, J. Seok-Soon, K. Seok-In, N. Byung, Kwan, Y. Dong-Yo, K. (2009). Time-dependent morphology evolution by annealing process on polymer: fullerene blend solar cells. *Advanced Functional Materials*. 19, p. 866-874.

Jeong, J. W. Huh, J. W. Lee, J. I. Chu, H. Y. Han, I. K. Ju, B. (2011). Effects of thermal annealing on the efficiency of bulk-heterojunction organic photovoltaic devices. *Current Applied Physics*. 10, p. S520-S524.

Jiang, X. X. (2007). Research of carrier transport in organic heterojunction solar cells. PhD Thesis. Changchun: Changchun Institute of Applied Chemistry.

Jo, J. Kim, S.-S. Na, S.-I. Yu, B.-K. Kim, D.-Y. (2009). Time – Dependent Morphology Evolution by Annealing Processes in Polymer: Fullerene Blend Solar Cells. *Advanced Functional Materials*, 19, p. 866-874.

Jung, J. W. Jo, W. H. (2010). Annealing-free high efficiency and large area polymer solar cells fabricated by a roller printing process. *Advanced Functional Materials*. 20, p. 1-9.

Juster, N. J. (1963). Organic Semiconductors. *Journal of Chemical Education*. 40, p. 547-555.

Kalita, G. Masahiro, M. Koichi, W. Umeno, M. (2010). Nanostructured morphology of P3HT: PCBM bulk heterojunction solar cells. *Solid State Electronics*, 54, p. 447-451.

Karagiannidis, P. G. Georgiou, D. Pitsalidis, C. Laskarakis, A. Logothetidis, S. (2011). Evolution of vertical separation in P3HT: PCBM thin films induced by thermal annealing. *Materials Chemistry and Physics*, 129, p. 1207-1213.

Karagiannidis, P. G. Kassavetis, S. Pitsalidis, C. Logothetidis, S. (2011). Thermal annealing effect on the nanomechanical properties and structure of P3HT: PCBM thin films. *Thin Solid Films.* 519, p. 4105-4109.

Kim, K. Liu, J. Namboothiry, M. A. G. Carroll, D. L. (2007). Roles of donor and acceptor nanodomains in 6% efficient thermally annealed polymer photovoltaics. *Applied Physics Letters*, 90, 163511, p. 1-3.

Kim, Y. Bradley, D. D. C. (2005). Bright red emission from single layer polymer light-emitting devices based on blends of regioregular P3HT and F8BT. *Current Applied Physics*, 5, p. 222-226.

Kim, Y. Choulis, S. A. Nelson, J. Bradley, D. D. C. (2005). Device annealing effect in organic solar cells with blends of poly (3-hexylthiophene) and soluble fullerene. *Applied Physics Letters*. 86, 063502, p. 1-3.

Kim, Y. Choulis, S. A. Nelson, J. Bradley, D. D. C. Cook, S. Durrant, J. R. (2005). Composition and annealing effects in polythiophenes/fullerene solar cells. *Journal of Material Science*, 40, p. 1371-1376.

Kim, Y. Cook, S. Tuladhar, S. M. Choulis, S. A. Nelson, J. Durrant, J. R. Bradley, D. D. C. Giles, M. McCulloch, I. Ha, C-S. Ree, M. (2005). A strong regioregularity effect in self-organizing conjugated polymer films and high-efficiency poythiophene: fullerene solar cells. *Nature Materials*, 5, p. 197-203.

Klauk, H. (ed.) (2012). *Organic Electronics II.* USA: Wiley-VCH.

Klimov, E. Li, W. Yang, X. Hoffman, G. G. Loos, J. (2006). Scanning Near-Field and Confocal Raman Microscopic Investigation of P3HT-PCBM systems for Solar Cell Applications. *Macromolucles.* 39, p. 4493-4496.

Kokubu, R. Yang, Y. (2012). Vertical phase separation of conjugated polymer and fullerene bulk heterojunction films induced by high pressure carbon dioxide treatment at ambient temperature. *Physical Chemistry and Chemical Physics*, 14, 8313-8318.

Koster, L. J. A. Milhailetchi, V. D. Blom, P. W. M. (2006). Bimolecular recombination in polymer/fullerene bulk heterojunction solar cells. *Applied Physics Letters*, 88, 052104, p.1-3.

Kovalenko, A. Guerrero, A. Garcia-Belmonte, G. (2014). Role of Vertical Seggregation in Semitransparent Organic Photovoltaics. *Applied Materials and Interfaces*, 7, p. 1234-1239.

Krebs, F. C. (ed) (2008). *Polymer Photovoltaics – A Practical Approach.* USA: SPIE.

Kroto, H. W. Heath, J. R. O'Brien, S. C. Curl, R. F. Smalley, R. E. (1985). C_{60}: Buckminsterfullerene. *Nature*. 318, p. 162-163.

Kuik, M. Koster, L. J. A. Wetzelaer, G. A. H. Blom, P. W. M. (2011). Trap-Assisted Recombination in Disordered Organic Semiconductors. *Physical Review Letters*, 107, p. 256805-1 – 256805-5.

Lampert, M. A. Mark, P. (1970). Current Injection in Solids. *Academic.* New York.

Langevin, P. (1903). *Ann. Chim. Physics*, 28, 433.

Leever, B. J. Bailey, C. A. Marks, T. J. Hersam, M. C. Durstock, M. F. (2012). In Situ Characterisation of Lifetime and Morphology in Operating Bulk Heterojunction Organic Photovoltaic Devices by Impedance Spectroscopy. *Advanced Energy Materials*. 2, p. 120-128.

Li, G. Yao, Y. Yang, H. Shrotriya, V. Yang, G. Yang, Y. (2007). "Solvent Annealing" Effect in Polymer Solar Cells Based on Poly(3-hexylthiophene) and Methanofullerenes. *Advanced Functional Materials*, 17, p. 1636-1644.

Li, G. Zhu, R. Yang, Y. (2012). Polymer solar cells. *Nature Photonics*, 6, p. 153-161.

Li, J. V. Nardes, A. M. Liang, Z. Shaheen, S. E. Gregg, B. A. Levi, D. H. (2011). Simultaneous measurement of carrier density and mobility of organic semiconductors using capacitance techniques. *Organic Electronics*, 12, p. 1879-1885.

Li, Y. Cao, Y. Gao, J. Wang, D. Yu, G. Heeger , A. J. (1999). Electrochemical properties of luminescent polymers and polymer light – emitting electrochemical cells. *Synthetic Metals*, 99, 243-248.

Li, Y. N. Vamvounis, G. Holdcroft, S. (2002). Tuning Optical Properties and Enhancing Solid-State Emission of Poly(thiophene)s by Molecular Control: A Postfunctionalization Approach. *Macromolecules*, 35, p. 6900–6906.

Liang, Y. Wu, Y. Feng, D. Tsai, S.-T. Son, H.-J. Li, G. Yu, L. (2009). Development of New Semiconducting Polymers for High Performance Solar Cells. *Journal of the American Chemical Society*, 131, p. 56–57.

Liang, Y. Yu, L. (2010). A New Class of Semiconducting Polymers for Bulk Heterojunction Solar Cells with Exceptionally High Performance. *Accounts of Chemical Research*, 43, p. 1227–1236.

Liao, H.-C. Ho, C.-C. Chang, C.-Y. Jao, M.-H. Darling, S. B. Su, W.-F. (2013). Additives for morphology control in high-efficiency organic solar cells. *Materials Today*, 16, p. 326-336.

Lof, R.W. van Veenendaal, M.A. Koopmans, B. Jonkman, H.T. Sawatzky, G.A. (1992). Band gap, excitons, and Coulomb interaction in solid C_{60}. *Physical Review Letters.* 68, p. 3924–3927.

Longo, C. Nogueira, A. F. De Paoli, M.- A. Cachet, H. (2002). Solid – State and Flexible Dye-Sensitized TiO_2 Solar Cells: a Study by Electrochemical Impedance Spectroscopy. *Journal of Physical Chemistry B*, 106, 5925-5930.

Lynn, P. A. (2010), *Electricity from Sunlight: An Introduction to Photovoltaics*, Wiley, UK.

Ma, W. Yang, C. Gong, X. Lee, K. Heeger, A. J. (2005). Thermally Stable, Efficient Polymer Solar Cells with Nanoscale Control of the Interpenetrating Network Morphology. *Advanced Functional Materials.* 15, p. 1617-1622.

Mao, H. Xu, B. Holdcroft, S. (1993). Synthesis and Structure – Property Relationships of Regioregular Poly (3-hexylthiophenes). *Macromolecules*, 26, p. 1163-1169.

Marks, R. N. Halls, J. J. M. Bradley, D. D. C. Friend, R. H. Holmes, A. B. (1994). The photovoltaic response in poly(p-phenylene vinylene) thin-film devices. *Journal of Physics: Condensed Matter*, 6, p. 1376-1794.

Mayer, A. C. Scully, S. R. Hardin, B. E. Rowell, M. W. McGehee, M. D. (2007). Polymer – based solar cells. *Materials Today*, 10 (11), p. 28 – 33.

Mayo, D. W. Miller, F. A. Hannah, R. W. (2003). Course Notes On The Interpretation of Infrared and Raman Spectra. Wiley – Interscience.

McCullough, R. D. (1998). The Chemistry of Conducting Polythiophenes. *Advanced Materials*, 10, p. 93-116.

McCullough, R. D. Tristram-Nagle, S Williams, S. P. Lowe, R. D. Jayaraman, M. (1993). Self-Orienting Head-to-Tail Poly(3-alkylthiophenes): New Insights on Structure-Property Relationships in Conducting Polymers. *Journal of the American Chemical Society*, 115, p. 4910-4911.

Messaad, K. Bosc, D. Haesaert, S. Thual, M. Lari, F., Froyer, G. Montembault, V. Henrio, F. (2008). Physical and Optical Properties of Poly(3-alkylthiophenes) with a View to the Fabrication of a Highly Nonlinear Waveguide. *The Open Materials Science Journal*, 2, p. 47-55.

Metz, B. Davidson, O. R. Bosch, P. R. Dave, R. Meyer, L. A. (eds.) (2007). *Contribution of Working Group III to the Fourth Assessment Report of the Intergovernmental Panel on Climate Change*. Cambridge University Press, UK.

Mihailetchi, V. D. Koster, L. J. A. Hummelen, J. C. Blom, P. W. M. (2004). Photocurrent generation in polymer-fullerene bulk heterojunctions. *Physical Review Letter*, 93, 216601

Mihailetchi, V. D. van Duren, J. K. J. Blom, P. W. M. Hummelen, J. C. Janssen, R. A. J. Kroon, J. M. Rispens, M. T. Verhees, W. J. H. Wienk, M. M. (2003). Electron Transport in Methanofullerene. *Advanced Functional Materials*. 13, p. 43-46.

Mihailetchi, V. D. Xie, H. de Boer, B. Koster, L. J. A. Blom, P. W. M. (2006). Charge Transport and Photocurrent Generation in Poly(3-hexylthiophene): Methanofullerene Bulk-Heterojunction Solar Cells. *Advanced Functional Materials*, 16, p. 699-708.

Milhailetchi, V.D. Xie, H. De Boer, B. M. Popescu, L. Hummelen, J. C. Blom, P. W. M. (2006). Origin of the enhanced performance in poly(3-hexylthiophene): [6,6]-phenyl C_{61}-butyric acid methyl ester solar cells upon slow drying of the active layer. *Applied Physics Letters*. 89, 012107, p. 1-3.

Miller, S. Fanchini, G. Yun-Yue, L. Cheng, L. Chun-Wei, C. Wei-Fang, S. Manish, C. (2008). Investigation of nanoscale morphological changes in organic photovoltaics during solvent vapour annealing. *Journal of Material Chemistry*, 18, p. 306-312.

Minami, T. (2008). Present status of transparent conducting oxide thin-film development for indium–tin–oxide (ITO) substitutes. *Thin Solid Films*, 516, p. 5822–5828.

Mora-Seró, I. Garcia-Belmonte, G. Boix, P. P. Vázquez, M. A. Bisquert, J. (2008). Impedance spectroscopy characterisation of highly efficient silicon solar cells under different illumination intensities. *Energy and Environmental Science*, 2, p. 678-686.

Mott, N. F. Gurney, R. W. (1940). *Electronic Processes in Ionic Crystals,* London: Oxford University Press.

Moulé, A. J. Bonekamp, J. B, and Meerhoz, K. (2006): The effect of active layer thickness and composition on the performance of bulk-heterojunction solar cells, *Journal of Applied Physics*, 100, 094503.

Nabok, A. (2005). *Organic and Inorganic Nanostructures*. USA: Artech House.

Nalwa, K. S. Kodali, H. K. Ganapathysubramanian, B. Chaudhary, S. (2011). Dependence of recombination mechanisms and strength on processing conditions in polymer solar cells. *Applied Physics Letters*, 99, 263301.

Nalwa, K. S. Mahadevapuraam, R. C. Chaudhary, S. (2011). Growth rate dependent trap density in polythiophenes-fullerene solar cells and its implications. *Applied Physics Letters*. 98, 093306, p. 1-3.

Nam, C-Y. Su, D. Black, C. T. (2009). High – Performance Air – processed Polymer – Fullerene Bulk Heterojunction Solar Cells. *Advanced Functional Materials.* 19, p. 3552-3559.

Nelson, J. (2002). Organic photovoltaic films. *Current Opinion in Solid State and Materials Science*, 6, p. 87-95.

Nelson, J. (2003). *The Physics of Solar Cells.* London: Imperial College Press.

Nelson, J. Gambhir, A. Ekins-Daukes, N. (2014). *Grantham Institute for Climate Change Briefing paper No 11*. Imperial College London.

Neville, R. C. (1978), *The Energy Conversion: The Solar Cell*, Elsevier, Amsterdam.

Nguyen, L. H. Hoppe, H. Erb, T. Günes, S. Gobsch, G. Sariciftci, N. S. (2007). Effects of Annealing on the Nanomorphology and Performance of Poly(alkylthiophen):Fullerene Bulk-Heterojunction Solar Cells. *Advanced Functional Materials*. 17, p. 1071-1078.

Norrman, K. Ghanbari-Siahkali, A. Larsen, N.B. (2005). Studies of spin-coated polymer films, *Annu. Rep. Prog. Chem. Sect*. C 101, p. 174–201.

Nunzi, J-M. (2002). Organic photovoltaic materials and devices. *C. R. Physique* 3, p.523-542.

O. Oklobia, T. S. Shafai, (2013). A quantitative study of the formation of PCBM clusters upon thermal annealing of P3HT/PCBM bulk heterojunction solar cell. *Solar Energy Materials and Solar Cells*, 117, p.1-8.

Oklobia, O. Shafai, T.S. (2013). A study of the donor/acceptor interfaces in a blend of P3HT/PCBM solar cell: Effects of annealing and PCBM loading on optical and electrical properties. *Solid-State Electronics.* 87, p. 64-68.

Onsager, L. (1934). Deviations from Ohm's Law in Weak Electrolytes. *The Journal of Chemical Physics*, 2, 599

Opitz, A. Wagner, J. Brütting, W. Salzmann, I. Koch, N. Manara, J. Pflaum, J. Hinderhofer, A. Schreiber, F. (2010). Charge Separation at Molecular Donor – Acceptor Interfaces: Correlation between Morphology and Solar Cell Performance. *IEEE Journal of Selected Topics in Quantum Electronics*, 16, p. 1707-1717.

Orimo, A. Masuda, K. Honda, S. Benten, H. Ito, S. Ohkita, H. Tsuji, H. (2010). Surface segregation at the aluminium interface of poly (3-hexylthiophene)/ fullerene solar cells. *Applied Physics Letters*, 96, 043305, p. 1-3.

Ouyang, J. Chu, C. Chen, F. Xu, Q. Yang, Y. (2004). Polymer Optoelectronic Devices with High-Conductivity Poly (3, 4-Ethylenedioxythiophene) Anodes. *Journal of Macromolecular Science*. 41 (12) p. 1497-1511.

p. 2067–2069.

Pacios, R. Bradley, D. D. C. (2002), Charge separation in polyflourene composites with internal donor/acceptor heterojunctions. *Synthetic Metals*, 127, p. 261-265.

Park, J. H. Kim, J. S. Lee, J. H. Lee, W. H. Cho, K. (2009). Effect of Annealing Solvent Solubility on the Performance of Poly(3-hexylthiophene)/Methanofullerenes Solar Cells. *Journal of Physical Chemistry C*. 113, p. 17579-17584.

Parlak, E. A. (2012). The blend ratio effect on the photovoltaic performance and stability of poly (3-hexylthiophene): [6, 6]-phenyl-C_{61} butyric acid methyl ester (PCBM) and poly (3-octylthiophene): PCBM solar cells. *Solar Energy Materials and Solar Cells*, 100, p. 174-184.

Peet, J. Kim, J. Y. Coates, N. E. Ma, W. L. Moses, D. Heeger, A. J. Bazan, G. C. (2007). Efficiency enhancement in low-bandgap polymer solar cells by processing with alkane dithiols. *Nature Materials*, 6, p. 497-500.

Peet, J. Senatore, M. L. Heeger, A. J. Bazan, G. C. (2009). The Role of Processing in the Fabrication and Optimization of Plastic Solar Cells. *Advanced Materials*, 21, p. 1521–1527.

Perepichka, I. F. Perepichka, D. F., Men, H. Wudl, F. (2005). Light-Emitting Polyhtiophenes. *Advanced Materials*, 17, p. 2281-2305.

Peter, S. (2009). *Electrical Characterisation of Organic Electronic Materials and Devices*, Wiley, New Jersey.

Petty, M. C. (2008). *Molecular Electronics: From Principles to Practice.* USA: Wiley.

Peumans, P. Uchida, S. Forrest, S. R. (2003). Efficient bulk heterojunction photovoltaic cells using small – molecular – weight organic thin films. *Nature*, 425, p. 158.

Pivrikas, A. Juška, G. Österbacka, R. Westerling, M. Viliūnas, M. Arluaska, K. Stubb, H. (2005). Langevin recombination and space-charge-perturbed current transients in regiorandom poly(3-hexylthiophene). *Physical Review B*, 71, 125205.

Pivrikas, A. Neugebauer, H. Sariciftci, N. S. (2011). Influence of processing additives to nano-morphology and efficiency of bulk-heterojunction solar cells: A comparative review. *Solar Energy*. 85, p. 1226-1237.

Quan, L. (2011). *Self-Organized Organic Semiconductors: From Materials to Device Applications*. Wiley: New Jersey.

Rand, B. P. Richter, H. (eds.) (2014). *Organic Solar Cells: Fundamentals, Devices, and Upscaling*. USA: CRC Press.

Reyes-Reyes, M. Kim, K. Carroll, D. L. (2005). High-efficiency photovoltaic devices based on annealed poly (3-hexylthiophene) and 1-(3-methoxycarbonyl)-propyl-1-phenyl-(6,6)C_{61} blends, *Applied Physics Letters,* 87, 083506.

Rispens, M. T. Meetman, A. Rittberger, R. Brabec, C. J. Sariciftci, N. S. Hummelen, J. C. (2003). Influence of the solvent on the crystal structure of PCBM and the efficiency of MDMO-PPV: PCBM 'plastic' solar cells. *Chemical Communications*. 17, p. 2116-2118.

Roman, L. S. Mammo, W. Petterson, L. A. A. Andersson, M. R. Inganäs, O. (1998). High quantum efficiency polythiophenes/C60 photodiodes. *Advanced Materials*, 10, p. 774-777.

Roman, L.S. (2005). Photovoltaic Devices Based on Polythiophene/C_{60}, In: Sam-Shajing, S., and Sariciftci, N.S. (eds.) *Organic Photovoltaics: Mechanisms, materials, and Devices.* Taylor and Francis, CRC.

Roncali, J. (1997). Synthetic Principles for Bandgap Control in Linear π-Conjugated Systems. *Chemical Reviews*, 97, p. 173-205.

Sariciftci, N. S. Braun, D. Zhang, C. Srdanov, V. I. Heeger, A. J. Stucky, G. Wudl, F. (1993). Semiconducting polymer-buckminsterfullerene heterojunctions: Diodes, photodiodes, and photovoltaic cells. *Applied Physics Letters*. 62, p. 585-588.

Scharber, M. C. Mühlbacher, D. Koppe, M, Denk, P. Waldauf, C. Heeger, A. J. Brabec, C. J. (2006). Design Rules for Donors in Bulk-Heterojunction Solar Cells – Towards 10% Energy – Conversion Efficiency. *Advanced Materials*, 18, p. 789-794.

Scherrer, P. (1918). Zsigmondy's Koloidchemie. *Nachr. Chaft.* 98, p.394.

Shaheen, S. E. Ginley, D. S. Jabbour, G. E. (2005). Organic – based photovoltaics: towards low-cot power generation. *MRS Bulletin*, 30, p. 10-19.

Shaheen, S.E. Vangeneugden, D. Kiebooms, R. Vanderzande, D. Fromherz, T. Padinger, F. Brabec, C.J. Sariciftci, N.S. (2001). Low band-gap polymeric photovoltaic devices. *Synthetic Metals*, 121, p. 1583-1584.

Shockley, W. Read, W. T. (1952). Statistics of the Recombinations of Holes and Electrons. *Physical Reviews*, 87, p. 835-842.

Shrotriya, V. Ouyang, J. Tseng, R. J. Li, G. Yang, Y. (2005). Absorption spectra modification in poly(3-hexylthiophene): Methanofullerenes blend thin films. *Chemical Physics Letters.* 411, p. 138-143.

Shrotriya, V. Yang, Y. (2005). Capacitance-voltage characterization of polymer light-emitting diodes. *Journal of Applied Physics*, 97, p. 1-5.

Shrotriya, V. Yao, Y. Li, G. Yang, Y. (2006). Effect of self-organization in polymer/fullerene bulk heterojunctions on solar cell performance. *Applied Physics Letters*. 89, 063505, p. 1-3.

Singh, J. (1994). *Semiconductor Devices.* McGraw-Hill: Singapore

Singh, J. Baessler, H. (1974). Solution of the Onsager Ion Recombination Model in One Dimension. *Physica Status Solidi b*, 63, p. 425-430.

Sirringhaus, H. Brown, P. J. Friend, R. H. Nielson, M. M. Bechgaard, K. Langwveld-Voss, B. M.W. Spiering, A. J. H. Janssen, R. A. J. Meijer, E. W. Herwig, P. de Leeuw, D. M. (1999). Two-dimensional charge transport in self-organized, high-mobility conjugated polymers. *Nature*, 401, p. 685 – 688.

Socrates, G. (2001). *Infrared and Raman Characteristic Group Frequencies: Table and Charts*. John Wiley & Sons

Streetman, B. G. (1995). *Solid State Electronic Devices*. Prentice-Hall, NJ, USA.

Stübinger, T. Brütting, W. (2001). Exciton diffusion and optical interference in organic donor-acceptor photovoltaic cells. *Journal of Applied Physics*, 90, 3632.

Sun, S-S. Sariciftci, N. S. (eds.). (2005). *Organic Photovoltaics: Mechanisms, Materials, and Devices*. USA: Taylor & Francis.

Sun, Y. Liu, J. Ding, Y. Han, Y. (2013). Decreasing the Aggregation of PCBM in P3HT/PCBM blend Films by Cooling the Solution. *Colloids and Surfaces A: Physicochemical and Engineering Aspects*. 421, p. 135-141.

Swinnen, A. Haelderman, I. vande Ven, M. D'Haen, J. Vanhoyland, G. Aresu, S. D'Olieslaeger, M. Manca, J. (2005). Tuning the Dimensions of C_{60} – Based Needlelike Crystals in Blended Thin Films. *Advanced Functional Materials*. 16, p. 760-765. *Synthetic Metals*, 87, p. 171–174.

Sze, S. M. (1985). *Semiconductor Devices Physics and Technology*. Wiley.

Sze, S. M. Kwok, K. N. (2007). *Physics of Semiconductor Devices.* John Wiley & Sons: New Jersey.

Tachiya, M. (1988). Breakdown of the Onsager theory of germinate ion recombination. *The Journal of Chemical Physics*, 89, 6929

Tan, N. N. Hung, T. D. Anh, V. T. BongChul, K. HyunChul, K. (2014). Improved patterning of ITO coated with gold masking layer on glass substrate using nanosecond fiber laser and etching. *Applied Surface Science*, 336, p. 163-169.

Tan, S. X. Zhai, J. Xue, B. Wan, M. Meng, Q. Li, Y. Jiang, L. Zhu, D. (2004). Property influence of polyanilines on photovoltaic behaviours of dye-sensitized solar cells. *Langmuir*, 20, p 2934-2937.

Tang, C. W. (1985). Two layer organic photovoltaic cell. *Applied Physics Letters*. 48, 183, p. 183-185.

Thompson, B. C. Fréchet, J. M. J. (2008) Polymer - Fullerene Composite Solar Cells. *Angewandte Chemie*, 47, p. 58-77

Tredgold, R. H. (1966). *Space Charge Conduction in Solids,* Elsevier: Amsterdam.

Tsakalakos, L. (ed.) (2010). *Nanotechnology for Photovoltaics*. Boca Raton: Taylor & Francis Group.

Tsoi, W. C. James, D. T. Kim, J. S. Nicholson, P. G. Murphy, C. E. Bradley, D. D. C. Nelson, J. Kim, J.-S. (2011). The Nature of In-Plane Skeleton Raman Modes of P3HT and Their Correlation to the Degree of Molecular Order in P3HT: PCBM Blend Thin Films. *Journal of the American Chemical Society*, 133 (25), p. 9834-9843.

Tsoi, W. C. Spencer, S. J. Yang, L. Ballantyne, A. M. Nicholson, P. G. Turnbull, A. Shard, A. G. Murphy, C. E. Bradley, D. D. C. Nelson, J. Kim, J-S. (2011). Effect of Cystallization

on the Electronic Energy Levels and Thin Film Morphology of P3HT: PCBM Blends. *Macromolecules*, 44, p. 2944-2952.

Tvingstedt, K. Vandewal, K. Gadisa, A. Zhang, F. Manca, J. Inganäs, O. (2009). Electroluminescence from Charge Transfer States in Polymer Solar Cells. *Journal of the American Chemical Society*. 131, p.11819-11824.

Tyagi, M. S. (1988). *Introduction to semiconductor materials and devices,* Wiley: Canada.

van Bavel, S. S. Bärenklau, M. de With, G. Hoppe, H. Loos, J. (2010). P3HT/PCBM Bulk Heterojunction Solar Cells: Impact of Blend Composition and 3D Morphology on Device Performance. *Advanced Functional Materials*, 20, p. 1458-1463.

Wang, C. Jimison, L. H. Goris, L. McCulloch, I. Heeney, M, Ziegler, A. Salleo, A. (2010). Microstructural Origin of High Mobility in High-Performance Poly(thieno-thiophene) Thin-Film Transistors. *Advanced Materials*, 22, p. 697-701

Wang, M. Xie, F. Du, J. Tang, Q. Zheng, S. Miao, Q. Chen, J. Zhao, N. Xu, J. B. (2011). Degradation mechanism of organic solar cells with aluminium cathode. *Solar Energy Materials and Solar Cells*, 95, p. 3303-3310.

Wang, M. Zheng, S. Wan, X. Su, Y. Ke, N. Zhao, N. Wong, K. Y. Xu, J. (2013). Limit of *V*oc in polymeric bulk heterojunction solar cells predicted by a double-junction model. *Solar Energy Materials and Solar Cells*, 108, p. 17-21.

Wang, Q. Moser, J-E. Grätzel, M. (2005). Electrochemical Impedance Spectroscopic Analysis of Dye-Sensitized Solar Cells. *Journal of Physical Chemistry B.* 109, p.14945-14953.

Watts, B. Belcher, W. J. Thomsen, L. Ade, H. Dastoor, P. C. (2009). A Quantitative Study of PCBM Diffusion during Annealing of P3HT: PCBM Blend Films. *Macromolecules*, 42, p. 8392-8397.

Wenham, S. R. Green, M. A. Watt, M. E. Corkish, R. (2007), *Applied Photovoltaics*, Earthscan, UK.

with polyethylene dioxythiophene-polystyrene sulfonate as the transparent anode.
Wöhrle, D. Meissner, D. (1991). Organic Solar Cells. *Advanced Materials*, 3, p. 129-138.

Woo, C. H. Thopmson, B. C. Kim, B. J. Toney, M. F. Fréchet, J. M. J. (2008). The Influence of Poly (3-hexylthiophene) Regioregularity on Fullerene-Composite Solar Cell Performance. *Journal of the American Chemical Society*. 130, p. 16324-16329.

Wu, S. Li, J. Tai, Q. Yan, F. (2010). Investigation of High-Performance Air-Processed Poly(3-hexylthiophene)/Methanofullerene Bulk Heterojunction Solar Cells. *Journal of Physical Chemistry C*, 114, p. 21873-21877.

X. Yang, J. Loos, S. C. Veenstra, W. J. H. Verhees, M. M. Wienk, J. M. Kroon, M. A. J. Michels, R. A. J. Janssen, Nano Letters, 5 (2005), 579-583.
Xin, H. Kim, F. S. Jenekhe, S. A. (2008). Highly Efficient Solar Cells Based on Poly (3-butylthiophene) Nanowires. *Journal of the American Chemical Society*, 130, p. 5424-5425.

Xu, Z. Chen, L.-M. Yang, G. Huang, C.-H. Hou, J. Wu, Y. Li, G. Hsu, C.-S. Yang, Y. (2009). Vertical Phase Separation in Poly(3-hexylthiophene): Fullerene Derivative Blends and its Advantage for Inverted Structure Solar Cells. *Advanced Functional Materials*, 19, p. 1227-1234.

Xue, B. Vaughan, B. Poh, C.-H. Burke, K. B. Thomsen, L. Stapleton, A. Zhou, X. Bryant, G. W. Belcher, W. Dastoor, P. C. (2010). Vertical Stratification and Interfacial Structure in P3HT: PCBM Organic Solar Cells. *Journal of Physical Chemistry*, 114, p. 15797-15805.

Yacobi, B. G. (2002). *Semiconductor Materials: An Introduction to Basic Principles*. USA: Kluwer Academic Publishers.

Yadav, B. C. Kumar, R. (2008). Structure, properties and applications of fullerenes. *International Journal of Nanotechnology and Applications*. 2, p. 15-22.

Yin, Z. Wei, J. Zheng, Q. (2016). Interfacial Materials for Organic Solar Cells: Recent Advances and Perspectives. *Advanced Science*, 1500362, p. 1-37.

Yoon, Y. Kim, H. J. Cho, C.-H. Kim, S. Son, H. J. Ko, M.-O. Kim, H. Lee, D.-K. Kim, J. Y. Lee, W. Kim, B. J. (2013). Carrier Lifetime Extension via the Incorporation of Robust Hole/Electron Blocking Layers in Bulk Heterojunction Polymer Solar Cells. *Applied Materials and Interfaces*, 6, p. 333-339.

Yu, G. Gao, J. Hummelen, J. C. Wudl, F. Heeger, A. J. (1995). Polymer Photovoltaic Cells: Enhanced Efficiencies via a Network of Internal Donor-Acceptor Heterojunctions. *Science*, 270, p. 1789-1791.

Yu, G. Heeger, A. J. (1995). Charge separation and photovoltaic conversion in polymer composites with internal donor/acceptor heterojunctions. *Journal of Applied Physics*. 78, p. 4510-4515.

Zen, A. Pflaum, J. Hirschmann, S. Zhuang, W. Jaiser, F. Asawapirom, U. Rabe, J. P. Scherf, U. Neher, D. (2004). Effect of Molecular Weight and Annealing of Poly(3-hexylthiophene)s on the Performance of Organic Field-Effect Transistors. *Advanced Functional Materials*, 14, p. 757–764.

Zhao, C. Qiao, X. Chen, B. Hu, B. (2013). Thermal annealing effect on internal electrical polarization in organic solar cells. *Organic Electronics*, 14, p. 2192-197.

Zhao, Y. Xie, Z, Qu, Y. Geng, Y. Wang, L. (2007). Solvent-vapour treatment induced performance enhancement of Poly(3-hexylthiophene): Methanofullerenes bulk-heterojunction photovoltaic cells. *Applied Physics Letters*. 90, 043504, p. 1-3.

Zhou, H. Yang, L. You, W. (2012). Rational Design of High Performance Conjugated Polymer for Organic Solar Cells. *Macromolecules*, 45, p. 607 – 632

Zhuo, Z. Zang, F. Wang, J. Wang, J. Xu, X. Xu, Z. Wang, Y. (2011). Efficiency improvement of polymer solar cells by iodine doping. *Solid-State Electronics*, 63, p. 83-88.